8-2020

Aeroacoustics of Supersonic Jet Interacting with Solid Surfaces and its Suppression

Seyyed Saman Salehian

AEROACOUSTICS OF SUPERSONIC JET INTERACTING WITH SOLID SURFACES AND ITS SUPPRESSION

By

Seyyed Saman Salehian

A Dissertation Submitted to the Faculty of Embry-Riddle Aeronautical University

In Partial Fulfillment of the Requirements for the Degree of

Doctor of Philosophy in Aerospace Engineering

August 2020

Embry-Riddle Aeronautical University

Daytona Beach, Florida

AEROACOUSTICS OF SUPERSONIC JET INTERACTING WITH SOLID SURFACES AND ITS SUPPRESSION

By

Seyyed Saman Salehian

This Dissertation was prepared under the direction of the candidate's Dissertation Committee Chair, Dr. Reda Mankbadi, Department of Aerospace Engineering, and has been approved by the members of the Dissertation Committee. It was submitted to the Office of the Senior Vice President for Academic Affairs and Provost, and was accepted in the partial fulfillment of the requirements for the Degree of Philosophy in Aerospace Engineering.

DISSERTATION COMMITTEE

Reda Mankbadi — Digitally signed by Reda Mankbadi, Date: 2020.07.28 20:19:14 -04'00'

Chairman, Dr. Reda Mankbadi

Anastasios Lyrintzis — Digitally signed by Anastasios Lyrintzis, Date: 2020.07.29 14:55:34 -04'00'

Member, Dr. Tasos Lyrintzis

Vladimir Golubev — Digitally signed by Vladimir Golubev, Date: 2020.07.30 20:12:30 +03'00'

Member, Dr. Vladimir Golubev

Eduardo Divo — Digitally signed by Eduardo Divo, Date: 2020.07.30 10:29:52 -04'00'

Member, Dr. Eduardo Divo

Marwan Al-Haik — Digitally signed by Marwan Al-Haik, DN: cn=Marwan Al-Haik, o=Embry Riddle Aeronautical University, ou=Aerospace Engineering, email=alhaikm@erau.edu, c=US, Date: 2020.07.31 16:42:38 -04'00'

Graduate Program Coordinator, Dr. Marwan Al-Haik

7/31/2020

Date

Dean of the College of Engineering, Dr. Maj Mirmirani

8/1/2020

Date

Senior Vice President for Academic Affairs and Provost, Dr. Lon Moeller

8/3/20

Date

ACKNOWLEDGEMENTS

I wish to express my sincere gratitude to my Ph.D. advisor, Dr. Reda Mankbadi, for his continued support, guidance, and encouragement throughout the years I have had the pleasure of knowing him and working under his supervision. A special thanks goes to my committee members, Dr. Tasos Lyrintzis, Dr. Vladimir Golubev, and Dr. Eduardo Divo, for their invaluable insight and incentive, throughout this research.

I would like to appreciate the support of Florida Center for Advanced Aero-propulsion (FCAAP). Consultations with Dr. Jonas Gustavsson of FCAAP, Florida A&M University/Florida State University, provided valuable information on interpretation of experimental measurements for the supersonic impinging jet. A special thanks goes to Dr. Konstantine Kurbatskii of ANSYS, INC, for his guidance and recommendations, which resulted in the implementation of novel numerical approaches and beta-testing the features of the numerical solver. The helpful suggestions by Mr. Mohsen Batoei of ESI North America is greatly appreciated. I would also like to thank Dr. James Bridges of Acoustics Branch at NASA Glenn Research Center for providing guidance and perspective on objectives sought after by the NASA Fundamental Aeronautics Program.

The simulations presented in this research were carried out using the VEGA cluster with the support of the High-Performance Computing (HPC) at Embry-Riddle Aeronautical University.

Last but not least, I would like to thank my dear family, for their never-ending support and love that has always been the light to my darkest hours.

ABSTRACT

The noise generated by supersonic jet is of primary interest in the high-speed flight. In several flight conditions jet exhaust of the propulsion system interacts with solid surfaces. For example, jet impingement on ground for a rocket lift-off, or interactions influenced by the integration of the engine with the airframe. Such complex applications require consideration of the role of acoustic-surface interactions on the noise generation of the jet and its radiation. Numerical analysis of supersonic jet noise involved in these scenarios is investigated by employing Hybrid Large Eddy Simulation – Unsteady Reynolds Averaged Simulation approach to model turbulence.

First, the supersonic impinging jet noise reduction using aqueous injectors is investigated. The technique employed to suppress impingement noise, involves injecting liquid water from the ground surface. The Volume of Fluid model is adopted to simulate the two-phase flow. The flow field and acoustic results agree well with the existing experimental data. The possible mechanisms of noise reduction by water injection are investigated.

Second, supersonic jet noise reduction by employing the shielding effect of a flat plate parallel to the jet is investigated. The numerical simulations model the shielding effect of the flat plate on the acoustics of supersonic jet, and results agree with the corresponding experimental data. The physical mechanisms involved in the flow-surface interactions are investigated. With understanding these mechanisms, a slightly wavy plate is proposed including theoretical background to determine the parameters needed for the way wall to provide acoustic reduction efficiently. Results show that the proposed wavy shield can effectively reduce both the level and extent of the jet noise source as compared to that of a flat shield.

TABLE OF CONTENTS

LIST OF FIGURES

Figure Page

Figure Page

Figure Page

Figure Page

Figure Page

Figure Page

Figure Page

Figure Page

LIST OF TABLES

SYMBOLS

$\boldsymbol{T}$	Viscous stress tensor, Lighthill stress tensor
$\boldsymbol{D}$	Deformation gradient tensor
$\boldsymbol{j}$	Diffusive heat flux
$\boldsymbol{\Psi}$	General dependent tensor field
$\boldsymbol{T}$	Viscous stress tensor
$\boldsymbol{u}$	Velocity vector
A	Amplitude
L	Length Scale
M	Mach number, Momentum flux
F	Volumetric force
E	Volumetric energy
U	Velocity in jet exhaust direction
S	Volumetric energy heat source, rate of strain tensor
D	Equivalent hydraulic diameter of the rectangular nozzle
H	Heaviside step functions
T	Temperature, recorded period
Q	Heat flux
R	Specific gas constant
u_i, or u, v, w	Velocity component along x, y, z directions respectively
x_i, or x, y, z	Cartesian coordinate
t	Time
k	Turbulent kinetic energy, von Karman constant

f	Frequency, Shielding function, flux
r	Radial distance, distance between source and observer
c	Speed of sound
d	Nozzle diameter
m	Mass
h	Vertical distance of the shielding plate from the nozzle lip
p	Pressure
τ	Stress tensor
St	Strouhal number
Re	Reynolds number
ρ	Density
α	Volume phase fraction, coefficient
δ	Kronecker delta
θ	Observer angle with respect to the impinging jet axis
ψ	Observer angle with respect to the free/shielded jet axis
μ	Dynamic viscosity
λ	Wavelength
ν	Kinematic viscosity
ϕ	Phase shift
Ω	Vorticity tensor
ω	Specific dissipation rate

Accent Marks

$\bar{}$	Time-averaged quantity
$\hat{}$	Fourier transform, normal component
$\vec{}$	Vector
$\dot{}$	Time rate of change

Superscripts

LES	LES component
$RANS$	RANS component
$'$	Fluctuating component
$+$	Positive direction
$-$	Negative direction
j	Jet exit quantity

Superscripts

max	Maximum value
min	Minimum value
p,q	Phase identification in VOF formulation
t	Turbulence quantity
th	Nozzle throat quantity
TE	Trailing edge quantity
o	Stagnation quantity
a	Ambient quantity
n	Normal component

w	Water quantity
$wall$	Wall quantity

ABBREVIATIONS

AMG	Algebraic Multi Grid
ANC	Active Noise Control
AR	Aspect Ratio
BBSAN	Broadband Shock Associated Noise
CAA	Computational Aeroacoustics
CFD	Computational Fluid Dynamics
CFL	Courant-Friedrichs-Lewy
DES	Detached Eddy Simulation
DNS	Direct Numerical Simulation
DRP	Dispersion Relation Preserving
DOP	Duct Over Pressure
EPNdB	Effective Perceived Noise in dB
FAA	Federal Aviation Administration
FAR	Federal Aviation Regulation
FFT	Fast Fourier Transform
FWH	Ffowcs Williams-Hawkings Method
HLU	Hybrid LES URANS
HWB	Hybrid Wing Body
ILU	Incomplete Lower Upper
IOP	Ignition Over Pressure
LEE	Linearized Euler Equations
LES	Large Eddy Simulation

LRM	Linear Relaxation Method
LST	Lighthill Stress Tensor
MFR	Mass Flow Ratios
NPR	Nozzle Pressure Ratio
OASPL	Overall Sound Pressure Level
ODE	Ordinary Differential Equations
PAA	Propulsion Airframe Aeroacoustics
PIV	Particle Image Velocimetry
QAT	Quiet Aircraft Technology
QSL	Quasi-Static Loads
QueSST	Quiet Supersonic Technology
RANS	Reynolds Averaged Navier-Stokes
RMS	Root Mean Square
SBES	Stress-Blended Eddy Simulation
SDES	Shielded Detached Eddy Simulation
SGS	Sub Grid Scale
SIF	Surface-Integration Formulation
SLH	Specific Latent Heat
SPL	Sound Pressure Level
SRB	Solid Rocket Booster
TKE	Turbulent Kinetic Energy
TVD	Total Variation Diminishing
URANS	Unsteady Reynolds Averaged Navier-Stokes

VLES	Very Large Eddy Simulations
VOF	Volume of Fluid
V/STOL	Vertical and/or Short Take-Off and Landing
WMLES	Wall-Modeled Large-Eddy Simulation

1. Introduction and Literature Review

The Federal Aviation Administration (FAA) in the U.S. has implemented detailed noise certification requirements in Federal Aviation Regulation (FAR, 2005). For instance, the maximum noise levels should not exceed the limit of 108 in Effective Perceived Noise in decibels (EPNdB) during approach and flyover stages. Such limitations have motivated various research efforts to predict and control un-installed engine noise. However, engine noise is modified because of the installation on the aircraft. Most conventional aircraft engines now use high bypass ratio configurations, which increases its size and may intensify the installation effects. Jet noise is a key component of the engine noise and it could be the most affected component due to the airframe integration, or any possible interaction with the solid surfaces. Such interactions can modify noise generation and radiation significantly, and if these effects are understood, the interaction with the solid surface can even be utilized to minimize noise radiation.

The noise generated by supersonic jet is of primary interest in the design of high-speed flight vehicle. In several flight conditions jet exhaust of the propulsion system interacts with solid surfaces. For example, jet impingement on ground for a rocket lift-off, or interactions influenced by the integration of the engine with airframe, require consideration of the role of such interactions on the generated noise. Various scenarios where jet-solid surface interaction is involved, are categorized for both aircraft and rockets. The flow physics involved in these situations and the sources of the radiated noise are identified and reviewed. Next, computational approaches are reviewed and their appropriateness to the present complex situation are discussed. Finally, the techniques

and approaches to mitigate the jet noise are reviewed. In addition, relevant and appropriate approaches for the scenarios where the jet is interacting with solid surfaces are discussed.

1.1. The Physics of Supersonic Jet Noise in Aircraft and Interaction Situations

Supersonic jet noise can be a deterministic factor in the design of future military and high-speed commercial aircrafts. Current aircraft designs may employ complex geometry exhaust systems to maximize efficiency or reduce noise. The subsonic jet engines have benefited from the large bypass ratio design, by means of improving the engine efficiency and noise emission. For supersonic aircraft, sonic boom has been the most investigated issue. This has led to embedded engine designs which often exhaust gases over aft-airframe surfaces.

NASA has led the Quiet Aircraft Technology (QAT) program and has included the aeroacoustics effects of installation, or Propulsion Airframe Aeroacoustics (PAA) (Thomas, 2003). Integration of the engine and airframe puts the engine exhaust near the aircraft's surfaces and leads to jet-surface interaction noise. These surfaces may be integrated with the propulsion system such that, can be used to shield observers on the ground from exhaust noise. On the other hand, scenarios such as: supersonic jet exhaust interaction with the ground plane, ground effects of Vertical and/or Short Take-Off and Landing (V/STOL), and supersonic jet impingement on blast deflectors on aircraft carrier decks, all involve interaction of the supersonic jet with solid surfaces. First, the sources of noise are reviewed here, then the physics behind the interaction of jet with solid surface is followed.

1.1.1. Origin of Noise in Aircraft

Aircraft noise emission is one of the undesirable environmental effects in aviation. It can lead to public annoyance, sleep disruption, negative effect on academic performance of children, and in addition to its possible hearing hazards, it could increase the risk for cardiovascular disease of people living in the vicinity of airports (Basner et al., 2017). Various components of a complex system such as the conventional mid-range transport aircraft shown in Figure 1.1, correspond to noise generating mechanisms. Generally, aircraft noise sources can be categorized into airframe and engine noise sources for conventional aircraft configurations.

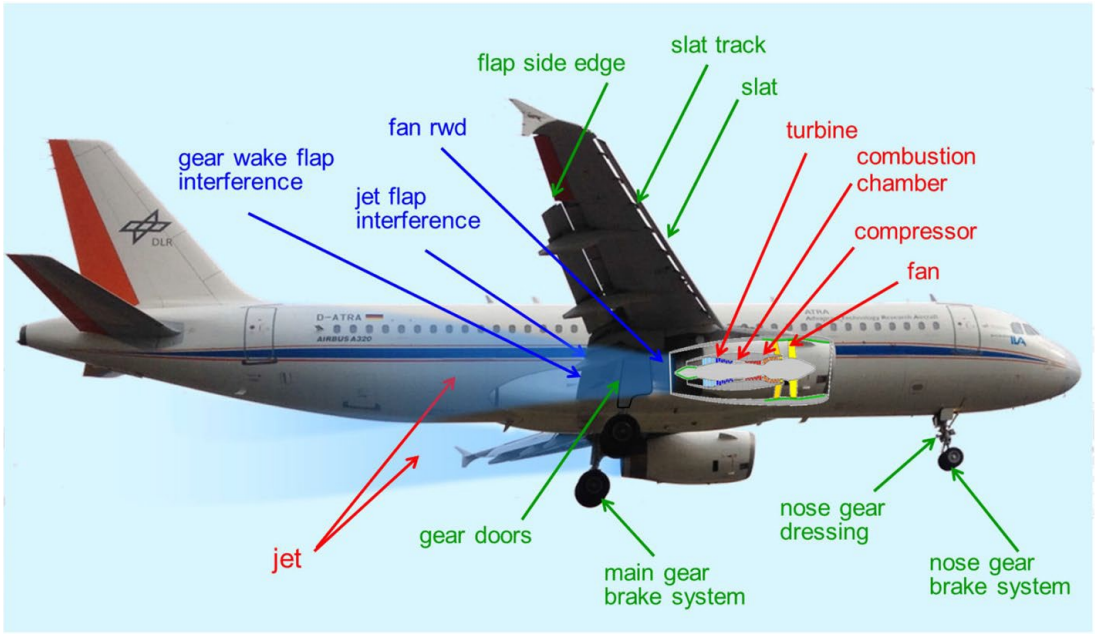

Figure 1.1 The aircraft noise components (Bertsch et al., 2019).

Airframe components play significant role in the overall aircraft noise generation. The contribution of the airframe has become more prominent with the evolution of high bypass ratio engines. Airframe noise can be much more significant in the approach phase than the takeoff phase, as it is illustrated in Figure 1.2. In this figure, the maximum

perceived noise level in dB is illustrated for each component during takeoff. To mitigate airframe noise, a thorough understanding of the inherent mechanisms behind the noise generation becomes crucial.

Although, the airframe self-generated noise is an important factor, the principal noise source, especially during takeoff, is the engine, as it can be seen in Figure 1.2. The main noise sources originate from fan/compressor, turbine, and exhaust jet. Compressor and turbine noise results from the interaction of pressure fields and turbulent wakes from rotating blades and stationary vanes. The introduction of a single fan significantly reduces the compressor and jet noise in high-bypass engines. However, jet noise remains the significant component in takeoff, which is of specific importance since during takeoff the source of noise are near observers and instrumentations on the ground.

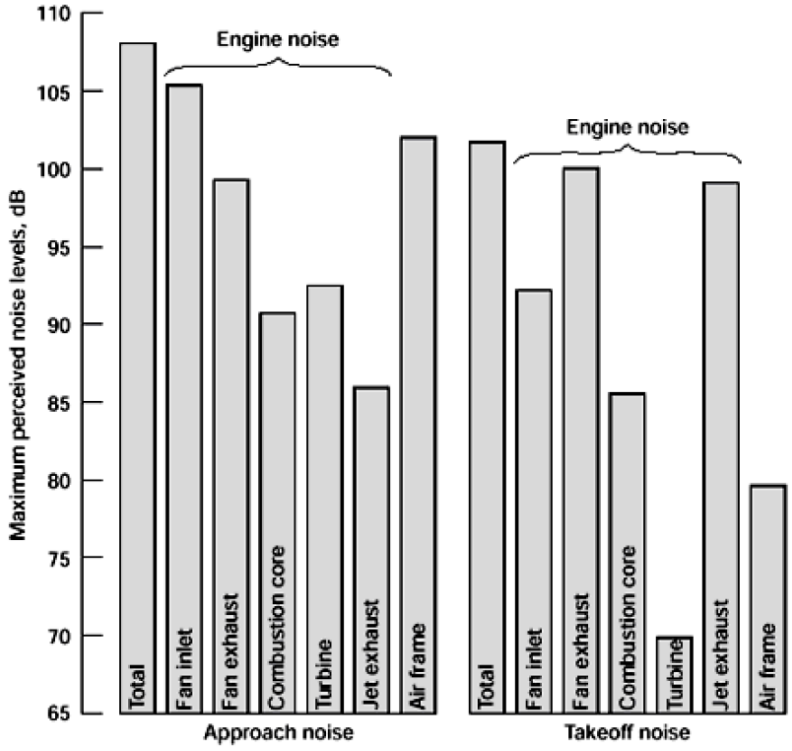

Figure 1.2 Typical modern aircraft noise levels (Gliebe, 2003).

1.1.2. The Physics of Free Jet and Its Radiated Noise

Jet exhaust noise is caused by the unsteady flow fluctuations in the jet shear layer which is due to the turbulent mixing of the exhaust gases with the atmosphere. The small structure turbulent created near the exhaust duct have high energy and cause high frequency noise but downstream of the exhaust, jet the larger structures, create low frequency noise. In addition, for supersonic jets the shock pattern formed inside the jet core, produces additional noise.

Lighthill's (1952, 1954) acoustic analogy has been the main theory towards understanding jet noise and the quadrupole nature of the sources of the jet mixing noise. Later investigations by Schlinker (1975) and Laufer et al. (1976), suggested models that include two sources. In their observations of high supersonic jets, the locations and distributions of the noise sources radiated to the 90^o and those radiated to the 150^o directions were distinctly different, suggesting existence of two noise sources in the turbulence of the jet flow. These angles were measured from nozzle exit. Other researchers (Crow & Champagne, 1971; Brown & Roshko, 1974) reported the observation of large coherent structures in turbulent jets and free shear layers as an addition to the classical small-scale turbulence.

The large turbulence structures could be sought to be due to nonlinear instabilities (Kelvin–Helmholtz instability waves) generated near the nozzle exit, which grow quickly as convected or propagated downstream. Figure 1.3 shows the fine-scale turbulence that can be addressed as a compact source (Tam et al., 2008). However, the large turbulence structures of full-scale jet engines are non-compact sources that are coherent over distances comparable to the jet diameter. Figure 1.4 illustrates the large turbulence

structures in the mixing layer of a Mach 1.3 jet studied by Thurow et al. (2003).

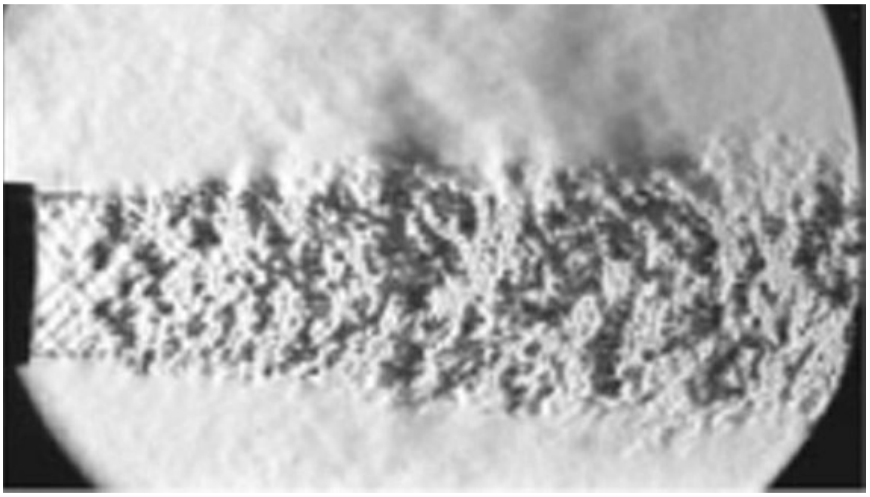

Figure 1.3 Spark schlieren photograph of a Mach 1.4 jet (Tam et al., 2008).

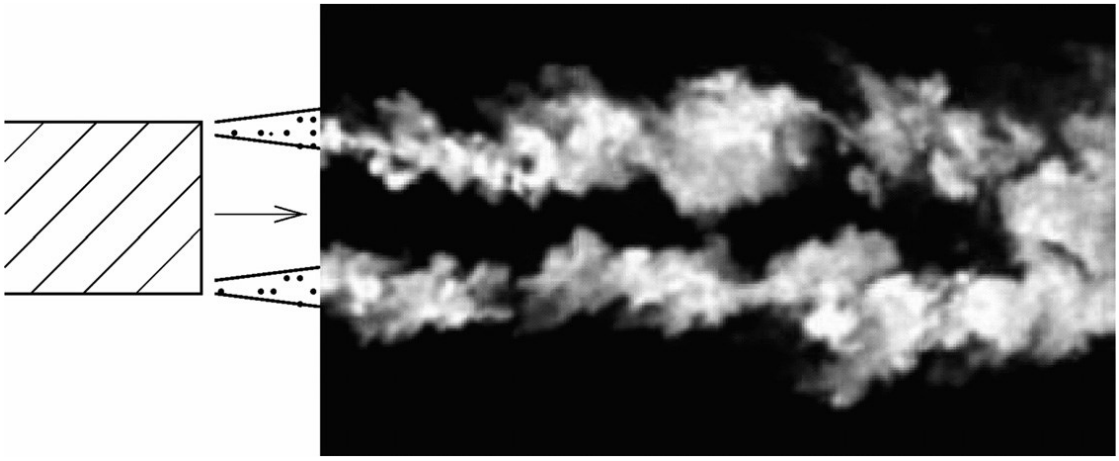

Figure 1.4 Large turbulence structures in the mixing layer of a Mach 1.3 jet (Thurow et al., 2003).

Generally, the scales of the structures are defined relative to the jet diameter, the small turbulent eddies dimensions are much smaller than the jet diameter, while the dimensions of the large-scale structure are of the same order as the jet diameter. Further

investigation (Dahl & Papamoschou, 2000; Tam & Zaman, 2000; Viswanathan 2002, 2004) have used the similarity spectra fit based on experimental measurements to support the two-noise source model proposed earlier (Tam & Chen, 1994; Tam 1995). The fine scale turbulence noise dominates in the sideline and upstream directions. However, the large turbulence structures noise radiates primarily downstream (Tam, 2009). This confirms the earlier hypothesis of Mankbadi and Liu (1984) in calculating the noise as based on two sources, the large-scale structure, and the fine-scale turbulence.

In addition to the turbulent mixing noise, there is another source of noise for imperfectly expanded jets which induce a shock-cell structure inside the flow. The interaction of the turbulence in the jet mixing layer with the shock cell system is responsible for the so-called "shock-associated" noise component of jet noise. Shock-associated noise includes two distinct components: 1) tonal screech noise, and 2) broadband noise.

Screech noise is studied initially by Powell (1953) and subsequently studied by other researchers (Davies & Oldfield, 1962; Powell et al.,1992). Raman (1999) summarize the knowledge and efforts towards understanding screech tones. The model addressed by these studies suggests that an acoustic feedback-loop between the nozzle and shock structures, explains the tone generation mechanism of supersonic jets. Based on this model, vorticity disturbances that originate from the nozzle lip are convected downstream and interact with the shock-cell pattern of the jet plume. The consequent acoustic waves of this interaction propagate back to the nozzle where they initiate new disturbances, closing the loop.

Broadband shock-associated noise (BBSAN) is also related to screech due to their

similar generation mechanism, except the resonant loop (André et al., 2013). The BBSAN is initially investigated by Martlew (1969), followed by Harper-Bourne and Fisher (1973) adapting Powell's model. Extensive studies were carried out by Norum and Seiner (1982), who associated pressure and turbulence fluctuation levels to acoustic measurements. Tam (1990) assumed that screech suppresses the BBSAN, and according to the observation of the pressure measurements by Norum and Seiner (1982), suggested that strong screech tones cause a rapid disintegration of the shock-cell structure, leading to the BBSAN attenuation.

Another irritating component of supersonic jet noise, initially investigated by Ffowcs-Williams et al. (1975), is referred to as crackle noise. Crackle is characterized by intermittent positive pressure fluctuations radiating downstream at an angle associated with the peak jet noise. Such waves are somewhat different from Mach waves which are long, straight and have about equal angles. The crackle waves are mainly due to the high kinematics of the heated supersonic jets and are characterized by the presence of strong positive pressure impulses resulting in a strongly skewed far-field pressure signal. Such strong positive pressure impulses are associated with N-shaped waveforms involving a shock-like compression; Hence, crackle noise is very annoying to observers when it occurs. Unlike broadband shock-associated noise which dominates at upstream angles, crackle reaches a maximum at downstream angles associated with the peak jet noise directivity.

1.1.3. Jet Parallel to a Surface

One can consider two situations of jet-parallel surface interactions. In the first one, the distance between the jet and wall is zero, so it resembles a wall jet flow. In the second

situation, the jet is parallel to the wall but there is a distance between the jet and the surface, so sound reflection is a factor.

In certain aircraft configurations, high-speed jets are exhausted near parallel solid surfaces which significantly affect the flow field and the noise generation. Another situation of jet-parallel surface scenario is observed in aircraft carriers or runways when supersonic jets from aircraft interact with the ground during takeoff and landing operations. The strong levels of noise generated by the jet and the interaction of these waves with the ground become a dangerous safety hazard for those who work near the aircraft.

From the conceptual point of view, the reflection and diffraction of the waves emitted from the jet due to the presence of wing can also be regarded as jet interaction with solid surfaces some distance away. Head and Fisher (1976) studied the interaction between an unheated jet and a reflective surface. They observed some effects on noise due to reflections from the wall. The low frequency was found to be influenced by the near-field edge diffraction of the quadrupole noise source. The high frequency increase was attributed to the incoherent noise reflection off the lower surface of the wing (Southern, 1980). Moreover, Brown and Ahuja (1984) performed parametric study on the interaction between the jet noise and wing, their results show similar trends as that of Head and Fisher (1976) in terms of low frequency augmentation and high frequency increase.

Mead and Strange (1998) investigated the under-the-wing installation effects on jet noise. They reported the measurement of the high installation noise level in the low frequency range. They carried out experiments under static conditions and the effect of forward flight was not considered. The forward flight effect is extremely important in the

interaction between the flow around the wing-flap and the jet. Several investigations were conducted at the Boeing company (Bhat & Blackner, 1998; Blackner & Bhat, 1998; Shivashankara & Blackner, 1997) to include the effect of forward motion of the aircraft. Bhat (1998) studied the sensitivity of installation noise to a range of parameters, such as the wing-flap settings, jet engine location, and pitching angle. The installation effect was reported to increase noise up to 6 dB.

Following these experiments, some empirical prediction methods were developed to determine installation noise (Bhat & Blackner, 1998; Lu, 1986). Since the noise levels were high, many studies focused on reduction technologies. Mengle et al. (2006) investigated the effect of chevrons on installed engines. Their experimental results show that the installation effects of chevrons in conventional nozzles are reversed at approach and takeoff. This trend is not observed in isolated nozzles. In addition, it was reported that certain azimuthally varying chevrons give larger total installed noise benefits at both conditions compared to conventional chevrons.

The interaction of the exhaust jet and flaps can generate new noise sources, which is mainly known as jet–flap interaction noise. The principal mechanism is believed to be the impact of the downwash of the wing-flap on the jet flow. Figure 1.5 illustrates interaction between the jet and wing in the conventional under-the-wing configuration. Generally, the acoustic waves emanated from the jet hit the aerodynamic surfaces, and the reflection of such waves may influence the instability waves near the nozzle as they exit the shear layer and modify the turbulent structure of the jet.

Such modifications in the flow field are referred to as new sources of noise that change the perceived noise. Since the real configuration of jet-wing-flap is rather

complex, the effect of flaps on the jet is mostly investigated independently.

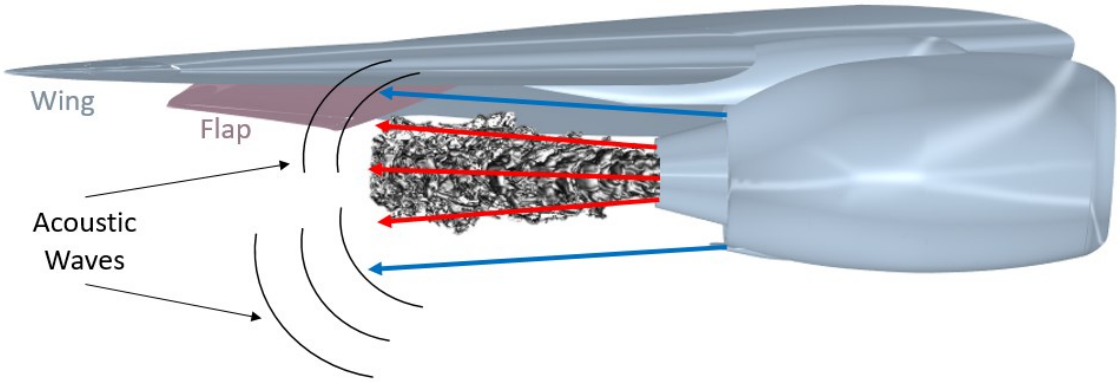

Figure 1.5 Schematics of jet flow and acoustic wave interactions with aerodynamic surfaces.

Due to the complexity of the installation effects of the jet-flap interactions, some studies have investigated this configuration along with pylon effects. For example, Faranosov et al. (2016) performed experiments for a typical swept wing with an installed dual-stream nozzle and removable pylon. The effect of flap deflection angle on jet-flap interaction noise was studied with and without the pylon for static and flight conditions. These experiments show that for both cases of with and without the pylon, jet-flap interaction noise remains qualitatively the same and is very sensitive to the flap deflection angle for static and flight conditions. However, the intensity of jet-flap interaction noise increases for the full configuration with the pylon installed.

Another scenario of jet-parallel flow is when propulsion systems are embedded on top of the aircraft with the aim of shielding jet noise and maximizing aircraft performance, such as in the Hybrid Wing Body (HWB) concept (Liebeck, 2002). Czech et al. (2012) investigated a configuration with the pylon-oriented opposite to the airframe surface

together with chevron design and showed a considerable shielding effectiveness and overall noise reduction compared to isolated jet noise. A Hybrid Wing Body configuration under NASA's N+2 tested by Henderson and Doty (2012), enhances the design by moving the engine nacelles forward of the trailing edge to effectively shield the engine aft noise, as shown in Figure 1.6 from Heath et al. (2013). Form the jet noise reduction perspective, this design mainly relies on the jet shielding. Papamoschou and Mayoral (2011) considered enhancing aft-body effect as illustrated in Figure 1.7 and studied optimizing the HWB effect on noise reduction.

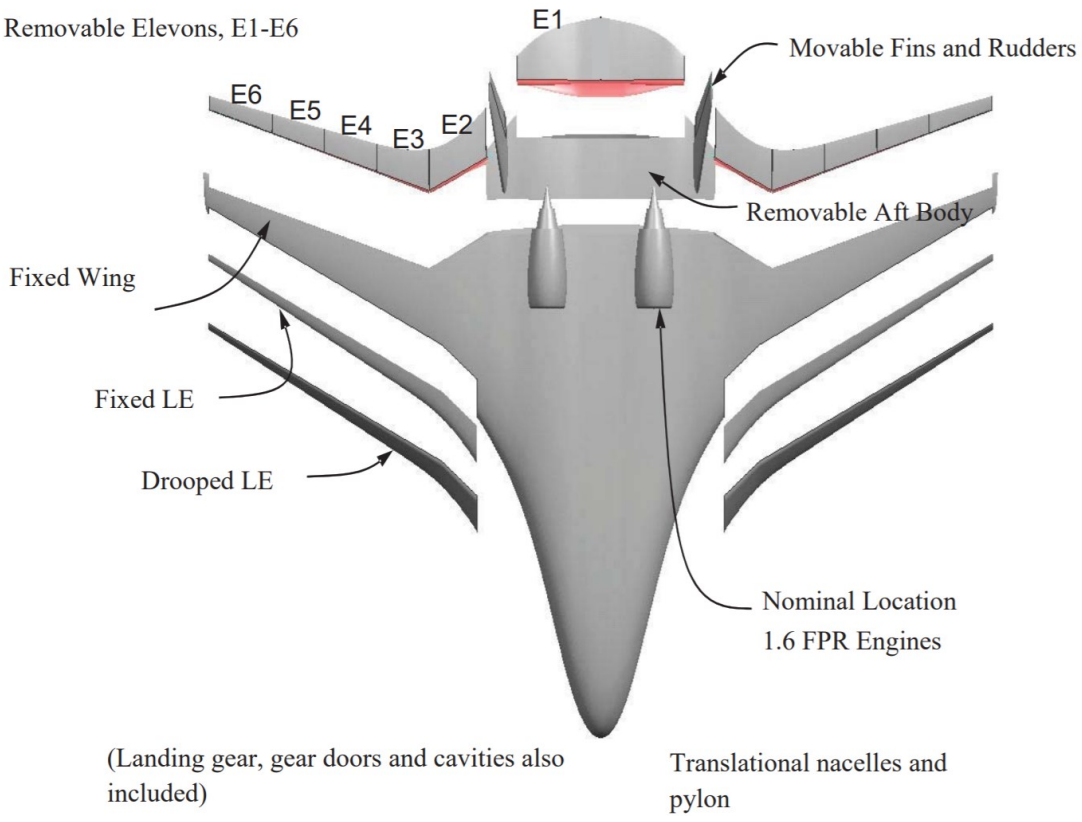

Figure 1.6 General HWB arrangement (Heath et al., 2013).

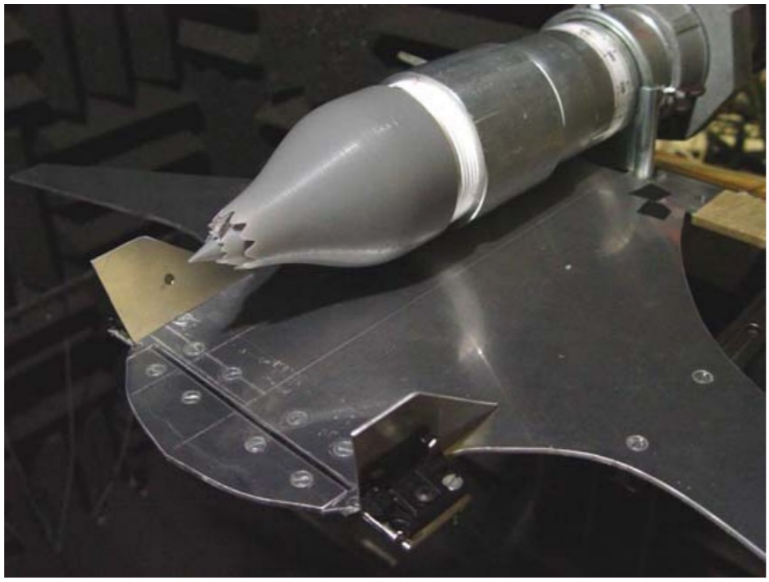

Figure 1.7 Test configurations of the shielding design of the HWD (5.8% scale model of the engine nozzle) (Papamoschou & Mayoral, 2011).

1.1.4. Jet Impingement on a Solid Surface

During certain configurations, high-speed jet of an aircraft engine is exhausted either normal to a solid surface, or with some inclination angle. These scenarios are shown in Figure 1.8 and Figure 1.9. The main application of the normal impingement investigation is related to V/STOVL aircraft in hover. High speed jet impingement leads to significant unsteady loads on the vehicle surface and increases the noise levels. Generally, noise generation mechanism in impinging jets are believed to originate from feedback-loop. The feed-back loop is investigated by several researchers (Henderson et al., 2005; Ho & Nossier,1981; Krothapalli et al., 1999; Nossier & Ho, 1982). The feedback-loop starts as instability waves in the initial jet shear layer, which amplifies and becomes vortical structures. The vortical structures are reflected upon impingement, create large pressure fluctuations and travel back upstream as acoustic waves, and when they reach the nozzle exit, they excite the shear layer instabilities completing the feedback-loop.

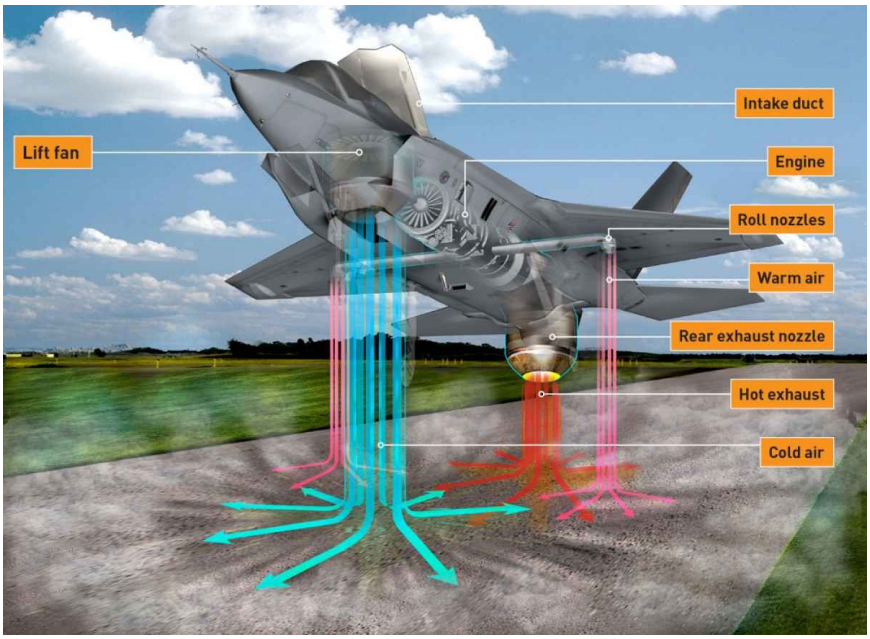

Figure 1.8 F-35B in hover (Infosources, 2018).

Figure 1.9 F-14 Tomcat launching from the aircraft carrier USS Kitty Hawk (US Department of Defense, 2018).

Another scenario of jet impingement occurs when blast deflectors are used for military aircrafts. One of the main areas of interest is the aircraft carrier environment.

Noise conditions on the flight deck of naval vessels have motivated researchers concerned with the health and safety of crew members. During aircraft takeoff and landing maneuvers, the sources and directionality of typical free jets are influenced by additional parameters, such as an acoustically reflective ground plane or the exhaust deflector. During takeoff of a conventional aircraft on the confined flight deck of carriers, the jet exhaust impinges on a jet blast deflector to divert high temperature flow away from nearby aircraft and personnel. This results in flow field and acoustic signature to be significantly altered due to the physical interference of the deflector with the jet flow.

Nonomura et al. (2011) simulated a Mach 2 jet impinging on a flat plate at an incidence angle of 45 deg, and predicted the existence of three primary acoustic waves: 1) Mach waves generated in the shear layer of the main jet, 2) acoustic waves generated from the jet impingement, and 3) Mach waves generated in the shear layer of the outward-propagating wall jet. Following up on these categories, Akamine et al. (2015) experimentally investigated types 2 and 3 acoustic waves, and concluded that type 2 waves originate from a spatially compact region surrounding the impingement point, propagating upstream at broad angles from the impingement surface, whereas type 3 waves emanate from a distributed region along the wall jet, propagating at shallow angles along the impingement surface.

1.2. The Physics of Supersonic Jets in Rockets

The extreme nature of acoustic environments near the plume of rockets, requires understanding of the vibroacoustic loading placed on space vehicles during launch. The acoustic loads can be harmful to the payload, vehicle structure, propellant storage, as well as electronics and navigational component. Identification of the sources responsible for

noise generation are crucial to assess applicability of any noise suppression system idea. Lubert (2017) reported that noise levels of rockets are around 170 – 200dB and are concentrated in the low-to-mid frequency range, and this is exactly the range where the transmitted energy and power can cause damage to buildings and humans.

1.2.1. Sources of Noise in Rockets

One of the early studies of noise generated by rockets was published by Cole et al. (1957) for rockets with thrusts of 4500 – 580,000 N. The acoustic measurement reported as dimensionless frequencies suggested relevance to previous findings in the jet noise studies. In addition, Cole et al. (1957) found that the overall sound power generated by rockets could not be predicted based on Lighthill's (1952) theory for subsonic jets. Their data indicated a dependence on velocity to the fourth power. Although some similarities were found in terms of noise sources of rocket exhausts and the term “supersonic jets”, it should be noted that the speed of sound in a rocket exhaust is close to three times the speed of sound in ambient. Thus, in the maximum sound source region, the mean flow remains supersonic with respect to the speed of sound in the atmosphere.

Cole et al. (1975) suggested that, entrainment of the cooler atmospheric air and heat transfer from the rocket plume would both acts to reduce the speed of sound in the plume, thus decreasing the peak frequency of the radiated sound. Moreover, the general opinion of research community agreed on Mach wave radiation to be the main mechanism of noise radiation, as reported by McInerny (1990).

It is also generally agreed by recent researchers (Allgood et al., 2011) that in rocket engines there are three types of supersonic jet noise: broadband shock-associated noise, screech tones and turbulent mixing noise. Ground acoustic data measured during launch

is typically referred to as near or far-field. Following ignition, the engine exhaust is deflected out. Typically, the exhaust trench is covered, and acoustic levels on the vehicle peak as the plume begins to splash over the pad a few seconds after ignition. Later attempts towards understanding the noise sources of moved towards the lift-off noise (launch pad noise), to account for the complex time dependent phases of rocket launch.

1.2.2. Lift-Off (Normal and Inclined Impingement)

Panda et al. (2011, 2012, 2014) have tested a 5% scaled model of the Ares I vehicle in a static firing to determine the noise sources with different types of water injection and different elevations of the vehicle. Panda et al. (2014) reported that that the noise sources during liftoff of the Antares vehicle were found to vary with time.

During engine ignition, the launch mount was the source. As the engine came to full power and the hot plume came out of the duct, the exit face of the duct was found to be the most prominent source. Hence, suggested effectiveness of cooling by duct water to keep acoustic levels to a reasonable value in this phase. As the rocket started to elevate, hot plume spread over the pad, and a large region on the top of the pad became a loud noise source. As more and more plume emerged out of the hole, the plume itself became the noise source, and duct exhaust was no longer a source.

A key finding of these studies was to show that, during the rocket launching, the flow field of engine exhaust impingement behaves differently at varying lift-off heights, which is defined as the distance between the nozzle exit and the launch platform. Hence, the flow field and acoustic sources vary during lift-off. Apart from rocket launch tests, simplified models for the two configurations of engine exhaust impingements, the normal and inclined jets impinging on plates have been extensively studied.

The nearfield flow structures of an impinging jets depend primarily on the operational conditions of the nozzle (Mach number of the jet at the nozzle exit, the ratio of the static pressure at the nozzle exit to the ambient static pressure), like free jets. For impinging jets, the flow field is also affected by the impingement, the distance from the nozzle exit to the intersection point of the jet axis and the impinged surface. In practice, its nondimensional form is preferred, which is usually normalized by the nozzle exit diameter. The flow field of the normal impinging jet is like those in the free jet in a certain region near the nozzle exit, which is called the free jet region. The region downstream of the free jet region and close to the plate is called the impingement region, and the region where the wall jet emerges is called the wall jet region (Jiang et al., 2019). The comparison of flow field structure of the normal impinging jets and the free jets are illustrated in Figure 1.10 and Figure 1.11, respectively. Flow structures in the free jet region resembles a similar feature as in the free jet under the same nozzle operational conditions.

The structure of the reflected shocks may resemble a conical shape (Henderson, 2002), and slipstreams would appear at the triple points, where the incident shocks, the reflected shocks and the Mach disk intersect. When the jet is not extremely under-expanded, quasi-periodic shock cells could appear repeatedly (Franquet, 2015). The shear layers would merge at the jet axis as the jet develops downstream, causing nearfield shock structures disappear and thence the potential core of the jet ends. When the impinged plate is near the potential core, there would be further interaction between the impinging jet and the plate (Jiang et al., 2019). Iwamoto (1990) reported that in the impingement region, variation of impingement distance (for the same pressure ratio and

jet Mach number), does not affect the distance between the standoff shock and the plate, as well as the locations of the shock cells upstream of the standoff shock.

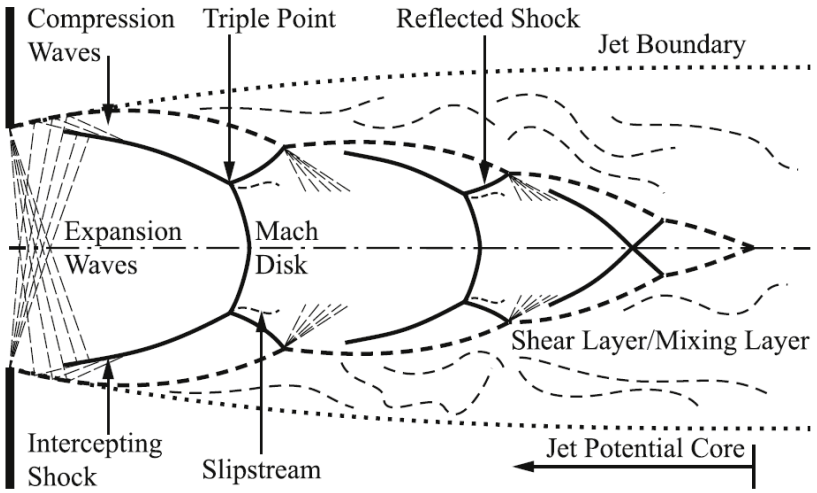

Figure 1.10 Schematics of an under-expanded free jet (Jiang et al., 2019).

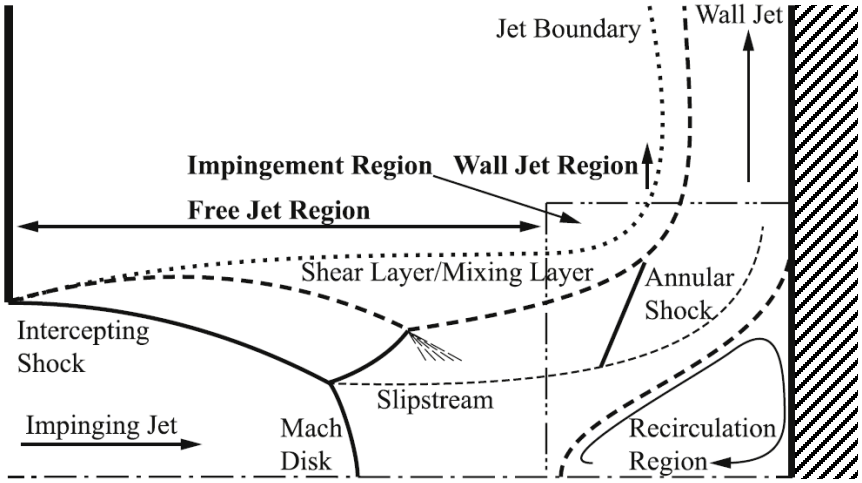

Figure 1.11 Normal impinging jet (Jiang et al., 2019).

Large rockets are usually launched from launch pads, which include deflector system. The deflector system is designed such that the exhaust impinges onto the deflector and

deflects away from the rocket. The impinging jet may induce standoff shocks (or plate shocks) and wall jets. The flow structures of inclined impinging jets resemble those of normal impinging jets under a small inclined angle, while the flow downstream of the impingement region would be more complex as the inclined angle increase (Nakai et al., 2006). Such modifications in the shock structure in the impingement region can be observed in Figure 1.12.

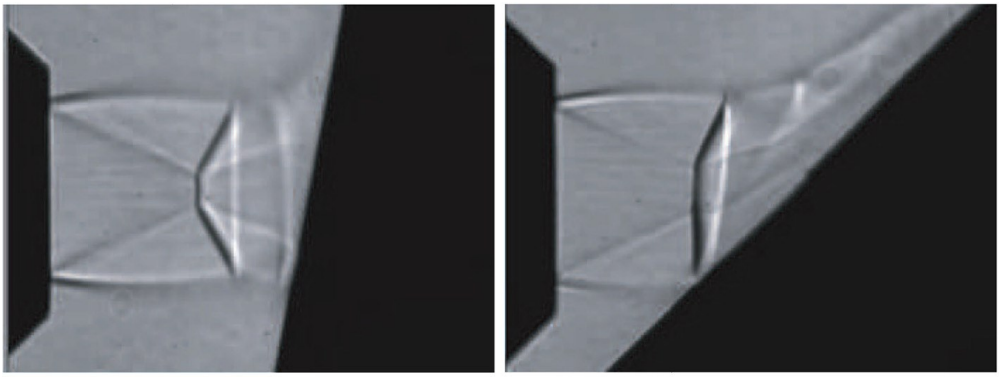

(a) $\theta = 10°$ (b) $\theta = 45°$

Figure 1.12 Schlieren graphs of inclined impinging jets with different inclined angles (Chan et al., 2014).

1.2.3. Blast-Off

The ignition of Solid Rocket Booster (SRB) is a dangerous moment during the launch of heavy lift rockets. This transient is characterized by the generation of a strong Ignition Over Pressure (IOP) wave in the exhaust hole (Osipov, 2015). The IOP wave may propagate toward the vehicle and potentially cause vehicle.

The overpressure is composed of the Ignition Overpressure (IOP), which emanates from the launch table, and of the Duct Over Pressure (DOP), which emanates from the launch ducts. Several studies (Alestra, 2003; Ikawa, 1985; Troclet et al., 1999) agree on

definitions of waves emanated during blast off. Figure 1.13 illustrates this point with a picture of the ARIANE 5 launch pad. The overpressure is a deterministic load case, presenting discrete spikes at some frequencies depending on the geometrical configuration of the launch pad, with significant levels for frequencies lower than 20 Hz. This low-frequency excitation excites the launch vehicle and induces Quasi-Static Loads (QSL) at the payload/launcher interface, which the payload must endure. Hence, it is very important to predict these loads launches. Troclet et al. (2007) attempted to identify the sources of launch and showed good identification of the multi-parameter sources in the 0 – 40 Hz frequency domain, with partial acoustic data (launcher upper part sensors).

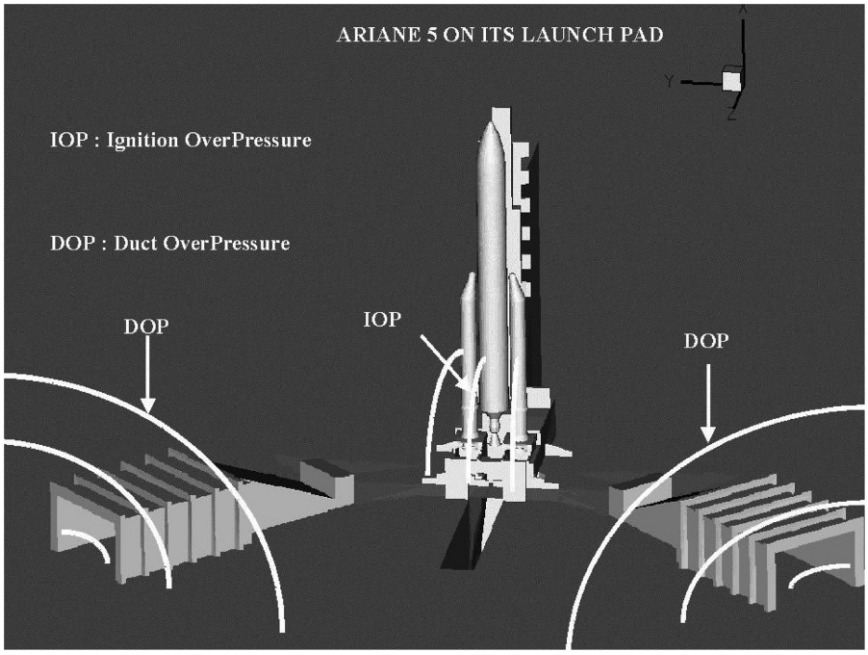

Figure 1.13 Definition of the overpressure waves (Troclet et al., 2007).

1.3. Noise Computation Approaches

Jet noise is produced by the unsteady turbulent fluctuations in the jet. Reynolds-

Averaged Numerical Simulations (RANS) can predict turbulence only by means of time-averaged quantiles. But, the time-averaged quantiles do not directly produce noise, it is the time-varying that is needed. Thus, prior to 1990, industry relied on empirical formulas for prediction of engine noise. The success of such approach is limited particularly when addressing new designs that include various options for propulsion-airframe integration. We discuss here how jet noise can be calculated with and without the airframe integration effects.

In the 80's, lacking full computational power, an attempt to calculate the jet noise produced by the Large eddies was given by Mankbadi and Liu (1984) and is compared with the experiment of Lush (1971). They modeled the large eddies as a wave packet with a radial profile that follows that of the nonlinear stability theory. Thus, the unsteady Navier-Stokes equations can be transformed into a set of Ordinary Differential Equations (ODE), which are easier to solve computationally. The solution is then plugged into Lighthill's equation to obtain the far field. Their solution shows that the large eddies are responsible for the peak noise, as demonstrated in Figure 1.14. This opened a new avenue: namely, instead of attempting to resolve all the turbulence scales, we resolve only the large scales, which was shown by Mankbadi and Liu (1984) to be responsible for the peak noise. Thus, Large Eddy Simulations (LES) may be adequate for resolving the noise-efficient sources.

In the early 1990's Computational Aeroacoustics (CAA) were developed in which the aerodynamically-generated noise is predicted based on direct computation of the governing equations. The full, compressible, time-dependent Navier-Stokes equations govern the noise generation and propagation process. Conventional Computational Fluid

Dynamics (CFD) codes based on Reynolds-Averaged equations are not appropriate for calculating sound. Noise is obtained via numerically capturing the unsteady, small oscillations in the pressure signal. This is not a trivial task, as discussed below.

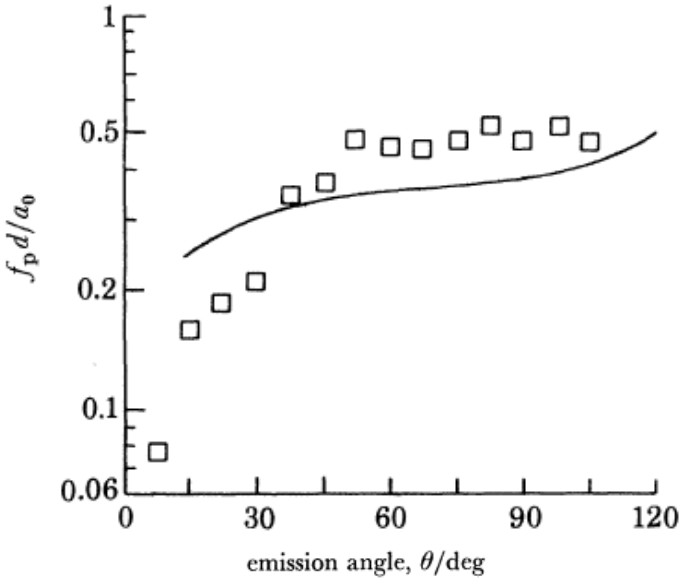

Figure 1.14 Peak of jet noise predicted by Mankbadi and Liu (1984) and compared with experimental data of Lush (1971).

1.3.1. Numerical Issues in Capturing the Unsteady Flow and Noise Scales

Capturing the noise sources requires capturing the unsteady flow in the noise - producing region. For the exhaust noise, the source of jet noise is the turbulence created by the jet mixing with the surrounding air. Jet mixing noise in subsonic jets is "broadband" in nature (that is, it spans a broad frequency range without having specific tone content), and it is centered at relatively low frequencies ($St \sim 0.5$). Supersonic jets have additional shock-related noise components that generally peak at a higher frequency than the mixing noise. To explain the flow physics, let us consider the flow structure in a round jet. The flow region can be split into three regimes: an initial region, transitional,

and fully developed. The initial region is where most of the noise is generated. The shear layer at the nozzle lip grows and expands until it reaches the center line. This marks the end of the potential core, where the mean centerline velocity is constant. The length of the potential core can vary from $x/d = 6$ for subsonic flows to $x/d = 12$ for supersonic flows.

The dominant noise sources in the initial region can sometimes be classified into two modes. The jet column mode, which peaks at Strouhal number based on the diameter of about $0.5 - 0.8$. The other is the shear-layer mode, which scales with the lip momentum thickness (about 3% of the diameter) and peaks at Strouhal number based on the momentum thickness around 0.01. The supersonic flow may be complicated further by the presence of shock waves. The generated acoustic waves are about 10^{-4} of the mean flow. Because the long propagation field, numerical dispersion and dissipation can alter the sound frequency and dampens the amplitude. Therefore, to capture such small oscillations a high-order discretization scheme is needed. Some of the schemes widely used in computational aeroacoustics includes high-order MacCormack-type schemes (Hixon, 1997), Compact Scheme (Lele, 1992), and Dispersion Relation Preserving (DRP) scheme (Tam & Webb, 1993). A review of high-order computational schemes is provided by Kurbatskii and Mankbadi (2004).

Boundary Treatments: Even if the numerical discretization scheme used is of high order, the acoustic field may not be properly captured. The computational domain must be finite and boundary conditions must be applied in an approximate way at the boundaries. The later usually downgrades the accuracy level, dampens the acoustic waves, or creates spurious modes. Therefore, various new boundary treatments were

developed and tested to allow the acoustic waves to properly propagate through the boundaries. Outflow treatments were developed based on asymptotic analysis of the linearized Euler equation. Radiation boundary conditions were developed based on the asymptotic solution of the acoustic wave radiation, among others (Giles,1990; Hixon et al., 1995; Mankbadi & Ali, 1999; Thompson, 1990). Figure 1.15 shows the effect of various boundary treatments in computing the sound field associated with an acoustic source in a uniform flow. As the figure shows, spurious modes are created at the inlet or outlet, which are minimized when the boundary treatment described by Tam and Webb (1993) is used.

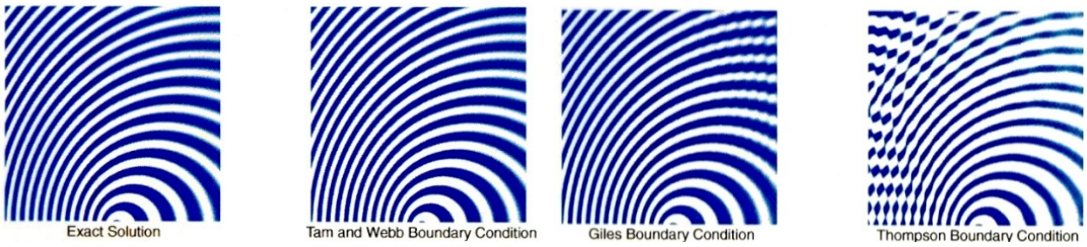

Figure 1.15 Effect of implementing various boundary treatments on the calculated acoustic field associate with an acoustic monopole in a uniform flow (Hixon et al., 1995).

1.3.2. Extension of the Near Field to the Far Field

Since the FAA noise restrictions are based on sound measurements away from the aircraft, usually experimental data of the radiated noise is taken far from the aerodynamically- generated noise sources. So, the far-field sound needs to be calculated. The noise generation process is usually nonlinear, and it is computationally expensive. On the other hand, the sound propagation is usually a linear process because the amplitude of the pressure waves is small. If the noise source is identified by some means,

then several techniques can be used for calculating the associated radiated noise.

Lighthill's Acoustic Analogy: In the pioneering work of Lighthill (1952), the governing Navier-Stokes equations are manipulated such that the left-hand side represents the wave equation while the right-hand side represents the sound source. The radiated sound field is then obtained as a volume integral of the time dependent Lighthill Stress Tensor (LST), $\rho u_i u_j$. But, since the time-fluctuating of Lighthill's stresses cannot be obtained with Reynolds-averaged CFD, only empirical models were used in utilizing Lighthill's to estimate the far field noise that led to questionable results. However, in the study by Mankbadi and Liu (1984) the Lighthill stress tensor was calculated by integrating the time dependent NSE across the radius and using the nonlinear stability theory to obtain the shape of the radial profiles.

Solution of the resulting ODE enabled calculating, for the first time, the noise sources in a round jet based on the unsteady NSE. This made it possible to conduct the Lighthill's volume integration while using the time-dependent sources and with proper accounting for the retarded time. The results have shown that this wave-like Large Scale structure is responsible for producing the peak noise at the measured spectra, and in explaining the forwarded quadrupole type directivity pattern. The seminal work of Lighthill was extended by Ffowcs-Williams and Hawkins (1969) to account for the presence of solid boundaries. This enabled tackling situations where solid boundaries exist, such as prediction of rotor noise or jet-airframe interactions.

Kirchhoff Method: Lyrintzis and Mankbadi (1996) proposed the use of Kirchhoff formulation to predict jet noise. However, this method was proposed earlier by George and Lyrintzis (1986) and was described by Lyrintzis (1994). In this formulation, an

enclosed surface is established around the source regime. It is assumed that the pressure distribution and its derivatives on this surface is known and that the process outside of it is linear. A surface integral solution of the governing wave equation is then obtained for sound radiation in terms of both the pressure signal as well as its normal derivative on the surface. The method is simple compared to Lighthill's, but both the pressure and its normal derivative are needed on the surface, which are to be obtained through a numerical solution of the governing equations inside Kirchhoff's surface. The computational results are usually not very accurate close to the boundaries because of the boundary treatment approximations, and this is particularly true for the normal derivatives. Therefore, Kirchhoff results suffer from the drawback of dependency on the location of Kirchhoff's surface. This drawback is resolved by Mankbadi et al. (1998), wherein a new Surface-Integration Formulation (SIF) is obtained which requires only the pressure signal on the Kirchhoff's surface.

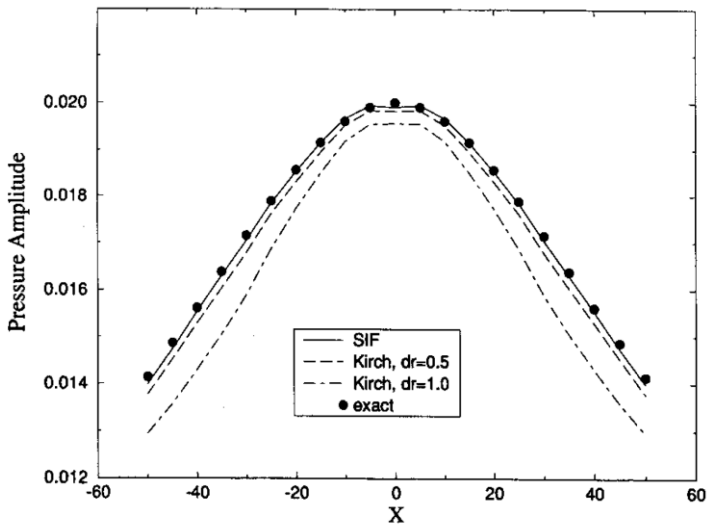

Figure 1.16 The radiated acoustic field associated with a point source inside a cylindrical surface calculated using Kirchhoff's method and with the pressure-only method of (Mankbadi et al., 1998).

Figure 1.16 shows the result of Kirchhoff compared with Mankbadi et al. (1998) in predicting the noise radiation by a point source. The figure shows that Kirchhoff results are dependent on the accuracy to of calculating the pressure derivative, which makes it strongly grid dependent. The Mankbadi et al. (1998) method using only the pressure (but not its derivative) does not suffer from this problem. For more details on integral methods, see the review by Lyrintzis (2003).

1.3.3. Large Eddy Simulations

Because of the size of the computation domain, the accuracy needed, and the large Reynolds numbers, Direct Numerical Simulations (DNS) of the full Navier-Stokes equations to resolve all the scales are not practically feasible. Therefore, use of LES is more attractive, where the unresolved scales are modeled using a simple turbulence mode. While these small scales are not resolved, their effect on the resolved scales is accounted for.

A detailed review on the application of LES approach for jet noise prediction is given by Lyrintzis and Coderoni (2020). The first LES-based computation of the noise sources in a supersonic jet was given in Mankbadi et al. (1994). LES is used to compute the noise sources while Lighthill theory is used to predict the corresponding far-field noise. The first-numerically obtained picture of Lighthill stress tensor in a supersonic jet is shown in Figure 1.17. We note the wavy-like nature of the Lighthill stress model that cause the pressure fluctuations shown in Figure 1.17, much like the semi-analytically derived by Mankbadi and Liu (1981). In the later, the large-scale structure was obtained via the nonlinear, integral instability theory for the largescale structure coupled with the presence of fine-grained random turbulence.

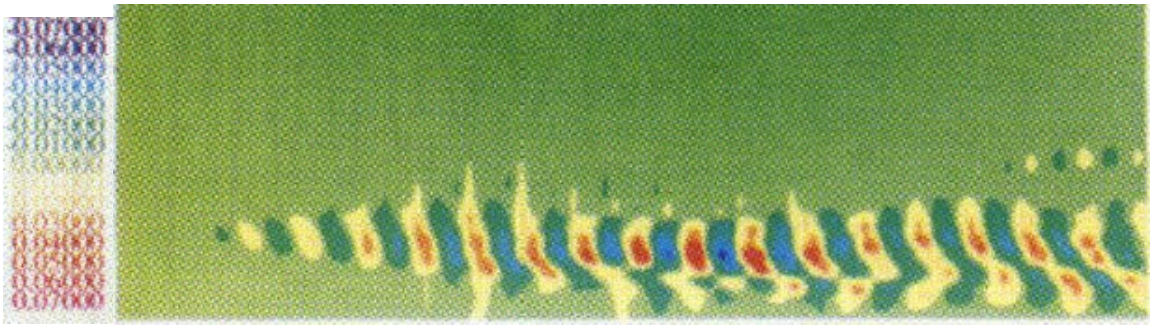

Figure 1.17 Lighthill Stress tensor St =0.5 (Mankbadi, 2008).

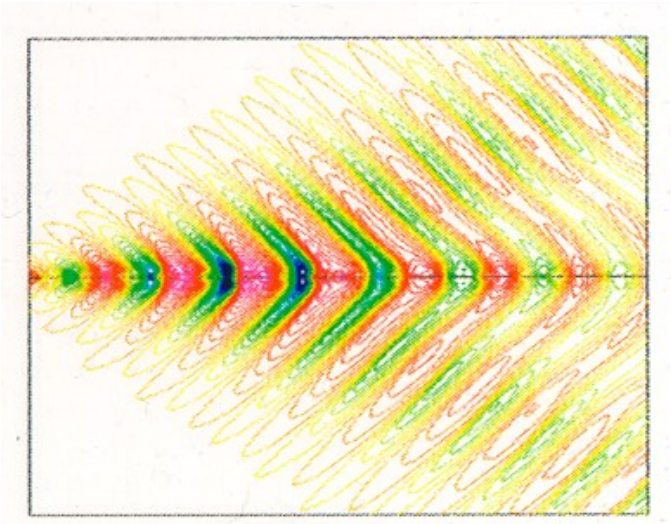

Figure 1.18 Pressure from the LES of an axisymmetric supersonic jet (Mankbadi, 2008).

LES was then developed to capture both the noise generation and propagation by Mankbadi et al. (2000). The results shown in Figure 1.17 and Figure 1.18 are for an unheated jet at the Mach number of 2.1 and Reynolds number of 70,000. These results are compared in Figure 1.19 with the corresponding experimental results of Trout and McLaughlin (1982) and shows good agreement. In Figure 1.20 LES of Mach 2.1 jet is illustrated when excited by the first helical mode as obtained from the linear instability theory. The figure shows that in this case the 3D nature of the pressure field is enhanced.

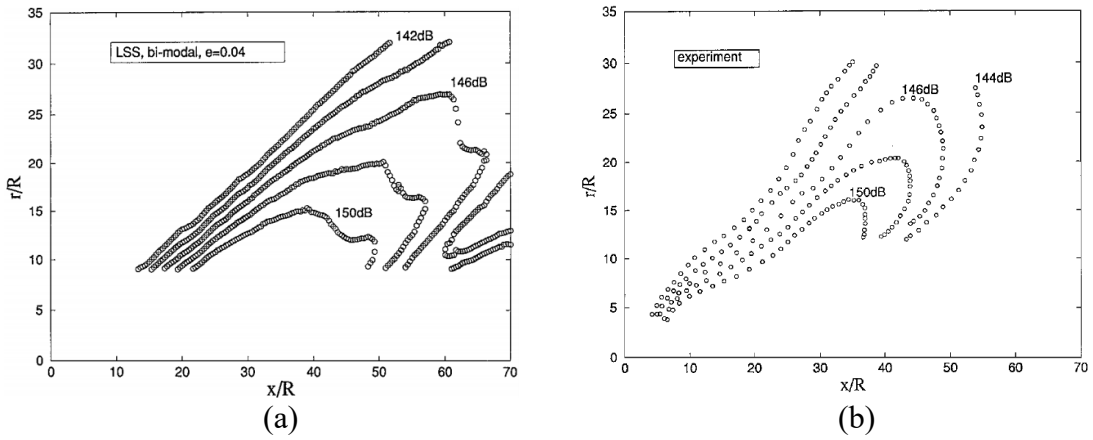

Figure 1.19 (a) Large-scale simulations of supersonic jet noise. (Mankbadi et al., 2000). Compared with (b) the corresponding experimental data (Trout & McLaughlin, 1982).

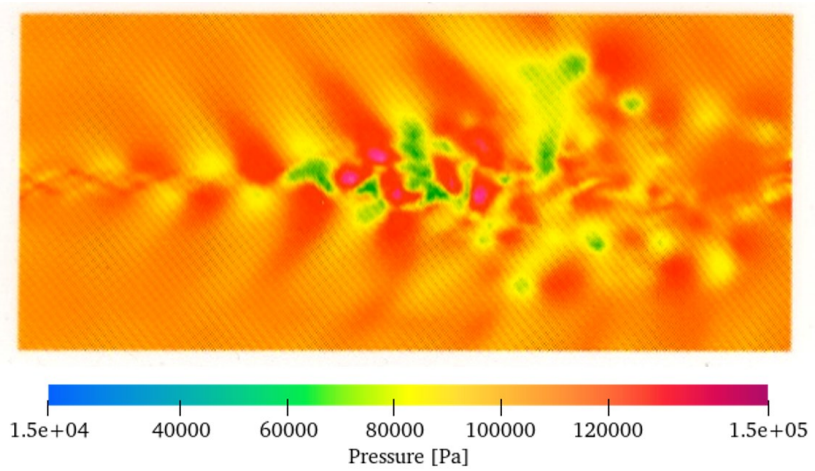

Figure 1.20 Full 3D LES simulations of a supersonic jet at M=2.1 excited at the first helical mode showing the pressure near (Mankbadi, 2008).

1.3.4. Faster Simulations Using Linearized Euler Equations

Linearized Euler Equations (LEE) has been proposed both as an extension technique, as well as for directly predicting the unsteady noise sources in the flow field along with its radiated noise. For using LEE only as an extension technique, Shih et al. (1997) developed a less expensive approach in which LES is used to solve the noise-generation

region, but LEE is used outside of this region wherein the process is linear and inviscid. The results were practically the same as the corresponding full LES but with less CPU requirements.

LEE is expected to perform well in capturing noise propagation but is usually not thought for capturing the nonlinear noise generation process. However, Mankbadi et al. (1998) showed that for supersonic jets free from shocks, LEE can successfully capture the noise generation process for a given mean flow. Thus, LEE can be used for prediction of noise generation as well. The results of Mankbadi et al. (1998), though linear, agreed quite well with the experimental results (Trout & McLaughlin, 1982).

This is because in this case, the dominant noise source is the Mach waves, which is produced by the large-scale wave like structure. One cavitate to note is that because LEE is linear, spurious modes may be easily amplified and, therefore, extra attention is needed when implementing boundary conditions for LEE calculations. The successful boundary treatments are shown in Figure 1.21 for a supersonic jet with $M = 2.1$. A snapshot of the unsteady jet flow as well as the radiated sound is shown Figure 1.22a along with contours of the computed noise level in Figure 1.22b. These levels and directivity were found to be in excellent agreement with the corresponding experiment of Trout and McLaughlin (1982) for supersonic jet as shown in Figure 1.23.

Figure 1.23 shows the predicted SPL in which the initial disturbances were axisymmetric but was taken either to be at $St = 0.2$ or computer-generated random disturbances. Figure 1.24 shows the predicted directivity at $r/d = 24$ in which the initial input disturbance to jet was taken to be either an axisymmetric or the first helical mode

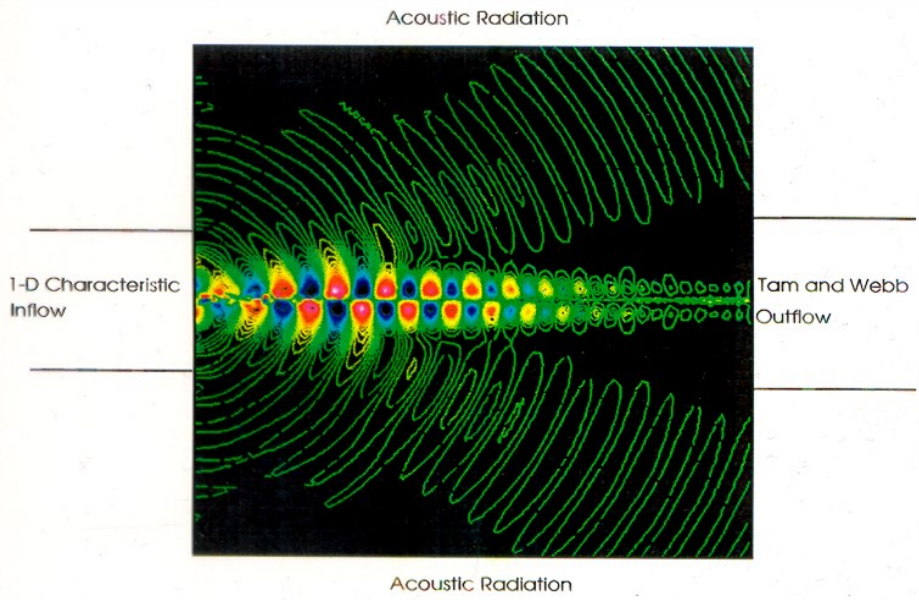

Figure 1.21 Prediction of the unsteady flow and acoustics of a supersonic jet using LEE (Mankbadi et al., 1998).

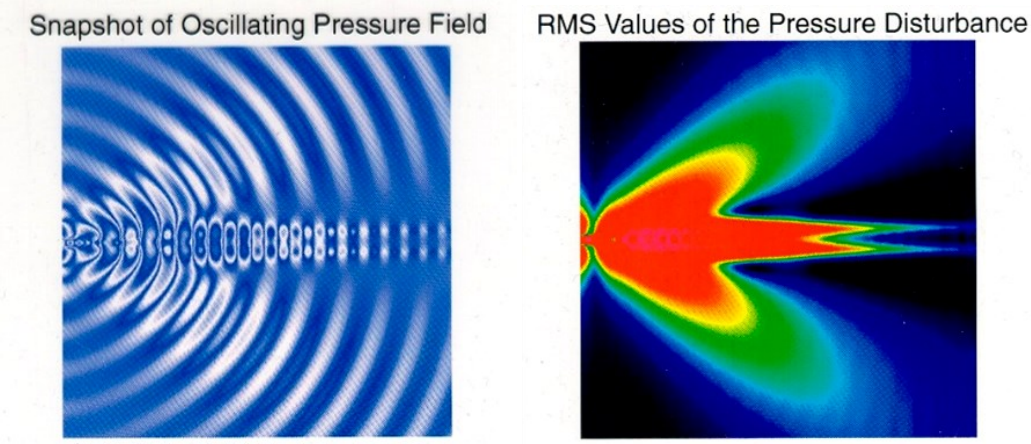

Figure 1.22 (a) Snapshot of the oscillating pressure field, (b) RMS of the acoustic pressure distribution (c) (Mankbadi et al., 2000).

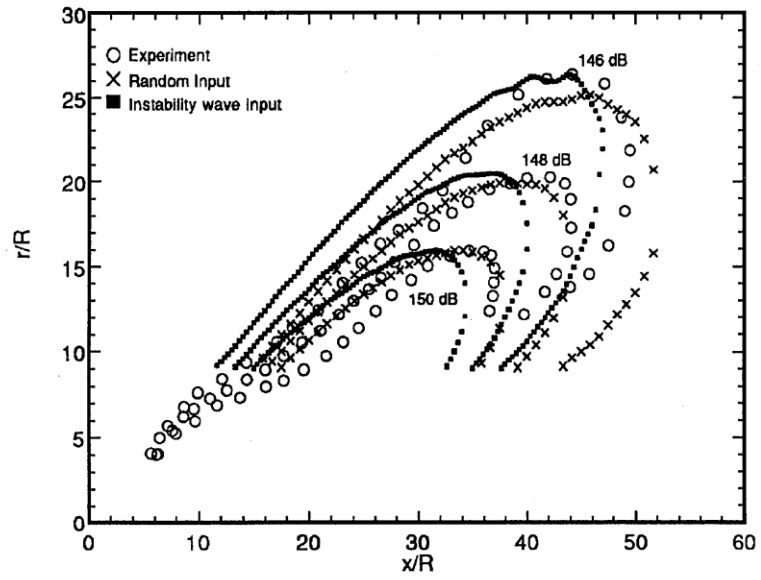

Figure 1.23 Prediction of LEE for a supersonic Jet $M = 2.1$ in comparison with experimental data (Mankbadi et al.,1998).

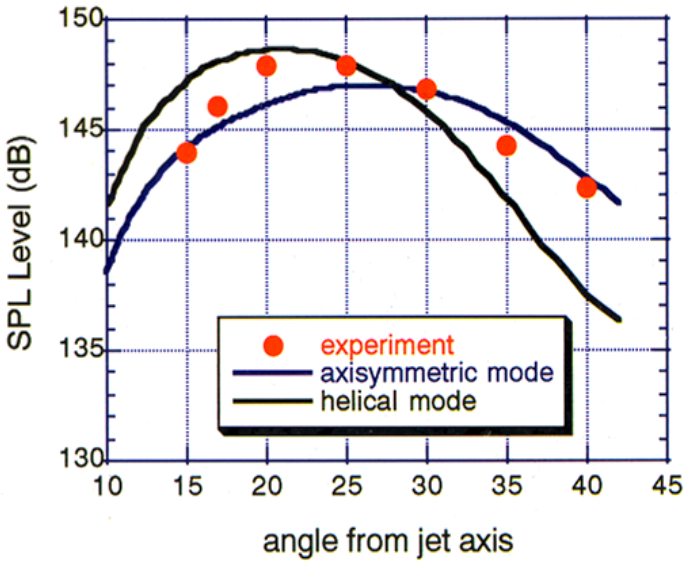

Figure 1.24 Directivity at R/d=24 The initial input disturbance to jet was taken to be either an axisymmetric or the first helical mode (Trout & McLuaglin, 1982).

1.3.5. Very Large Eddy Simulations

In Very Large Eddy Simulations (VLES), introduced in Mankbadi et al. (2000), Unsteady Reynolds Averaged Simulations (URANS) is used to simulate solid boundaries and LES otherwise. In this case, only the very large scales are resolved near the boundaries. In this case, the unresolved scales are larger than that in LES. Therefore, a higher-order turbulence model needs to be used there.

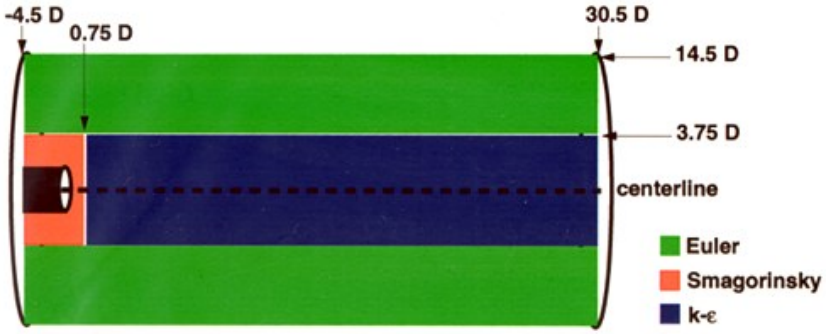

(a)

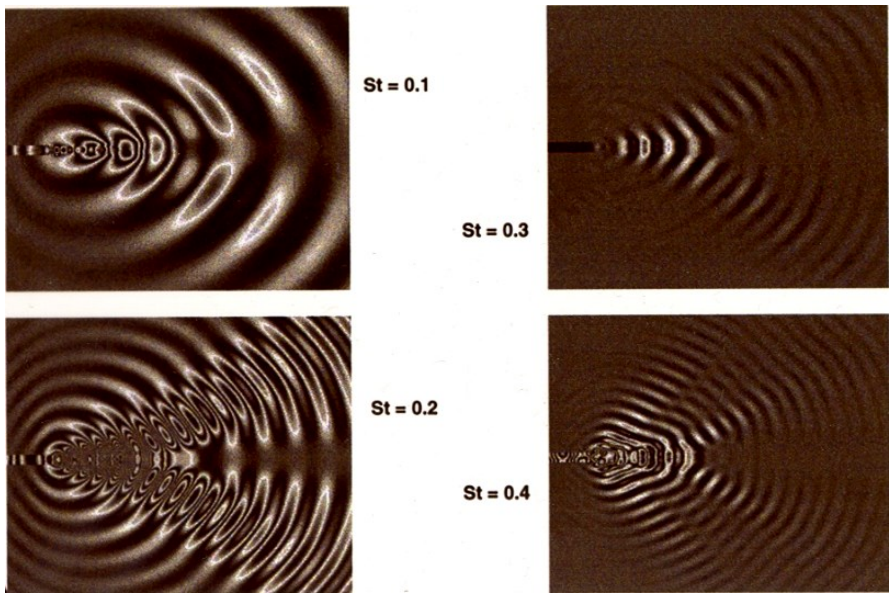

(b)

Figure 1.25 VLES Simulations (URANS+ LES). (a) Zones of governing equation. (b) pressure oscillation at various Strouhal numbers (Mankbadi et al., 2000).

Figure 1.25 shows the results for VLES of $M = 1.4$ jet, heated at $T = 953\ K$ with a co-flow. The computational domain is set on a rectangular grid with $231 \times 140 \times 10$ points in the axial, radial, and azimuthal directions, respectively. The k-epsilon turbulence mode is used near and inside the nozzle, the Smagorinsky model is used for the near field. Outside the jet, the viscous and turbulence terms are set to zero thus Euler equations are used. This zonal distribution is shown in Figure 1.25a. The real part of the pressure escalation is shown in Figure 1.25b for various Strouhal numbers.

1.4. Jet Noise Control

In the vast literature of the jet noise control, several techniques and approached are employed to mitigate the jet noise. However, most of these studies have focused on the free jets. Although these studies have provided abundance of details on the mechanisms that have the capability of manipulating flow field such that reduce the noise, but interaction effect due to installation or any other sort of presence of solid surfaces are mostly ignored. Throughout the following literature review, the objective is to summarize the key factors that can be learnt from previous work in free jet noise control, and apply these principles to the situations where the interaction effects are present and sometimes significantly increase the noise, as described in the previous sections.

Generally, the jet noise reduction is achieved either via passive or active control. In passive noise control, such as chevrons or bypass flow, there exists a fixed design that modifies the flow field and consequently alters the acoustics. On the other hand, in all forms of active noise control such as: jet excitation, fluidic injection (whether gas or liquid), or plasma actuation, the actuator is a mechanism that can be switched on when desired. The latter option is more attractive for applications that could benefit from a

feed-back control system, that can provide an open-loop or a closed loop control. Effective application of such control devices requires deep understanding of noise generation and radiation mechanisms in the jet itself, and the additional elements of noise introduced due to the solid surface interactions.

1.4.1. Free Jet Passive and Active Noise Control

In passive control, some permanent change in the design is implemented. This is distinguished from "Active" control which can be switched on or off as the need arises. While there are several technologies for passive control, the discussion in this section is limited to passive control based on mixing control. The level of initial jet mixing determines the rate at which the jet spreads in the transverse direction as well as its axial extend. This obviously has a significant effect on the jet interaction with the airframe, and on the radiated noise. Hence, mixing control as an indirect approach to control noise in installed engines is discussed here.

Since turbulence produces the broad-band noise, manipulating the mixing process between the jet and the surrounding fluid is believed to play a key role in reducing the noise-efficient large-scale structure. So, one popular concept is to use a chevron at the nozzle lip for early mixing of the jet right at the exit to reduce the development of the larger scale structure downstream. Also, early mixing at the nozzle tip increases the fine-grained turbulence level and increases the momentum thickness. These two parameters reduce the development of the large-scale structure, which is the dominant noise source.

Another technique is to have the mixing happening rapidly and shorter inside the nozzle where liners can be introduced to reduce the noise. To demonstrate this, LES of internal flows using the DRP scheme are shown in Figure 1.26. The figure shows a

snapshot of the instantaneous flow associated with an acoustic source inside the duct as if representing internal noise.

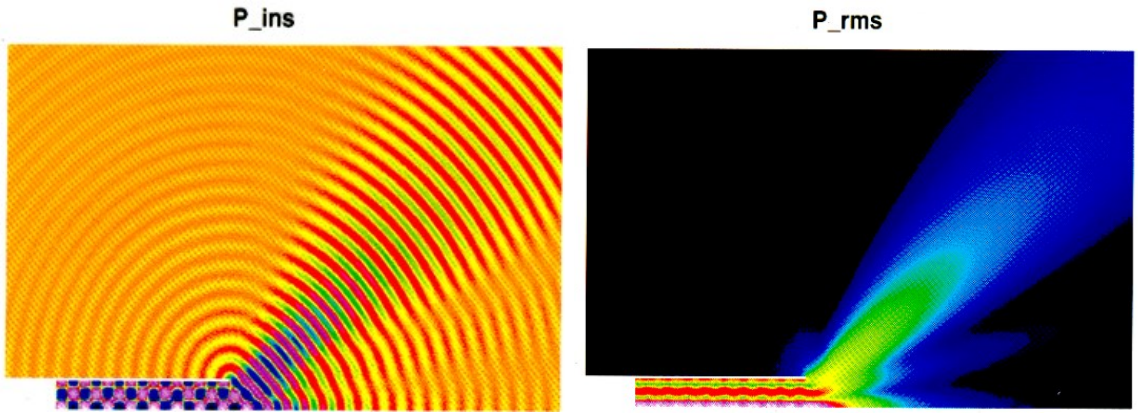

Figure 1.26 LES of an internal duct and its radiated field using the DRP scheme for a point source inside the duct at ω=10.3 rad/s. (a) Instantaneous pressure, (b) RMS of pressure fluctuations (Mankbadi et al., 2000).

Another example is shown in Figure 1.27, which considers the simplified ejector/mixing configuration shown in the figure. Because of flow separation and instabilities resulting from the mixing of two streams, the flow is usually unsteady characterized by various vortex generations, which is unlikely to be captured by RANS and, therefore, LES is needed. In this figure, a supersonic flow at the inlet of the primary nozzle is considered, while the flow in the bypass channel is subsonic. Absorbing boundary conditions are used. The resulting root mean square of the pressure fluctuations is shown in Figure 1.28. Another example of passive control is high-bypass engines, which produces less noise compared to the equivalent turbojet. Given the same thrust, the bypass air act as co-flowing jet that reduces the noise in two ways. First, it reduces the strength of the velocity gradient at the initial region of the jet, which in turn reduces the

development of the noise-producing large-scale structure. Secondly, the noise produced by the inner jet losses some of its amplitude through absorption and reflection as it passes through the outer co-flowing stream. Hixon et al. (1997) numerically simulated the effect of bypass on noise radiation. In their study, the area ratio of $A_{outer}/A_{inner} = 1.25$ was considered. Depending on the inf flow conditions, this corresponds to bypass ratios of 2 – 5. The results show that bypass reduced the noise by about 7 dB at low emission angels when compared with the no bypass flow cases.

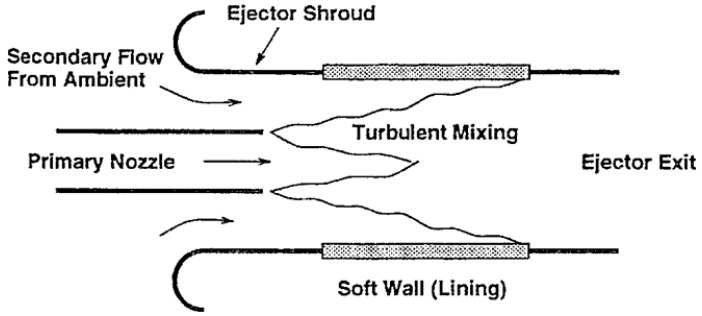

Figure 1.27 Simplified ejector-mixture configuration (Dong & Mankbadi, 2000).

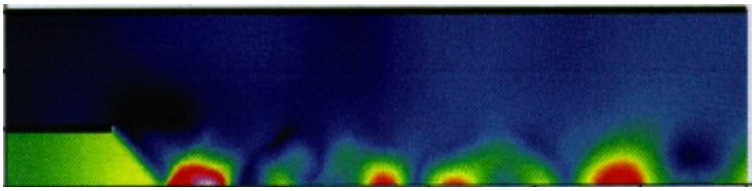

Figure 1.28 RMS of the pressure fluctuations inside the duct as obtained by LES (Dong & Mankbadi, 1996).

In Active Noise Control (ANC), a small disturbance (input) is introduced somewhere in the flow field via an actuator to modify the flow field and its radiation pattern. Modifying the jet flow via ANC has been extensively studied both numerically and

experimentally for various applications. Next, the active noise control through excitation of the jet is reviewed, followed by fluidic injection approaches.

Figure 20 shows the effect of exciting the jet at a pair of Strouhal numbers (St) on the spreading rate of the jet. The figure shows that excitation has a dramatic effect on increasing the spreading rate, which has technological applications in low observables. Thus, one approach for reducing jet noise is through manipulation of the flow mixing and turbulence generation. Further details can be found in the works by several other studies in the literature (Mankbadi, 1985, 1991; Mankbadi et al., 1989; Raman et al., 1988; Raman & Rice, 1988; Zaman & Hussain, 1980).

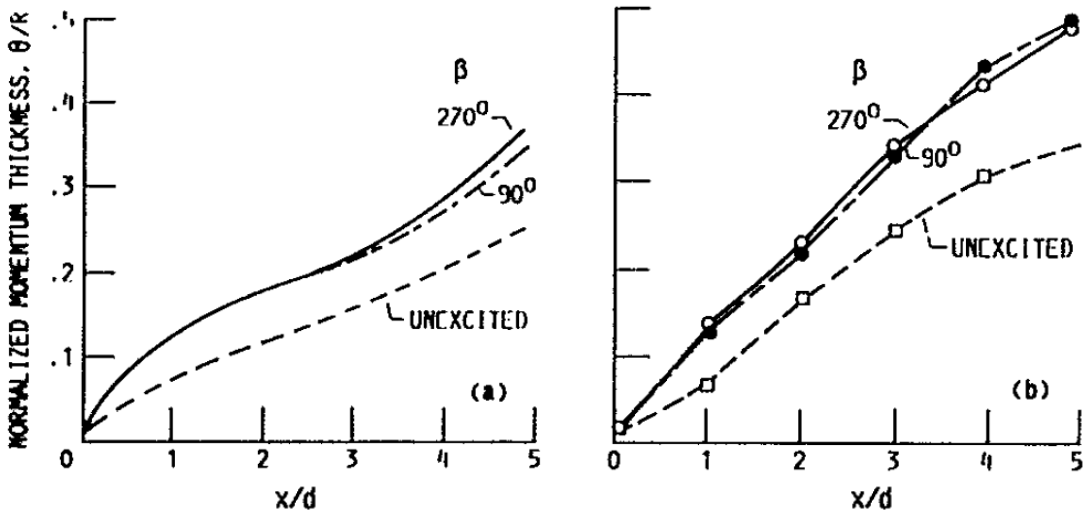

(a) (b)

Figure 1.29 (a) Development of momentum thickness for excitation and unexcited case (a) computation (Mankbadi, 1991) and (b) Experimental data (Mankbadi et al., 1989).

LES have been used to demonstrate the effect of open-looped excitation on supersonic jet noise (Mankbadi et al., 1994). In Figure 1.30 from Mankbadi et al. (1999), a supersonic jet at Mach number was actuated with different types of signals. Four cases are shown in the figure. In the top two figures a single frequency mode ($St = 0.4$) was

used but at different levels of energy levels $(0.04, 0.001)$. In the bottom left figure bi-modal excitation at two frequencies of fundamental and subharmonic $(St = 0.4, 0.2)$ were imposed at the jet exit. At the bottom right figure disturbances at random frequencies were used. These numerical experiments give some guidance in the control process.

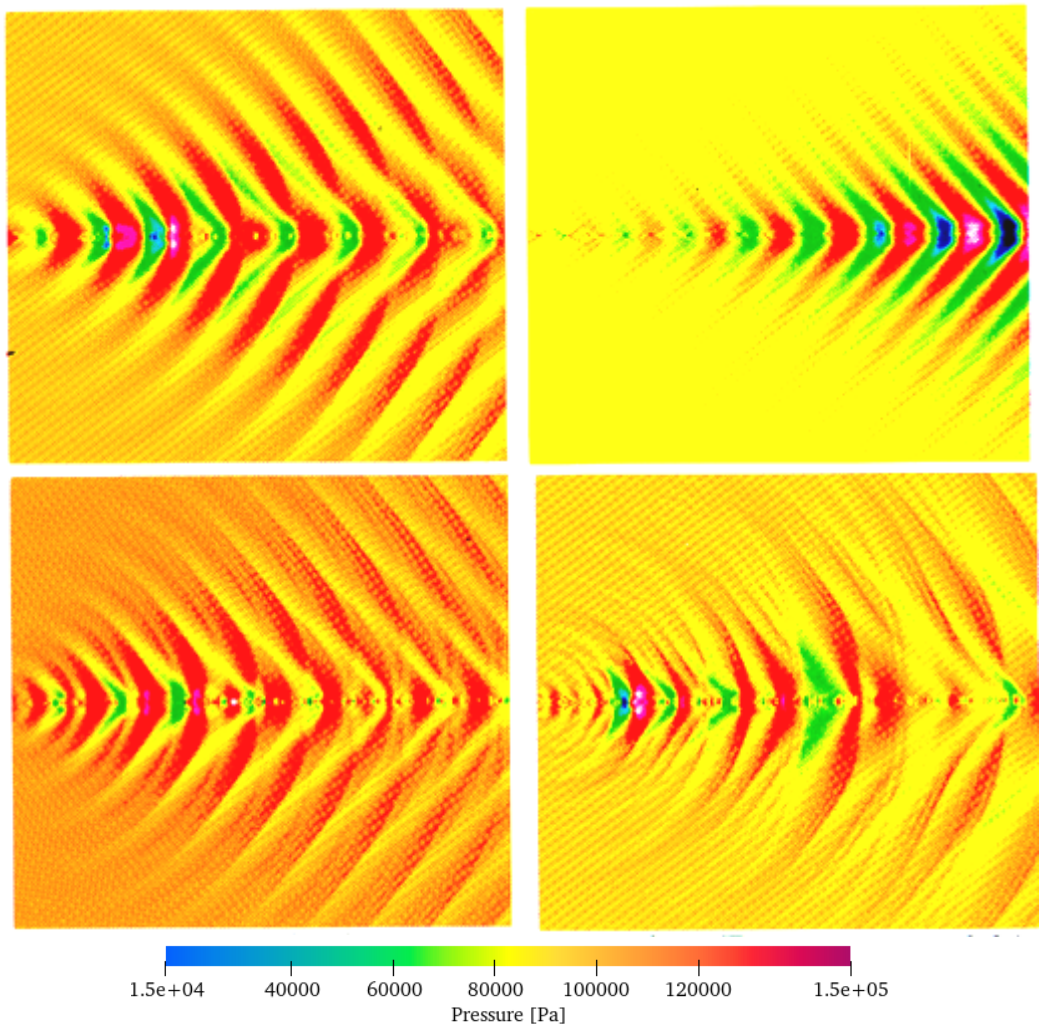

Figure 1.30 Snapshots of the instantaneous pressure fluctuations in a $M = 2.1$ round jet for four different cases of inflow excitation (Mankbadi et al., 1999).

For single frequency excitation the amplitude matters as demonstrated in the top two figures. It is also clear from the bottom left figure that bi-modal fundamental-subharmonic excitation has a pronounced effect on the control process. This is believed to be due to the vortex-pairing mechanism. In the studies by Mankbadi (1985a, 1985b), shown in Figure 1.31, a theoretical analysis was given which shows that if a jet is excited at a single frequency, its subharmonic could be considerably amplified. This was demonstrated experimentally (Zaman & Hussain, 1980). In fact, Arbey and Ffowcs-Williams (1984) experimentally demonstrated that for a subsonic jet that if the jet is excited at a subharmonic of the peak frequency, the radiated noise is reduced. While this was for subsonic flow, it provides some guidance and evidence for the supersonic case.

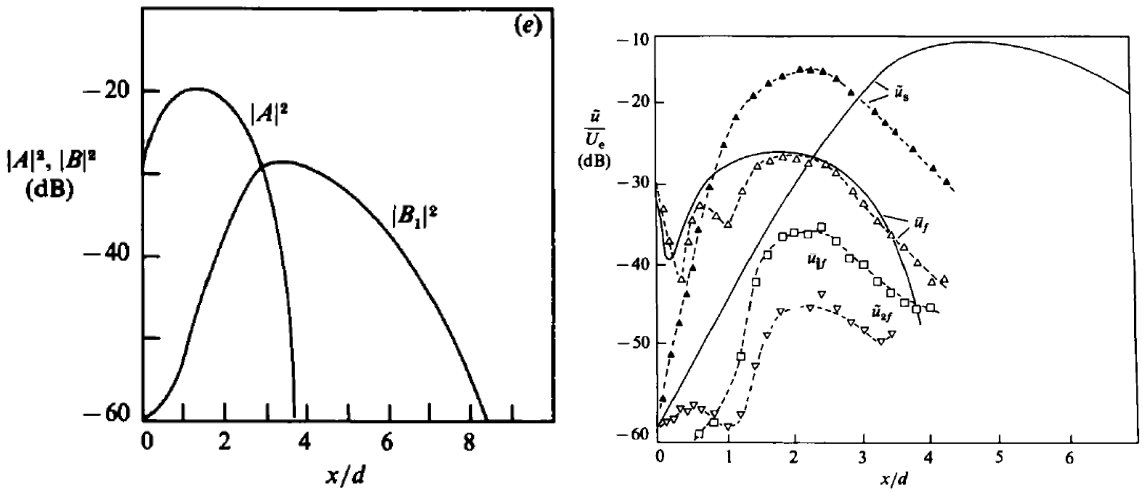

(a) (b)

Figure 1.31 (a) Predicted fundamental and subharmonic energies along the jet at fundamental Strouhal number of St=4.8 (Mankbadi, 1985a) (b) Predicted development of the fundamental's and first subharmonic's centerline axial velocity components at St=0.8, and comparison with experiment (Zaman & Hussain, 1980).

The noise mitigation can be achieved through injection process and excitation of the jet flow. Such modification in the flow field depends on various injection configuration and operating condition of the main jet and actuation. Generally, the fluidic actuation can be categorized as aqueous and gaseous injection. Henderson (2010) has reviewed the aspects of fluid injection towards jet noise reduction. Aqueous injection involves a two-phase flow that leads to modification of the jet plume and radiated noise through the process of droplet evaporation and momentum transfer between droplets and the main jet. The momentum transfer process effectively reduces the jet velocity and the radiated noise. On the other hand, gaseous injection introduces vortices that evolve with axial distance from the jet and could impact turbulence. While both types of injection can impact mixing and shock associated noise, the physical changes in the jet plume that lead to noise reduction could be different.

The ability to use compressor bleed air as the injection medium on an aircraft, has attracted more researcher to investigate gas injectors than water injectors. The initial studies on the interaction between gaseous injectors and main jet plume began in the 1940s with jet-in-crossflow research, which is extensively reviewed by Margason (1993). These studies led to understanding the identification of counter-rotating vortices and the possible effects on jet plumes. Chauvet (2007) showed when multiple jets inject into the main jet, the resulting vortex pairs initially move toward the main jet axis until their mutually induced velocity becomes strong enough to cause them to separate and forming a new pair that moves away from the jet centerline.

The connection between the fluidic injection and mechanical chevrons (serrations at the nozzle trailing edge that penetrate the flow) is explored by Alkislar et al. (2007, 2008)

to investigate the effectiveness of noise reduction achieved from fluidic injection. Additionally, unsteady injection has been explored for the purpose of exciting jet instabilities and enhancing jet mixing. For high speed jets, enhanced mixing has been achieved with unsteady microjet injection in experiments by Ibrahim et al. (2002), as well as engine tests (Kibens, 1999).

Gaseous injection has been shown to reduce screech tones, broadband shock noise, and mixing noise in hot and cold main jets. Krothapalli et al. (2002), as well as, Henderson and Norum (2008) have employed various injector configurations that resulted in eliminating screech with about a 1% mass flow ratio injection. Henderson and Norum (2008) also showed increasing injection pressure decrease broadband shock noise due to alteration of shock cell structure due to the injection process. Henderson and Norum (2007) observed lower broadband shock noise reductions for hot main jets than cold jets (overall sound pressure level reduction of 3.8 dB in a hot main jet). The low broadband shock noise reductions (Greska & Krothapalli, 2005; Martens & Haber, 2008) may suggest higher injection pressure requirement to achieve effective reduction.

Moreover, Coderoni et al. (2018, 2019) used LES for numerical analysis of fluidic injection as a tool for noise reduction for both heated and unheated jets and observed a maximum noise reduction of about 3 dB. Prasad and Morris (2019) performed LES using a finite-volume solver and showed that upstream injectors at each azimuthal location further enhances the BBSAN reduction.

Water injection studies can be categorized in two areas: (1) injection for launch vehicles where injection flow rates are not concerned, and (2) injection for inflight use where water is limited. Mass Flow Ratios (MFR) for launch vehicle studies in this period

have been as high as 800% while MFR well below 100% are typically investigated for in-flight use (Henderson, 2010).

For low mass flow ratios appropriate for aircraft related applications, experiments have investigated water droplet behavior as well as turbulence characteristics of the main jet. Krothapalli (2000, 2003) showed that mass flow rate of around 5% modifies the main jet turbulence and results in reductions of 30% in the normal component of the RMS velocity and 40% in the peak shear stress, that could consequently modify the noise generated by fine scale turbulence and large scale structures in the main jet. Several experimental studies (Greska & Krothapalli, 2004, 2005; Norum, 2004), observed that, the injection mass flow rate, water pressure, momentum flux ratio (ratio of the injected flow momentum to the momentum of the main jet), and injection angle have a significant impact on the radiated noise. For hot over-expanded supersonic jets, microjet systems (using 2.8 MPa) implemented on an F404 engine and in complementary laboratory scale experiments produced only slight reductions in broadband shock noise with MFR equal to 8% on the engine and 14% at laboratory scales.

These studies also showed reduction in overall sound pressure level of 6.6 dB, in the shock noise dominated forward arc with MFR around 46%. Washington and Krothapalli (1998) showed that Screech tones are eliminated with MFR values of as low as 10%. Additionally, Norum (2004) observed that the main jet temperature is an important factor in the noise reduction capability of water injectors.

Figure 1.32 shows the impact of water injection on a cold and hot over expanded jet measured by Norum (2004). At angles greater than 90° (in the upstream direction relative to the nozzle exit), Broadband shock noise becomes less significant relative to mixing

noise as the main jet temperature increases. Since water injection is less effective at reducing mixing noise than shock noise, reductions at both small angles to the jet and in the peak jet noise direction are lower for the hot jet than the cold jet.

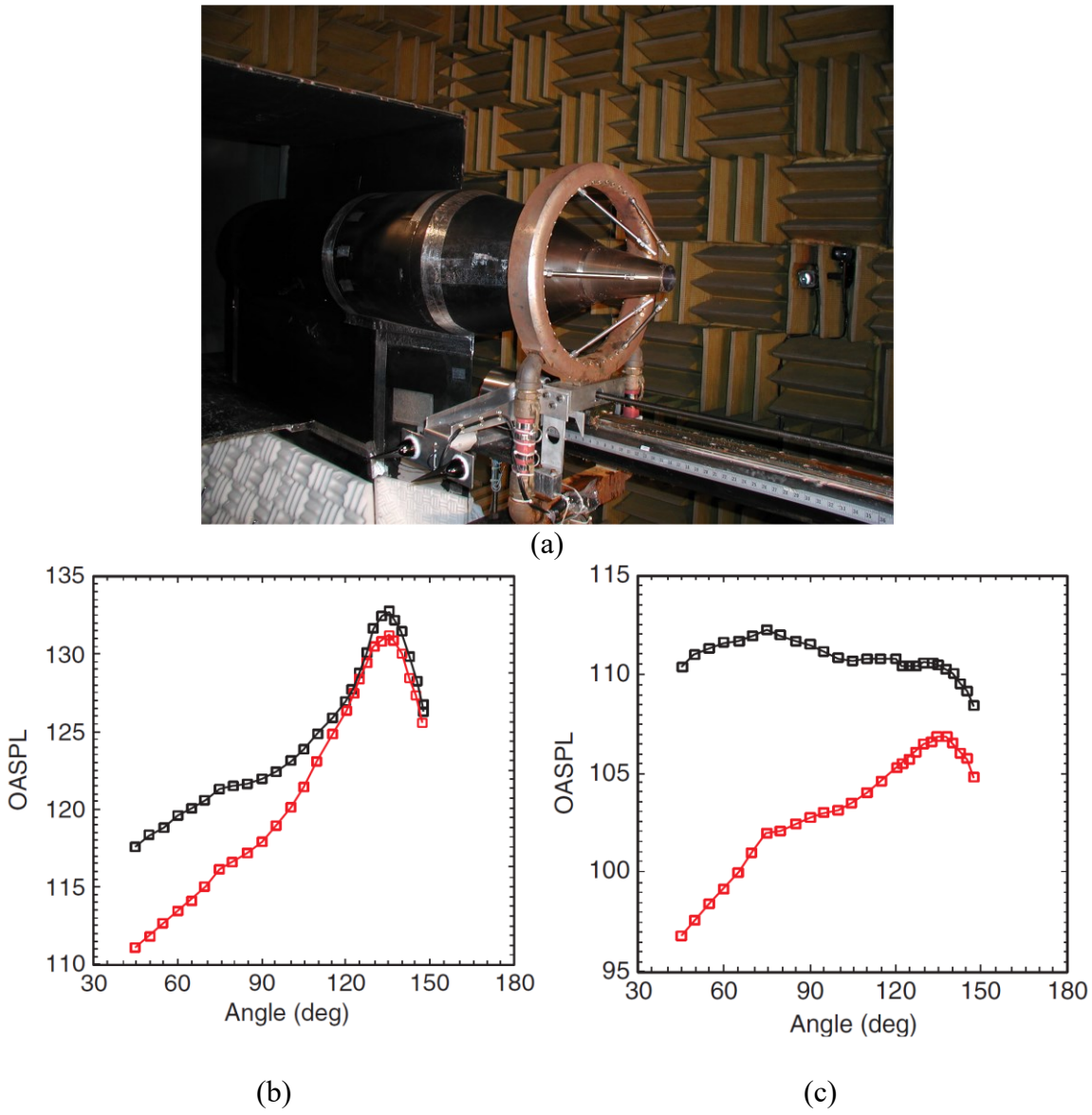

Figure 1.32 (a) Water injection hardware with 6 injectors. Directivity from a (b) cold, and (c) hot over-expanded main jet. Black and red data are for the no injection case and for water injection MFR = 33% (Norum, 2004).

1.4.2. Noise Mitigation of Jet Impinging on a Perpendicular Solid Surface

As discussed earlier, flow field of the impinging jet could be divided into the free jet region, the impingement region, and the wall jet region. The flow structures and the acoustic characteristics of the impinging jet in the free jet region show similarity to those of the free jet. In addition to the noise originated from the free jet region, it involves the noise reflected by the plate and noise induced by the interactions.

Several investigations have targeted active and passive control techniques reduce the adverse effects of the impinging jet. Elavarasan et al. (2001) used a baffle plate aiming to disturb the upstream propagation of the acoustic waves generated on the impingement plane, and consequently break the acoustic feedback loop responsible for generation of large scale coherent vortical structures. These investigations showed 16% recovery in lift loss and 11 dB noise reduction in the near field. This reduction was due to reduce instabilities at the nozzle lip when the region near the nozzle was shielded from the upstream propagation of the acoustic waves generated upon impingement. Wiley et al. (2010) used a resistance screen on the ground plane, which led a reduction in Overall Sound Pressure Level (OASPL) of up to 5 dB in the near field. This technique was effective in the reduction of the broadband noise, however, insignificant effect on amplitudes of impinging tones was reported.

Aside from passive control, active control techniques are also investigated in various configurations for the impinging jet noise reduction. Sheplak and Spina (1994) used high speed co-flow to shield the main jet from the near field acoustic disturbances which created a reduction in the overall sound pressure levels of 10-15 dB, but the mass flow required made this impractical for applications outside the laboratory. Alvi et al. (2000,

2003) implemented high momentum fluidic microjets around the nozzle, which, introduced streamwise vortices and modified the development of large-scale coherent structures and resulted in the disruption of feedback loop, reduction of tones to 22 dB. These finding motivated Annaswamy et al. (2002) to design a closed loop control mechanism to provide optimal reduction of these tones over the entire range of operating conditions. These closed-loop strategies provided an additional 8-10 dB reduction, compared to an open loop one, at the desired operating conditions.

Impinging jets involving multiphase flows during rocket launching are commonly employed. In general, a water injection system is included in a launch pad for large vehicles to cool down the launch system and reduce the noise. The water jet could be atomized by the engine exhaust producing many discrete droplets. Additionally, the exhaust is decelerated by the momentum exchange with the liquid phase. Most of the noise reduction by the aqueous jet comes from the heat reduction and the deceleration of the exhaust, which reduce the energy of both the main jet and the turbulent structures. Washington and Krothapalli (1998) suggest that the water injection affects the dominant sources of the turbulent mixing located at the end of the potential core region of the jet and reduces the mixing noise. This approach, however, if used for aircrafts or rockets would require carrying water on board.

Alternatively, for rocket launch or aircraft carriers, it is more practical to inject water from the impingement pad (launch pad or deflector). Ignatius et al. (2008, 2014) and Ragaller et al. (2011) have considered supersonic jets impinging on a perpendicular plate and have shown, experimentally, that injecting water from microjets through the impingement plate can reduce noise. They conjectured that water injection from the

ground plane reduces the sources of sounds due to impingement.

Ignatius et al. (2008, 2014) reported that trend is not the same for all the injection system configurations. For the injections at the launch platform bottom, the noise reduction level reaches the limited value of 2 dB at a lift-off height of $8d$. However, for the injections near deflector duct cover plate, the noise reduction level remains about 1 dB at all the lift-off heights tested. The influence of the impingement distance on the injection configurations is also observable in the scale model experiment by Malbqui et al. (2015), confirming that the injection at the duct entrance is effective before the lift-off height reaches $5d$, while the noise reduction effectiveness of the injection on the launch platform is noticeable for $5d < h < 30d$. Ragaller et al. (2011) showed when the impingement distance is 8 times of the nozzle throat diameter, the impinging tone appears, and the injection reduces the peak of the impinging tone. For a temperature ratio (stagnation temperature at the nozzle inlet/ambient temperature) of 1.0 or 2.04, the noise in the high frequency band is reduced as well. On the contrary, for a temperature ratio of 2.81, noise of the high frequency band is enhanced. More detailed discussion about these experimental measurements and comparison with numerical simulations are provided in the next chapters.

1.4.3. Noise Mitigation of Jet Impinging on an Inclined Solid Surface

When the inclined angle is small, the flow field and acoustic characteristics between normal and inclined impinging jets are similar. As the inclined angle increases, the characteristics of the noise spectra could show remarkable difference. Worden et al. (2013) measured the nearfield and far field spectra for normal and 40 degrees inclined impinging jets. It was shown for the inclined impinging jet, on the contrary, no impinging

tone is observed under the same conditions, unless the jet temperature is high very high. As discussed earlier, Nonomura et al. (2011) predicted the existence of three primary acoustic waves: 1) Mach waves generated in the shear layer of the main jet, 2) acoustic waves generated from the jet impingement, and 3) Mach waves generated in the shear layer of the outward-propagating wall jet. Figure 1.33 shows illustrates types of waves.

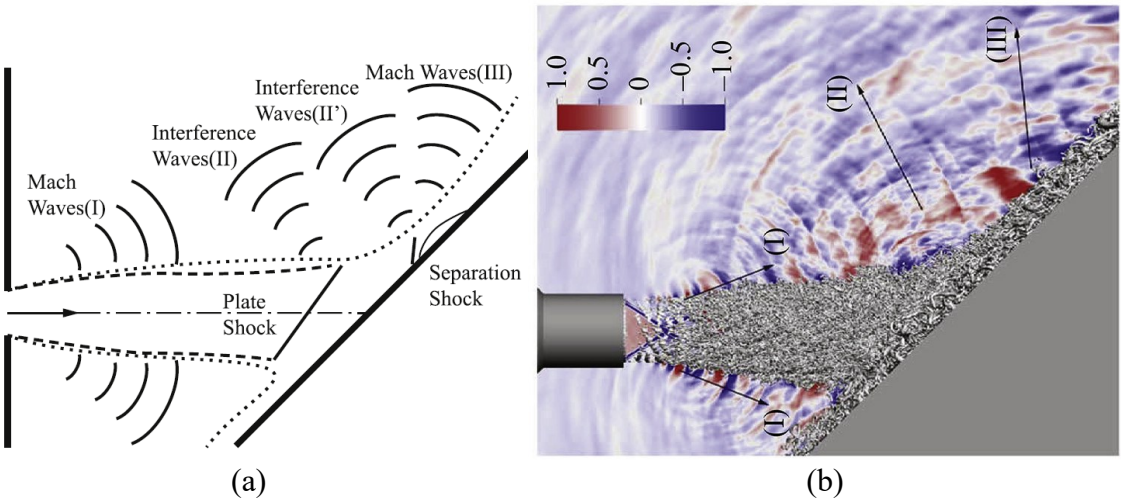

Figure 1.33 (a) Three types of acoustic waves (Jiang et al., 2019). (b) Isocontour of Q-criterion and contour of normalized gauge-pressure (Brehm et al., 2016).

Two sources contributing to type 2 acoustic waves are discovered by Nagata et al. (2013), and previously investigated by Honda et al. (2011). The first one is the interaction between the main jet shear layer and the plate shock. The second one is the interaction between the main jet shear layer and the separation shock induced by the stagnation bubble. These two sources are easier to distinguish at a relatively small inclined angle, while the acoustic waves generated by the two sources are not distinguishable at far field. It is shown by Nonomura et al. (2015) that at a smaller inclined angle, the plate shock is stronger, the OASPL is higher and the dominant frequency is lower.

Kurbatskii et al. (2014) studied the effect of inclination angle on mean flow and noise radiation from impinging rocket plume. The flow and acoustic field of a supersonic jet impinging on a solid plate at different inclination angles was studied computationally using Wall-Modeled Large-Eddy Simulation (WMLES) model.

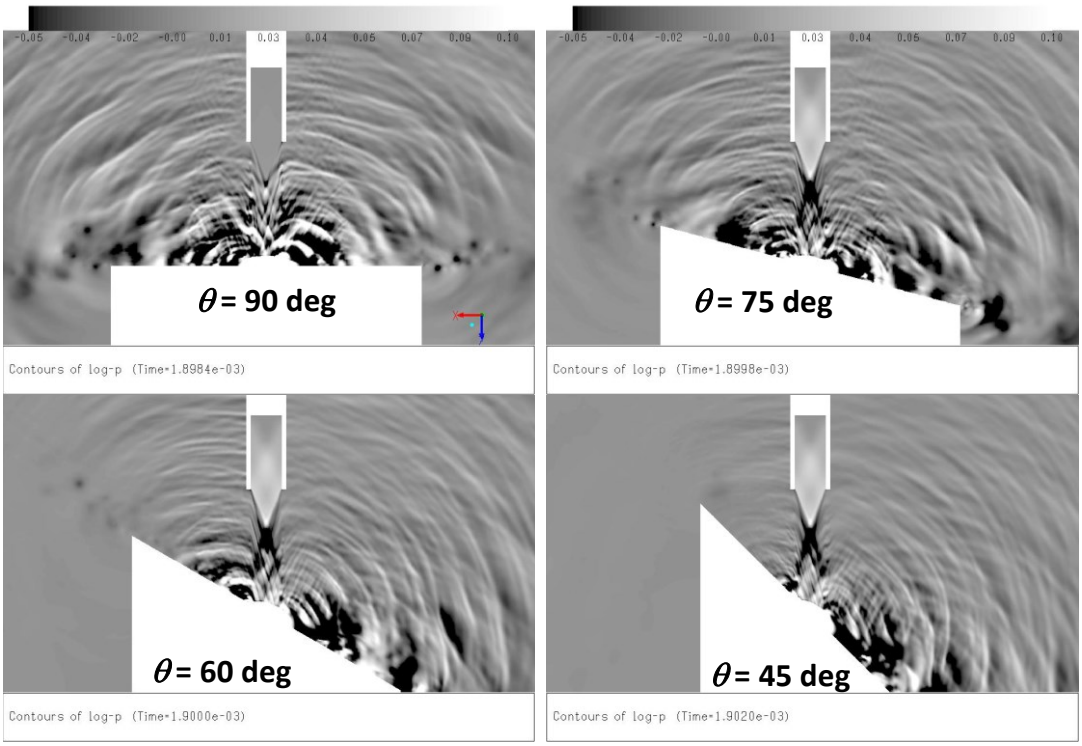

Figure 1.34 Instantaneous pressure field at different inclination angles, plotted on a log scale (Kurbatskii et al., 2014).

The flow field shown in Figure 1.34, illustrates that the stagnation point of the impingent jet is affected by the inclination angle. The surface pressure oscillates due to separation and reattachment and this could be an additional source of noise. Figure 1.36 shows the effect of inclination angle on the OASPL from various microphone locations shown in Figure 1.35. These results show about 10 dB reduction of the peak noise when

the inclination angle is changed from 90 to 45 degrees.

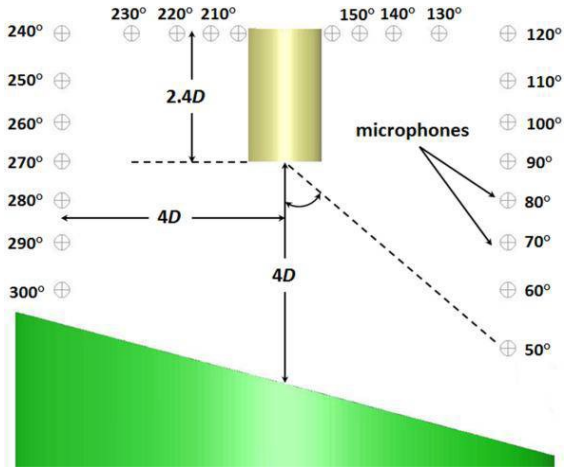

Figure 1.35 Array of microphone locations (Kurbatskii et al., 2014).

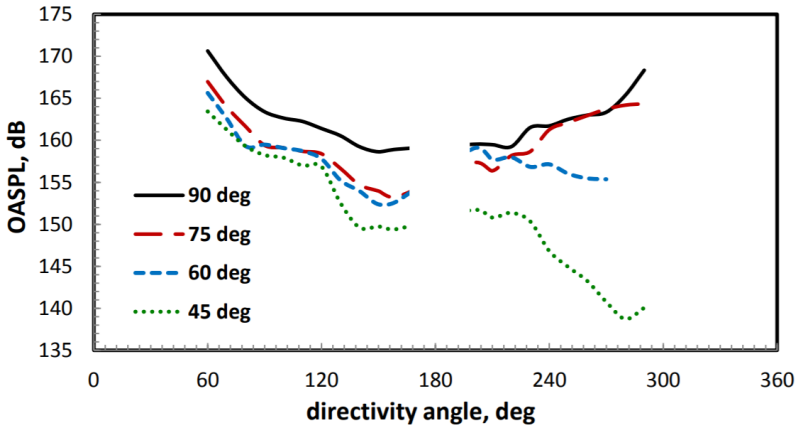

Figure 1.36 Liner plot of OASPL directivities for different plate inclination angles (Kurbatskii et al., 2014).

1.4.4. Noise Mitigation of Jet Interacting with a Parallel Solid Surface

One of the earliest works on investigation of air jets exhausting parallel to large flat plates was by Janos and Hoffman (1969) at NASA Langley Research Center where the impingement forces, moments, and centers of pressure caused by air jets exhausting

parallel to flat plates were measured. In the more recent years, many newer aircraft concepts involve over-the-wing engine designs which provide a shielding effect for the jet exhaust noise propagated towards the ground. This has been a driving factor for investigations with noise reduction objectives. In many of these concepts, rectangular geometries for the jet nozzle are preferred for ease of integration. A high aspect ratio rectangular exhaust geometry with extended beveled surfaces shield noise from reaching the ground, can also fall into the category of Airframe integration approach to reduce noise.

A series of tests conducted at NASA Glenn Research Center (Brown, 2012; Podboy, 2012) in order to study the propulsion/airframe integration under Jet-Surface Interaction Tests (JSIT), were intended to guide analytical studies towards development of prediction model. Bridges (2014) and Zaman et al. (2015) have focused on the noise generation mechanism in subsonic jets, and investigated the effects of surface length, distance from the nozzle, lip to the trailing edge, and beveled nozzle configurations. Two sets of a rectangular nozzle on an aft deck configuration were tested. The beveled nozzle, where the lower lip of the nozzle was extended with the sidewalls becoming triangles. And the rectangular nozzle fitted with a surface that fit flush to the lower lip and extended outward from the sides of the nozzle.

In addition, Aikens et al. (2015), carried out LES simulations to analyze the converging-diverging beveled nozzle. Bridges (2014), tested rectangular jets of various Aspect Ratios (AR) in the proximity of a flat surface. Moreover, in an effort towards integration of airframe with the nozzle design, Bridges (2015) investigated far-field acoustic measurements of a family of high aspect ratio rectangular nozzles in the high

subsonic flow regime with various designs. These experiments reported that, having an extended lip on one broad side did produce up to 3dB more noise in all directions, while extending the lip on the narrow side produced up to 2dB more noise, primarily on the side with the extension. Adding non-intrusive chevron, made no significant change to the noise, while inverting the chevron produced up to 2dB increase in the noise.

Regarding the supersonic jet/plate interactions, McLaughlin et al. (2008) carried out experimental and numerical studies on a 1.5 Mach jet at various distances from a flat surface and observed that both scrubbing and trailing edge noise detected in low frequencies increased, as the distance between flat plate and the jet is reduced. Brown et al. (2014) and Clem et al. (2013) provided flow field and acoustic data for a supersonic round jet with a design Mach number of 1.5, operating in the over-expanded, ideally expanded, and under-expanded supersonic flow regimes. The plate was placed at a radial distance h, normalized by the jet exit diameter $D = 50.8\,mm$. They tested a range of distances between $0.5 \leq h\ /\ D \leq 5$. For noise testing, the surface was assembled using multiple pieces of 12.7-mm thick aluminum to allow six surface lengths x_{TE} between $2 \leq x_{TE}\ /\ D \leq 15$. Reduction in broadband shock-associated noise was observed both in the shielded direction, 60° and 90° microphone angles, when the flat surface was long enough to cover the shock cells in the potential core.

Mora et al. (2016) tested a supersonic rectangular nozzle of 2:1 aspect ratio and 1.5 Mach number with and without the plate for various nozzle expansion conditions and documented a range of plate positions where crackle levels were significantly intensified. In their study, the plate could be positioned at different stand-off distances, starting where the plate touches the inner wall of the nozzle exit at $h/D = 0$ and can be moved away

from the jet up to $h/D = 4$. Mora et al. (2016) reported that, $h/D = 1$ and 3 have similar OASPL compared to the no-plate configuration. The, $h/D = 0$ configuration increases noise levels significantly starting at angle of 128º. Similar behavior has been also reported by (Powers et al., 2018). The acoustic directivity shown in Figure 1.37, revealed the shielding effect of the flat plate at various angles. More detailed discussion about these experimental measurements and comparison with numerical simulations are provided in the next sections.

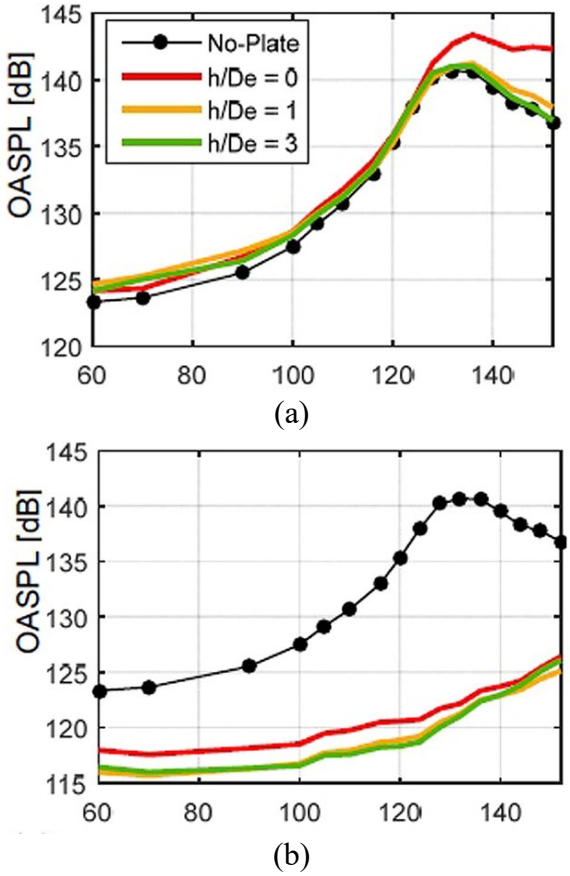

Figure 1.37 Far field acoustic directivity of the (a) reflected side and (b) shielded side (Mora et al., 2016).

1.5. Research Objectives

The main objectives of current dissertations are presented and described here:

1. **Numerical simulation of liquid-gas interaction in the compressible supersonic medium**. Numerical aspects of simulating the unsteady supersonic flow structure and its radiated sound is a challenging task by itself due to the resolution and accuracy required. Introduction of water injection complicates the problem further as it creates material interfaces with sharp density discontinuity causing numerical stiffness and numerical instabilities. The complexities introduced due to the multi-physics nature of the problem, requires appropriate selection of governing equations, numerical scheme, and the boundary conditions, to perform stable and accurate numerical simulations. This research addresses the numerical aspects of predicting the fluctuating flow field and its nearfield sound associated with rocket lift off. As a model problem, an impinging supersonic jet where in water is injected from the impinging plane through microjets is considered here. The stiffness resulting from the sharp density gradient across the gas-liquid interface adversely effects convergence and stability. Furthermore, the governing equations becomes strongly coupled when the phase-fraction equation is introduced. So, one of the goals of this dissertation is to provide, detailed analysis of the numerical techniques appropriate for simulation of such a complex problem, that can provide accurate results.
2. **Investigation of the effect of water injection on flow field and acoustics.** The investigation of supersonic impinging jet and noise reduction via water injection, discussed in Chapter 1, is continuation of the studies supported by ULA® to study

impinging jets during rocket lift-off or ascend. The water injection technique is most suitable to be injected from the solid surface such as the blast deflectors, or the rocket launch pad. Although the jet noise reduction using water injection has been studied since 60's. the near nozzle injection has shown to be less practical for in-flight application, since the aircraft would need to carry huge and heavy water tank. Here a supersonic cold jet is considered that impinging perpendicular to a flat surface that has six microjets injecting liquid water from the ground. The experimental measurements from Florida State University is used in this research for comparison and validations. Due to the multiphase nature of the problem, the experiments only provide acoustic data. There are very few, if any, data in the literature, that explain the physical mechanisms involved in the noise reduction due to water injection from the impingement pad. One of the main goals of this research is to provide detailed investigation of the physical mechanisms responsible for noise reduction due to water injection. The valuable flow field results obtained from the numerical simulations in this dissertation can provide details of the effect of water injection on flow field and acoustics of the supersonic impinging jet.

3. **Investigation of the acoustic shielding effect flat surface parallel to the jet exit**. The numerical investigations discussed in Chapter 2 of this dissertation is stemmed from the interest of NASA Glenn research center led by Dr. Bridges at acoustics branch. In several experiments carried out at NASA Glenn, the shielding effect of a flat plate and interaction is investigated. However, the results were shown to be highly sensitive to several parameters, such as: operating

condition of the jet, the length of the flat plate, and the distance between the nozzle the plate. The experimental measurement provided by Dr. Gutmark's group at University of Cincinnati, is used in this research as a benchmark for validation on the numerical simulations. Here, a heated supersonic jet with the Mach number of 1.5 is considered that is issued from rectangular nozzle positioned near a flat surface parallel to the jet exhaust direction. One of the observations reported in the experimental studies is the noise reduction in the shielded side (behind the plate side). However, the noise levels are increased on the reflected side of the plate. Hence, one of the important objectives of this research is to perform numerical simulations to investigate the physical mechanisms of shielding effect and noise increase on the reflected side.

4. **Proposing a novel surface profile design to provide additional noise reduction for the shield plate**. By understanding the acoustic effect of a flat plate and the mechanisms involved, modifications to the existing flat plate shield can be implemented to reduce the noise more effectively. Although the flat plate shield provides considerable noise reduction on the shielded side of the surface, but the noise level reduction is very sensitive to the length of the surface. On the other hand, the flat plate can be modified, to provide further noise reduction. Hence, a new wavy wall profile is suggested in this dissertation based on theoretical estimations. The objective of this research is to propose a wavy sinusoidal profile. One of the important aspects of this research is the theoretical investigations on estimation of certain parameters of the wavy wall profile that can effectively reduce the jet noise. Next objective is to study various parameters

of the wavy wall profile and compare the noise reduction with the conventional flat shield design.

1.6. Dissertation Organization

In this section the organization of the dissertation is presented.

In the first section of Chapter 2, the problem statement and the specific research goals are described to explain the motivation, and the details of the objectives set to be achieved. Next, the numerical approach is described. Specifications of the numerical scheme, the space and time discretization, and turbulence modelling, is described. The numerical stiffness and instabilities introduced due to the material interfaces with sharp density discontinuity is explained, and the appropriate implementations in numerical solver is described to achieve the first item of the research objectives. Then the boundary treatment and the computational grid is discussed, to explain the required grid spacing to capture the acoustic waves, and the water jet break-up phenomena in the domain. The surface integral approach and the specific treatment used for predicting the far field acoustics is described. A comprehensive sensitivity study of location of the integral surfaces is explained to ensure numerical results are not highly sensitive to flow passing through the control surfaces.

In the following section of Chapter 2, the results of the baseline case are presented. The flow filed and acoustic data are compared with the available experimental data. Then the results for the case with water injection are presented. The water jet break-up and the trajectory of the water droplet lumps is illustrated, along with its consequent effect on acoustic waves. The acoustic results for both cases are compared with the experimental data, and the overall effectiveness of water injection is quantified. Then the effect of

water injection on the flow perturbations of the impinging jet is investigated. The main mechanisms involved in the noise reduction due to water injection are concluded. First, it is illustrated that as the generated sound waves propagates outward, they encounter some water droplets. The scattering of the propagating sound waves is shown, explaining the reduction of the amplitude of the transmitted waves. Second, it is shown that the injection introduces small disturbances that interact with the noise generating large-scale flow structure. This is achieved by benefiting from the numerical results, that enable the visualization of the large-scale structures. Finally, due to the higher density of the water and the direction of injection, reduction is observed in the physical extent of the noise-producing wall region via exchange of the momentum. This explains the effect water injection on wall jet region. After discussing the noise sources due to the normal impingement in this chapter, jet interaction with a solid surface parallel to the jet is targeted.

In Chapter 3, the acoustic shielding effect of the flat surface parallel to the jet exhaust is addressed. The geometry of the rectangular nozzle, and the dimensions of the flat plate shield is explained, followed by the specific research objectives. Next, the numerical approach appropriate for this specific problem is described. Although there exist some similarities between the numerical approach in this chapter and the one mentioned in Chapter 2, such as: governing equations, and turbulence modelling. But, since there is no multiphase flow modelling involved here, the focus of the numerical approach is on capturing acoustic waves and modelling the acoustic shielding effect. To this end, an open source solver is chosen to implement the numerical schemes and boundary conditions, appropriate for numerical simulation of acoustic shielding effect. The specific

formulation of the surface integral approach is described. The implemented formulation simplifies the famous Farassat 1A formulation (Farassat, 1998), making it more suitable to model effect of the shielding plate. In the first two appendices of this dissertation (APPENDIX A – Verification Benchmark: Pulsating Sphere, APPENDIX B – Verification Benchmark: Shock Capturing), benchmark validations are presented, for the verification of the implemented numerical approach for the far field acoustic prediction, and capturing shock discontinuities, respectively.

Followed by the numerical approach, the results for the heated supersonic jet is presented. The isolated jet flow field and acoustic results are validated with the available data. The effect of flat plate on the supersonic jet is investigated for two scenarios. First, where the plate is placed near the nozzle lip, and creates a wall-jet flow. Second, where, the plate is at a certain distance from the nozzle, and only the acoustic reflections interact with the jet. In both of these scenarios, the shielding effect of a solid surface is investigated as a noise reduction approach, targeted for supersonic aircraft concepts with an integrated design of the engine and airframe. Two main mechanisms were found that affect the efficiency of the flat shield. It is shown that, when the flat shield is close to the jet, part of the flow acts as a wall jet, and intensifies fluctuations, and adversely affects the noise source. However, when the flat shield is away from the jet flow, the radiated acoustic field reflects from the solid surface and can amplify the jet noise source. In the latter case, it is crucial that the numerical simulations accurately predict the reflection waves, without introducing dissipations at the solid boundaries. To ensure the accuracy of implemented numerical schemes, for capturing the reflection of acoustic waves from a solid boundary, a verification benchmark problem is provided in APPENDIX C –

Verification Benchmark: Acoustic Reflection from Wall.

The mechanisms described in this chapter, lay out the groundwork for the proposal of a new design for the airframe surface under the top-mounted engine to utilize these mechanisms to effectively reduce the noise source. The general idea behind the wavy wall design is described, by revisiting the theoretical studies (Arbey & Ffowcs Williams, 1984; Mankbadi 1985a, 1985b). The wavy wall profile is utilized such that the acoustic waves reflecting from the shield are manipulated in a way to reduce the noise source itself. The estimation of the wavy wall design parameters is explained, by utilizing theoretical relationships, as well as, employing findings from the validated numerical results. The effect of the wavelength of the dominant noise sources in the jet flow, and the corresponding phase shift difference between the wavy wall wavelength is described as a noise mitigation approach. By adjusting the appropriate wavy wall parameters nonlinear interaction between the fundamental and its harmonic is introduced. It is illustrated how this mechanism can reduce the net noise source and the total radiated noise.

Chapter 4 reports the concluding remarks regarding each part of this work, discussed in Chapter 2 and Chapter 3. In addition, detailed discussion about suggestions of future research for each part is provided separately.

Parts of this dissertation were published in journal publications and conference papers. The numerical aspects of simulation of supersonic impinging jet and its noise reduction via water injection is published by Salehian et al. (2018). In particular, the specific numerical approach appropriate for overcoming numerical stiffness of simulation of water droplets in a supersonic flow, are described. Then, the extension of this study

including the acoustic results for both base case and the water injection case are published by Salehian and Mankbadi (2020c). The analysis of the acoustic shielding effect of a parallel plate close to the nozzle exit is explained in Salehian and Mankbadi (2019). Targeting the integrated engine-top design of future supersonic aircrafts, more details of the acoustics of the shielding plate and the mechanisms involved are explained by Salehian and Mankbadi (2020b). The specific effect of the acoustic reflections on the flow field and acoustics of the jet, when the plate is at a certain distance from the jet, is reported (Salehian & Mankbadi, 2020a).

2. Numerical Simulation of Rocket Launch Noise Suppression via Aqueous Injection from Impingement Pad

The focus of this research is to understand the effect of water injection from the launch pad on the noise generated during rocket's lift-off. To simplify the problem, a supersonic jet impinging on a flat plate with water injection from the impingement plate, is considered. The Volume of Fluid (VOF) model is adopted in this work to simulate the two-phase flow. A Hybrid LES – URANS (HLU) approach is employed to model turbulence, wherein URANS is used near the walls, and LES is used elsewhere in the computational domain. The numerical issues associated with simulating the noise of two-phase supersonic flow are addressed. The pressure fluctuations on the impingement plate obtained from numerical simulations agrees well with the experimental data. Furthermore, the predicted effect of water injection on the far-field broadband noise is consistent with that of the experiment. The possible mechanisms for noise reduction by water injection are discussed.

2.1. Motivation, Problem Statement, and Research Objectives

During rocket launch, the exhaust plume generates significant fluctuations in the flow and the acoustic field causing structural vibrations, which can adversely affect the payload and the sensitive instrumentations on board. A similar situation is encountered on aircraft carriers wherein aircraft's takeoff can cause noise pollution for the ground personnel.

To address this problem, several experimental investigations have shown that injecting water in the initial region of unbounded supersonic jet can reduce noise (Greska et al., 2004; Krothapalli et al., 2003; Marchesse et al., 2002; Zoppellari & Juve, 1998).

Washington and Krothapalli (1998) suggest that the water injection affects the dominant sources of the turbulent mixing located at the end of the potential core region of the jet and reduces the mixing noise. This approach, however, if used for aircrafts or rockets would require carrying water on board.

Alternatively, for rocket launch or aircraft carriers, it is more practical to inject water from the impingement pad (launch pad or deflector). Ignatius et al. (2008, 2014) and Ragaller et al. (2011) have considered supersonic jets impinging on a perpendicular plate and have shown, experimentally, that injecting water from microjets through the impingement plate can reduce noise. They conjectured that water injection from the ground plane reduces the sources of sounds due to impingement. Particle Image Velocimetry (PIV) of a supersonic impinging jet by Elavarasan et al. (2000) revealed important flow features such as oscillating slipstream shear layers and large-scale structures.

Numerical attempts to simulate water injection in supersonic jets are limited. Tsutsumi et al. (2008, 2009) used URANS to estimate the sound sources. Vu et al. (2014) employed multiphase numerical simulations to track the water injected from a rain-bird nozzle used for sound suppression system during launch. In the study presented here, LES is employed in the near field to capture the unsteady flow fluctuations, which are absent in previous simulations.

Simulating the effects of water injection may help optimize the design of the water suppression system in real launch situations. Therefore, an impinging supersonic jet is considered here, in which water is injected from the impinging plane through aqueous microjets. This is taken as simplified model of rocket lift-off noise. A full LES would be

the appropriate approach. However, to reduce the resolution requirements for such complex geometries, the HLU approach is adopted. In this approach, URANS is used near the walls, whereas LES is used elsewhere in the domain. This approach has been successfully adopted for jet noise prediction in single-phase supersonic flows (Brown and Frendi, 2012; Mankbadi et al., 2000, 2016) and, and is extended here to consider the two-phase case. As we need to validate our numerical results, the simulation parameters are taken here to correspond to that of the experiment of Ragaller et al. (2011).

Numerically simulating the unsteady supersonic flow structure and its radiated sound is a challenging task by itself due to the resolution and accuracy required while ensuring that no spurious modes are introduced at the out flow boundaries that would reflect back and contaminate the solution (Mankbadi et al., 1994, 2000). When water droplets are present, it complicates the problem further as it creates material interfaces with sharp density discontinuity causing numerical stiffness and numerical instabilities. These difficulties, along with the governing equations, numerical scheme, and the boundary conditions are discussed in the following sections. The phenomenon of vaporization of water in a hot-impinging jet, or the actual rocket plume impingement is not considered here. The problem is simplified here by considering the cold case as in experiment (Ragaller et al., 2011), where evaporation is minimum. The work can then be taken as a steppingstone to consider further complicated situations. Results for the base case with no injection are presented in first, followed by the results for the water injection case compared with the base case are presented.

The sketch of the computational domain shown here in the in Figure 2.1 is provided to represent the experimental set up carried out at the anechoic facility of the Advanced

Aero-Propulsion Laboratory at Florida State University. Further details of the experimental studies can be found in Ragaller et al. (2011). A supersonic Jet $M = 1.5$ impinging on a flat plate with six inclined microjets are mounted on the ground plane which are equally spaced along a 2.0 inch ($50.8\ mm$) radius centered on the jet axis, inclined at a 30° with respect to the jet axis. All six microjets have an inside diameter of $1mm$. The supply pressure measured just upstream of the water jet nozzles in the manifold was kept at a constant 800 psig (5515.81 kPa). The nozzle has a throat diameter of $d_{th} = 33\ mm$ and exit diameter of $d = 36\ mm$, and the flat plate is placed at $h = 8d$ from the nozzle exit.

Also, Figure 2.1 illustrates the installed experimental set up by Ragaller et al. (2011). The Mach number used here is less than that of rockets at lift-off, but this Mach number is used in our simulations here due to the limited experimental data for ground water injection into an impinging air jet. Nevertheless, the connection to application for rocket lift-off is not too unrealistic since the injection is from the ground and the jet plume is supersonic as in rockets launch. In addition, the nozzle geometry has a contoured design and is operating at the design conditions as mentioned in Gustavsson et al. (2010), However, as it is shown in in the following sections, the presence of the lift plate affects the ambient pressure near nozzle exit, and causes the jet to exhaust, instead, as near-ideally-expanded.

The schematics of the problem in Figure 2.2, as well as our numerical results of the flow field to be given later, are presented in a vertical orientation for better representation of the impinging jet problem. However, it should be noted that the experiment was carried out such that the gravity force and jet axis would stand in a perpendicular

orientation. As such, the gravity force modeled in numerical simulations is also perpendicular to the jet axis and along the flat plate to follow the experimental set up. The flow specifications of the main jet and the aqueous microjets (for the injection case) are summarized in the Table *2.1*.

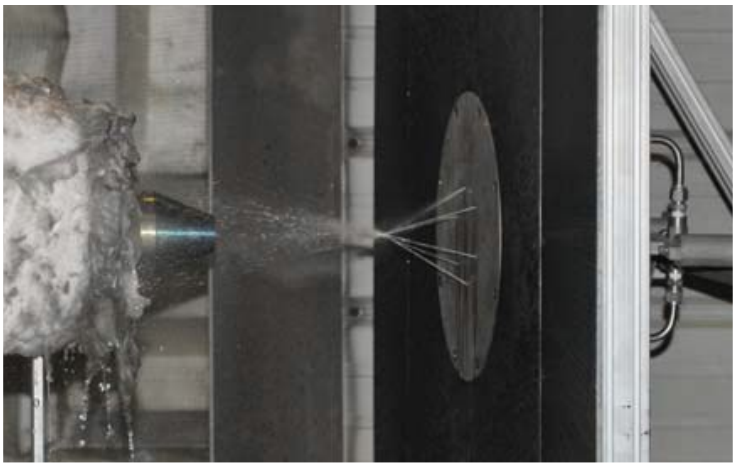

Figure 2.1 The experimental set-up, illustrating the water flow only (Ragaller et al., 2011).

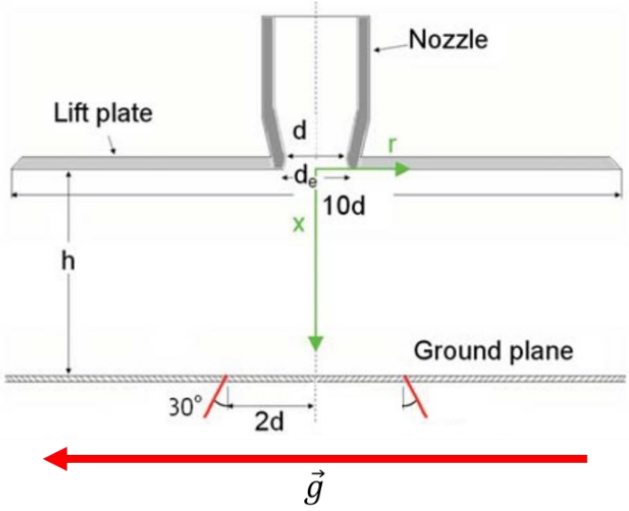

Figure 2.2 Schematics the nozzle and the and the impingement plate.

Table 2.1

Flow specifications of main jet and the microjets modeled in the simulations.

	Mach Number (Ma)	**Reynolds Number (Re)**	**Total Pressure (P_o)**	**Total Temperature (T_o)**	**Exit Velocity (U)**	**Mass Flow Rate ($\dot{m}$)**
Main Jet	1.5	1.24×10^6	$3.67\ MPa$	$295\ K$	$430\ m/s$	$0.75\ kg/s$
Microjets	0.3 (a_{air})	1.1×10^4	$5.51 MPa$	$300\ K$	$105\ m/s$	$0.08\ kg/s$

Several experimental data for a cold jet impinging problem (Ragaller et al., 2011; Gustavsson et al., 2010) shows a somewhat constant mean temperature of $290\ K$ (with less than $5\ K$ deviation in fluctuations) on the flat plate from $r/d = 0 - 3.5$ for the cold jet case ($TR = T_o/T_a = 1$), suggesting that the evaporation of water droplets is not significant due to absence of significant temperature raise. Moreover, required high temperature based on Specific Latent Heat (SLH) is calculated here for completeness. The SLH for vaporization of water as a pure liquid, is used from Datt (2011) $SLH = 2264.7\ KJ/Kg$, with the mass flow rate of the water injection, the required heat for evaporation would be $\dot{Q} = \dot{m} \times SLH = 181.17\ KJ/s$. Using the energy equation for this value of heat ($\dot{Q} = \dot{m} c_p (T_{min} - T_w)$), where $c_p = 4182\ J/KgK$ for liquid water, the minimum value for the high temperature in the domain must reach at least $T_{min} = 840.5\ K$ to provide enough energy for evaporation of water. Whereas, the temperature does not reach anywhere close to this value based on the measurements by Ragaller et al. (2011). Hence, the effect of evaporation is not considered in the current simulations.

On the other hand, the numerical approach adopted here accounts for the two-phase flow model of liquid – gas interactions, inclusion of evaporation effects would require addition of more complex numerical simulation to account for gas – liquid water – vapor interaction. Current simulation is a step toward calculating the real heated jets (with

evaporation) associated with rockets, which would be of interest for future studies.

2.2. Numerical Approach

In this section the numerical aspects of predicting the fluctuating flow field and its nearfield, as well as the extension of the nearfield to far field is discussed. Here, the governing equations, numerical scheme, and the boundary conditions are presented, followed by the acoustic surface integral approach to capture the far field acoustics. Then the computational grid is presented, and relevant remarks are made about turbulent scales, and acoustic wavelength that are captured in numerical simulations.

2.2.1. Governing Equations and Volume of Fluid Method

For the solution of multiphase flows, the Eulerian approach is adopted here. In the Euler approach, different phases are treated mathematically as interpenetrating continua wherein the volume of each phase cannot be occupied by the other phases. Phase volume fraction is defined as a continuous function of space and time and their sum is equal to one (Yeoh & Tu, 2009). VOF method of as a Euler approach is employed here, which tracks the separating surface by defining a scalar indicator between zero and unity, to distinguish different phases of fluids. The main advantage of VOF method is that instead of solving a set of governing equations for each phase, a single set of momentum and energy equations shared by both phases are solved, and the volume fraction for each of the fluids in each computational cell is tracked throughout the domain. The coupling between the phases accounts for the forces exchanged and heat transfer across the interface. This method is ideal for problems which involve gas-liquid interactions, and therefore is used herein.

The material properties to be used in the governing equations such as density, are

defined as:

$$\rho = \sum \alpha_q \rho_q \tag{1}$$

Here, q represents each phase, and α is the phase fraction. The other properties such as viscosity and thermal conductivity are defined in a similar manner. By solving the following continuity equation for the volume fraction of the phases, the interphase between the phases is captured:

$$\frac{1}{\rho_q}\left[\frac{\partial}{\partial t}(\alpha_q \rho_q) + \nabla.(\alpha_q \rho_q \overrightarrow{v_q}) = \sum_{p=1}^{n}(\dot{m}_{pq} - \dot{m}_{qp})\right] \tag{2}$$

where, $\dot{m}_{qp}$ is the mass transfer from phase q to phase p and $\dot{m}_{pq}$ is the mass transfer from phase p to phase q. The other equation, which completes the phase-fraction continuity equation, is that in each cell the summation of each phase's volume fraction is unity:

$$\sum_{p=1}^{n} \alpha_q = 1 \tag{3}$$

The momentum and energy equations are given by:

$$\frac{\partial}{\partial t}(\rho \vec{v}) + \nabla.(\rho \vec{v}\vec{v}) = -\nabla p + \nabla[\mu(\nabla \vec{v} + \nabla \vec{v}^T)] + \rho \vec{g} + \vec{F} \tag{4}$$

$$\frac{\partial}{\partial t}(\rho E) + \nabla.\left(\vec{v}(\rho E + p)\right) = \nabla.(k \nabla T) + S \tag{5}$$

The unknown variables in the momentum and energy equations can represent either of the two phases or both, depending on whether the cell is occupied by one phase or by both phases identifiable by the interface. The mixture material properties such as density and viscosity contain the information about the phase fraction as given by Equations (2 and 3). Here $\vec{F}$ represents the volumetric forces at the interface, such as surface tension, drag, and wall shear forces, and g represents gravity. Also, the energy equation is shared

in a similar fashion. The energy, E, is defined as:

$$E = \frac{\sum_{q=1}^{n} \alpha_q \rho_q E_q}{\sum_{q=1}^{n} \alpha_q \rho_q} \tag{6}$$

The term S, in the energy equation, Equation (5), is the volumetric heat source term that can model the vaporization and condensation if needed (neglected here). In this VOF model, when a surface is encountered that separates the two phases, forces and energy transfer are accounted for. Thus, drag and heat transfer are calculated. As explained earlier, the phase exchange due to evaporation is negligible for the cold jet impingement scenario, thus phase change is not considered here. Moreover, surface tension effect is ignored due to high velocities of the fluids in the domain.

The volume of fraction equation is solved through implicit time discretization, and a standard finite-difference interpolation scheme is used to obtain the face fluxes for all cells, including those near the interface. The compressive scheme (Ubbink, 1997), is a high-resolution differencing scheme and is recommended to be used for the interface capturing to solve the discretized implicit volume fraction equation. In our solution procedure, we chose the coupled option in which the phase fraction is coupled with the rest of Navier-Stokes equations. The details of this approach are discussed below.

2.2.2. Numerical Scheme

Recently the use of a structured mesh over unstructured mesh in LES has been debated. There have been several attempts for developing high-order schemes on unstructured grid, which are reviewed by Huynh et al. (2014). In the study by Mankbadi and Georgiadis (2015), it was shown that a second-order control volume scheme can be modified to conduct LES with accuracy comparable to that of the structured high-order schemes, if the grid resolution is fine enough. In theory, if we were to replace a second

order spatial discretization scheme with a fourth order scheme on structured grid, we can reduce our grid size by 1/8th to obtain the same accuracy. However, this is an overestimation because: (1) with unstructured grids you can use less points to represent complex boundaries than for structured grid. (2) Changing the expansion ratio in structured grid reduces its accuracy. (3) Boundary treatment for the structured high-order schemes are problematic. In most cases you will need to use a low-order boundary treatment, extend the domain to include sponge layer, matching layer, or an exit layer, etc. (4) High-order schemes are usually more CPU intensive than unstructured grid (larger stencils, or more derivatives are needed to be computed). Thus, in realty, that 1/8th estimate in reduction of the grid point is quite an over-estimation. As such, we use here an unstructured control-volume approach. This will allow us to model complex geometries as used in the launch pad or in corresponding experimental investigations.

The numerical simulations presented in this work are carried out using ANSYS® FLUENT R18.2, which is a full Navier-Stokes solver that implements the finite-volume approach. In the following sections, some of the important specifications of the numerical set up are explained, and some valuable remarks are made in terms of the required considerations for such a complex numerical problem. Further details about the numerical aspects of simulation are given in (Salehian et al., 2018).

In the present problem of two-phase impinging jet, there are regions of high compressibility as near the jet exit, and regions of low compressibility away from the jet or as when it encounters water droplets. Usually, for low-compressibility flows, the pressure- based segregated formulation is used (e.g. SIMPLE or PISO). On the other hand, density-based solvers tend to be the appropriate choice for highly compressible

flows. Given the physics of the current problem in terms of containing compressible and incompressible regimes, and our need to use the VOF method, we choose to work with the pressure-based coupled solver. The coupled pressure-based method successfully extends applicability of pressure-based segregated techniques to problems where the inter-equation coupling is strong. This is well investigated and reported by several studies (Abgrall & Karni, 2001; Boger, 2014; Klein, 1995). Unlike the pressure-based segregated algorithm in which the momentum equations and pressure corrections equations are solved one after another in a decoupled manner, the pressure-based coupled algorithm solves the momentum equations and the pressure corrections as a closely coupled system of equations. This enables successfully capturing the high- and the low- Mach number regions with improved rate of convergence.

2.2.3. Spatial and Temporal Discretization

The control-volume technique is used here to solve the governing equations. The conventional upwind procedure would cause the numerical dissipation to restrain the predictive capabilities of LES whenever it is of the same order of magnitude or larger than the Sub Grid Scale (SGS) dissipation (Castiglioni & Domaradzki, 2015). Since we need to accurately predict the noise sources, such as the large structures in the shear layer, we use here a QUICK-type scheme (Leonard and Mokhtari, 1990) to minimize dissipation. As described by Leonard and Mokhtari (1990), this scheme computes a higher-order value of the convected variable by forming a weighted average of second-order upwind and central interpolations of the variables when employed for hexahedral cells. This is appropriate for quadrilateral and hexahedral meshes where unique upstream and downstream faces of the cells can be identified. For unstructured or hybrid meshes

the second-order upwind discretization scheme will be used at the faces of non-hexahedral and at partition boundaries when the parallel solver is used. To reconstruct the face values, the gradients of the flow variables are calculated. The cell-based least squares approach is adopted in these simulations. The solver chooses the weighted average of upwind and central interpolations, such that it does not generate solution extrema.

The bounded second-order implicit time scheme (Versteeg & Weeratunge, 2007) is used to march the solution in time. The time step was selected here to ensure that the important frequencies are appropriately resolved. A constant time step of 1×10^{-6} physical seconds is used to ensure capturing the highest needed non-dimensional frequency of 1.09 (fd/U_j). The highest resolvable frequency for capturing the main acoustic behavior of the supersonic jets is described in detail by several studies (Brown & Frendi, 2012; Mankbadi et al., 1994, 2000, 2016). This corresponds to non-dimensional time step with respect to the nozzle exit velocity and nozzle throat diameter. The corresponding convective and acoustic maximum CFL corresponding to this time step are 0.9 and 0.59, respectively. In order to verify the independency of results to time step size, the time step was tested from 1×10^{-7} to 1×10^{-6} with increments of 2×10^{-7} (physical seconds) with no effect on the final stable solution of the HLU simulations.

The solution initialization for the water injection case is done in two steps. First, a full pseudo-transient steady state solution is carried out to provide an approximate steady-state solution. Next, a more accurate URANS simulation is carried out to provide a better estimate of the flow-field. This is used as the starting initial guess for the LES simulations. The simulations continue until there is an established flow fluctuations and

acoustics field.

For any statistical data presented here, a sequence of 16,384 samples, with a sampling frequency of 200 kHz are collected, which covers the physical time period of around 980 non-dimensional time (non-denationalized by d/U_j). It should be mentioned that the sampling rate used here is very close to the sampling rate used in the experimental measurements with sampling rate of 204 kHz. To obtain acoustic data, the collected pressure time history is converted into spectrum by using Fast Fourier Transform (FFT). Generally, applying the FFT function on a random complex signal without the use of averaging, results in spurious fluctuations of amplitudes between the neighboring modes of the Fourier spectrum. To obtain a smooth spectrum, a single period sample is divided into several segments. Here, each segment contains 4096 samples with hanning window and 50% overlap. The FFT is then applied on each segment and the resulting spectra are averaged. This procedure can significantly suppress the spurious fluctuations of the spectrum based on the number of samples in each segment.

2.2.4. Turbulence Modeling (URAN-LES Switch)

The Navier-Stokes equations are solved to obtain the transient simulations with a hybrid URANS and LES. The turbulence viscosity is defined following the Boussinesq's hypothesis, thus, the governing equations for URANS and LES become formally identical. Where $\vec{v}$, p, and ρ in Equation (4) denote the URANS averaged or spatially filtered (LES) velocity. Hence, the eddy viscosity ν_t approximates the sub-grid scale (LES) or Reynolds (URANS) stress tensor τ_{ij}, which represents the non-resolved turbulent momentum transfer.

The hybrid simulation here includes the Stress-Blended Eddy Simulation (SBES)

(Straka et al., 2018) which is a hybrid URANS-LES turbulence model that uses the same shielding function as the Shielded Detached Eddy Simulation (SDES) (Gritskevich et al., 2012) formulation and adds the ability to blend the underlying URANS model directly to any existing algebraic LES model. The stress-blending function defined as:

$$\tau_{ij}^{SBES} = f.\tau_{ij}^{RANS} + (1-f)\tau_{ij}^{LES} \tag{7}$$

During the simulation, the $k-\omega$ turbulence model (Wilcox, 1998) and Smagorinsky-Lilly model (Smagorinsky, 1963) are solved on the entire domain respectively to compute τ_{ij}^{RANS} and τ_{ij}^{LES}, and the adaptable blending function f determines in which regions they are applied.

In Detached Eddy Simulation (DES) formulations, the switch between RANS and LES is based on the turbulent length scale L_t, and maximum grid size Δ_{max} . This criterion enforces RANS when $C_{DES}\,\Delta_{max} > L_t$, while LES is implemented when $C_{DES}\,\Delta_{max} \leq L_t$, where C_{DES} is a DES constant. When $\Delta_{max} \leq L_t$, a DES limiter is activated and switches the model from RANS to LES mode. The goal is to run RANS mode for attached flow regions, and to switch to LES mode in detached regions away from walls. To avoid possible non-physical separation in the attached boundary layer due to the limiter (Menter & Kuntz, 2004), the shielding function, f, is defined in a similar manner to that of Gritskevich et al. (2012) as:

$$f = 1 - \tanh\left[\left(C_{d_1} r_d\right)^{C_{d2}}\right] \tag{8}$$

$$r_d = \frac{\nu_t + \nu}{k^2 d_w^2 \sqrt{\frac{S_{ij}^2 + \Omega_{ij}^2}{2}}} \tag{9}$$

where d_w^2 is the wall distance, $k = 0.41$ is the von Karman constant, $C_{d_1} = 2$, and $C_{d2} = 0.4$. Thus, the shielding function shields the URANS wall boundary layer region against influences from the LES model and provides faster transition from URANS to LES in separating shear layers. The URANS-LES switch may affect the resolved structure in the inner wall layer, which is believed to be a negligible sound source in the present problem.

2.2.5. Numerical Stiffness

One of the main problems in numerical simulation of multiphase supersonic flows is the numerical stiffness which is mainly caused by the high-density differences between the phases (water and air) across the interfaces. For example, Boger (2014) investigated the numerical simulation of compressible flows in two-phase domain and has stated that simulation of droplets or bubbles with small radii is often not possible. In the present work, the presence of water-droplets in the flow introduces high density gradients. This is addressed here as pointed by Ubbink (1997) through the time accurate implicit compressive VOF scheme. This approach provides better convergence and a relatively sharp interface capturing. In addition, the second order upwind scheme used for interpolation of density provides stability for supersonic flows, and the weighted QUICK-type scheme accounts for the higher accuracy required.

As pointed out earlier, in this VOF model for multiphase supersonic flows, the governing equations are coupled, and we use the pressure-based coupled control volume solver. To speed up convergence, the solver uses Algebraic Multi Grid (AMG) solver to accelerate the convergence by computing corrections on a series of coarse grid levels. The more effective AMG smoother (Hutchinson & Raithby, 1986) based on the Incomplete Lower Upper (ILU) decomposition technique is used here.

In addition, the solver formulations take advantage of gradient limiters used on higher-order schemes to prevent spurious oscillations near shocks, discontinuities, or rapid local changes in the flow field. The A non-differentiable limiter based on the Minmod function (Barth & Jespersen, 1998) is utilized here to limit the reconstructed solution overshoots and undershoots. The differentiable limiter (Venkatakrishnan, 1993), which uses a smooth function to impose the monotonicity condition, was also tested for this study. This limiter only showed to affect number of iterations that takes for the absolute value of residual tolerance to reach order of magnitude of 1×10^{-8}.

2.2.6. Boundary Treatment

The experiment explicitly provides the total pressure upstream of the nozzle and states that it is monitored and maintained constant to provide the operating conditions for the nozzle. The Nozzle Pressure Ratio (NPR), and Temperature Ratio, are assigned according to the values provided in Table *2.1*, so that the nozzle operates at $NPR = 3.67$, and $TR = 1.00$, similar to the experimental setup. As such, the isentropic compressible relations are calculated to impose steady static temperature and pressure at the inflow boundary. In our numerical solution, the total pressure and total temperature boundary conditions are used to calculate the static pressure and temperature with isentropic relations. At the nozzle inflow boundary, the total conditions are specified to calculate the static thermodynamic properties. This is done by using pressure inlet boundary condition with the input total pressure and total temperature. The nozzle interior, lift plate, and the impingement walls are specified as adiabatic no slip wall boundaries. The adiabatic condition for the wall is chosen since the experiment does not provide specifics on the heat transfer on the impinging wall, hence the adiabatic condition seems to be a fair

estimate for boundary condition set up of the walls.

The far field boundary is specified by a given static (ambient) pressure for the outlet boundary condition. The characteristics-based, non-reflecting boundary condition is used to avoid the wave reflections from the computational boundary that can contaminate the interior acoustic field. The non-reflecting boundary condition used here is based on the characteristic wave relations derived from the Euler equations reformulated into an orthogonal coordinate system such that one of the coordinates is normal to the boundary. The amplitude of the incoming pressure and entropy waves are computed from the Linear Relaxation Method (LRM) (Poinsot & Lele, 1992). The input of the outlet boundary condition includes a specified pressure value at the exit boundary, the relaxation factor, and the local pressure value at the boundary. Further details of such characteristic analysis are provided by Thompson (1987, 1990). The edges of the entire computational domain are illustrated in Figure 2.3. Here, blue represents the non-reflecting outlet boundary condition, green represents the pressure inlet boundary conditions for the main nozzle and the microjets, and orange represents the wall boundary, respectively.

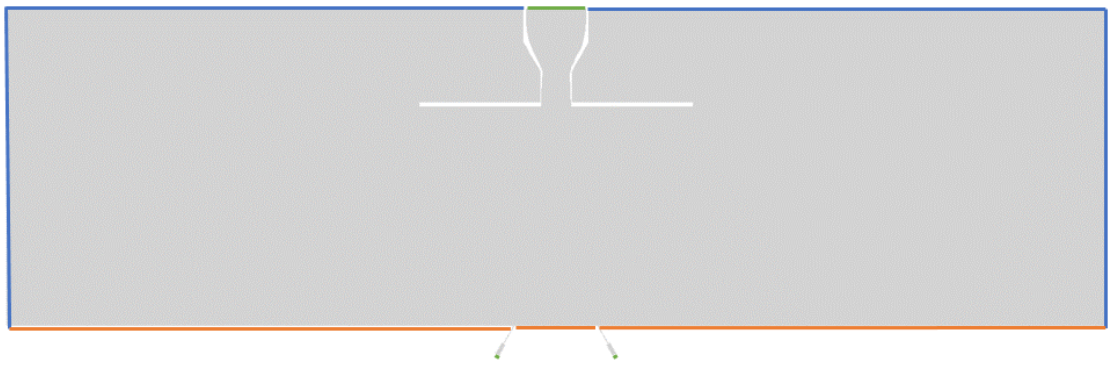

Figure 2.3 Boundary conditions.

2.2.7. Computational Grid

Grid points are clustered in the shear layer region and the injectors, but no extensive attempt is made to resolve the wall boundary on the lift plate. However, grid spacing on the ground wall plane was kept constant such that it provided maximum value of $y^+ = 30$ on the impinging plate. The boundary layer is modeled using the URANS as explained in Section 2.2.4, hence, finer grid spacing on the ground plane to model boundary layer would be defeat the purpose of employing HLU approach. As explained Mankbadi et al. (2000, 2016), it is suggested by to maintain a range of $30 < y^+ < 300$ To model the boundary layer using HLU or any wall modeled LES approach, such that the first grid point distance from the wall would satisfy the law of the wall (Versteeg, 2007).

The computational grid consists of about 60 million unstructured hexahedral dominant cells. In LES, solution is considered converged when it becomes stable with no cycle-to-cycle variation of the fluctuations. This has been achieved for these results. Increasing the mesh size will enable capturing higher frequencies. Here, about 15 points per wavelength are maintained in the acoustic regime. Typically, there is a general agreement in the research community that at least 6-8 points per wavelength is required for capturing the acoustic waves in the near field for high order schemes (Such as 6^{th} order compact scheme). However, it is suggested to maintain double of that requirement when 2^{nd}-3^{rd} order schemes are employed in Hexahedral finite volume grids (Davidson, 2009). As it can be seen in Figure 2.4, this minimum grid spacing is kept as the maximum possible grid spacing for capturing acoustics, but the shear layer region and the impinging wall region have much finer grid spacing as explained earlier. Based on using the speed

of sound, it can be estimated that the maximum frequency resolved is 13 kHz. This corresponds to $St = 0.85$ which covers the range of interest.

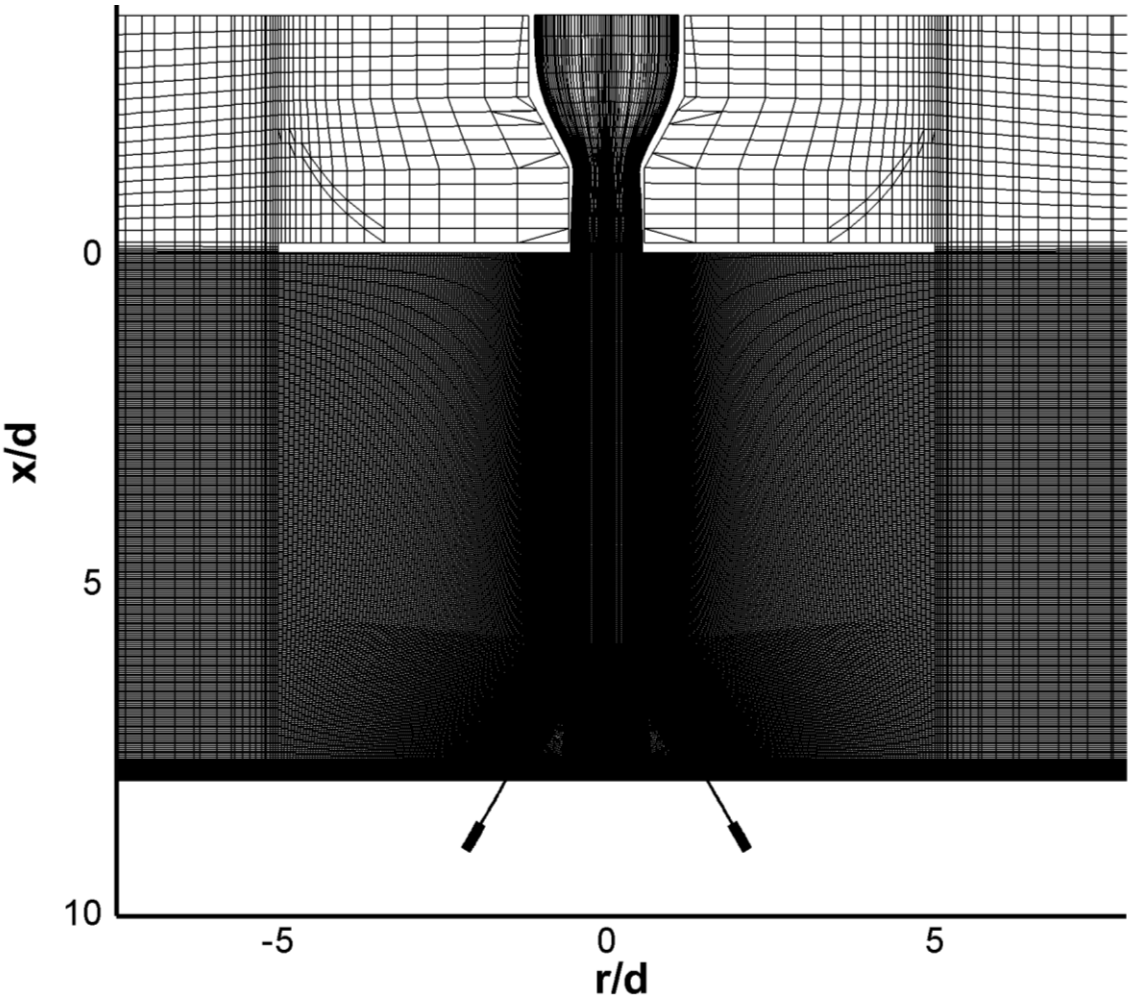

Figure 2.4 Cutaway of the grid on x-r plane, and qualitative of representation of the cells.

The injector region outfitted from the ground plane is illustrated in Figure 2.5, showing the clustered grid spacing inside the water injector, continuing into the open domain to capture the water stream breakup.

The far-field is spherical and highly stretched to avoid any unwanted reflections back

into the domain, as shown in Figure 2.6. This grid is constructed using the ANSYS® Workbench Meshing tool. The injector faces are connected to the wall at the interface wall with the non-conformal approach. Most of the grids are clustered near the shear layer regions and the impinging wall.

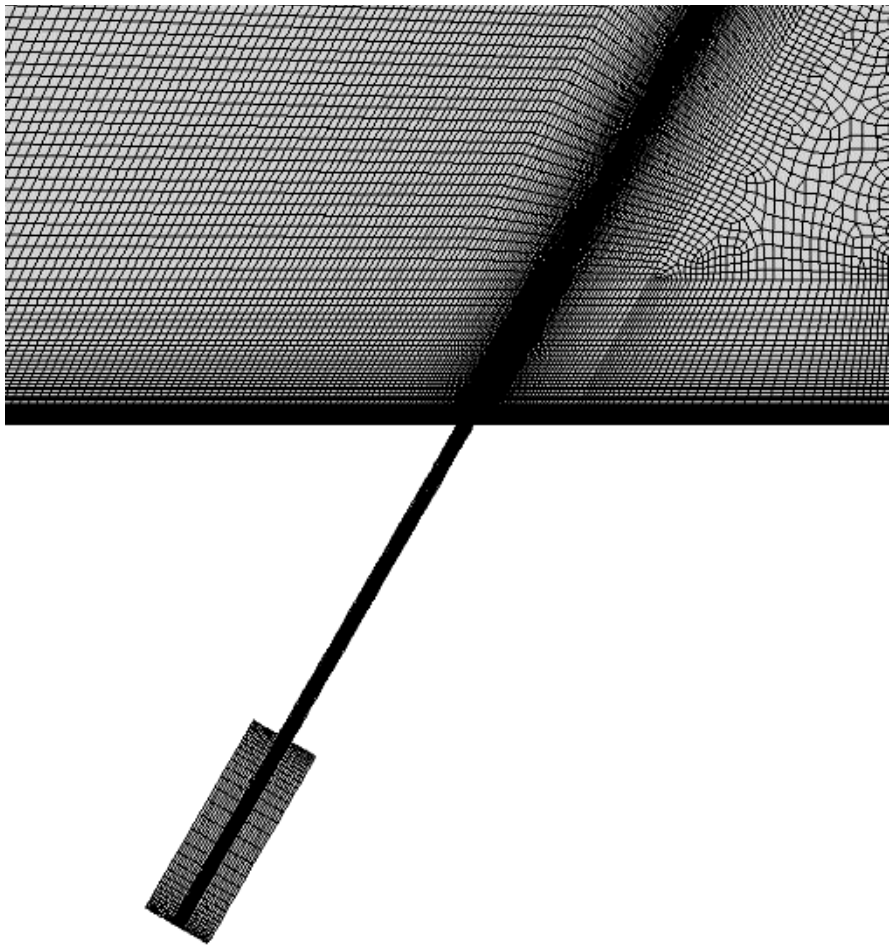

Figure 2.5 Grid spacing clustered inside the water injector.

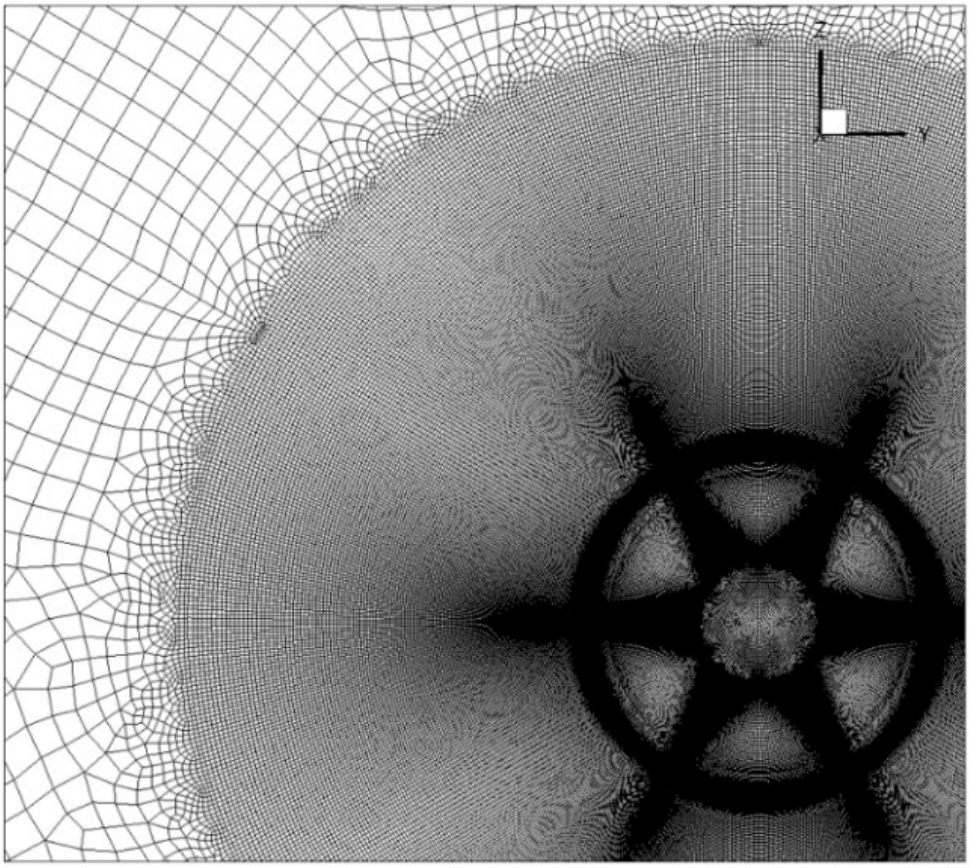

Figure 2.6 Grid spacing on the ground surface.

2.2.8. The FWH Surface Integral Approach

The near to mid field acoustics are directly predicted by LES. The far field acoustics is obtained using the Ffowcs Williams–Hawkings (FWH) extension technique (Ffowcs-Williams and Hawkins, 1969). The FWH equation is an inhomogeneous wave equation derived by manipulating the Navier-Stokes equations. The complete solution consists of surface integrals and volume integrals.

For a non-permeable surface, the volume integral term denotes the quadruples outside the permeable surface. If one assumes that the control surface contains all acoustic sources, the volume integrals outside this surface can be dropped. More detailed

information can be found in a detailed review by Lyrintzis (2003).

In the current simulation, a cylindrical surface concentric with the jet core with a radius of 5 throat diameters was set as the FWH surface, which was found to be adequate for the jet flow. But to investigate the sensitivity of the FWH surface to the passage of the wall jet vorticities across the FWH surface near the impingement plate, the lower part of the surface is extended further away. Figure 2.7 illustrates the FWH surface and how the lower part of the surface is extended. For far-field acoustic analysis, the flow field data are stored at the 4 different possible surfaces (FWH1, FWH2, FWH3, and FWH4) for which the cylinder near the wall is extended to 5, 6, 7, and 8 nozzle radii, respectively.

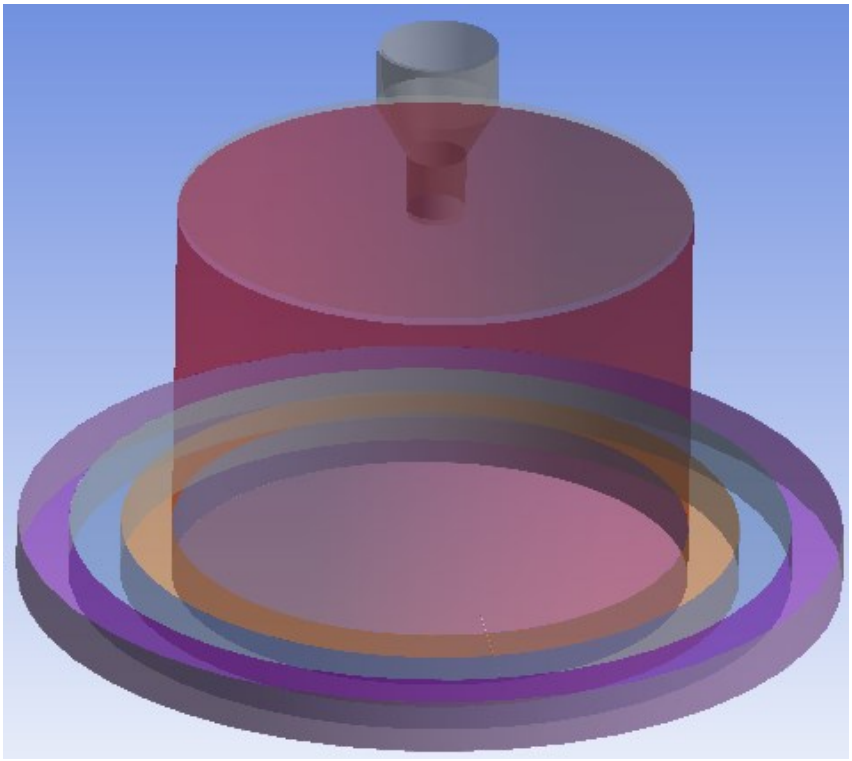

Figure 2.7 Illustration of nozzle, lift plate, and FWH surfaces. FWH1 (red), FWH2 (Orange), FWH3, (Blue), and FWH4 (Magenta).

FWH1 surface is the cylinder that extends from the edge of the lift plate at the nozzle all the way to the impingement plate. It should be noted that the computational grid inside of the FWH region and on the control-surfaces have been kept fine and uniform. To be able to capture near field acoustics, a minimum of 12-15 point per wavelength is maintained inside the FWH surface region, which enables capturing waves up to 13 kHz. The bottom region only (FWH extension) contains around 15 million cells. The collected data from all FWH surface is collected simultaneously to provide consistency.

2.3. Results for the Base Case without Injection

As mentioned before after acquiring the initial pseudo-transient steady state solution, URANS simulations were carried out to get initial data for LES. Here results for both RANS and HLU simulations are provided.

2.3.1. The Flow and Acoustic Fields

Since the RANS results do not produce fluctuations (transient turbulence fluctuations) over time except for the development of water injection stream, only the results for the final time step of the RANS simulation are presented which corresponds to about 2 milliseconds of flow time.

Figure 2.8 shows the Mach number, calculated based on mixture velocity and temperature and air specific gas constant to be able to show a reasonable Mach number values based on the main jet. As it was expected, the RANS results do not show any fluctuation by means of capturing acoustics emanating from the jet stream and from the reflections. These are used as initial data for the HLU simulations.

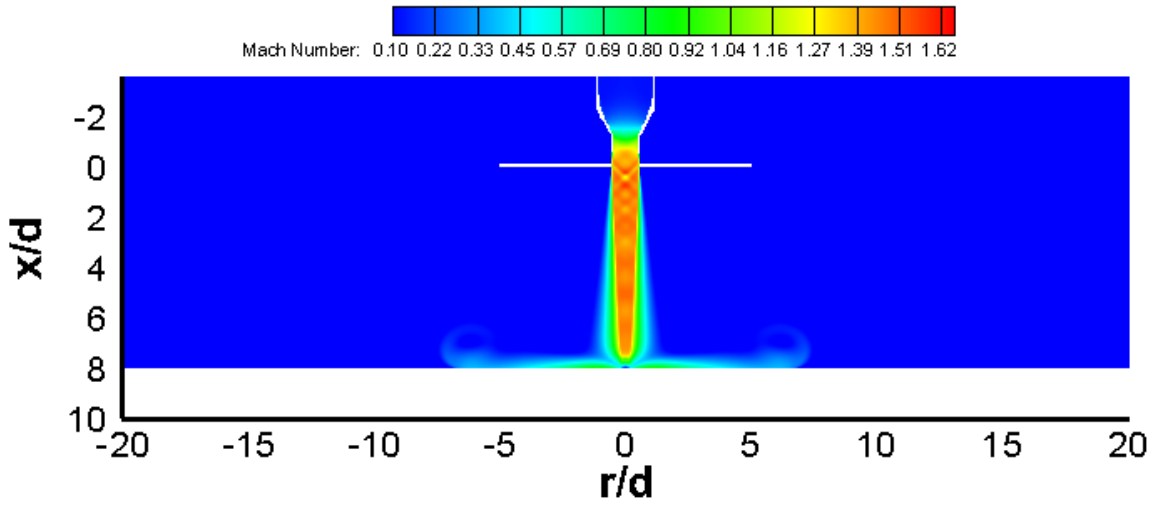

Figure 2.8 Mach number contour from URANS simulations (No Injection).

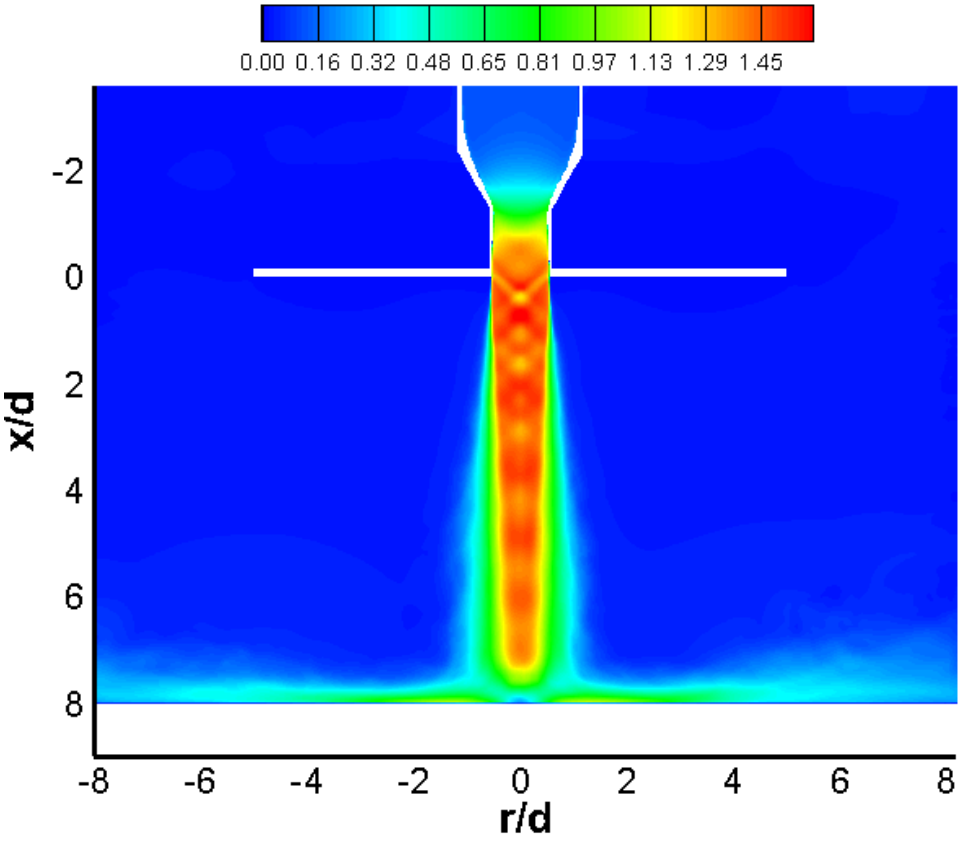

Figure 2.9 Time averaged Mach number contour from HLU simulations (No Injection).

The LES results for the base case with no injection are presented here. The time-averaged contour of Mach number is presented in Figure 2.9. The figure shows existence of weak shock cells in the plume, although nozzle has a contoured geometry and operating at the design NPR conditions. The lift plate causes the ambient pressure in the vicinity of the nozzle exit to slightly deviate from the value required to achieve ideally expanded conditions. Also, the figure shows the radial extent of the high-speed ($M \cong 1$) wall jet on the impingent plate around $r/d = 3 - 4$. The corresponding snapshot of the Mach contour of the baseline case are shown in Figure 2.10. The figure shows the fluctuations in the jet plume and shear layers, as well as in the wall flow.

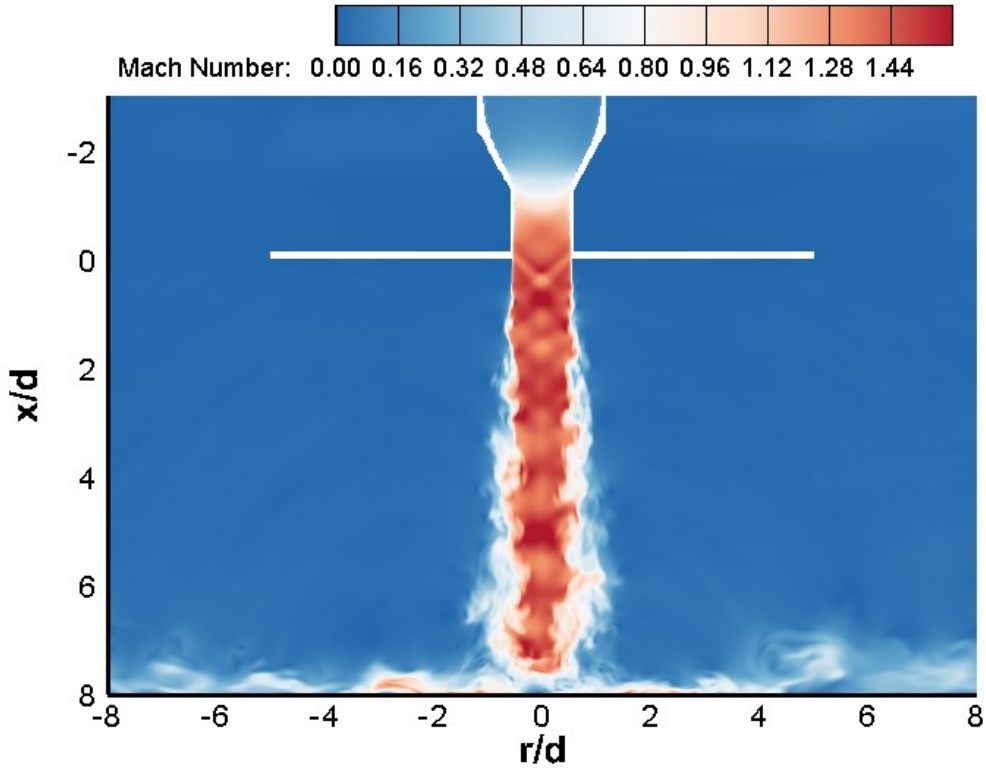

Figure 2.10 Instantaneous Mach number contour from HLU simulations (No Injection).

Figure 2.11 shows the corresponding pressure fluctuations of the flow and the acoustic fields. The fluctuating component of pressure, p' is calculated by subtracting the time-averaged mean pressure $\bar{p}$, from the instantaneous pressure, p.

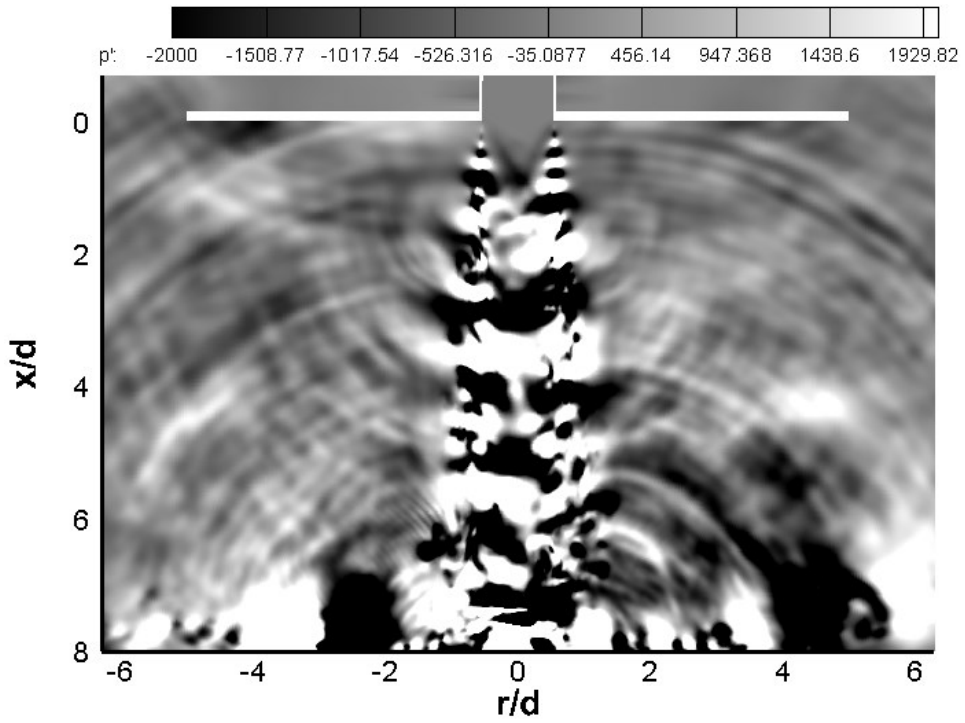

Figure 2.11 Instantaneous fluctuating pressure from HLU simulations (No Injection).

The fluctuations shown in the figure are after subtracting the time-average of the pressure fluctuations. One can identify two sets of acoustic waves: 1) Weak acoustic waves that seem to originate at $x/d = 1 - 2$ near the shear layer. (2) A strong set of spherical waves that seem to originate at $x/d = 8, r/d = 0$. The second set of waves are due to the combinations of two dominate noise sources. Acoustic waves originating from the fluctuations in the mid-shear layer structure ($x/d = 4 - 6$), and along with the fluctuation in the free shear layer of the wall jet. This can explain the strong spherical

waves originating at around $x/d = 8$. It should be noted that the spherical waves as they travel towards the nozzle exit, they reflect from the lift plate and can add to the radiated sound.

Figure 2.12 shows the RMS of the pressure fluctuations on the ground plate from the simulation. This is compared with the corresponding experimental data from experimental measurements (Ragaller et al., 2011; Gustavsson et al., 2010).

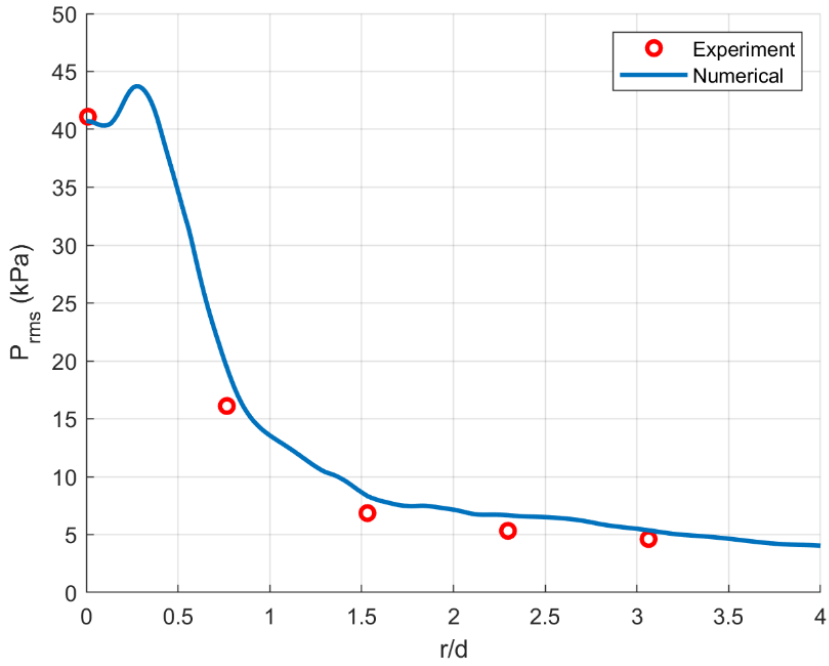

Figure 2.12 Overall pressure fluctuation amplitude as a function of radial distance r/d.

The figure shows the RMS of the calculated pressure fluctuations fit right-on the experimental data at the location of pressure transducers with less than 5% relative error, which is within the uncertainty of the experimental data. As in the experimental repots (Ragaller et al., 2011; Gustavsson et al., 2010), the RMS values of ground plane pressures are accurate within $\pm 1.4\ kPa$. In addition, the computational results confirm

that the fluctuations decrease monotonically with increasing r/d, going from near $40\ kPa$ near the centerline to $10\ kPa$ at $r/d = 2$. The centerline RMS amplitude corresponds to about 25% of the jet dynamic pressure, demonstrating the highly unsteady flow. The computation shows that the peak RMS is very close to jet core impingement region around $r/d = 0.25$. This is consistent with the presence of a stagnation bubble in this location as pointed out by the experiment.

2.3.2. Acoustic Spectra and FWH Surfaces Sensitivity

F shows acoustic spectra at $r/d = 15$ and $\theta = 90$. The angle θ, ψ is measures from the jet axis direction, and $\theta = 90$ represents location at the same elevation as the wall plate. It is a common trend in jet noise computations, to compute the noise spectra at multiple circumferential locations at a given $(r/d, \theta)$, and then average all of the spectra to get one averaged spectrum at the given $(r/d, \theta)$ location. However, this procedure is not employed here due to the asymmetry of the water injection case.

As illustrated in Figure 2.2, the simulation mimics the orientation set up of the experiment by applying the gravitational force perpendicular to the jet axis. This does not affect the acoustic signature for the baseline case, but causes asymmetry for the water injection case, since water droplets tend to be carried and clustered more in the $-(r/d)$ (gravity) direction, as it is shown in the following sections. Hence, to be consistent, the circumferential averaging procedure is not used for either cases. The experimental data are obtained from Gustavsson et al. (2010). The sequence of data is recorded on each FWH surface as mentioned earlier and the acoustic data at $r/d = 15$ and $\theta = 90$ is calculated using FWH acoustic extension as described in Section 2.2.8. As described earlier, the acoustic signal is calculated by collecting data from different FWH surfaces

simultaneously, as shown in Figure 2.14, illustrating the sketch of the different patches of the FWH surfaces. The domain in this figure is cut in 1/6th for better representation of the surfaces and should not be mistaken as if the non-full computational domain.

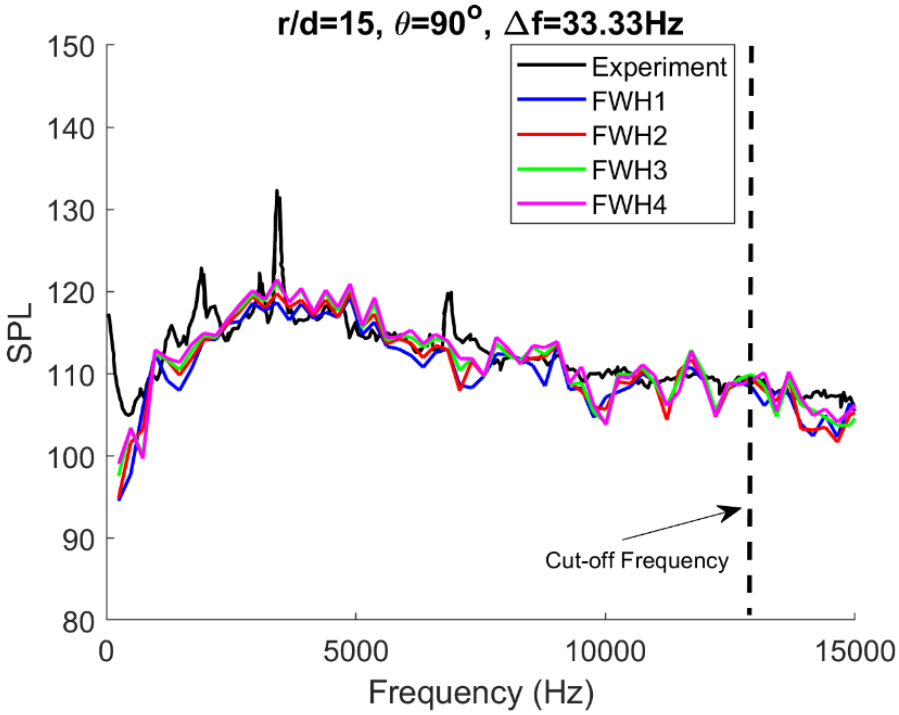

Figure 2.13 Acoustic spectra at $r/d = 15$, $\theta = 90°$.

Generally, the results in Figure 2.13 from all FWH surfaces show favorable agreement with experiment, both in terms of the predicted level of acoustics, as well as the trend of spectra. Practically speaking, the variation between FWH3 and 4 are minimum. Therefore, FWH4 is considered converged, and used here. It can also be inferred from Figure 2.13 that the extension of FWH surfaces does not severely affect spectra and the broadband noise level. This means that the pseudo noise, the artificial error explained by Lyrintzis (2003), which is due to the non-linearities or vorticity

passing through FWH surface, have little effect on the spectra.

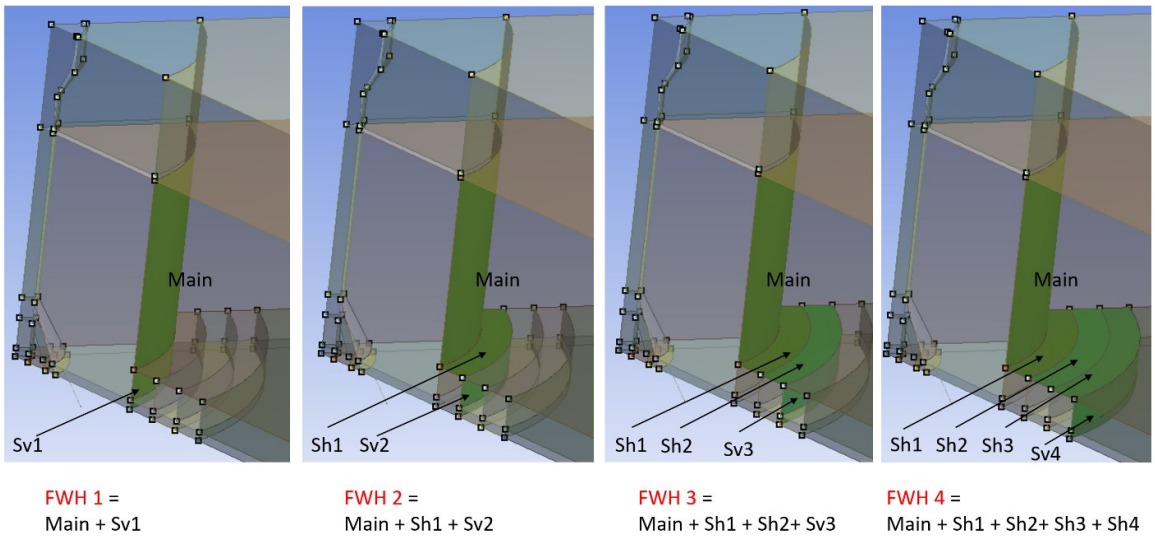

Figure 2.14 Sketch of the different patches of the FWH surfaces.

To examine the spectra closely, a zoomed-in near the peaks in the spectra is shown in Figure 2.15 in log scale. It can be observed that, the location of the acoustic peak is well predicted by the numerical results. However, the level of the tone at 3500 Hz observed in the experiment and the corresponding subharmonics in 2000 and 6500 Hz are not predicted by the simulations. The dominant tone and the corresponding subharmonics represent the impinging waves that impact on, and reflect from, the ground plane and hit the lift plate near the nozzle exit. Capturing the tone due to the wave travelling back and forth between the lift plate and the ground plane requires much longer time signal. To be exact each FFT segment must include at least one period of such traveling wave, which would require about 4 times longer signal to be collected based on the current simulations. Achieving such prediction with the current computing power in hand was not feasible due to the time-consuming computational simulations.

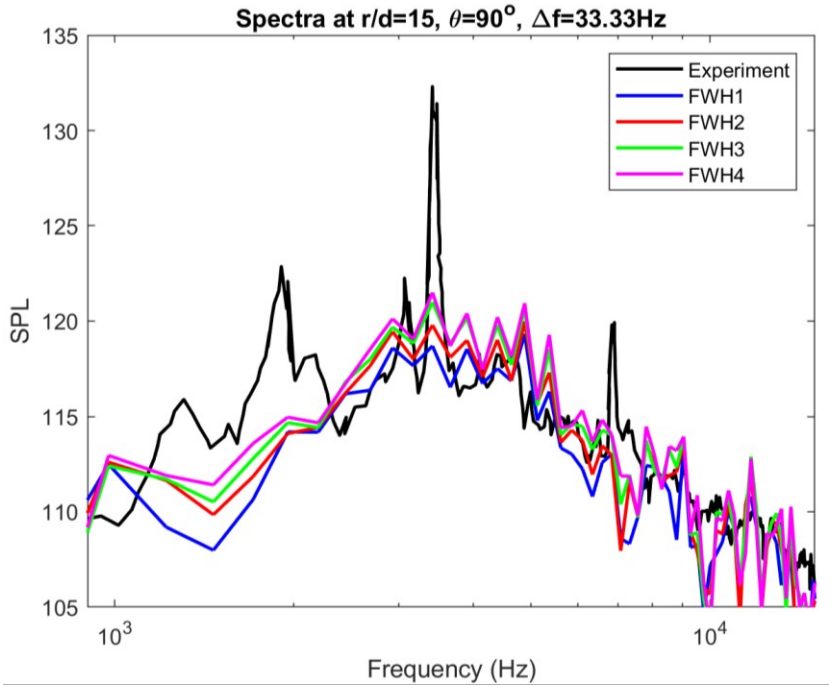

Figure 2.15 Zoomed-in Spectra at $r/d = 15$, $\theta = 90°$, in log scale.

The accuracy of the numerical approach for capturing these tones were verified in similar studies by Mankbadi et al. (2016) with similar time sample and numerical accuracy as current studies. However, the distance between the flat plate and the lift plate in the current simulations is twice of the distance mentioned in (Mankbadi et al., 2016). Hence, with even with the same numerical accuracy, more time samples would be required to capture the tones. On the other hand, the experimental studies in (Gustavsson et al., 2010) also mentioned the intermittency of capturing tones for various measurements for the ideally expanded jet. Gustavsson et al. (2010) described the peak tones in the spectra as impingement tones due to the highly unstable flow.

To determine whether these tones truly occur simultaneously, Gustavsson et al. (2010) studied variation of sampling frequency and signal sequence to calculate the overall spectrum. In these studies, spectra revealed consistency in both peak location and

broadband levels, though some peak amplitude variations were reported for the peaks near 3 and 9 kHz. This demonstrates that in the short sequence, all tones remain present, but their relative amplitudes do vary by some 5 dB, which indicates the level of the tones observed in the acoustic spectra are highly sensitive to data sampling. Additionally, in experimental studies (Gustavsson et al., 2010; Ragaller et al., 2011).

The impingement tones were found to be global in nature, however it was mentioned that the acoustic measurements in the far-field should be considered as purely qualitative, but not providing absolute acoustic level data for jet impinging on an infinite ground plane. This can explain why the predicted broadband peak of the noise agrees with the experiment, the sharp tones are under-predicted.

2.4. Results for the Water Injection Case

Like the baseline case, the flow field and acoustic data from simulations are reported here, and relevant comparisons with the experiment are provided. One of the important results from the water injection case is the water stream and trajectory, and concentration of the droplet. Hence, the contours of volume fraction of water are provided here in addition to other results.

2.4.1. Water Trajectory

The LES prediction of the water contours at different instances of time: 3.5, 4, 4.5, and 5 milliseconds are shown in Figure 2.16: a-to-d, respectively. The figure shows that the water is carried out by the air, and two regimes can be distinguished: for x/d from 7 to 8, it is continuous as it exits the microjet. But from x/d of 7 to 3 the water becomes droplets carried out by air. Different frames of volume fraction illustrate that the water droplet parcels further away from the injectors, have much lower velocities than that in

the region near the microjets where the water break-up occurs.

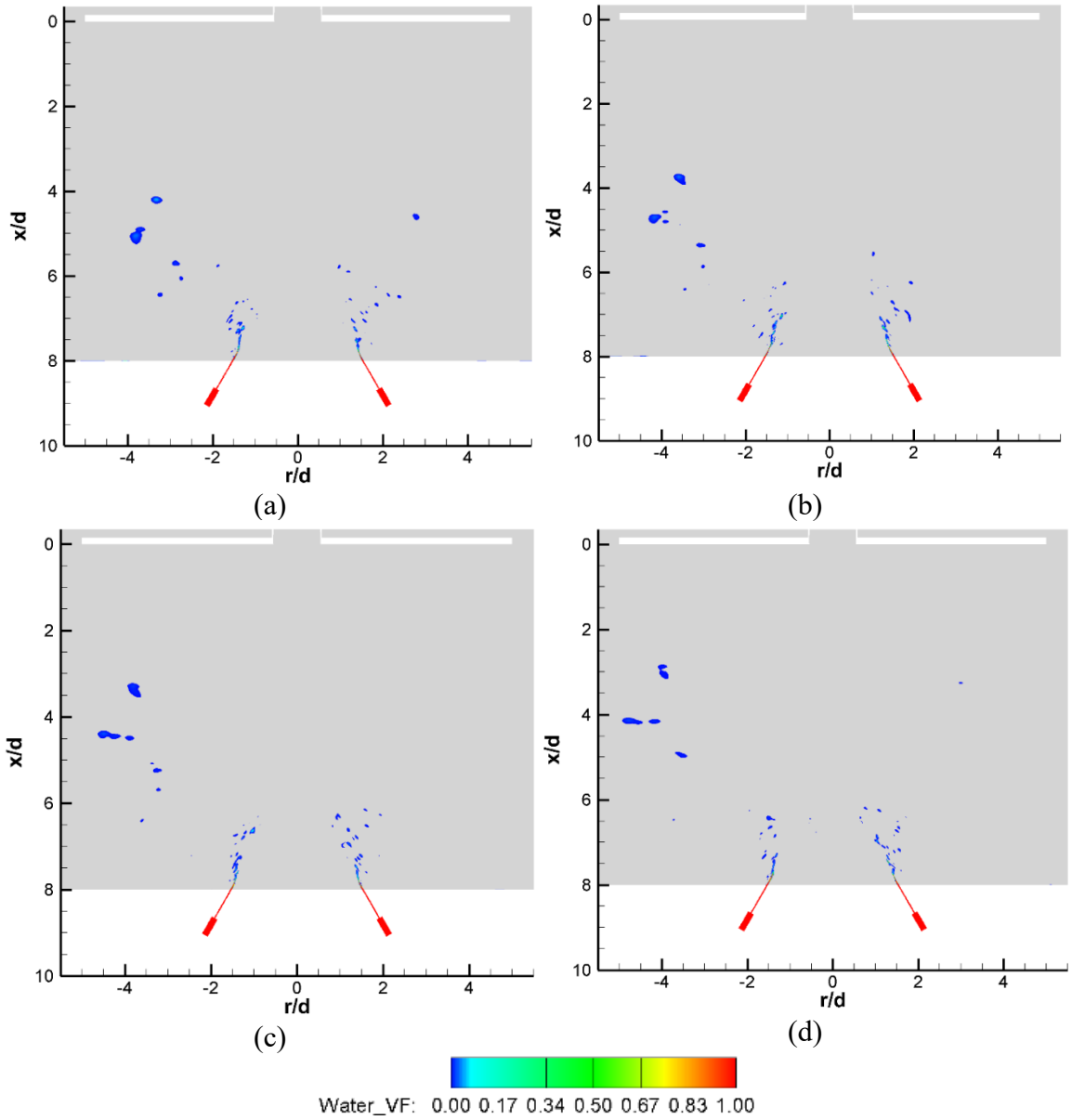

Figure 2.16 Contours of water volume fraction on the x-r cut plane at different instances of a) 3.5, b) 4, c) 4.5, and d) 5 milliseconds.

In addition, Figure 2.16shows that the left side contains more water than the right side because the gravity acts in the direction of negative $-(r/d)$ as in the experimental set up.

The gravitational force acts perpendicular to the jet axis and pulls the parcels, especially the bigger lumps, further away in the $-(r/d)$ direction. This is also illustrated as the density ratio in the domain later in the following sections.

2.4.2. The Flow and Acoustic Field

Figure 2.17 shows the time averaged Mach number contours for the baseline and the injected cases. The speed of sound used for both contours (baseline and water injection) is that of the ambient air. Since the water injected from the ground is cold water ($T_{water} = 300\ K$) and the nozzle exhausts a cold jet ($TR = 1$), the only difference in the mean Mach number would be the velocity fluctuations. With or without water injections, the shocks are weak.

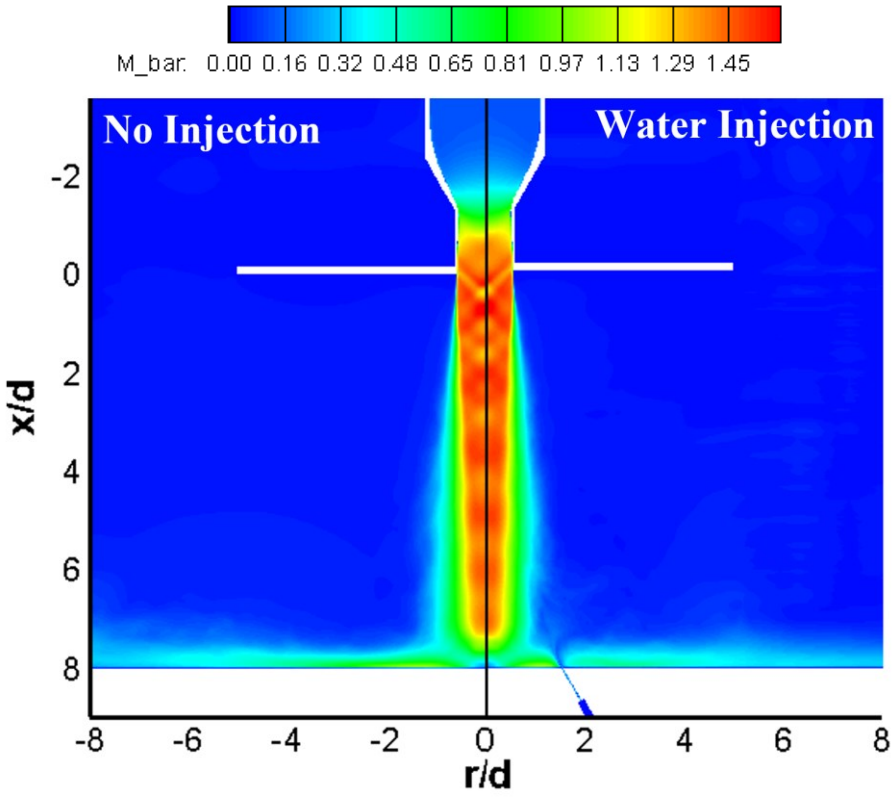

Figure 2.17 Time averaged Mach number, no injection (left), water injection (right).

Comparing the two figures, we can conclude that the shocks are hardly affected by water injection. This is because these weak shocks are in the initial region of the jet, but the water is injected farther away at $h = 8d$ from the impingement plate. This can also be evaluated in terms of the momentum imparted by the water compared to the momentum of the jet. The momentum at the main jet exit is $(\dot{m}\vec{v})_{jet} = 321\ kgm/s^2$, while all 6 water injectors impart momentum of $(\dot{m}\vec{v})_{water} = 50.5\ kgm/s^2$ from the ground plane in the opposite direction.

It can be observed that the radial extent of the impingement zone is considerably reduced because of the water injection, by focusing on the wall jet flow. This is clarified in Figure 2.18 by zooming on the ground plane. The reduction of radial extent of wall flow is also clearly shown in the time-averaged normalized radial velocity at r/d=5 shown in Figure 2.19. This is expected since the microjets in this case introduce momentum in the radial direction opposite to that of the wall jet.

The injected momentum component in the radial direction is a factor of several variables including injection fluid density, injection angle, injector diameter, etc. Hence this argument should not be generalized for any injection condition. In this specific case, the 60^o degree injection angle of high-density liquid affects the radial extent of the jet as illustrated in Figure 2.19. The discussion about the momentum is exchange is investigated further in the next section.

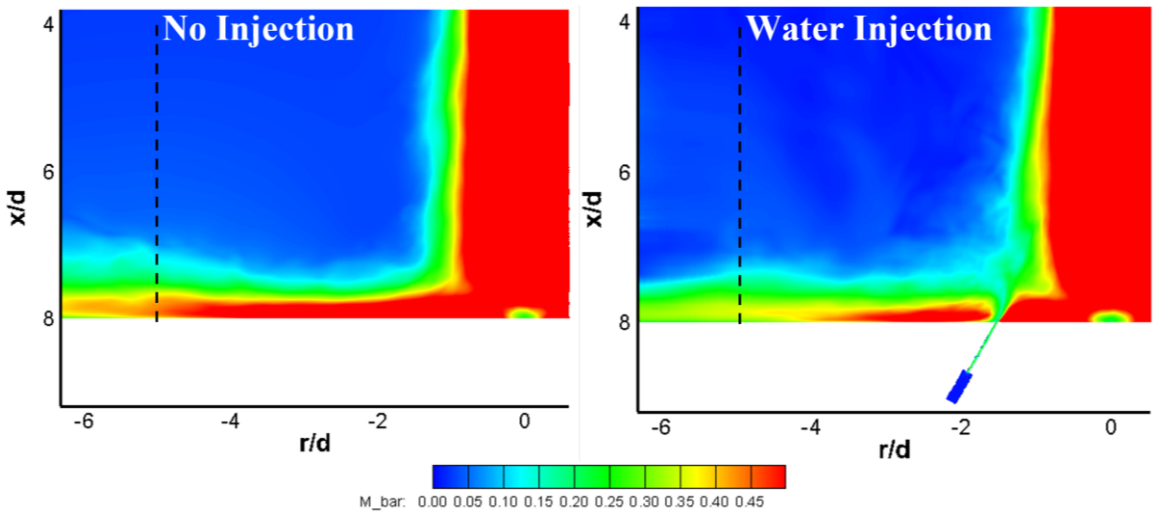

Figure 2.18 Time averaged Mach number on ground plane, baseline (left), water injection (right).

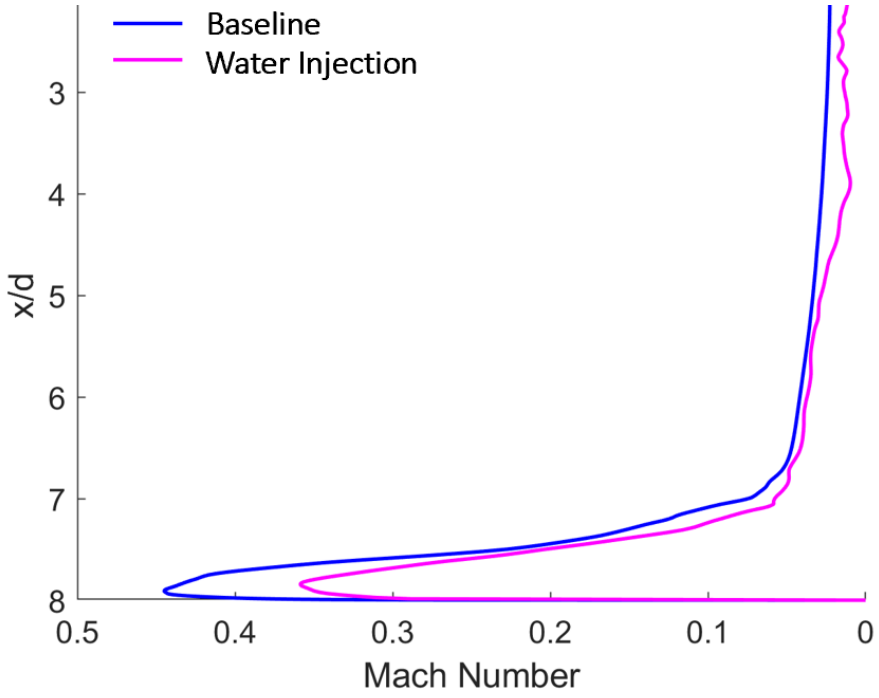

Figure 2.19 Time averaged Mach on FWH1 surface along x-direction at $r/d = -5$.

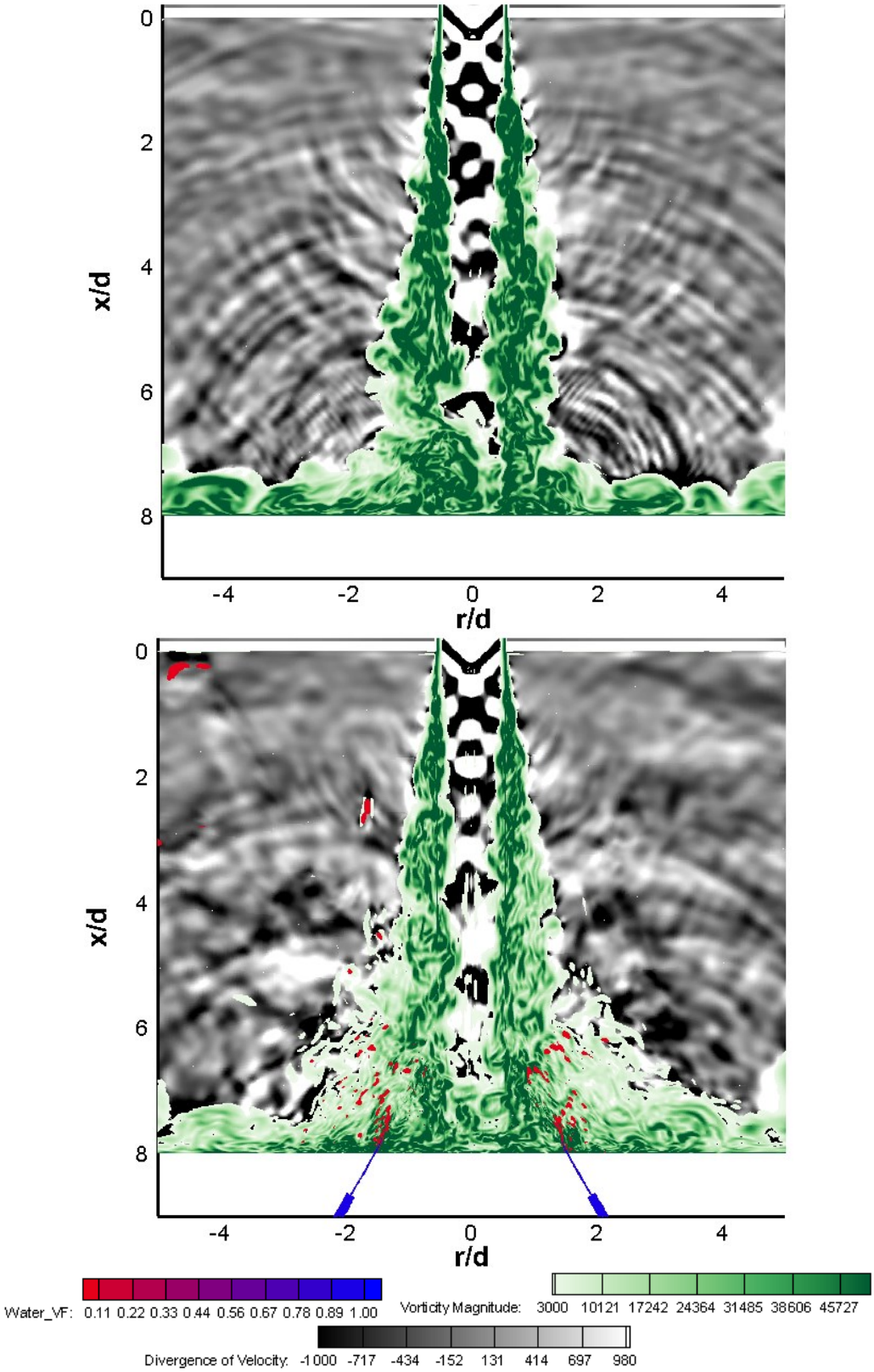

Figure 2.20 Instantaneous contours of dilatation, vorticity, and phase fraction. Baseline (top), water injection (bottom).

Figure 2.20 shows the snapshot of the pressure fluctuations in terms of the dilatation, overlaid on top of it is the vorticity field in green color. This figure illustrates the water jets introduce a smaller scale of motion and enhance turbulent mixing. There exist more smaller scale structures visible spanning a larger volume which can be explained by the promotion of turbulent mixing with the slow-moving air and the forward turbulence cascade. This would affect noise generation by breaking up larger structures, which are efficient in noise generation at the low-frequency range where the noise peaks. The figure also shows the water volume fraction in red color. Near the nozzle lip, it can be noted that the fluctuations are small and are hardly influenced by the injection from the bottom plate. Following the green vorticity contours, we can see that water injection considerably reduces the vorticity fluctuations in the jet shear layer in the $x/d = 4 - 8$ region. Moving on to the vorticity near the impingement plate, we can notice that injection not only reduces the vorticity fluctuations but also reduces the radial extent of the wall jet as well.

Since the jet stream is near-ideally expanded, weak shock cell structures are generated in the jet stream. It is important to investigate the effect of water injection on the shock cell structure, Although, this was shown in the time-averaged mean Mach contours, but it is worthwhile to illustrate the shocks with the numerical Schillerian figures. To investigate this thoroughly, the slices of numerical shadowgraphs are plotted in Figure 2.21, to visualize the effect of water injection on shock cells. The figures show that the shocks in the plume are not affected by the water injection, since the injectors are relatively far from the nozzle exit.

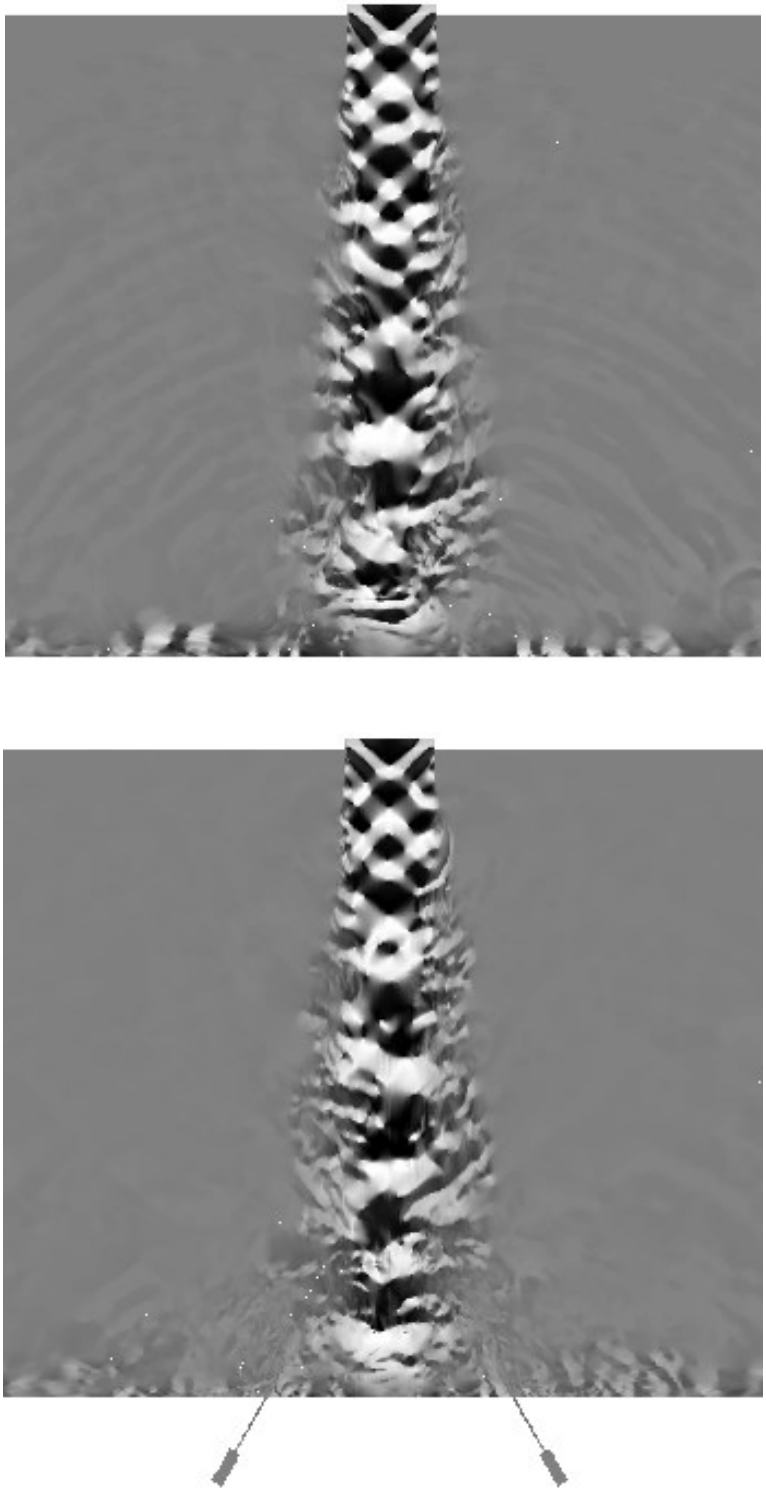

Figure 2.21 Numerical shadowgraph. Baseline (top), Water Injection (bottom).

Moreover, the disruption of semi-spherical waves due to the water injection, shown earlier, is also visible in the contours of density gradients depicted as numerical shadowgraph in Figure 2.21.

2.4.3. The Acoustic Spectra and Directivity

Since we are using FWH to extend the near field to the far field, we need to discuss the effect of the presence of water on FWH formulation. There are three regions where the water phase affects the radiated sound: 1) the sound generation region, 2) the sound in the near field inside the FWH surface, and 3) the sound transmission outside of FWH surface. As for the sound generation region, Crighton and Ffowcs Williams (1969) have considered sound generation by turbulent two-phase flow using Lighthill's theory (Lighthill, 1954) and did show that the sound generation is affected by the presence of two phases, which is as in region 1 here. In region 2 here, in the near field inside FWH surface, the water phase affects the radiated sound through absorption and scattering, which are accounted for here. To explain how the model employed here accounts for absorption and scattering of noise, let us assume a region where both air and water exist such as region 2 along r/d=2. Assuming two adjacent cells, one entirely filled with air denoted as cell (a) and the other entirely filled with water denoted as cell (w). As described by Equation (2) and (3) in Section 2.2.1, movement of high-density fluid from cell (w) to cell (a) affects the dilatation of fluid element as described by the flowing equation, ignoring the phase change:

$$\frac{D\rho}{Dt} = \rho\nabla.(\rho\vec{v}) \tag{10}$$

Hence, the change in the substantial derivative of the density affects the dilatation of the fluid element. This can be clearly seen in Figure 2.22 as the water parcel movement

affects waves in the region ($x/d = 2, r/d = -2$).

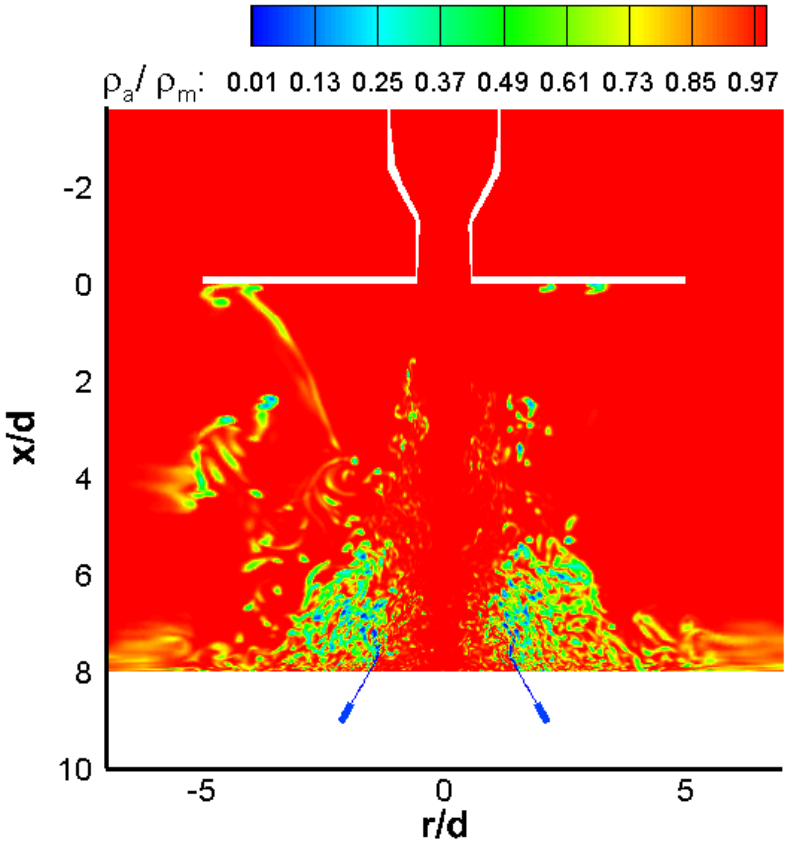

Figure 2.22 Ratio of the density of air to mixture.

In region 3, on FWH surface and outside of it, for the selected FWH surface used here, there is no presence for the water droplets. To verify this issue, we show in figure 15 the ratio of densities of air over density of mixture, which is an indication of the relative presence of water, as described in Section 2.2.1. This figure clearly shows the water is present in region 2 inside the FWH surface but is negligible outside of it. Thus, in the present work, the water affects the acoustic field inside the chosen FWH surface but is not present outside of it. Therefore, the use of FWH approach is acceptable here.

It should be noted that the water distribution in Figure 2.22 resembles that of the experiment, but the current numerical simulations appear to be producing larger droplet sizes. The VOF method does not predict the particle size or the number of particles, unlike Lagrangian approaches. However, it predicts the percentage of water in the air-water mixture in each cell. This gives only an indirect indication of how much water occupies a given domain. On the other hand, the surface tension is neglected here to simplify the numerical simulations, which is particularly complex here for the supersonic case. The surface tension plays a key factor in droplet formation and determines the time it takes the water to breakup into droplets. Thus, by neglecting the surface tension here, the predicted water droplets are expected to be of a larger size than that of the experiment. Having larger droplet sizes than that in the experiment can lead to the following scenarios: 1) more of the water momentum is used in interaction with the jet than break up and, forming droplets, 2) the sound scattering and absorption by the water droplets is larger than that of finer droplets in the experiment. These two factors can result in overestimating the noise suppression effects.

Figure 16 shows the effect of water injection on the far-field noise at $r/d = 92$. The ideal way to show the noise reduction in numerical results is through smoothing the spectra. The experimental data benefit from availability of large data samples to provide more averaging windows to smooth the spectra data. This is usually not the case in numerical simulation due to the constrained computational time. Figure 2.23 shows the far field spectra for the baseline and injection cases as reported by the experimental measurements (Ragaller et al., 2010). BSL and WINJ acronyms in the legends, represent baseline case and the water-injection case, respectively.

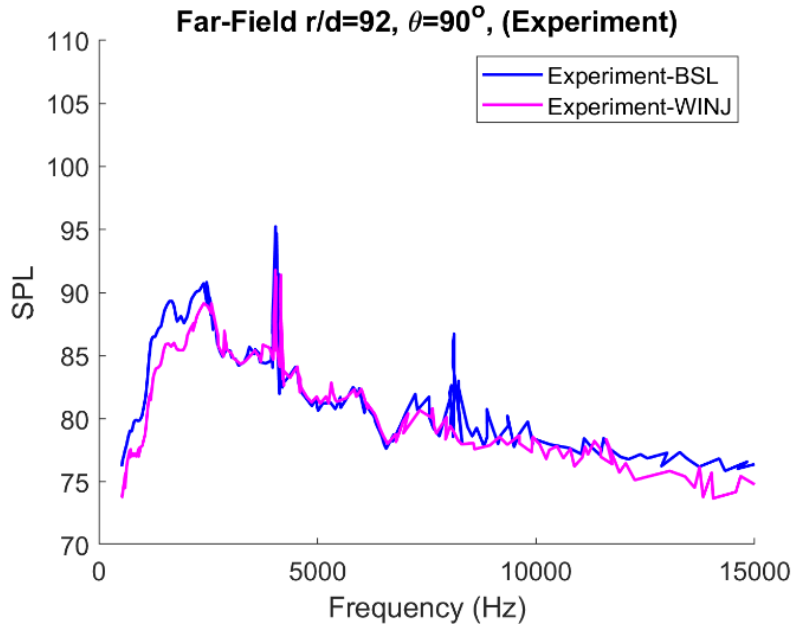

Figure 2.23 Far-field spectra at $r/d = 92, \theta = 90°$ (Experimental Measurements).

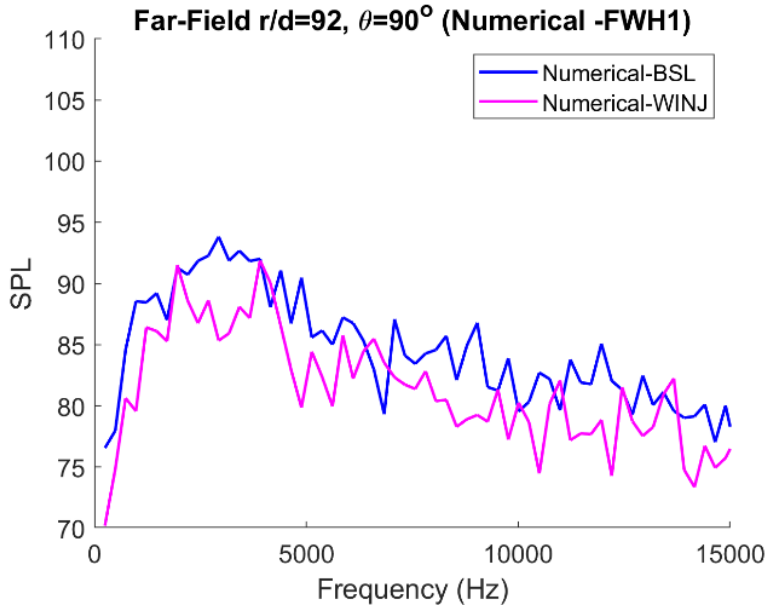

Figure 2.24 Far-field spectra at $r/d = 92, \theta = 90°$ (Numerical Results).

As illustrated by the experimental measurements, there exists small difference in the spectra of the baseline and water-injected cases in the experiment. The water injection

mostly suppresses the acoustic spectra at lower frequencies (between 100Hz to 4000 Hz) up to 3 dB. Also, the suppression is visible at around 7000 Hz. Figure 2.24 shows the spectra at the same microphone location as obtained from the current simulations. Due to limited number of samples to average out jagged spectra, the acoustic spectra from numerical results is not as smoothed as the experiment. This may also be the reason the tones are not as well-predicted by the computations.

However, the effectiveness of water injection can be seen in both measurements and the numerical results. This is particularly true at lower frequencies of the spectra, up to 4000 Hz, where both the numerical results and experimental data exhibit similar trend for the water effect. One of the factors that may explain why the current numerical results show discrepancy in reducing the noise than the corresponding experimental data is that the present computation do not account for the possible phase change or surface tension that may occur in the experiment as pointed out earlier.

In addition, the acoustic directivity plots are investigated and compared with the available experimental data. Figure 2.25 shows the directivity arc centered at the center of the nozzle exit at $r/d = 92$ from the nozzle exit. This figure also shows the distribution of water droplet lumps. The droplet lumps are more distributed in the direction of acting gravitational force shown in the picture. The OASPL is plotted as a function of directivity angle, θ, Figure 2.26. The OASPL values agree very well with the available experimental data, showing 1-2 dB reduction in the locations of interest, which are the far field observer 92 diameters away from the nozzle, parallel to the lift plate.

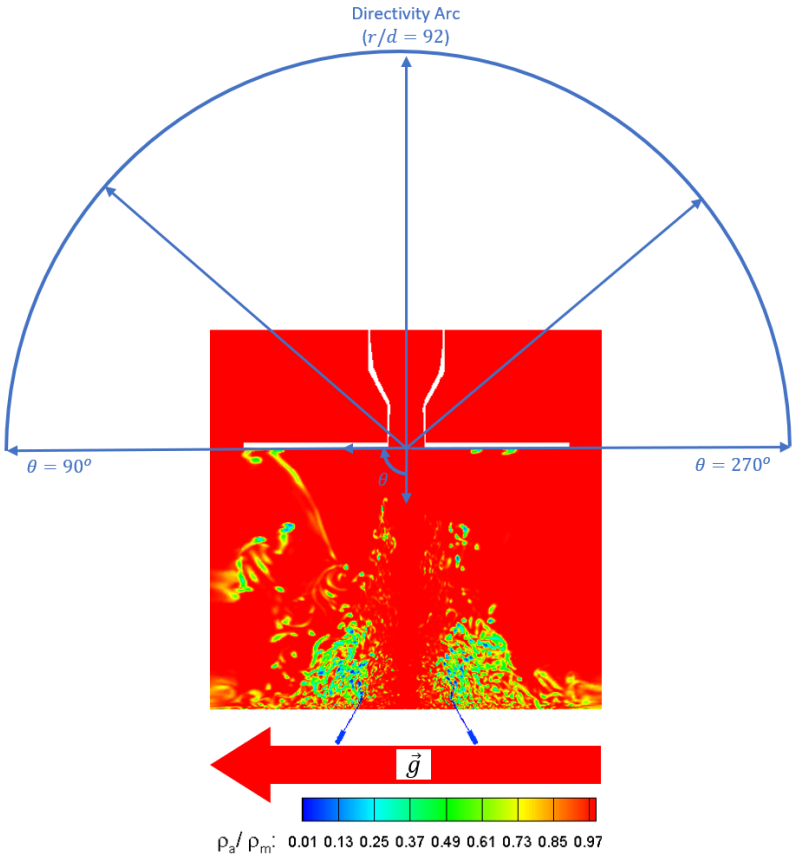

Figure 2.25 Sketch of the directivity arc.

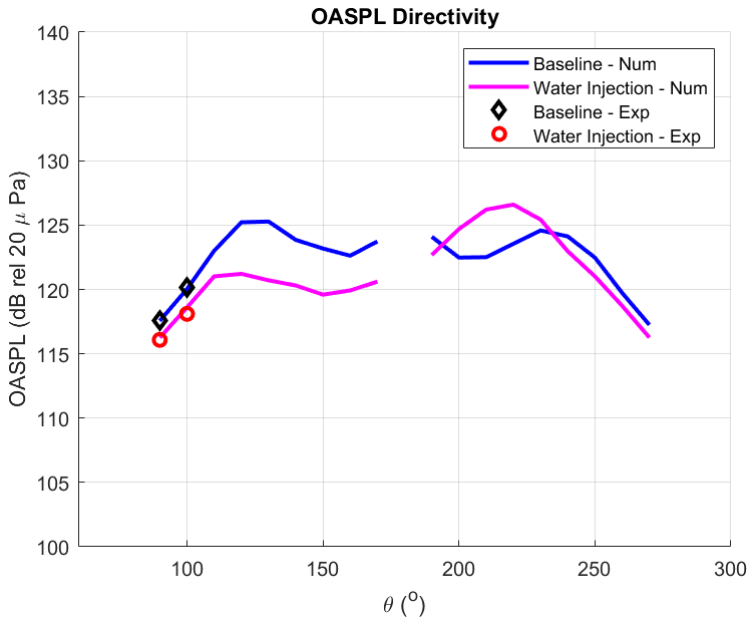

Figure 2.26 OASPL directivity plot and comparison with experiment.

Figure 2.26 illustrates a symmetric signature of the directivity, which is expected, due to the symmetrical nature of the baseline case. However, asymmetrical signature of the acoustic directivity is due to the asymmetrical distribution of water lumps because of the direction of gravity. To provide a clear picture of the effectiveness of the water injection, the noise reduction or increase is presented in a form of $\Delta OASPL$, which is defined as:

$$\Delta\, OASPL = OASPL_{(Water\ Injection)} - OASPL_{(No\ Injection)} \tag{11}$$

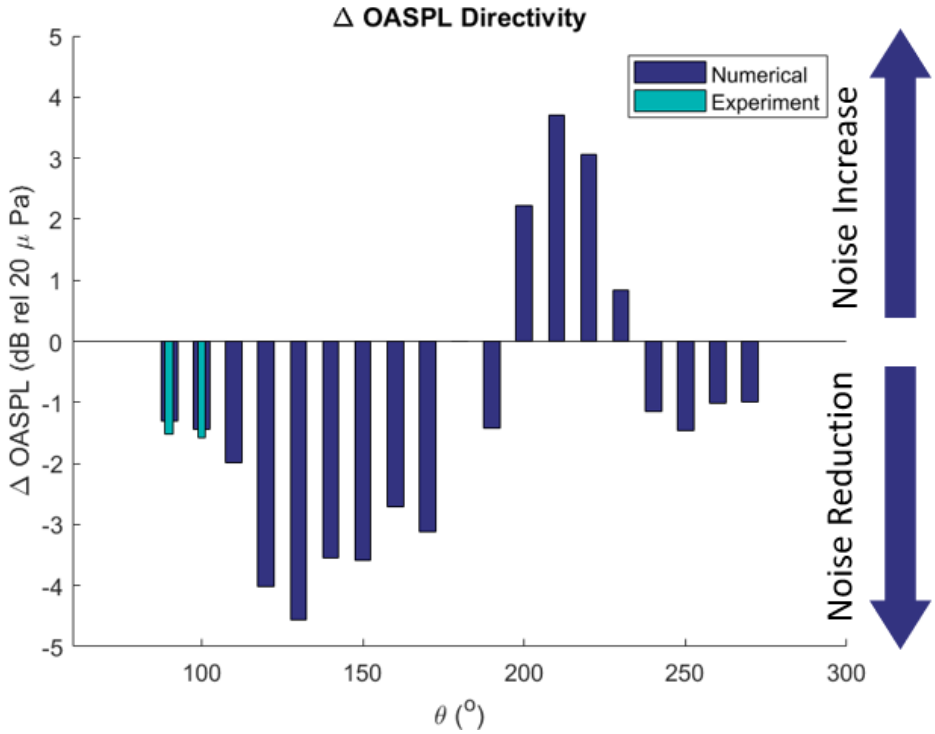

Figure 2.27 OASPL reduction effectiveness.

First, the 1-2 dB reduction is consistently shown in both numerical results and the experimental data. Second, the excessive reductions observed $\theta = 110^o - 160^o$, as well as the increase shown in the mirrored angles, are due to the uneven distribution of the water lumps. As it was shown earlier in Figure 2.20, the interaction of the bigger accreted

water lumps, drastically distort the acoustic waves, and may introduce new interactions in the acoustic field. As a result, the effectiveness of the water injection is merely affected due to the orientation of the problem set up. This basically could mean that "*more water, means more reduction*", while this statement is not far from intuition and previous observations explained earlier in Section 1.4.1. Nevertheless, the noise reduction in the point of interest (like the reported by the experiment) are shown to be somewhat symmetric. The effect of water injection on perturbations is investigated in detail to provide rational explanations on the physical mechanisms that water reduces noise.

2.4.4. Effect of Water on the Flow Perturbations

In Fig. 17 the RMS of pressure fluctuations are presented for both the baseline and the water injection cases. Also, we show in the figure the pressure fluctuations along various axial locations at $r/d = 0.5$. Focusing on the vicinity of the nozzle lip, water injection seems to have little to no effect on fluctuations near the lip. However, water injection seems to significantly reduce the pressure fluctuations both in jet plume, as well as on the on the ground plane. This is particularly clear for $x/d = 2 - 8$ along the axial direction at $r/d = 0.5$.

Several studies have indicated that the dominant sound source in supersonic jets is the noise-efficient large-scale structure near $x/d = 2 - 6$ (Mankbadi, 1992, 1994). Lighthill's theory links the far field noise to the flow fluctuations as it in the Lighthill's stress tensor. Since the velocity fluctuations and the pressure fluctuations are significant in the jet shear layer and on the ground plane, they seem to be the dominant noise sources. Water injection significantly affects these two sources. Thus, we can conclude that the main effect of the ground water injection is through exchange of momentum

resulting in reducing the noise-efficient large-scale flow fluctuations in both the jet plume and the wall jet near the impingement zone.

The injection of water at the inflow point does not directly produce sound at the input point since it is a steady injection. However, injection in general (gas or liquid) adds momentum that, in principle, can increase sound, but as in various gas injection cases (Heeb et al., 2013; Sinha et al., 2018), it is believed that the momentum addition / exchange results in reducing the noise-producing large-scale structure in the jet. Similar effects of water injection are also pointed out by Kandula (2008). Furthermore, in this experiment the momentum is added opposite to the direction of the main jet momentum in the axial direction, thus, it reduces the shear layer gradient. To explain the effect of water injection on shear layer, integral momentum equation is employed here. We can consider here the jet region that precedes impingement. In a free jet the x-momentum is conserved, thus:

$$M_2 = M_n \tag{12}$$

Here M stands for the jet axial momentum. The subscript 2 refereeing to the x location while the subscript n refers to the nozzle ext. Assuming an almost a top hat profile at the exit, the nozzle exit momentum can be approximated as $U_j^2 \frac{\pi}{4} D^2$, With water droplets coming from the base in the opposite direction to the jet flow, the momentum at cross section 2 is now reduced:

$$M_2 = M_n - M_w \tag{13}$$

where M_w refers to the incoming water momentum. Since we have:

$$M_2 = \int_0^\infty \rho\, U^2\, r dr \tag{14}$$

This leads to a reduction in dU/dr, hence a weaker shear layer instability and a

weaker velocity fluctuation. This reduction in velocity fluctuations RMS is illustrated in Figure 2.28.

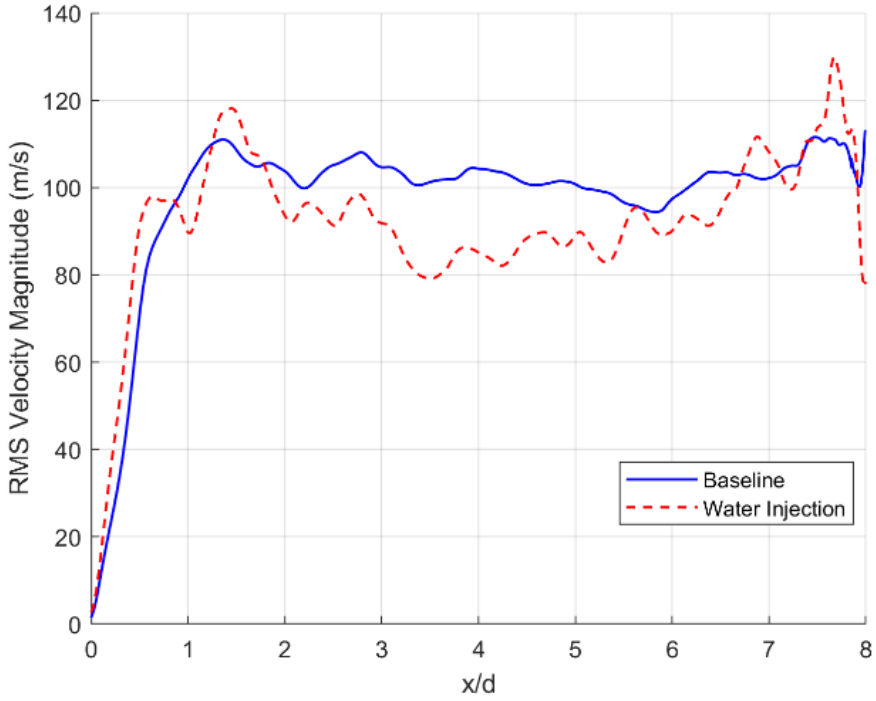

Figure 2.28 Shear layer velocity fluctuation RMS at r/d=0.5

Although the averaged mean Mach number contours of Figure 2.17 show small difference in the mean value of the shear layer, as illustrated in Figure 2.18, the injected water introduces the turbulent mixing in the shear layer in the regions away from the nozzle exit and the boundary layer ($2 < x/d < 6$). The high-density water in this region reduces the velocity fluctuations.

Also, the angle of injection on the base plate is such that it is introducing momentum that is opposing the wall jet momentum. This reduces the wall jet fluctuations, as illustrated in Figure 2.29. Following the same analogy regarding momentum transfer, we

can consider a control volume over the wall jet region, then using the momentum conservation. Thus, when flow between two stations along the radial direction is expressed as:

$$2\pi \int_0^b \rho U^2 r dy = 2\pi \int_0^b \rho U^2 r dy - \int_{r_1}^{r_2} \tau_w dr - \bar{M}_{wr} \quad (15)$$

As it is illustrated in Figure 2.29, the mean velocity is reduced due to water injection. The water injection effectively reduces the radial extent of the high velocity wall jet flow right after the injector locations as illustrated $r/d = 2 - 3$. However, the wall flow is restructured further away from at $r/d = 4 - 5$. This would suggest the momentum insert from the water injection in the opposite direction of the wall jet radial direction, would diminish velocity fluctuation in this region with the same mechanism mentioned earlier for the mid-shear layer region. As illustrated in Figure 2.29, flow fluctuations are reduced in wall jet flow region. The flow fluctuations at the wall are reduced by 20 % from $r/d = 2$ to $r/d = 5$, suggesting reduction of wall jet noise sources.

Many of the important kinematical and dynamical properties that was discussed earlies in terms of averaged properties, can be more clearly illustrated and understood by describing the flows in terms of individual patterns. Such patterns or flow regions are important because they are associated with relatively large contributions to certain average properties of the flow, such as turbulent mixing (Hunt et al., 1988).

Since the previous investigations illustrated effect of injectors on flow perturbations, and the SPL, it can be conjectured that the injectors affect the large-scale structures of the turbulence.

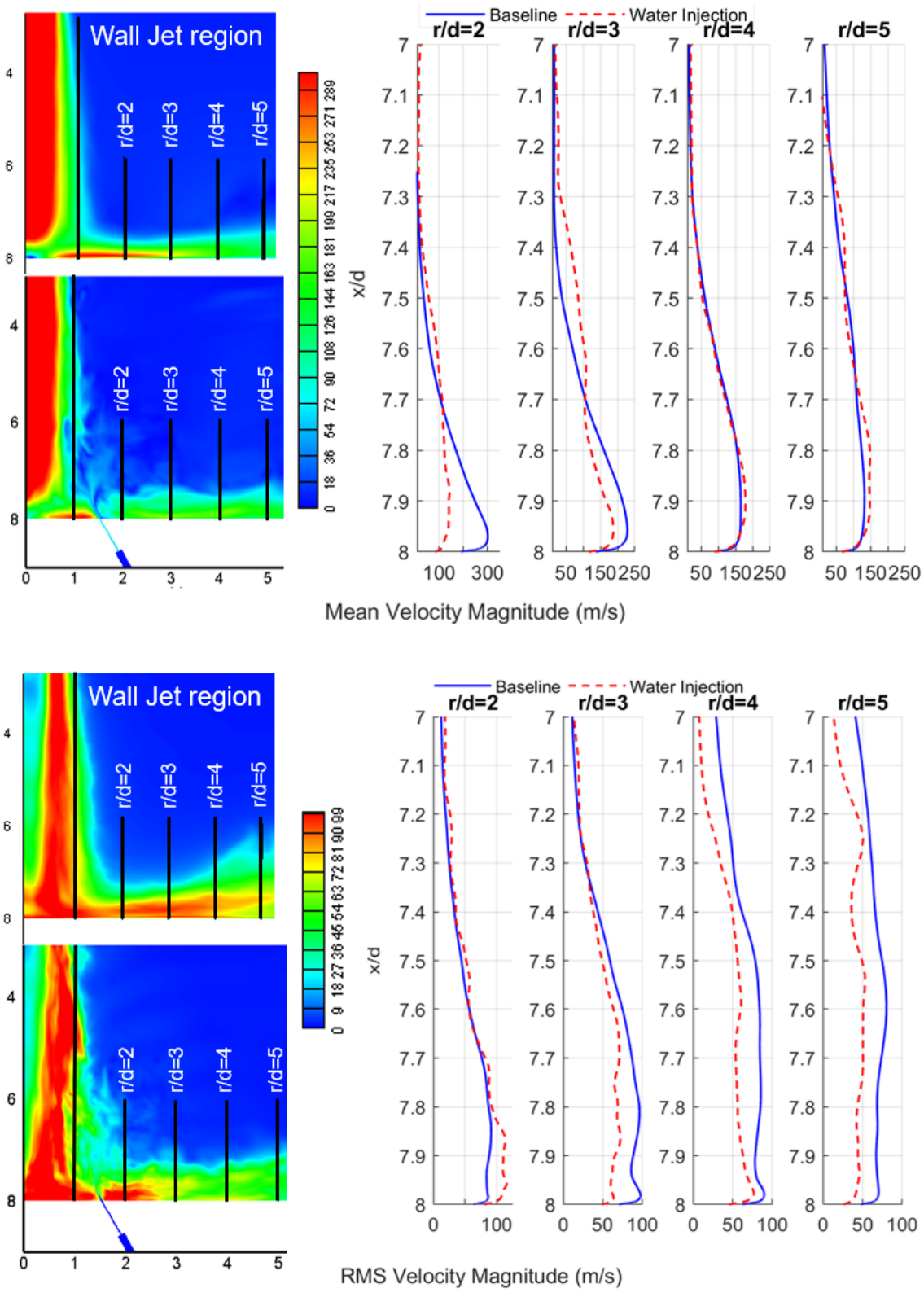

Figure 2.29 Wall jet flow region. (Top) Mean velocity magnitude, (Bottom) RMS Velocity Magnitude.

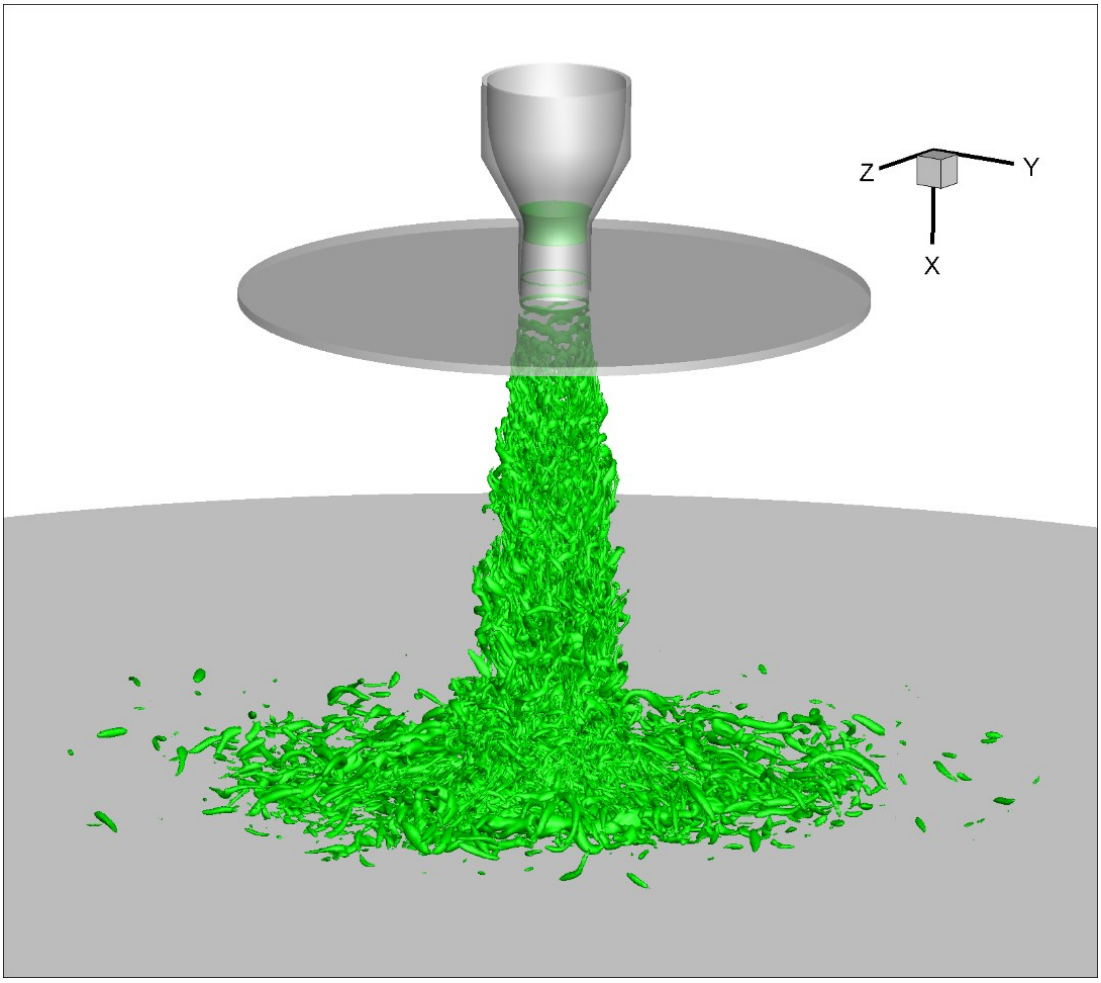

Figure 2.30 Iso-surfaces of Q-criterion $\left(1/2(U_j^2/d^2)\right)$ for the no injection case.

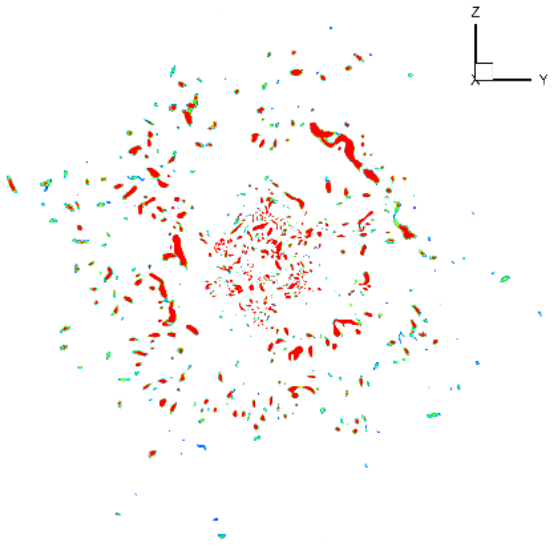

Figure 2.31 Slice cut of the Iso-surfaces in *Figure 2.30* at $x/d = 7.5$.

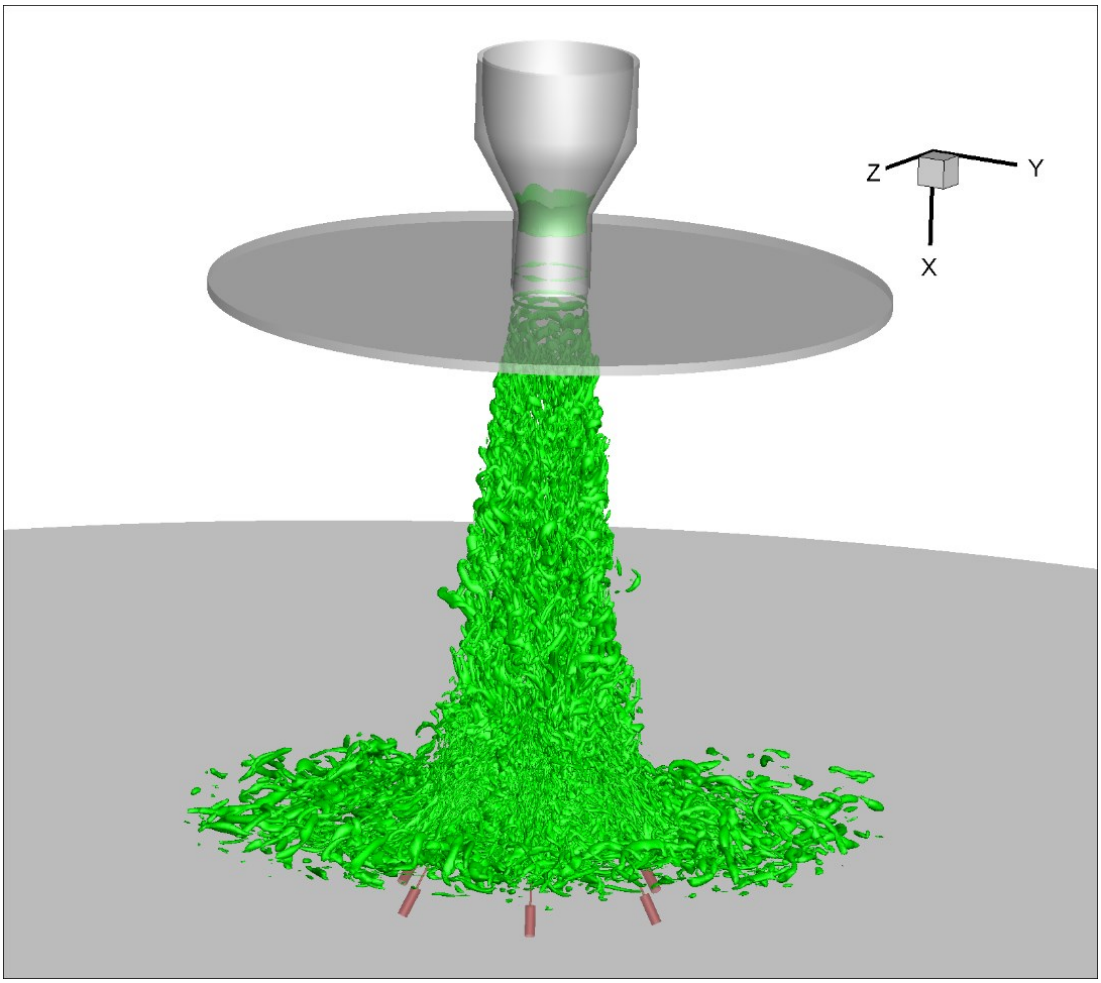

Figure 2.32 Iso-surfaces of Q-criterion$\left(1/2(U_j^2/d^2)\right)$for the water injection case.

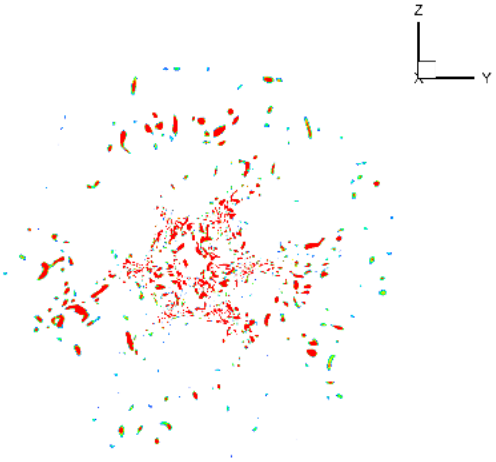

Figure 2.33 Slice cut of the Iso-surfaces in *Figure 2.32* at $x/d = 7.5$.

To reach a clear understanding of the mechanisms responsible for the noise reduction, the Q-criterion is calculated from the flow parameters to identify the larger turbulent structures. The Q-criterion is defined as a function of rate-of-strain tensor, S_{ij}, and vorticity tensor, Ω_{ij}, as described by Hunt et al. (1988).

In Figure 2.30 and Figure 2.32, the iso-surfaces of the Q-criterion for $Q = 1/2(U_j^2/d^2)$ are shown for the baseline and water injection case, respectively. The value of Q is chosen to highlight the larger turbulent structures. By comparing these two figures, the water injectors increase the turbulent mixing in the mid-shear layer of the jet. This effect was earlier illustrated by means of momentum transfer.

In addition, Figure 2.31 and Figure 2.33 show the iso-surfaces of the Q-criterion on a cut-plane surface at half a diameter away from the ground plane ($x/d = 7.5$), for the baseline and water injection case, respectively. These figures are intended to highlight the smaller turbulent structures near the ground plane. The injectors introduce additional vortical structures that grow and develop and generate a hexagram star pattern, due to the six injectors. These small-scale structures could be responsible for the increase in RMS of velocity fluctuations near the injectors (shown in Figure 2.29), and consequent energy transfer, and reduction of fluctuations further away in the boundary layer of the wall jet flow.

As previously described and illustrated Figure 2.11, the strong set of spherical waves originating from the stagnation point are due to the combinations of two dominate noise sources. Acoustic waves originating from the fluctuations in the mid-shear layer structure, and the fluctuation in the free shear layer of the wall jet. Both sources are affected by water injection and is consistent with the consequent reduction of the strong

spherical waves originating at around $x/d = 8$, $r/d = 0$. In conjunction with the previous statement, the pressure fluctuations of both baseline and the water injection cases are shown in Figure 2.34. The effect of water injection on reductions reducing spherical waves is visible when comparing the fluctuating pressure component.

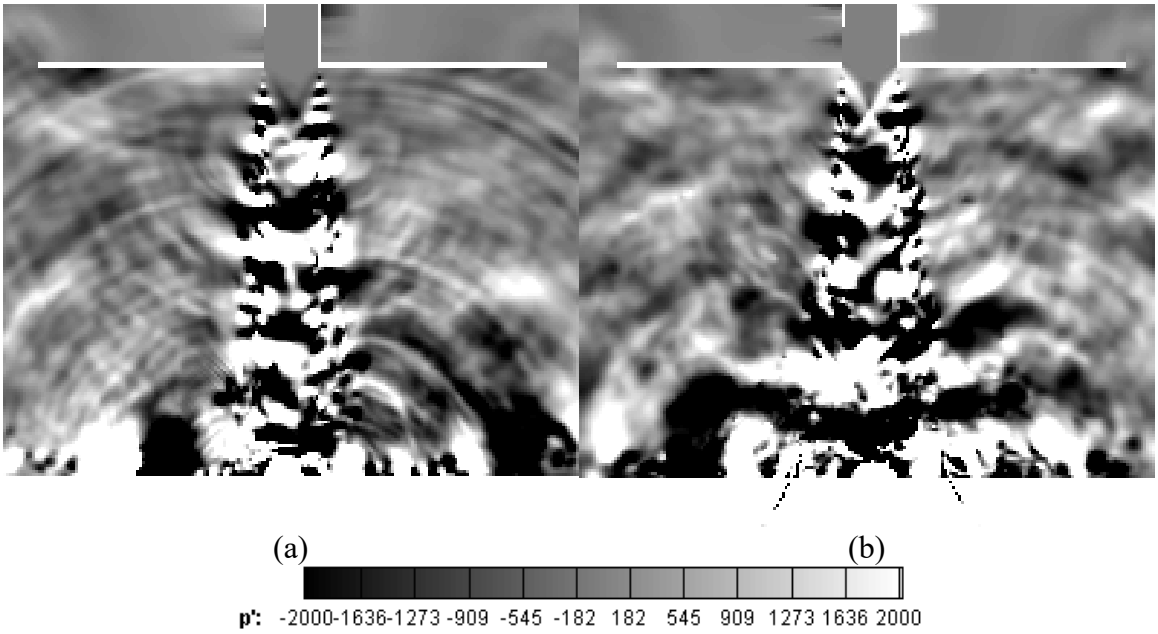

Figure 2.34 Instantaneous fluctuating pressure. (a) Baseline. (b) Water injection.

3. Numerical Simulation of Acoustic Shielding Effect of Parallel Surfaces on Supersonic Jet

The presence of a solid surface in the vicinity of a supersonic jet can affect noise radiation via several potential mechanisms. Examples include the interaction with the wing, flaps, or high-lift devices. It is considered here the case when the surface is in the flow direction and there is no impingement. The focus on two mechanisms: (1) flow perturbations introduced because of the flow-surface interactions, and (2) reflections of the radiated sound waves. The possibility of such mechanisms introducing perturbations in the initial region of the jet, is explored such that could result in suppressing the noise-efficient large-scale structure of the jet. HLU simulations in form of DES are carried out here to study the noise generated by a rectangular supersonic jet exhausting in the vicinity of a solid surface in the direction of the flow. The objective is to accurately calculate the noise generated by a rectangular supersonic jet issuing to an unbounded space, as well as, bounded by a flat plate parallel to the jet axis. The appropriate numerical approach and the computational grid is explained here. The far field acoustics is obtained using the FWH approach, in a similar way that was employed in the previous section. Both flow field and acoustic results achieved by computational simulations exhibit agreement with the corresponding experimental data.

Next, the possibility of replacing the conventional flat-surface airframe under a top-mounted aircraft engine by a wavy surface. With the knowledge and understanding obtained from mechanisms governing the jet-flat surface interaction, the modification of flat airframe surface under the engine to a slightly wavy one, is proposed. The work here presents the theoretical background to determine the parameters needed for the way wall

to work efficiently. Results show that the proposed wavy shield does reduce both the level and extent of the jet noise source as compared to that of a flat shield.

3.1. Motivation, Problem Statement, and Research Objectives

The noise generated by supersonic jets is of primary concern in the design of high-speed aircrafts. As described earlier in Section 1.4.4, several concepts suggest an integrated design of the engine and the airframe. Shielding of the jet by wing or other aerodynamic surfaces can be beneficial by reducing the noise levels perceived by the observers on the ground.

When a jet engine is installed on an aircraft, the jet noise is affected by the presence of solid surfaces in its vicinity. The focus here is on the top-mounted engine configurations. In this case the engine is mounted on the top. The distance between the jet exhaust plume and the airframe surface can vary. One of the thoughts-after advantage of such design is that the airframe surface will act as a shield to reduce the noise radiated to the far field. The shielding effect under the engine, depends on several parameters such as: the distance from the nozzle lip to the surface, typically referred to as (h/D), where D is the hydraulic diameter of the nozzle exit.

In the study of jet interaction with a parallel plate, acoustic shielding has a more obvious application for the two sets of design approaches, First, the general engine-top configurations, where typically the h/D parameter is around 2-3 , as shown in Figure 3.1a. This figure shows the NASA X-48C with the airframe designed such that provides the acoustic shielding. Second, Integrated airframe and propulsion design, where h/D is zero, providing a wall-jet flow condition, as illustrated in the two concepts future supersonic airliner concepts in Figure 3.1b. The left one is Northrop Grumman's concept

in collaboration with NASA based on the "flying wing" design. The four engines are embedded in the upper surface of the wing to achieve maximum noise shielding.

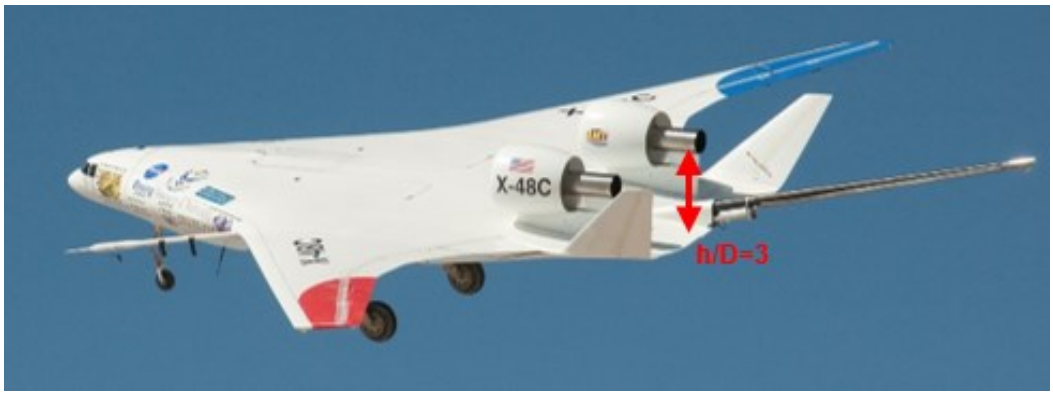

(a)

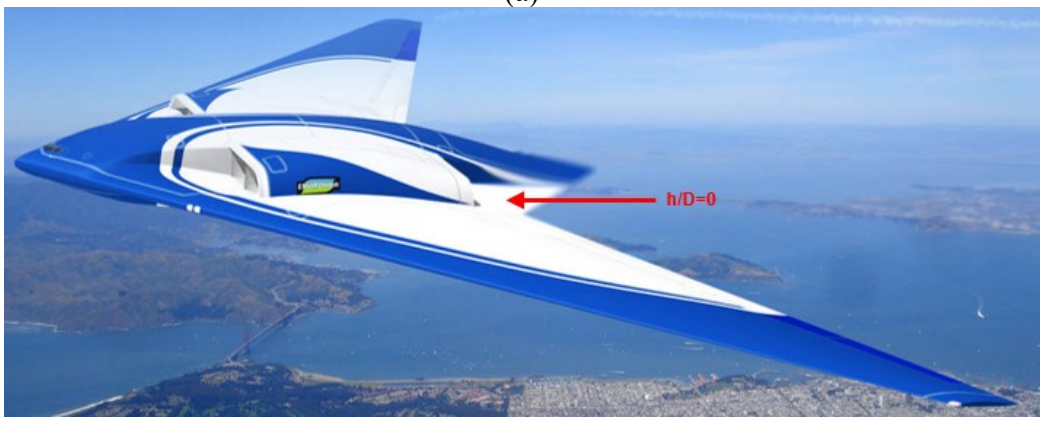

(b)

(c)

(d)

Figure 3.1 Several examples of the jet interaction with parallel surface. (a) NASA-Boeing X-48C Hybrid Wing Body Aircraft as it flies over Edwards AFB during a test flight (NASA, 2017). (b) Flying Wing aircraft (NASA, 2017). (c) Military Aviation (The Aviation Geek Club, 2020). (d) U.S. Navy F/A-18E Super Hornet of Strike Fighter Squadron 115 launches from the flight deck of the aircraft carrier USS Ronald Reagan (US Department of Defense, 2017).

But the study interaction effects have other applications as shown in the bottom row. This includes jet interaction with the wing in a conventional regional jet configuration, or the supersonic jet interaction with the ground plane on runway Figure 3.1c.

Another example of active pursuant of implementation of acoustic shielding targeting the quitter supersonic flight, is the QueSST project (Quiet Supersonic Technology). In partnership with NASA, the Lockheed Martin Skunk Works® team is working on solving the sonic boom challenge. The X-59 QueSST (Lockheed-Martin, 2020) is set to collect community response data on the acceptability of a quiet sonic boom generated by the unique design of the aircraft. NASA is seeking to establish an acceptable commercial supersonic noise standard to lift the ban on commercial supersonic travel over land, and in 2018 Skunk Works is selected for the design, build and flight test of the X-59. The breakthrough in supersonic flight can open the door to an entirely new global market for aircraft manufacturers and obviously provide much faster flights passengers. X-59 has the design Mach number of 1.5. Figure 3.2 shows that this concept design includes the acoustic shielding provided by the airframe under the engine.

Several efforts on understanding the effect of parallel solid surface on the flow physics and acoustics of the supersonic jet has been rigorously pursued by many researchers in the recent years. Following the valuable findings reviewed in Section 1.4.4, more recent studies have been carried out at NASA Glenn Research Center. For instance, Brown (2015) created empirical models that can predict acoustic effects for a range of jet flows and surface geometries. Bridges et al. (2016) extended the acoustic modeling of jet–surface interaction from simple single stream jets to a realistic dual-stream exhaust nozzle. Moreover, the experimental set up considered the presence of the flight stream

around the jet and surface to mimic practical flight conditions.

Figure 3.2 X-59 Quiet Supersonic Technology (Lockheed-Martin, 2020).

Here, the geometry of the numerical studies carried out in this work to study the shielding effect is explained. The geometry of the convergent–divergent (C-D) nozzle is obtained from an experimental study of the rectangular ($12.95mm \times 25.91mm$) supersonic jet carried out at university of Cincinnati (Baier et al., 2017, 2018; Mora et al., 2016). The equivalent diameter of the nozzle exit is $D = 20.65\ mm$.

Figure 3.3 shows the 2:1 aspect ratio rectangular nozzle with a C-D profile. The nozzle's area ratio is 1.18 with a design Mach number of 1.5, which corresponds to a nozzle pressure ratio (NPR) of 3.67. The nozzle temperature ratio (TR) is chosen such that resembles the experimental set-up as ($TR = T_0/T_a = 3.0$), where T_0 is the total temperature of the jet and T_a is ambient temperature. The nozzle is sharply C-D in the cross-sectional minor axis plane.

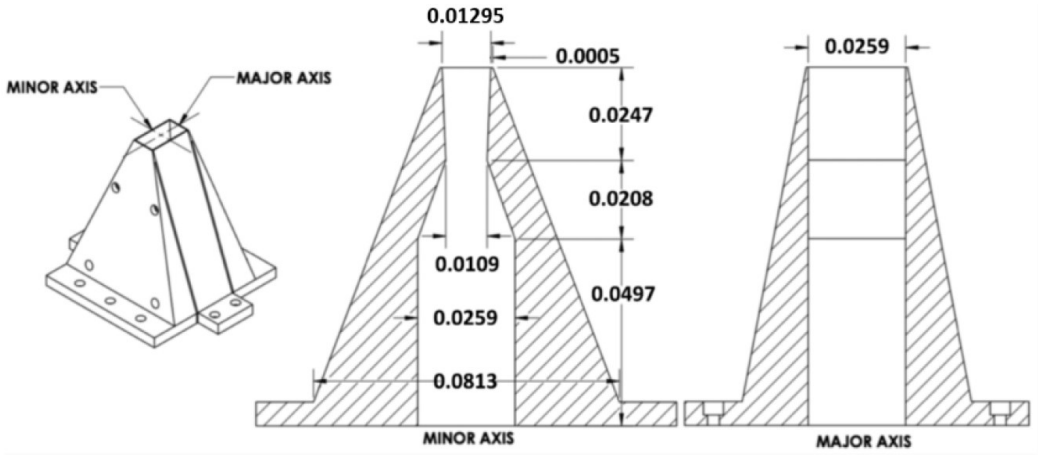

Figure 3.3 Nozzle geometry cross-sectional views (dimensions in meters) (Mora et al., 2016).

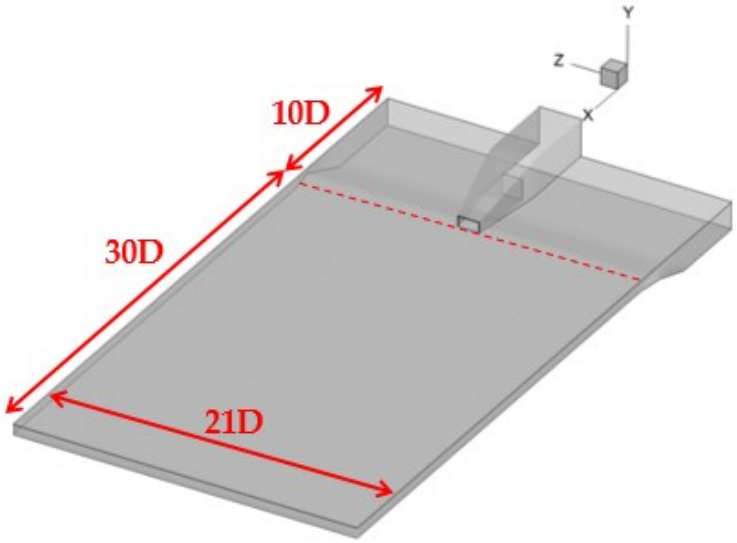

Figure 3.4 Orientation of the flat plate with respect to the rectangular nozzle.

To assess the value of wavy shield proposed in this work, the corresponding results of the wavy shield plate is compared with the base case of using a flat plate. In order to simulate the presence of an adjacent solid surface on the flow and acoustic field of supersonic jet, a flat plate with $12.7\ mm$ thickness which is placed parallel the jet axis and aligned with the nozzle's major axis, and it extends up to $x/D = 30$ downstream of

the jet axis and $z/D = 10.5$ in the major axis. This configuration is illustrated in Figure 3.4 and is explained in detail by Mora et al. (2016). For the simulations carried out here the flat plate is located such that the top surface of the plate is at $h/D = 0$, and 3 from the nozzle exit.

In addition to the flat plate cases investigated by experimental measurements, wavy wall profiles are considered to introduce disturbances in the flow and acoustic field with the aim of enhanced noise reduction. The specification of wavy wall profile depends on several parameters such as: distance of the mean line from nozzle lip (h/D), wavelength (λ), and amplitude (A_{wall}). These parameters and the theoretical work behind estimating their values are discussed in detail in the following sections. Figure 3.5 illustrates the wavy profile of the shielding plate and the rectangular nozzle.

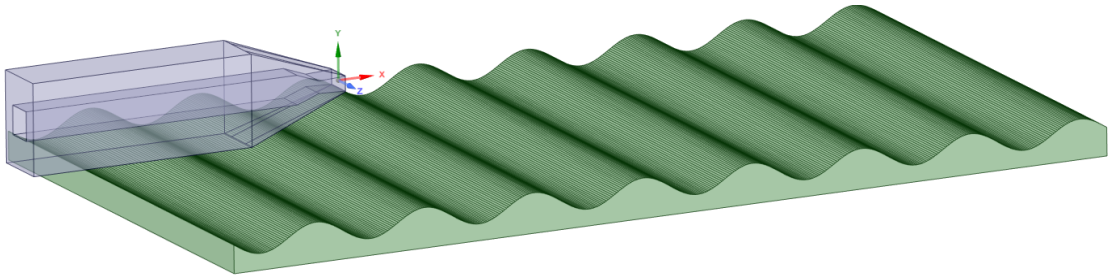

Figure 3.5 Sketch of the proposed wavy wall profile.

3.2. Numerical Approach

To demonstrate the computational capabilities of the current state of the art approach for accurate calculation of flow and acoustic field of jet-surface interactions, , a density-based compressible solver is employed with the advantage of Total Variation Diminishing (TVD) scheme to simulate the flow field of a supersonic, ideally expanded

heated jet exhausting from a 2:1 aspect ratio nozzle. HLU approach is used here to simulate the turbulence fluctuations of the flow and avoid computationally expensive LES simulations to model the near-wall boundary layer. Instead, URANS with the k-ω SST turbulence model is used near the walls. The FWH surface integral approach is used to predict the far-field acoustics.

3.2.1. Governing Equations and Numerical Scheme

The *rhoCentralFoam* solver in OpenFOAM is adopted for this study. OpenFOAM is an open source Computational Fluid Dynamics (CFD) software package consisting of a set of flexible C++ modules to resolve complex fluid flows. *rhoCentralFoam* is an unsteady, compressible solver, that uses semi-discrete, non-staggered, Godunov-type central (Kurganov & Petrova, 2001) and upwind-central (Kurganov et al., 2000) schemes proposed by Kurganov and Tadmor (2000). These schemes avoid the explicit need for a Riemann solver, resulting in a numerical approach that is both simple and efficient. The solver is a density based central scheme solver and solves the compressible Favre-averaged mass, momentum and energy governing equations in the Eulerian frame of reference (Greenshields et al., 2010). The continuity, momentum, and energy equations are solved in their conservative form as:

$$\frac{\partial \rho}{\partial t} + \nabla . [\rho \mathbf{u}] = 0 \tag{16}$$

$$\frac{\partial (\rho \mathbf{u})}{\partial t} + \nabla . [\mathbf{u}(\rho \mathbf{u})] + \nabla p + \nabla . \mathbf{T} = 0 \tag{17}$$

$$\frac{\partial (\rho E)}{\partial t} + \nabla . [\mathbf{u}(\rho E)] + \nabla . [\mathbf{u} p] + \nabla . (\mathbf{T} . \mathbf{u}) + \nabla . \mathbf{j} = 0 \tag{18}$$

where ρ is the density, $\mathbf{u}$ is the fluid velocity, p is the pressure, and $E = e + |\mathbf{u}|^2/2$ is

the total energy per unit mass with e being the specific internal energy. Here, $\mathbf{T}$ is the viscous stress tensor and is represented by Newton's Law for a non-inviscid flow as: $\mathbf{T} = -2\mu\text{dev}(\mathbf{D})$. Here, μ is the dynamic viscosity, $\mathbf{D}$ is the deformation gradient tensor $\mathbf{D} = [\nabla\mathbf{u} + (\nabla\mathbf{u})^{\text{T}}]/2$ and its deviatoric component is $\text{dev}(\mathbf{D}) = \mathbf{D} - (1/3)tr(\mathbf{D})\mathbf{I}$, where $\mathbf{I}$ is a unit vector. Also, $\mathbf{j}$ is the diffusive heat flux that is represented by Fourier's law as $\mathbf{j} = -k\nabla T$, where T is temperature and k is the conductivity.

In addition to the above equations, the system of equations is completed with the assumption of calorically perfect gas for which $p = \rho RT$ and $e = c_v T = (\gamma - 1)RT$, where R is the specific gas constant and $\gamma = c_p/c_v$ is the ratio of specific heats at constant pressure and volume, respectively.

3.2.2. Spatial and Temporal Discretization

Finite Volume method is applied for expressing the differential equations. In the application of the finite volume to polyhedral cells with an arbitrary number of faces, each face is assigned to an owner cell and a neighboring cell. This is explained in detail by Greenshields et al. (2010). The discretization of a general dependent tensor field $\mathbf{\Psi}$ of any rank is described by values $\mathbf{\Psi}_P$ at cell centers to values $\mathbf{\Psi}_f$ at cell faces.

In compressible fluid flows, properties are not only transported by the flow, also by the propagation of waves. This requires the construction of flux interpolations to consider that transports can occur in any direction (Marcantoni et al., 2012). The convective terms of the conservation equations in the forms of $\nabla.[\rho\mathbf{u}]$, $\nabla.[\mathbf{u}(\rho\mathbf{u})]$, $\nabla.[\mathbf{u}(\rho E)]$, and $\nabla.[\mathbf{u}p]$ are integrated over a control volume and linearized, and represented with the general nomenclature as follows:

$$\int_V \nabla.[\mathbf{u}\boldsymbol{\Psi}]dV = \sum_f [S_f.\mathbf{u}_f]\boldsymbol{\Psi}_f \approx \sum_f \phi_f \boldsymbol{\Psi}_f \tag{19}$$

where S_f is a vector normal to the face surface pointing out of the owner cell, and $\sum_f$ denotes summation over all faces and $[S_f.\boldsymbol{U}_f] = \phi_f$ is the volumetric flux. To obtain $\boldsymbol{\Psi}_f$ by splitting the flux in two outgoing and incoming to cell and integrating each of the terms over a control volume and discretizing the integral yields to:

$$\begin{aligned}\int_V \nabla.[\boldsymbol{U}\boldsymbol{\Psi}]dV &= \sum_f \phi_f \boldsymbol{\Psi}_f \\ &= \sum_f [\alpha\phi_{f+}\boldsymbol{\Psi}_{f+} + (1-\alpha)\phi_{f-}\boldsymbol{\Psi}_{f-} + w_f(\boldsymbol{\Psi}_{f-} - \boldsymbol{\Psi}_{f+})]\end{aligned} \tag{20}$$

The volumetric flux across a face is split into two components of $f+$ and $f-$, which are evaluated based on the cell values on either side of the face. The '$+$' and '$-$' sides refer to the owner and neighbor cells of a face, and a positive flux is in the direction of the face area normal vector which points out of the owner cell ('$+$' side) and into the neighbor cell ('$-$' side). The contributions of the two flux components to the flux evaluation are controlled by the weighted coefficient α, where it is calculated using absolute speed of the fastest traveling waves in the respective directions. For example, $\alpha = 0.5$, corresponds to an entirely central scheme. The directed convective fluxes mentioned above, are interpolated using the Van Albada scheme (Van Albada et al., 1997) to provide a second order spatial discretization that, as a TVD scheme, is appropriate for capturing flow discontinuities such as shocks, and the limiter automatically provides high order stable solution (APPENDIX C – Verification

Benchmark: Acoustic Reflection from Wall).

Additionally, the gradient terms are calculated as:

$$\int_V \nabla \boldsymbol{\Psi} dV = \sum_f S_f \boldsymbol{\Psi}_f = \sum_f [\alpha S_{f+} \boldsymbol{\Psi}_{f+} + (1-\alpha) S_{f-} \boldsymbol{\Psi}_{f-}] \tag{21}$$

The $f+$ and $f-$ interpolation uses the same limiter described for convective terms. Also, the discretization of Laplacian with diffusion coefficient Γ is described as:

$$\int_V \nabla.(\Gamma \nabla \boldsymbol{\Psi}) dV = \sum_f \Gamma_f S_f.(\nabla \boldsymbol{\Psi})_f \tag{22}$$

where Γ_f is interpolate linearly from cell center values.

In addition, second order implicit temporal discretization (Versteeg & Weeratunge, 2007) is used. This ensures overall second order of accuracy of the numerical simulations. Similar to the temporal discretization approach explained in Chapter 2, the time step was selected such that the important frequencies are appropriately resolved. The highest resolvable frequency for capturing the main acoustic behavior of the supersonic jets is selected similar to the time marching approach mentioned in Chapter 2. This corresponds to non-dimensional time step with respect to the nozzle exit velocity and nozzle throat diameter. The corresponding convective and acoustic maximum CFL corresponding to this time step are 0.9 and 0.59, respectively. The maximum resolvable should not be confused with the maximum cut-off frequency for capturing acoustics. The calculation of the cut-off frequency for acoustic analysis is described in Section 3.2.5.

3.2.3. Turbulence Modelling (URAN-LES Switch)

In this study, the $k-\omega$ SST DES turbulence model is adopted, where the URANS

models are employed in the boundary layer, while the LES treatment is applied everywhere else. Therefore, the computational cost is much efficient compared to the full LES that requires extensive near wall treatment. For the current simulations, a statistically steady solution is achieved with the $k - \omega$ SST RANS model first, then the DES simulations are carried out using the RANS results as an initial solution.

The URANS $k - \omega$ SST turbulence model relies on solving two transport equations for the turbulence kinetic energy, k, and turbulence specific dissipation rate, ω (Wilcox, 1998).

$$\frac{\partial(\rho k)}{\partial t} + \frac{\partial(\rho u_i k)}{\partial x_i} = \tilde{P}_k - \beta^* \rho k \omega + \frac{\partial}{\partial x_i}\left[(\mu + \sigma_k \mu_t) + \frac{\partial k}{\partial x_i}\right] \tag{23}$$

$$\frac{\partial(\rho\omega)}{\partial t} + \frac{\partial(\rho u_i \omega)}{\partial x_i} = \alpha\rho S^2 - \beta\rho\omega^2 + \frac{\partial}{\partial x_i}\left[(\mu + \sigma_\omega \mu_t) + \frac{\partial \omega}{\partial x_i}\right] + 2(1 - F_1)\rho\sigma_{\omega 2}\frac{1}{\omega}\frac{\partial k}{\partial x_i}\frac{\partial \omega}{\partial x_i} \tag{24}$$

where $F_1 = \tanh\left\{\left\{\min\left[max\left(\frac{\sqrt{k}}{\beta^*\omega y}, \frac{500\nu}{y^2\omega}\right), \frac{4\rho\sigma_{\omega_2}k}{CD_{k\omega}y^2}\right]\right\}^4\right\}$, $CD_{k\omega} = \max\left(2\rho\sigma_{\omega 2}\frac{1}{\omega}\frac{\partial k}{\partial x_i}\frac{\partial \omega}{\partial x_i}, 10^{-10}\right)$, and y is the distance to the nearest wall. The turbulent eddy viscosity is defined as:

$$\nu_t = \frac{\alpha_1 k}{\max(\alpha_1\omega, SF_2)} \tag{25}$$

where the function F_2 is defined as $F_2 = \tanh\left[\left[max\left(\frac{2\sqrt{k}}{\beta^*\omega y}, \frac{500\nu}{y^2\omega}\right)\right]^2\right]$, and S is the invariant of the strain rate. The production limiter used in the SST model that prevents

the accumulation of turbulence in the stagnation region is defined as $\tilde{P}_k = \min\left[\mu_t \frac{\partial u_i}{\partial x_i}\left(\frac{\partial u_i}{\partial x_j} + \frac{\partial u_j}{\partial x_i}\right), 10\beta^* \rho k \omega\right]$. And all the constants are used as defined by Mentar et al. (2003) as: $\beta^* = 0.09$, $\alpha_1 = 5/9$, $\beta_1 = 3/40$, $\sigma_{k1} = 0.85$, $\sigma_{\omega 1} = 0.5$, $\alpha_2 = 0.44$, $\beta_2 = 0.0828$, $\sigma_{k2} = 1$, $\sigma_{\omega 2} = 0.856$.

The DES formulation of the $k - \omega$ SST (Mentar et al., 2003; Strelets, 2001) model is achieved such that in the LES regions of the grid, the solution would reduce to a Smagorinski-like sub-grid model (Smagorinsky, 1963), such that the eddy viscosity is proportional to the magnitude of the strain tensor, and to the square of the grid spacing (Strelets, 2001). Therefore, the only term of the RANS model that is different in the DES mode is the dissipative term of the k transport equation, Equation (23). This equation in the DES model is defined as:

$$\frac{\partial(\rho k)}{\partial t} + \frac{\partial(\rho u_i k)}{\partial x_i} = \tilde{P}_k - \beta^* \rho k \omega \tilde{d} + \frac{\partial}{\partial x_i}\left[(\mu + \sigma_k \mu_t) + \frac{\partial k}{\partial x_i}\right] \tag{26}$$

where the length scale, $\tilde{d}$, is defined as:

$$\tilde{d} = F_{DES} = \max\left(\frac{L_t}{C_{DES}\Delta}, 1\right) \tag{27}$$

where Δ is the local grid spacing, which for a three-dimensional grid is defined as $\Delta = \max(\Delta x, \Delta y, \Delta z)$ and $C_{DES} = 0.61$. When the local grid is fine enough in all directions, compared to the turbulent length scale, the $\tilde{d}$ term grows larger than 1. This will in turn reduce k, hence allows the solution to resolve turbulence and it will reduce the amount of modeled turbulent shear stress and allow the region to be treated as LES.

3.2.4. Boundary Treatment

At the nozzle inlet, a total pressure condition of $3.67\ MPa$ is specified and the jet was

expected to be ideally expanded with a NPR value of 3.67. Temperature at the inlet of the nozzle is prescribed to $900K$ to ensure the TR=3.0. where ambient pressure is $P_a = 101325\ Pa$, and has a temperature value of $T_a = 300K$. Advective far-field condition was imposed on the rest of the domain boundaries, which corresponds to "*waveTransmisive*" boundary conditions in OpenFOAM. The non-reflecting boundary condition used here is based on the characteristic wave relations derived from the Euler equations reformulated into an orthogonal coordinate system such that one of the coordinates is normal to the boundary. The amplitude of the incoming pressure and entropy waves are computed from the Linear Relaxation Method (LRM) (Poinsot & Lele, 1992). This non-reflecting condition is based on the same idea of non-reflecting boundary condition as mentioned by Poinsot and Lele (1992) without full inter-field coupling.

The nozzle walls and any other solid surface (flat plate or wavy shield) are prescribed as adiabatic no-slip condition, so the RANS simulations near the wall can predict the boundary layer with the specified y^+. On the other hand, on the flat plate adiabatic slip conditions are imposed. Since the flat plate is only to reflect the acoustic wave, the no-penetration rule is enforced by imposing $\partial p/\partial n = 0$ for pressure, and zero normal velocity $\boldsymbol{u}.\hat{n} = 0$.

3.2.5. Computational Grid

The computational grid used in the current simulations contains hexahedrally dominant cells. The entire computational domain extends to $80D$ downstream of the nozzle exit and $10D$ upstream of the nozzle exit, also it extends radially up to $25D$ from both major and minor axis planes.

The grid spacing on nozzle walls is chosen such that it ensures $y^+$to have a value of

30 on the wall, and to make sure the close wall calculations of boundary layer in the RANS region are accurate. This value for y^+ is calculated considering the isentropic flow assumption along the nozzle and using the nozzle exhaust velocity U_j. As it is illustrated in Figure 3.6, the fine grid spacing on nozzle walls are gradually increased such that the volume inside the nozzle has the maximum element sizing of $D/50$. Such grid spacing is kept consistent for both baseline and with-plate (shielded) cases. Figure 3.6b illustrates the grid spacing in major plane that has the same y^+ and expands to same maximum grid spacing as mentioned earlier.

This grid spacing is maintained and extended up to $x/D = 5$ in the jet axis direction to capture turbulent mixing near nozzle exit, and then it is gradually increased up to $D/40$ in jet axis direction up to $x/D = 20$. These refinement regions are illustrated by blue boxes in Figure 3.7. Then another refinement box is placed that is extended to $x/D = 30$ (and maintained up to $x/D = 40$), which gradually increases the cell size up to maximum value of $D/30,$ shown in a similar fashion with blue box in Figure 3.7.

The grid spacing expands gradually in both major and minor directions up to $y/D = 6$, and $z/D = 10$ and reaching the grid spacing of $D/10$. This conservative coarsening in axial direction up to $x/D = 40$ and in major and minor directions is chosen to have a refined box to predict acoustics.

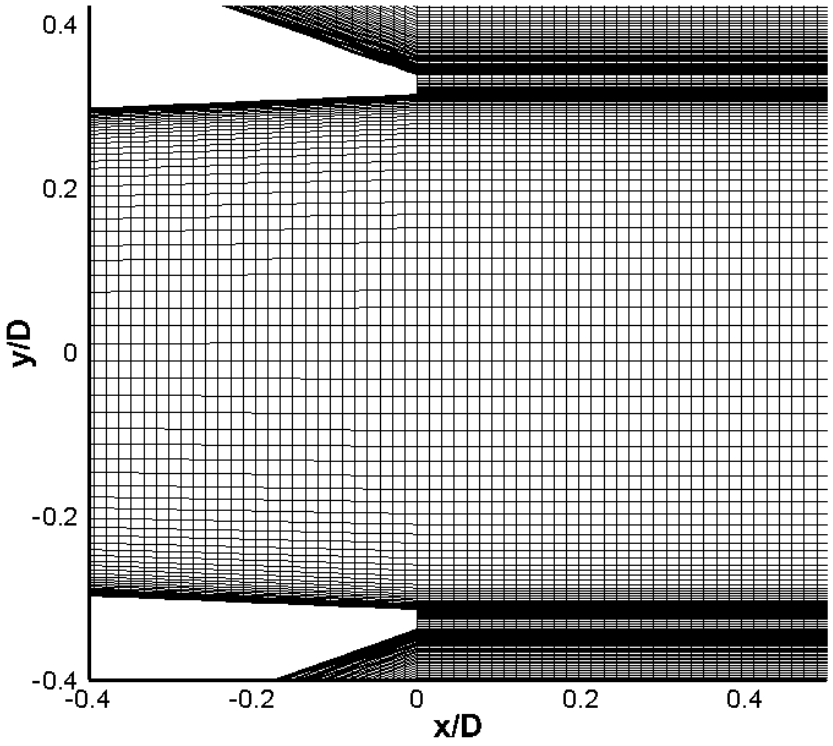

(a)

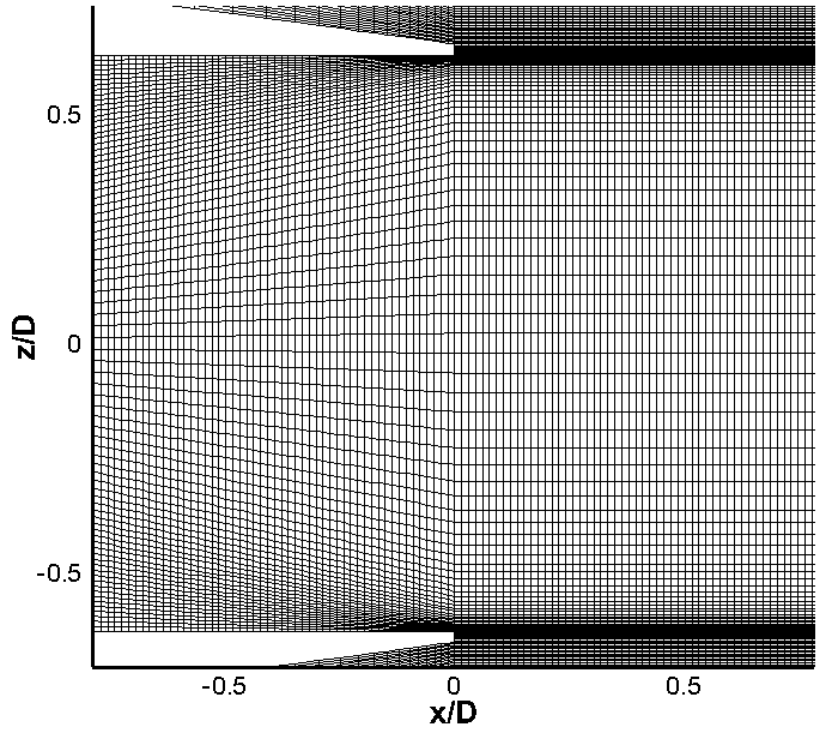

(b)

Figure 3.6 Planar cut of the computational grid near nozzle exit, (a) minor plane, (b) major plane.

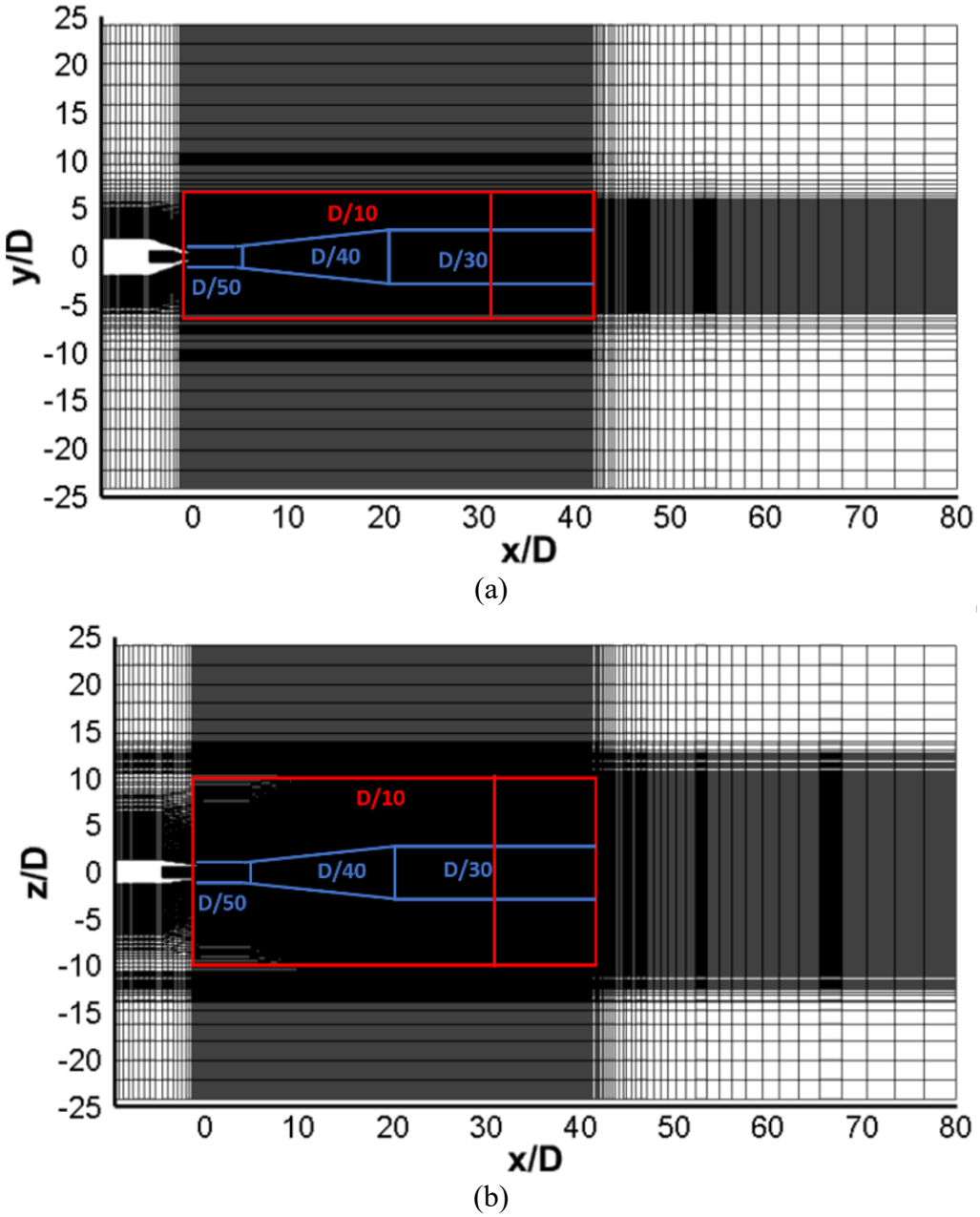

Figure 3.7 Planar cut of the computational domain of the baseline case, (a) minor plane, (b) major plane.

The FWH surface used in this study is a rectangular box from the nozzle exit extending to $y/D = 6$, and $z/D = 10$ in major and minor planes, and up to $x/D = 30$ in the jet axis direction. This near field region is illustrated with the red box in Figure 3.7.

The refined nearfield acoustic region has maximum grid spacing of $D/10$ and is to be used for FWH acoustic predictions. Sensitivity studies of the extent of the FWH up to $x/D = 40$ is investigated previously and reported by Salehian and Mankbadi (2019). Such grid spacing on FWH surface would ensure capturing acoustic waves up to Strouhal number $St = fD/U_j = 0.35$ where f is the frequency. This maximum frequency represents up to 70% of the spectra shown in experimental results and contains the important aspects of the trend in spectral analysis of the acoustic signal, such as the peak frequency of $St = 0.1$ observed in experimental results.

From the numerical point of view, the maximum resolvable frequency is calculated based on the assumption that, Minimum of 15 points (cells) per wavelength are required to capture the acoustic waves up to $St = 0.35$ with the current numerical scheme. Such requirement has been tested for prediction of waves using second-order finite volume schemes when applied to hexahedral cells.

The shielded case has the same grid spacing as the baseline case inside the nozzle, as well as in the refinement boxes mentioned above in Figure 3.7. The only difference is the in the dimensions of the near field acoustic box, while maintaining the same grid spacing of $D/10$. The near field region expands gradually in minor directions up to $z/D = 10$ like the baseline case and up to $y/D = 6$ in the reflected side, but the it is bounded by the flat plate at location of the flat plate ($y/D = -3$). The near field acoustic region is illustrated in Figure 3.8. No extensive grid spacing is maintained on the flat plate, since the jet does not hit the flat plate unless in much further distance from the nozzle exit ($x/D > 25$), and there is no need for boundary later grid enforcement. Moreover, here we focus on the reflection of the acoustic waves from the solid boundary, and since the

flat plate is at a considerable distance from the jet, boundary layer prediction on the flat plate is not considered. Figure 3.9 illustrates the grid spacing in the nearfield acoustic region, as well as near the flat plate. The wavy wall cases have the exact same grid spacing as mentioned for shielded cases ($h/D = 0, 3$).

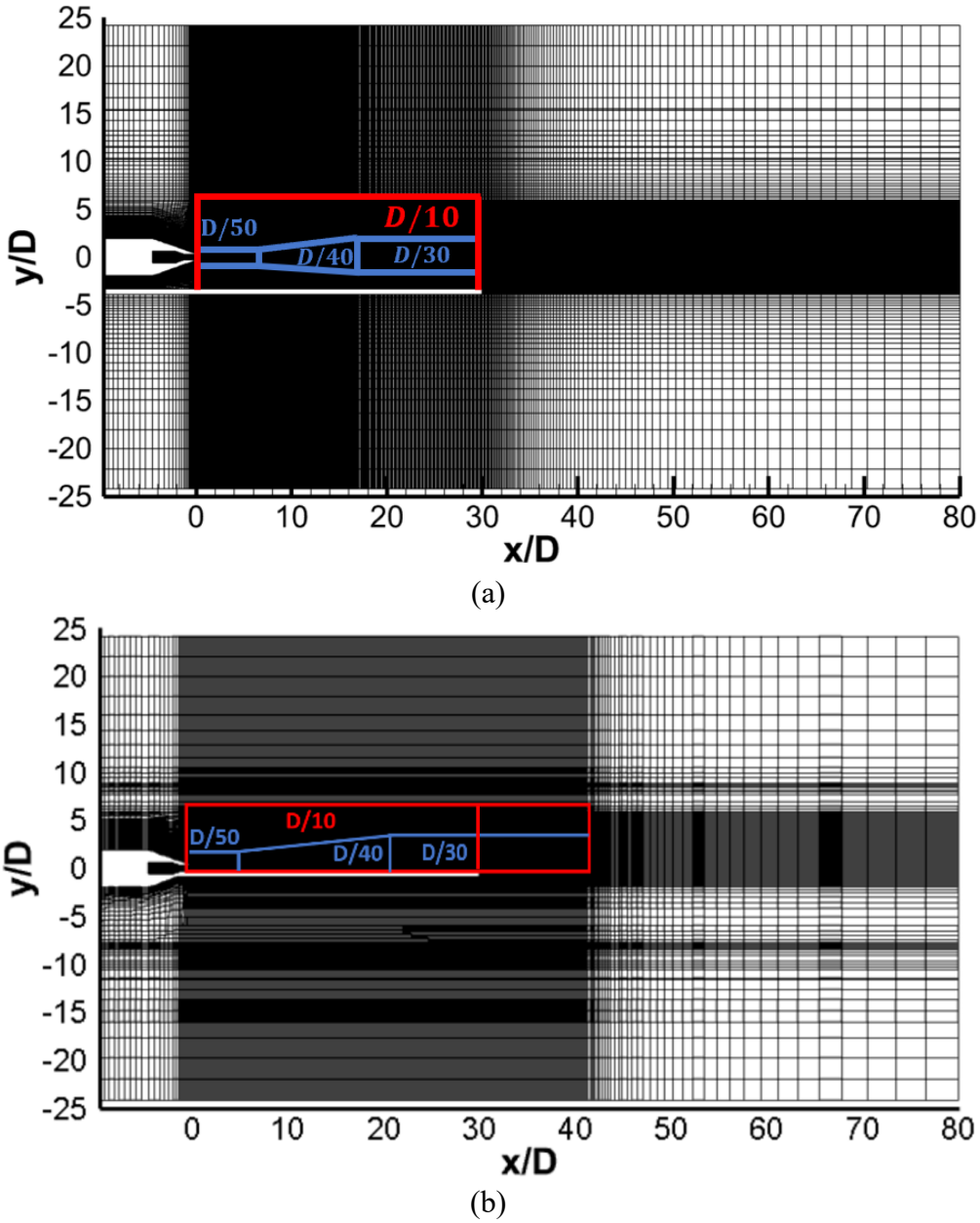

Figure 3.8 Planar cut of the computational domain of the shielded case in x – y plane. (a) ($h/D = 3$), (b) ($h/D = 0$).

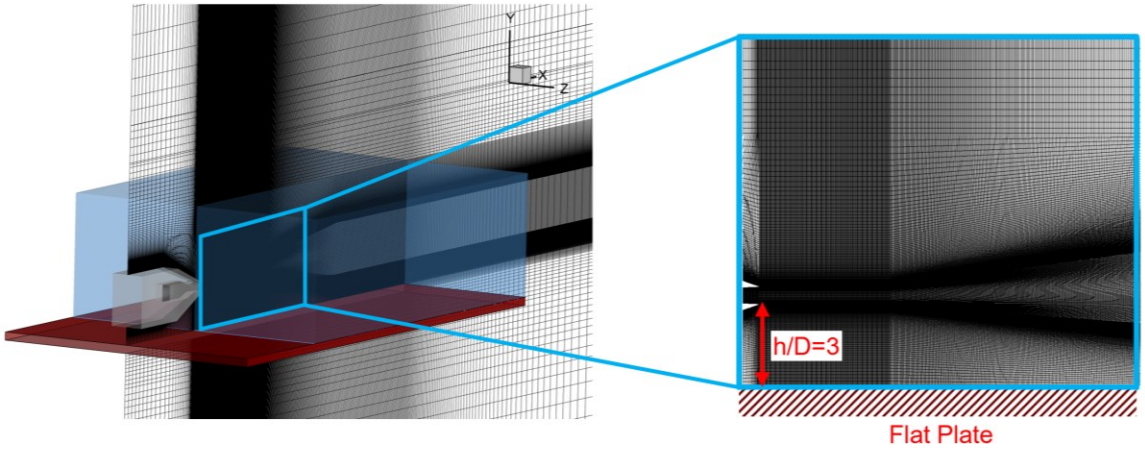

Figure 3.9 The computational domain of the shielded case ($h/D = 3$).

3.2.6. The FWH Surface Integral Formulation

Far field acoustics is obtained using the FWH integral technique. The FWH equation is an inhomogeneous wave equation derived by manipulating the continuity equation and the Navier-Stokes equations. If we assume that the control surface contains all acoustic sources, the volume integrals outside this surface can be dropped. To provide accurate, and clear documentation of the FWH formulations implement within OpenFOAM, the formulation and assumptions made for simplifications are provided here. Moreover, a verification of the implemented formulation in OpenFOAM is documented in APPENDIX A – Verification Benchmark: .

Starting from the general FWH equation:

$$\square^2 p'(x,t) = \frac{\partial}{\partial t}\left[(\rho_o U_n)\delta(f)\right] + \frac{\partial}{\partial x_i}\left[L_i \delta(f)\right] - \frac{\partial^2}{\partial x_i x_j}\left[T_{ij} H(f)\right] \tag{28}$$

The symbol , $\square^2$, is the wave or D'Alembertian operator in the three-dimensional space, T_{ij} is the Lighthill stress tensor, σ_{ij} is viscous stress tensor, δ_{ij} is the Kronecker delta, $\delta(f)$ and $H(f)$ are the dirac delta function and the Heaviside step functions, u_n is

the fluid velocity in the direction normal to the FWH surface, and v_n is the surface velocity in the direction normal to the surface, ρ and ρu_i are conservation variables utilized and obtained in the flow field, and ρ_o is the free-stream density value. The other terms on the RHS of the equation (Di Francescantonio, 1997) are:

$$U_n = U_i.\hat{n}_i = \left[\left(1 - {}^{\rho}/_{\rho_o}\right)v_i + \left({}^{\rho}/_{\rho_o}\right)u_i\right].\hat{n}_i = \left(1 - {}^{\rho}/_{\rho_o}\right)v_n + \left({}^{\rho}/_{\rho_o}\right)u_n \tag{29}$$

$$L_i = P_{ij}\hat{n}_j + \rho u_i(u_n - v_n) \tag{30}$$

$$T_{ij} = \rho u_i u_j - \sigma_{ij} + (p' - c^2\rho')\delta_{ij} \tag{31}$$

The Farassat 1A formulation of the FW-H equations developed by Brentner and Farassat (1998) is utilized such that the far field acoustic can be represented as:

$$p'(x,t) = p'_T(x,t) + p'_L(x,t) + p'_Q(x,t) \tag{32}$$

$$\begin{aligned} 4\pi p'_T(x,t) = &\int_{f=0}\left[\frac{\rho_o\left(\dot{U}_n + U_{\dot{n}}\right)}{r(1-M_r)^2}\right]_{ret} dS \\ &+ \int_{f=0}\left[\frac{\rho_o U_n((r\dot{M}_r + c(M_r - M^2))}{r^2(1-M_r)^3}\right]_{ret} dS \end{aligned} \tag{33}$$

$$\begin{aligned} 4\pi p'_L(x,t) = &\frac{1}{c}\int_{f=0}\left[\frac{\dot{L}_r}{r(1-M_r)^2}\right]_{ret} dS + \int_{f=0}\left[\frac{L_r - L_M}{r^2(1-M_r)^2}\right]_{ret} dS \\ &+ \frac{1}{c}\int_{f=0}\left[\frac{L_r((r\dot{M}_r + c(M_r - M^2))}{r^2(1-M_r)^3}\right]_{ret} dS \end{aligned} \tag{34}$$

Here, U and M are the surface motion velocity and Mach number, r is the distance

between source and observer. $\dot{L}_r, \dot{U}_n,$ and $\dot{M}_r$ represent the source time derivatives. The subscripts *r* or *n* denote a dot product of the vector with the unit vector in the radiation direction $\hat{r}$, or the unit vector in the surface normal direction $\hat{n}$ respectively. The term $L_M = L_i M_i$. The term *"ret"* refers to retarded time. The term, $f = 0$, represents closed surface integration on the control surface. The last term in Equation (32) is the volume integral which represent quadrupole (volume) sources in the region. The contribution of the volume integrals becomes small when the source surface encloses the source region. The above equations can be simplified for a control surface that is fixed in space, as permeable control surfaces (Lyrintzis, 2003).

The implemented FWH formulation in OpenFOAM is achieved by assuming the volume integral term can be ignored, the surface integrals are simplified as:

$$4\pi p'_T(x,t) = \int_{f=0} \left[\frac{\rho_o(\dot{U}_n)}{r}\right]_{ret} dS \tag{35}$$

$$4\pi p'_L(x,t) = \frac{1}{c}\int_{f=0} \left[\frac{\dot{L}_r}{r}\right]_{ret} dS + \int_{f=0} \left[\frac{L_r}{r^2}\right]_{ret} dS \tag{36}$$

$$U_i = \left(\rho/\rho_o\right) u_i \tag{37}$$

$$L_i = P_{ij}\hat{n}_j + \rho u_i u_n \tag{38}$$

where, all other terms can simplified to, $U_n = U_i.\hat{n}_i$, $\dot{U}_n = \frac{\partial U_n}{\partial t}$, $L_r = L_i.\hat{r}_i$, and, $\dot{L}_r = \frac{\partial L_r}{\partial t}$

3.3. Results for the Isolated Jet and the Flat Plate Wall Jet ($h/D = 0$) Cases

For validation purposes and comparison with experimental measurements, the isolated jet (no shielding plate) and the wall jet flow case (flat plate at $h/D = 0$) are presented here.

3.3.1. Grid Sensitivity Study of Isolated Jet Case

First a grid sensitivity study is carried out to validate the numerical results for the isolated jet case. Four refinement zones are depicted in Figure 3.10. the fine grid refinement regions have the grid spacing as described previously in Section 3.2.5. However, the coarse grid has bigger cell size as mentioned in Table *3.1*.

In Figure 3.11, the time averaged axial velocity component is compared with the data available in the literature. Red line represents the numerical LES simulation results presented by Viswanath et al. (2017) for a nozzle with NPR=3.67 and TR=3.0, which is the exact same operating condition as the current work.

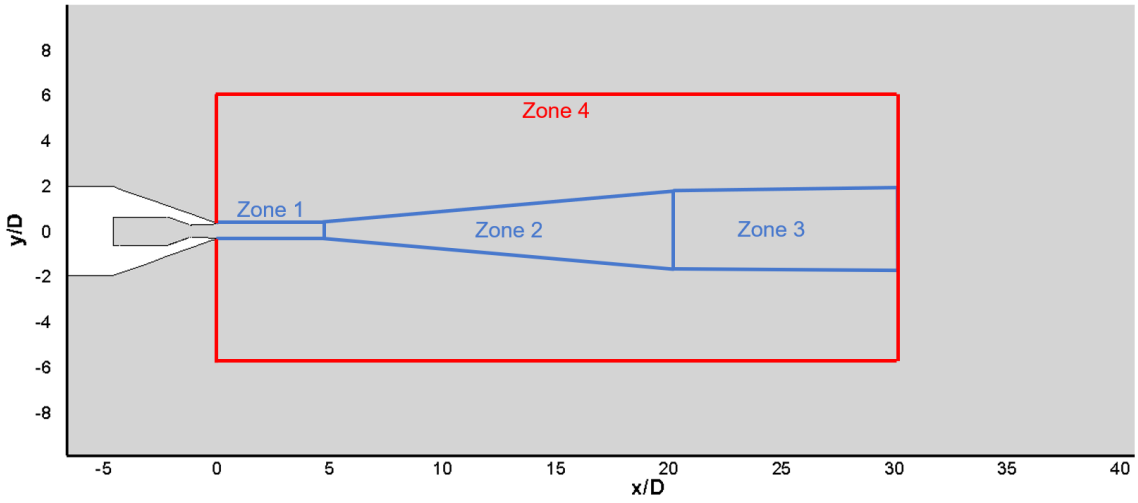

Figure 3.10 Refinement zones in the computational domain.

Table 3.1

Grid spacing of different refinement zones in the computational domain

	Zone 1	**Zone 2**	**Zone 3**	**Zone 4**
Coarse grid	D/25	D/20	D/15	D/5
Fine grid	D/50	D/40	D/30	D/10

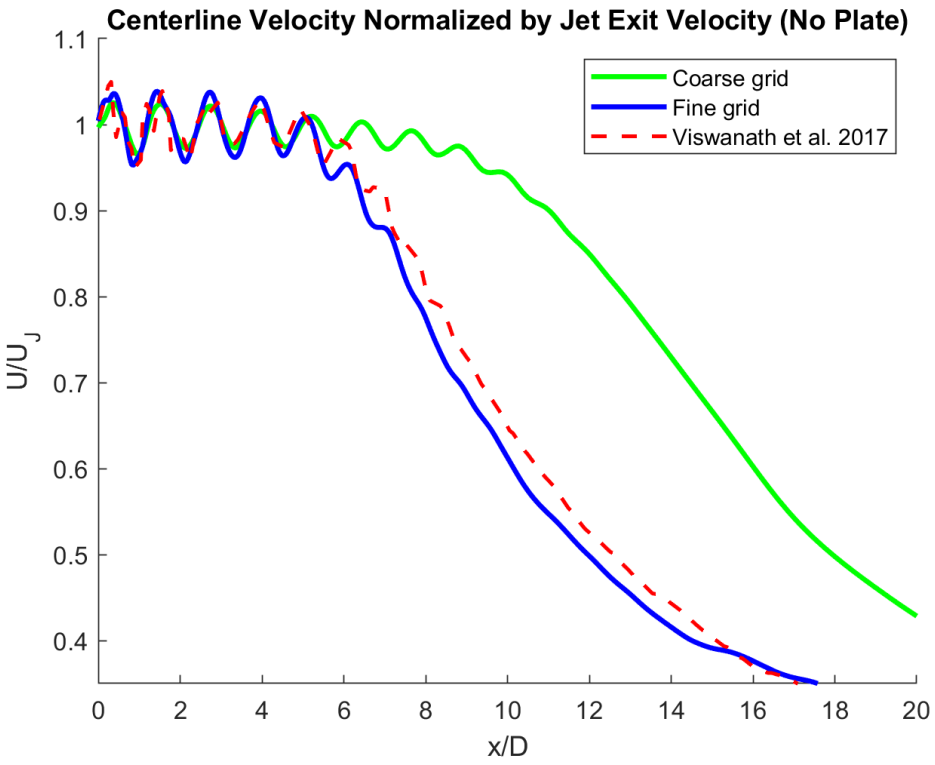

Figure 3.11 Time averaged center line velocity (Isolated Jet).

It can be observed that numerical from the fine grid show very good agreement with the available data (Viswanath et al., 2017) in literature. While the coarse grid results do not accurately predict the shocks, completely fail to predict the dissipation of the jet. The inability to capture the dissipation of the jet in the coarse grid results is mainly due to the nature of turbulence modeling. As described in Section 3.2.3, accurate prediction of the dissipation rate in DES formulations depends on the grid spacing.

The grid spacing similar to the fine grid carried out here was tested by Liu et al. (2015) and showed successful predictions of the behavior of a circular heated jet ($M = 1.5$) with a second order of accuracy numerical scheme. The grid sensitivity was carried out to confirm that the fine grid can accurately predict the shocks, and the dissipation

trend of the jet in a similar manner, and provide evidence on necessity of the described grid spacing here for the rectangular heated jet.

3.3.2. The Flow Field and Validations

Next, the time averaged velocity is illustrated in Figure 3.12, for the wall-jet case ($h/D = 0$) and compared with experimental data of the ideally expanded heated jet ($NPR = 3.67, TR = 2.4$) reported by Baier et al. (2017). The nozzle operating conditions of the experimental data are much closer to those of the current numerical results. The extension of the core of the jet predicted by the numerical simulation is in close comparison with the experiment. The core of the jet can be identified as the red region where $U/U_j = 1$, the numerical results predict the same extent for the plume as the experiment which is located at $x/D = 12$.

The Turbulent Kinetic Energy (TKE) is illustrated in Figure 3.13 and Figure 3.14. TKE here is normalized with respect to the jet velocity squared (TKE/U_j^2). The isolated jet case is compared with the experimental results for the ideally expanded heated jet ($NPR = 3.67, TR = 2.0$) reported by Baier et al. (2017), shown in Figure 3.13. Also, the shielded case shown in Figure 3.14, is compared with the experimental results for the ideally expanded heated jet reported by Baier et al. (2018) ($TR = 2.0$, and $TR = 2.4$). These experimental results are chosen for validation, since these results have the closest operating conditions to the current numerical simulations among all experimental results available in the literature for this nozzle geometry, at this time.

The numerical results exhibit the same structure of turbulence, especially in the near-wall region, as shown in Figure 3.14. Furthermore, the location of the separation of the boundary layer on the flat plate can be observed in Figure 3.14a, which is located at $x =$

$6D$ and agrees with the experiment (Figure 3.14b). The jet is held by the flat plate from one side, which prevents the dissipation of the jet from that side and causes the asymmetric structure of the kinetic energy dissipation. The potential core of the jet is affected by the flat plate, reducing the turbulence in the near nozzle region of the flat plate.

Moreover, the separation of the boundary layer from the flat plate induces fluctuations in the further downstream of the flat plat and gives rise to generation of a dipole-like source at the trailing edge of the flat plate. The acoustic results are presented for validation purposes, as well as, showing the shielding effect.

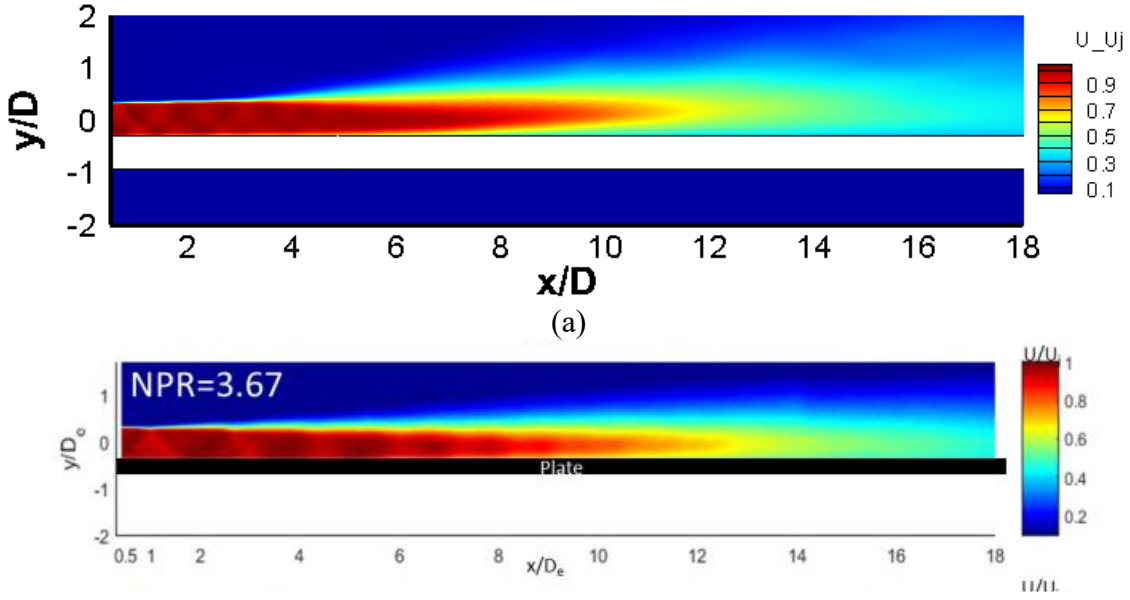

Figure 3.12 Time averaged velocity normalized by jet exit velocity U_j. Shielded case. (a) Numerical ($NPR = 3.67, TR = 3.0$), (b) Experiment ($NPR = 3.67, TR = 2.4$).

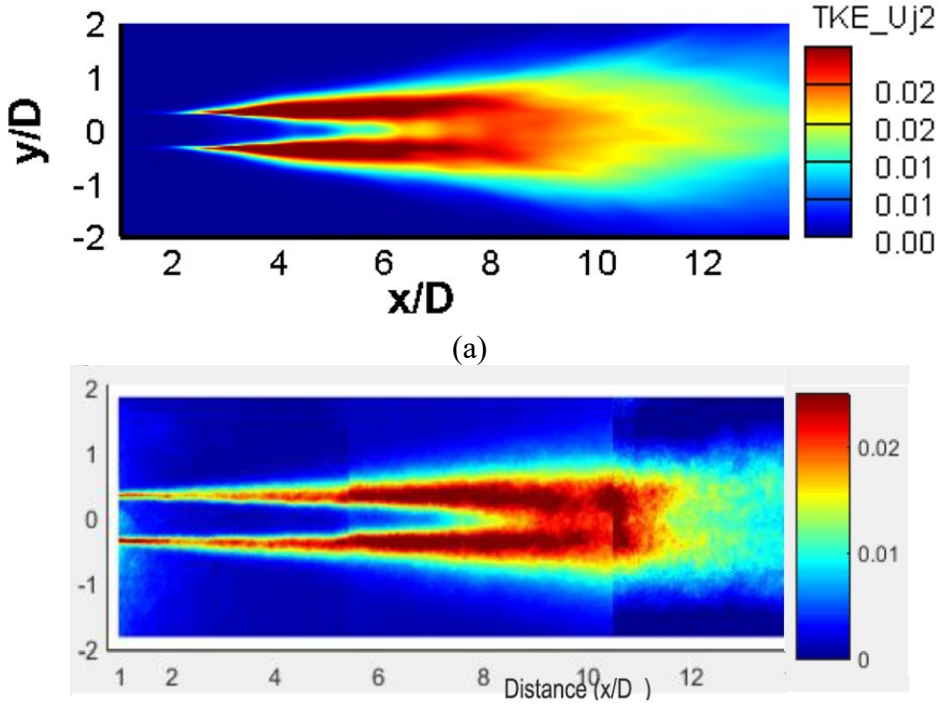

Figure 3.13 TKE normalized to jet velocity squared. Isolated jet. (a) Numerical ($NPR = 3.67, TR = 3.0$), (b) Experiment ($NPR = 3.67, TR = 2.0$).

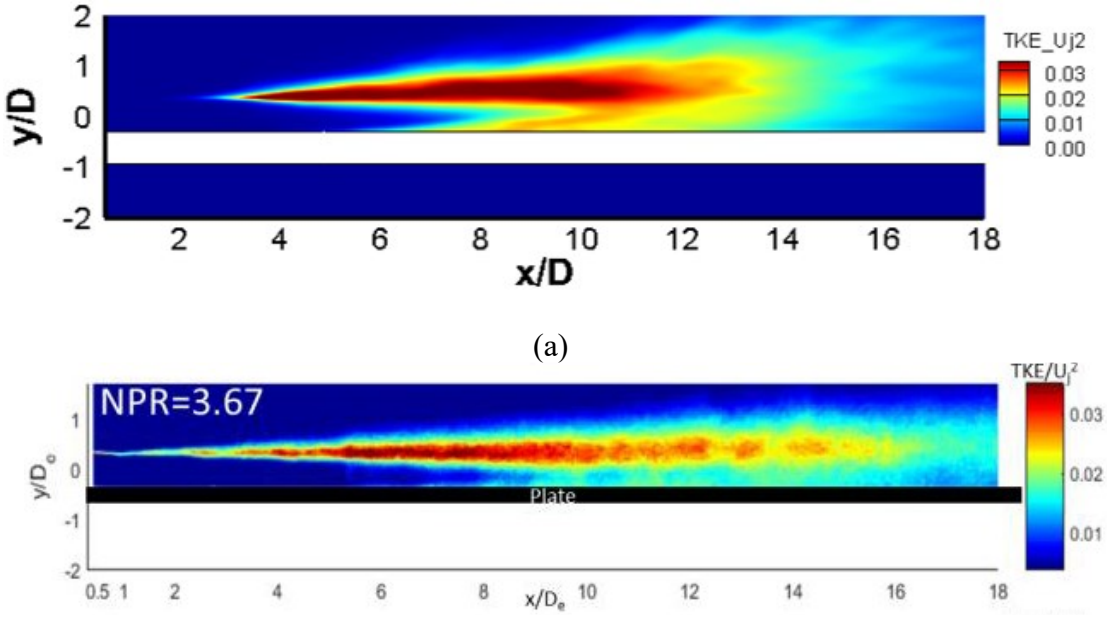

Figure 3.14 TKE normalized by jet velocity squared. ($h/D = 0$) case. (a) Numerical. ($NPR = 3.67, TR = 3.0$), (b) Experiment ($NPR = 3.67, TR = 2.4$).

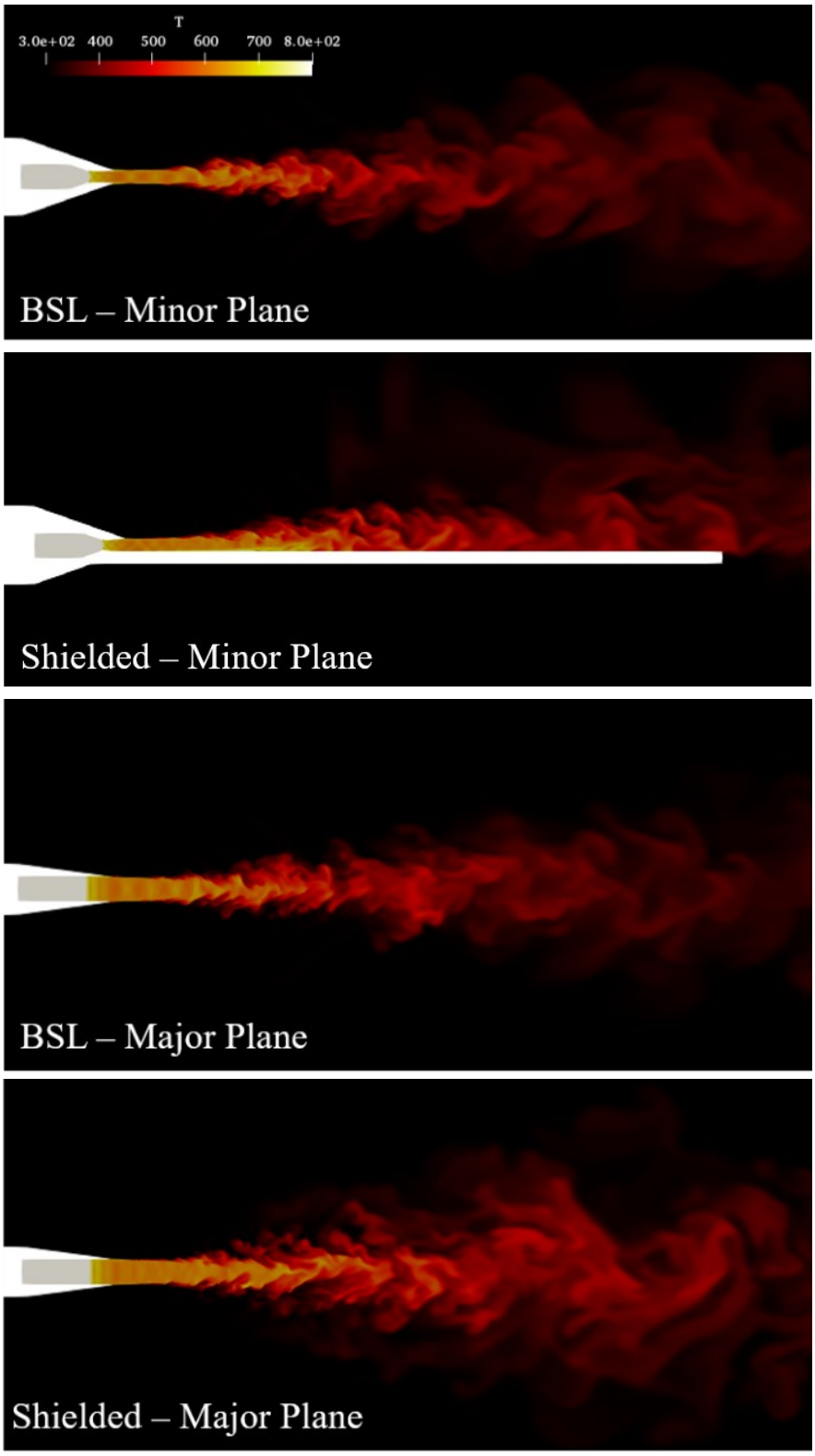

Figure 3.15 Instantaneous temperature, T $[K]$.

Since the heated jets are investigated in this study, it is worthwhile to look at the diffusion of the kinetic energy and the effect of flat plate on it. The contours of temperature in the minor plane, shows the jet dissipation pushed further downstream, as illustrated in Figure 3.15. Also, the major plane contours show that the flat plate causes the jet to scatter more in the z direction. The effect of the plate on acoustics is investigated in more detail by examining the acoustic spectra in the next section.

3.3.3. Acoustic Spectra and Shielding Effect

The numerical shadowgraph is calculated and compared with the shadowgraph results of the experiment reported by Mora et al. (2016) in Figure 3.16. Looking at the results for the nozzle without the plate, the Mach waves propagating downstream of the jet seem to be the main sources of noise in far field. Mora et al. (2016) mentioned existence of crackle noise, specifically for heated jets. Crackle (Ffowcs Williams et al., 1975) is characterized by intermittent positive pressure fluctuations radiating downstream at an angle associated with the peak jet noise. Such waves are somewhat different from Mach waves which are long, straight and have about equal angles (Ffowcs Williams & Maidanik, 1965).

To be able to investigate the effect of flat plate on radiated noise in far field, acoustic spectra are presented at two main microphone probes located at 152^o and 136^o as prescribed points A and B respectively. Similarly, two other probe angles are measured from the upstream of the jet axis, but on the shielded side. The acoustic results are calculated and compared with experimental data presented by Mora et al. (2016). The location of the probes, the reflected side, and the shielded side are illustrated in the schematics shown in Figure 3.17.

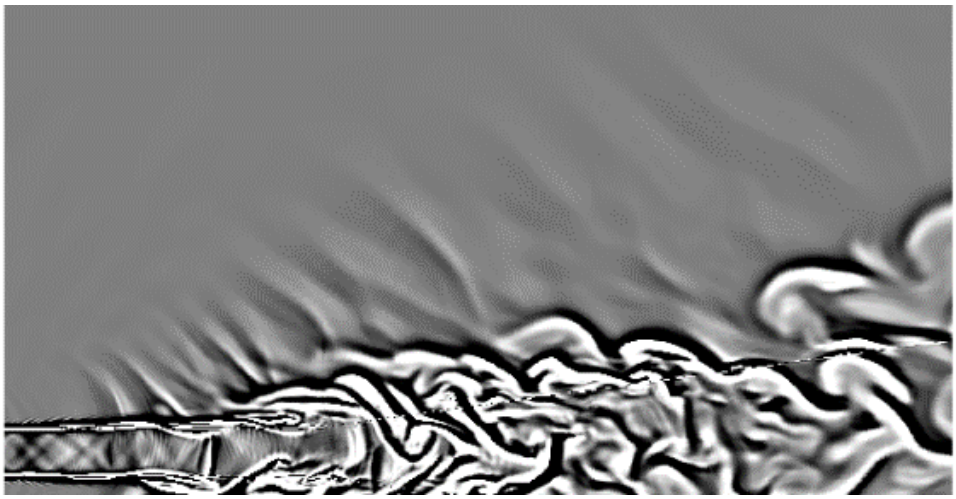

(a)

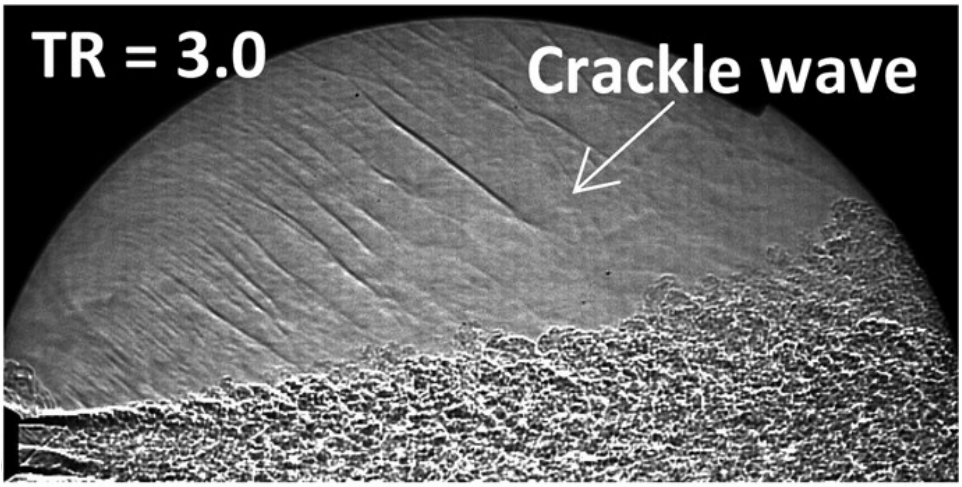

(b)

Figure 3.16 (a) Instantaneous numerical shadowgraph. (b) Instantaneous Schillerian from (Mora et al., 2016).

For the spectral data presented here, 4 sequences of 1024 samples are collected at a sampling frequency of 204.8 kHz. Fast Fourier transform was applied to obtain the narrowband noise spectrum. The frequency is normalized to obtain Sound Pressure Level (SPL) ($dB\ rel\ 20\ \mu Pa$), as a function of Strouhal number, as explained in the earlier sections. Figure 3.18 and Figure 3.19, compare SPL spectra between the reflected side and the shielded (point A and A', $\psi = 152^o$) for the free jet case. Generally, the results

shown in both figures show favorable agreement with the corresponding experimental data, both in terms of the predicted level of acoustics, as well as the trend of spectra.

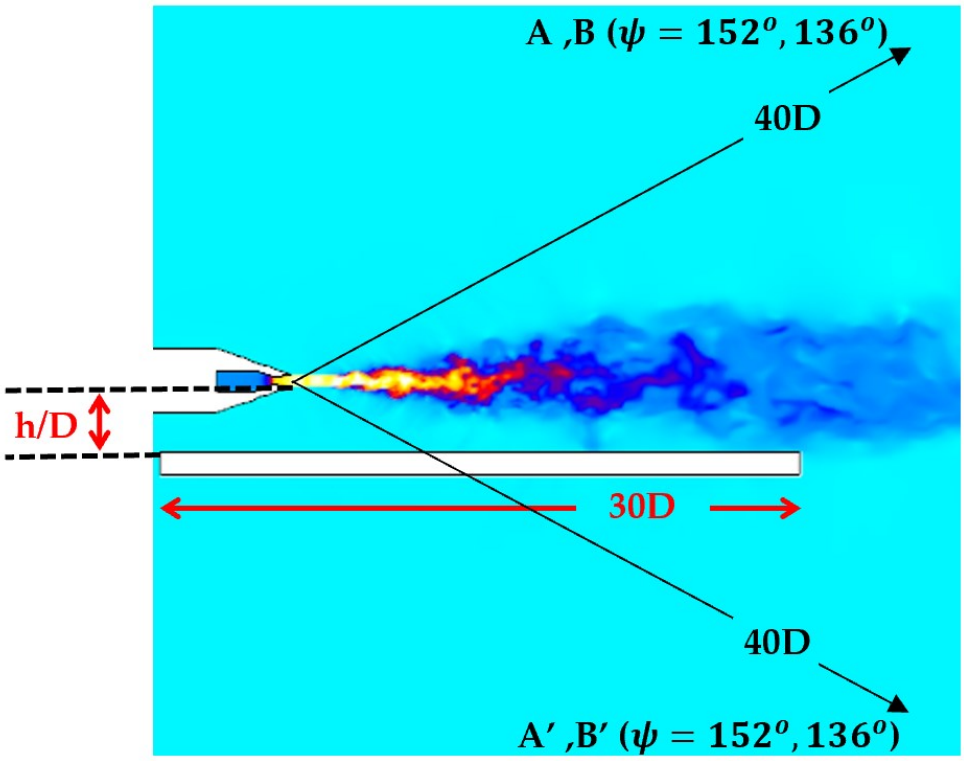

Figure 3.17 Schematics of the microphone probe locations

Figure 3.18 compares SPL spectra between the reflected side and the shielded side (point A and A', $\psi = 152^o$) for the free jet case, and Figure 3.19 shows the spectra for the same locations for the flat place bounded case. Similarly, Figure 3.20 and Figure 3.21, show the spectra for the baseline and shielded case respectively, for the probe locations B and B' ($\psi = 136^o$). Generally, the acoustic spectra results show favorable agreement with the corresponding experimental data, both in terms of the predicted level of acoustics, as well as the trend of spectra.

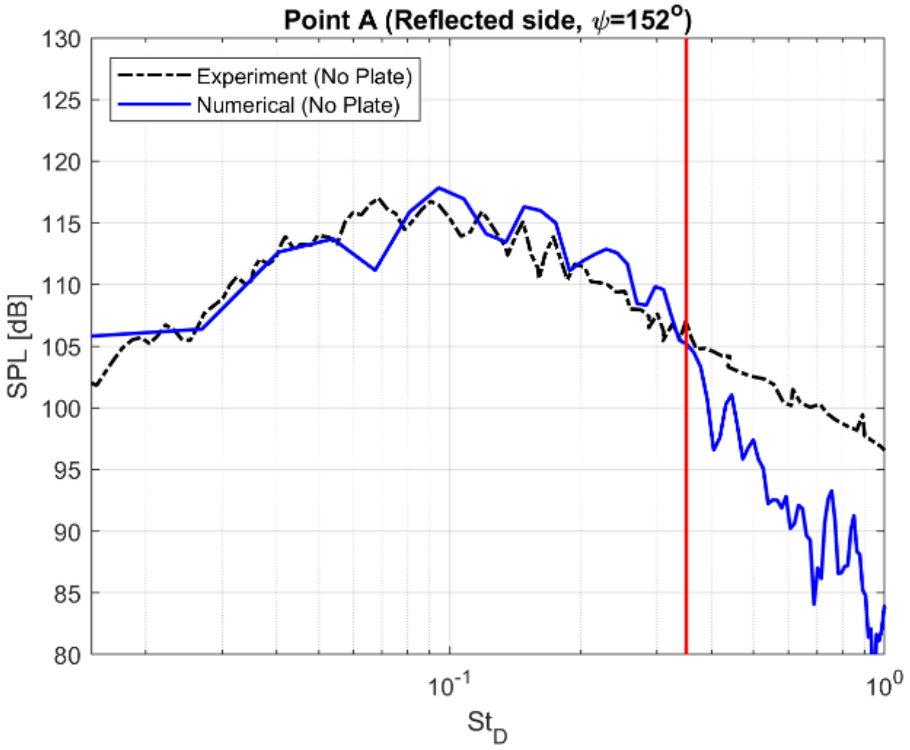

(a)

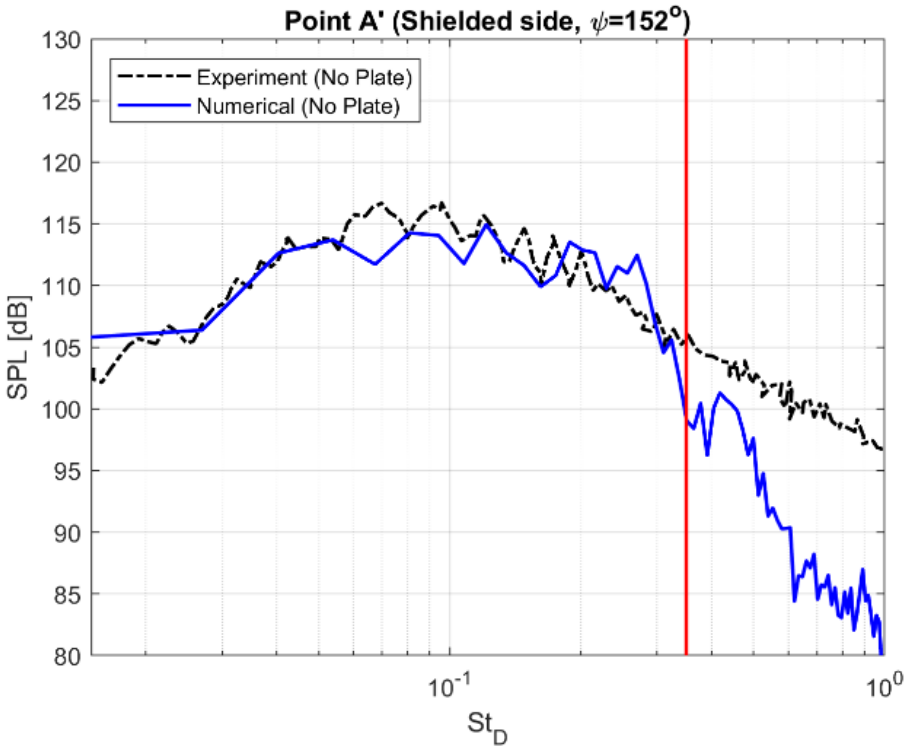

(b)

Figure 3.18 Acoustic spectra at $\psi = 152^o$ (a) reflected (A), and (b) shielded side (A'). (Isolated Jet, No Plate)

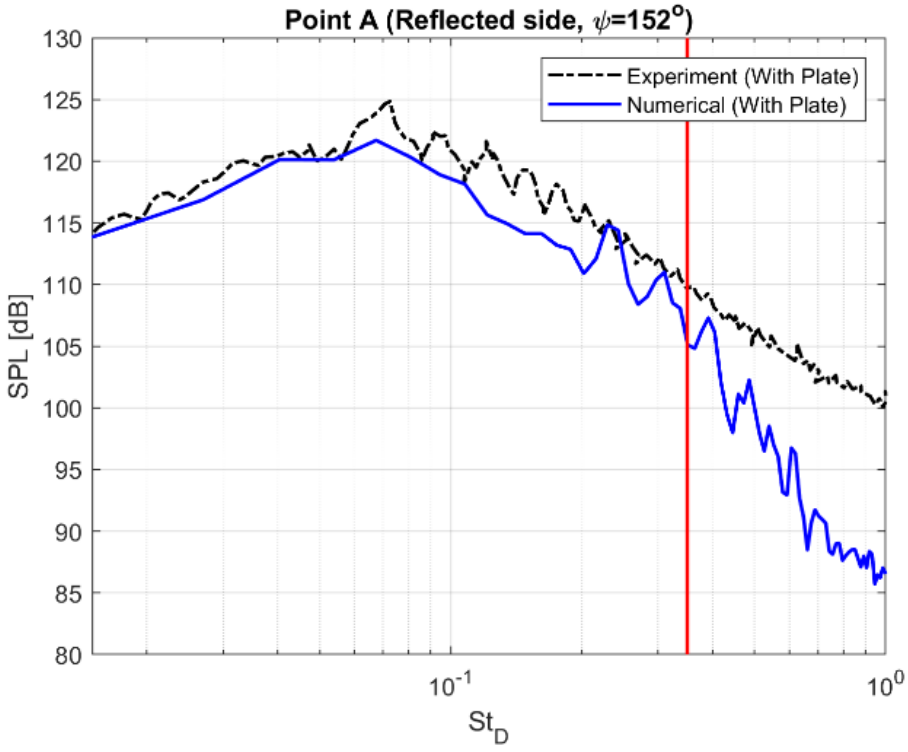

Figure 3.19 Acoustic spectra at $\psi = 152^o$ (a) reflected (A), and (b) shielded side (A'). (Jet with Flat Plate $h/D = 0$)

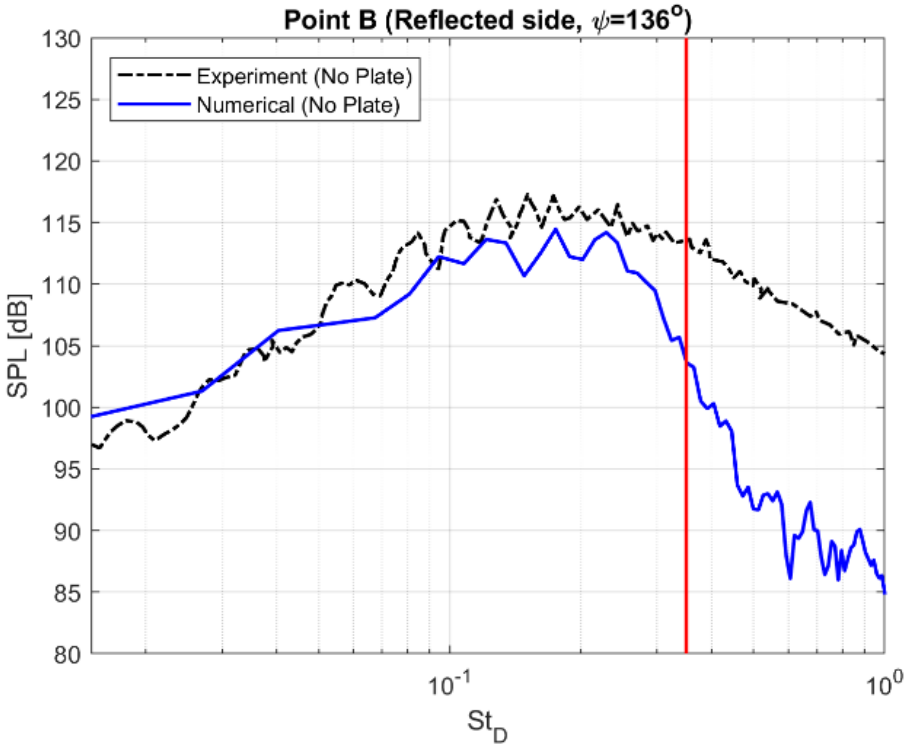

(a)

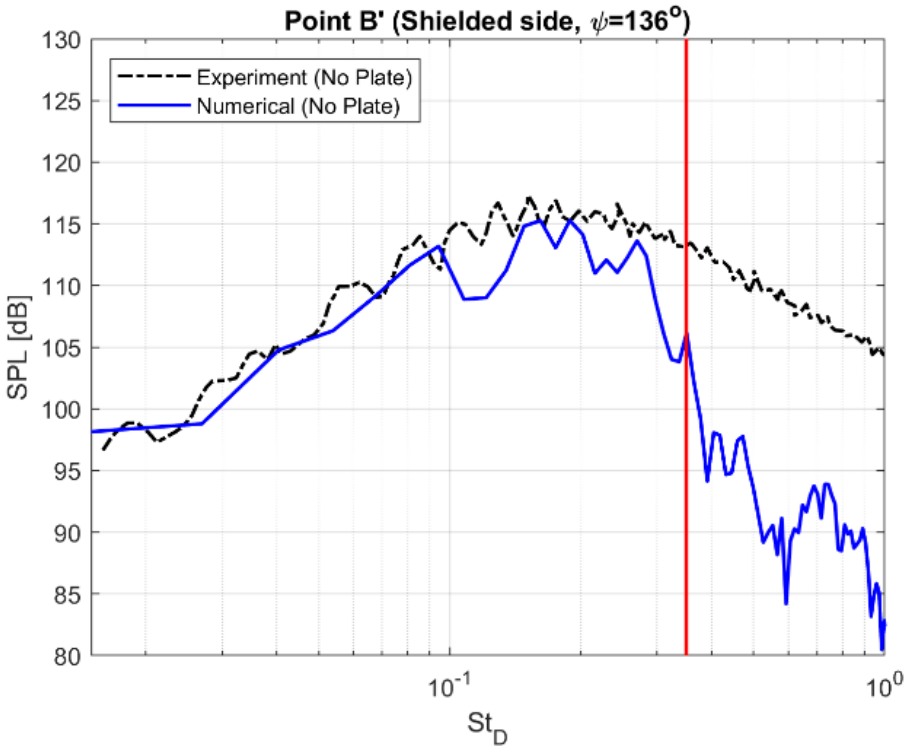

(b)

Figure 3.20 Acoustic spectra at $\psi = 136^o$ (a) reflected (B), and (b) shielded side (B'). (Isolated Jet, No Plate)

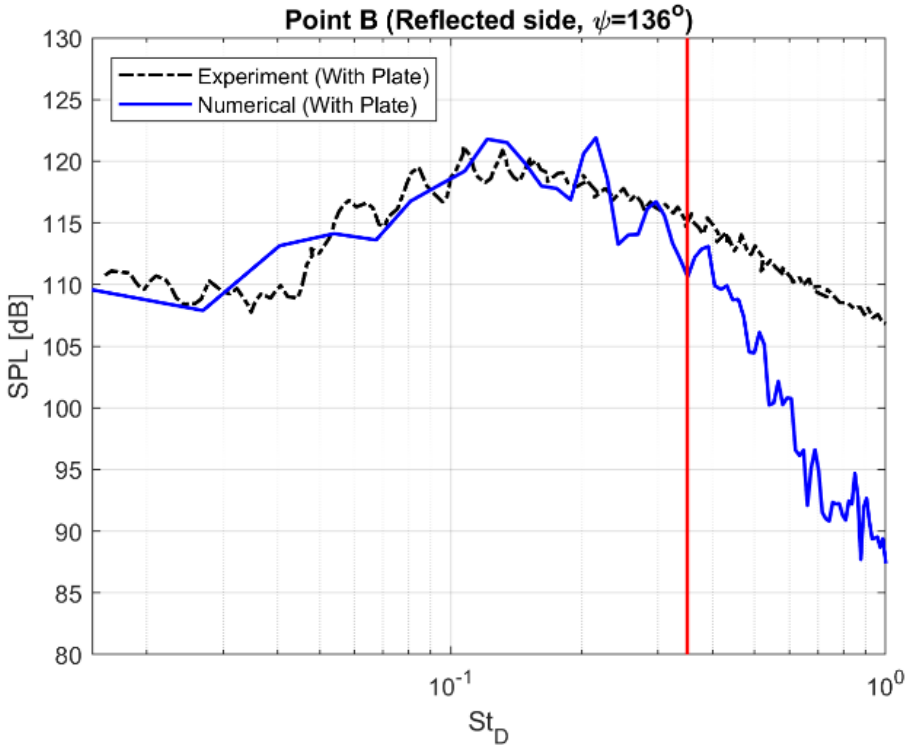

(a)

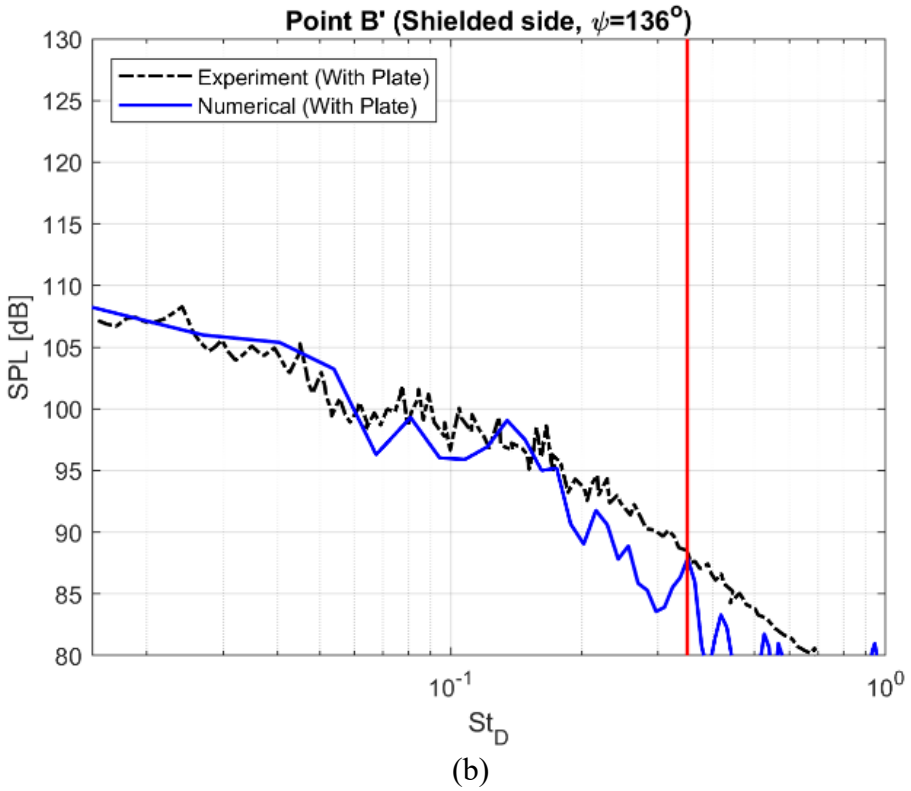

(b)

Figure 3.21 Acoustic spectra at $\psi = 136^o$ (a) reflected (B), and (b) shielded side (B'). (Jet with Flat Plate $h/D = 0$)

Comparing the SPL spectra in Figure 3.18a and Figure 3.19a, the shielded configuration increases noise levels across all frequencies, especially at the lower frequencies about 10 dB between more than the free jet. Mora et al. (2016) suggested that this low-frequency noise component is associated with the noise intensification generated by the jet-trailing edge interaction and the scrubbing noise mentioned by Bridges (2014) and Brown (2015). Similar behavior is observed when comparing Figure 3.20a and Figure 3.21a for the probe locations B and B' ($\psi = 136^o$), but in a smaller increase in SPL for the shielded configuration (about 5 dB).

As expected, drastic reduction in noise levels is observed for all plate configurations relative to the free jet. The observed reduction of noise levels is caused by the shielding effect of the plate on the noise sources from the jet plume. Such drastic reduction in the SPL is due to the dimension of the flat plate used in the numerical simulations and the experiment, and as mentioned in Clem et al. (2013), the noise reduction in the shielded direction is highly influenced by the dimensions of shielding surface.

The effect of the flat plate on the energy of the jet, discussed earlier by examining the TKE, can be observed in terms of vorticity as well. Figure 3.22 shows the dilatation field, overlaid on top of it is the vorticity, for the isolated jet and the shielded ($h/D = 0$) cases. These figures show the effect of plate on containment of energy of the jet due to the bounded nature of the physics in the shielded case ($h/D = 0$).

Also, the vorticity magnitude passing the trailing edge, suggests the introduction of new source of noise, like the airfoil trailing noise situation. This newly generated noise source is discussed in detail in the next section. Moreover, the waves are intensified on the upper side by the shielding plate. Plus, the acoustic shielding effect of the plate is

clearly shown in these figures. This figure qualitative exhibits the acoustic shielding noise reduction and the intensification of the reflected side waves.

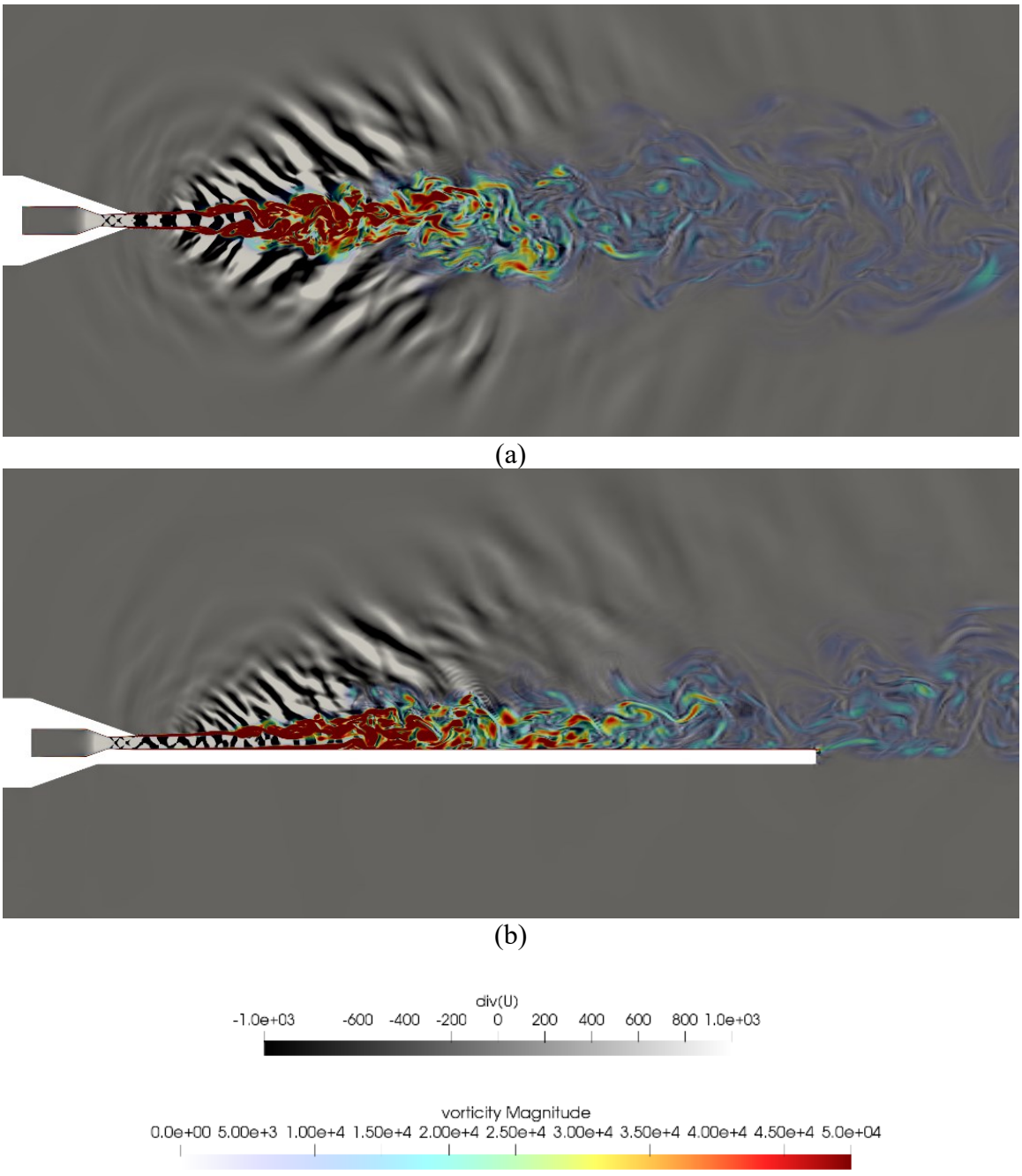

Figure 3.22 Instantaneous contours of dilatation and vorticity. (a) Isolated Jet. (b) Jet with flat plate ($h/D = 0$)

Both shielding effect and the trailing edge vortex, can be observed by visualizing the fluctuating component of pressure in Figure 3.23. The fluctuating component of the pressure is obtained by subtracting the time-averaged pressure from instantaneous pressure ($p' = p - \bar{p}$). This parameter shows the flow field pressure fluctuations in the shear layer, as well as the acoustic waves in the nearfield region. The trailing edge vortex, shown inside the red circle, acts as a dipole-like source leaving the trailing edge of the plate. In addition, the intensity of pressure fluctuations is magnified on top of the plate.

The recent theoretical work by Goldstein et al. (2019) employs rapid distortion theory and exhibits the asymmetry of the shear layer when it exhausts over a flat plate. To elaborate the mechanism that causes an increase of SPL in the shielded direction due to the flat plate, the Root Mean Square (RMS) of the fluctuation component of the pressure ($p' = p - \bar{p}$) is illustrated at axial cutting plane locations of $x/D = 5, 18$, and 30 in Figure 3.24. Comparing the evolution of pressure fluctuations along the jet axis for the free jet (a) with the shielded case (b), it can be observed that the flat plate maintains the energy of the jet much further from the jet exit. This was also shown earlier in TKE contours. The bounded nature of the shielding wall avoids the dissipation of the turbulence fluctuations in regions closer to the jet exit. The energized flow leaving the flat plate behaves as the vortex leaving the trailing edge of the flat plate. The trailing edge vortex has a dipole-like structure that acts as an additional source of noise that increases the SPL in the shielded direction.

In summary, (1) the intensification of the fluctuations on top of the plate due to the modifications of the flow structure, along with (2) the introduction the trailing edge vortex noise source, explain the increase of SPL on the reflected side.

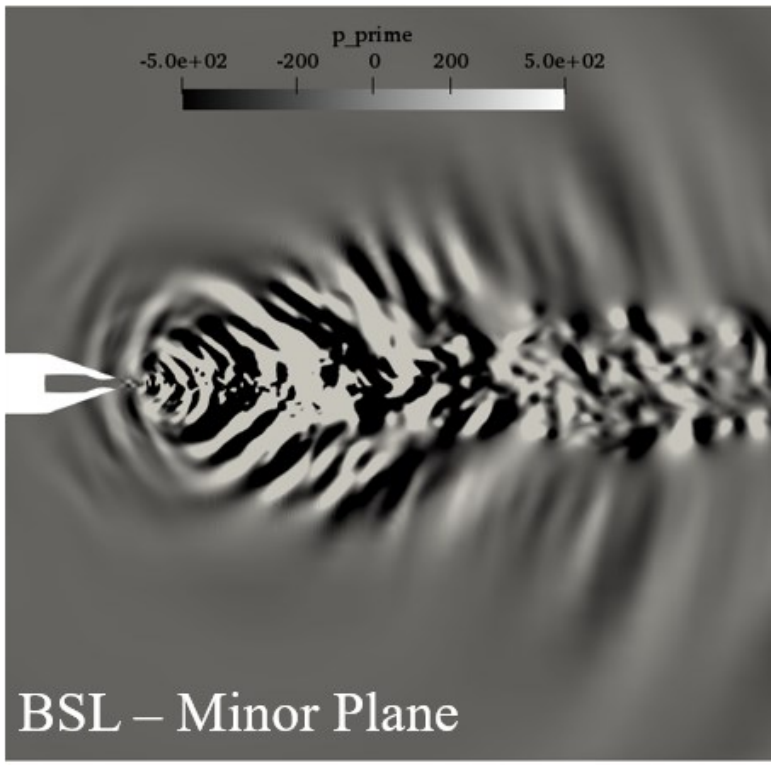

(a)

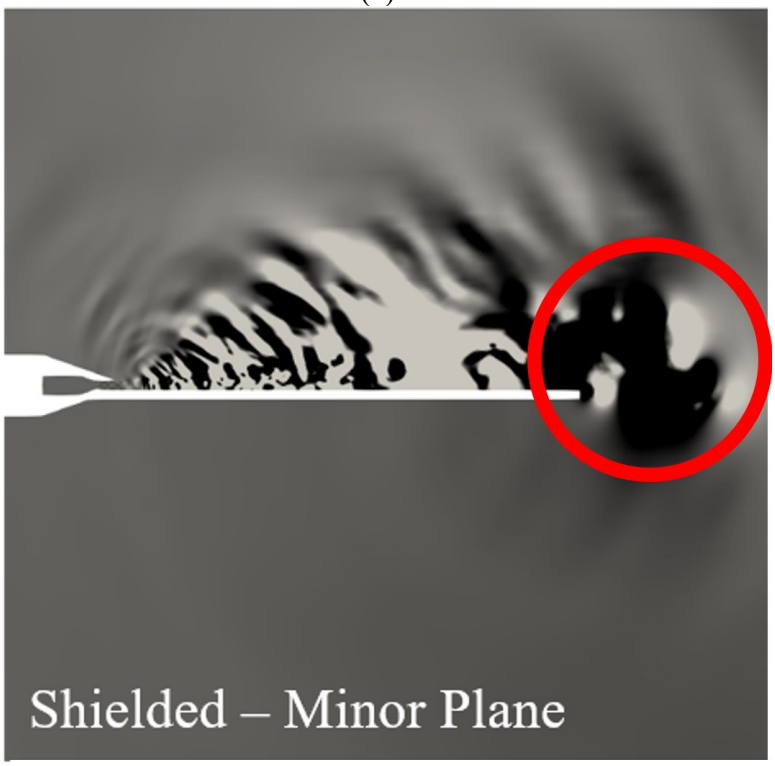

(b)

Figure 3.23 Instantaneous acoustic pressure, for (a) Isolated Jet, and (b) Jet with flat plate ($h/D = 0$).

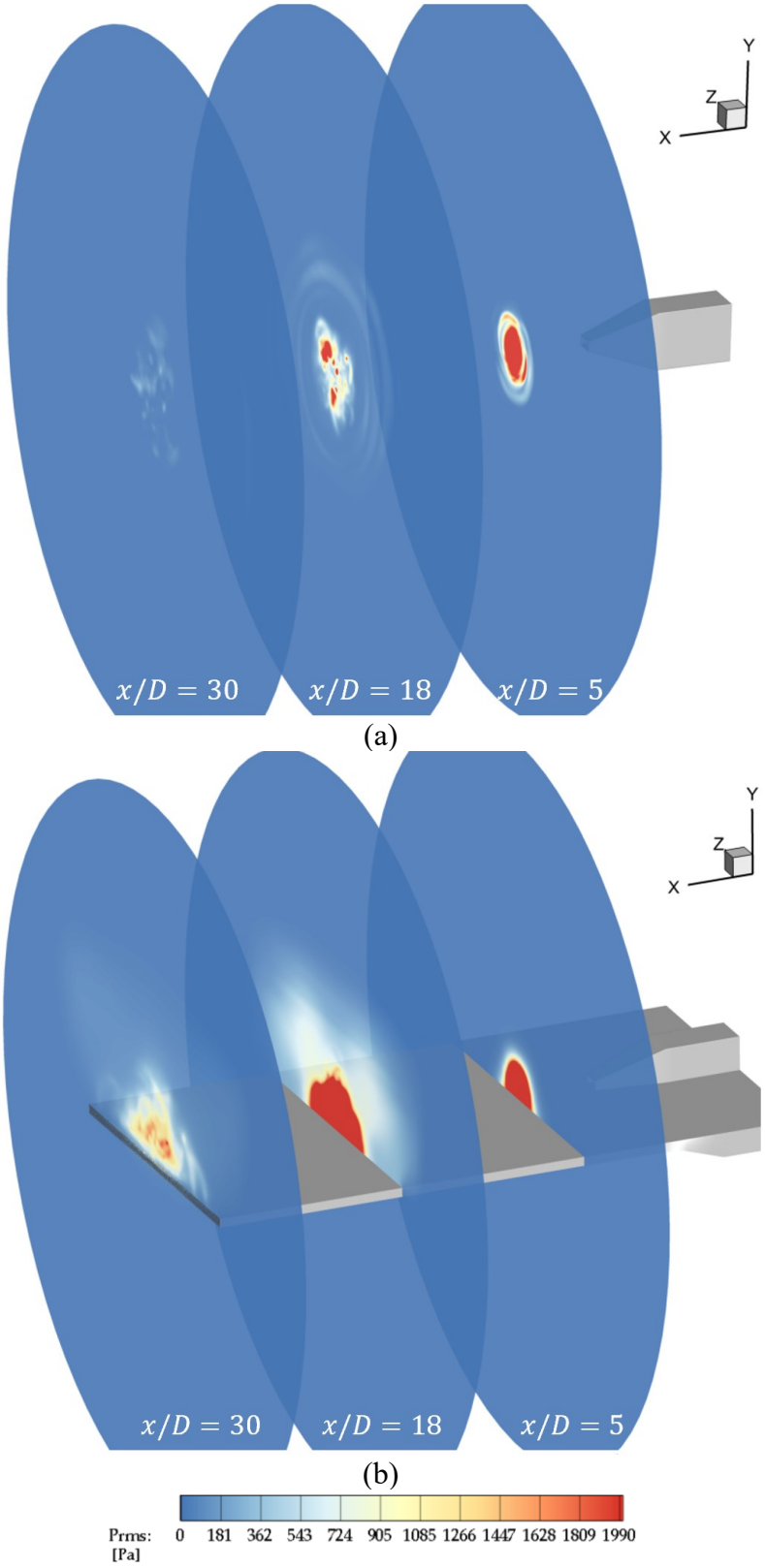

Figure 3.24 Evolution of the fluctuating pressure RMS along jet axis. (a) Isolated Jet. (b) Jet with flat plate ($h/D = 0$).

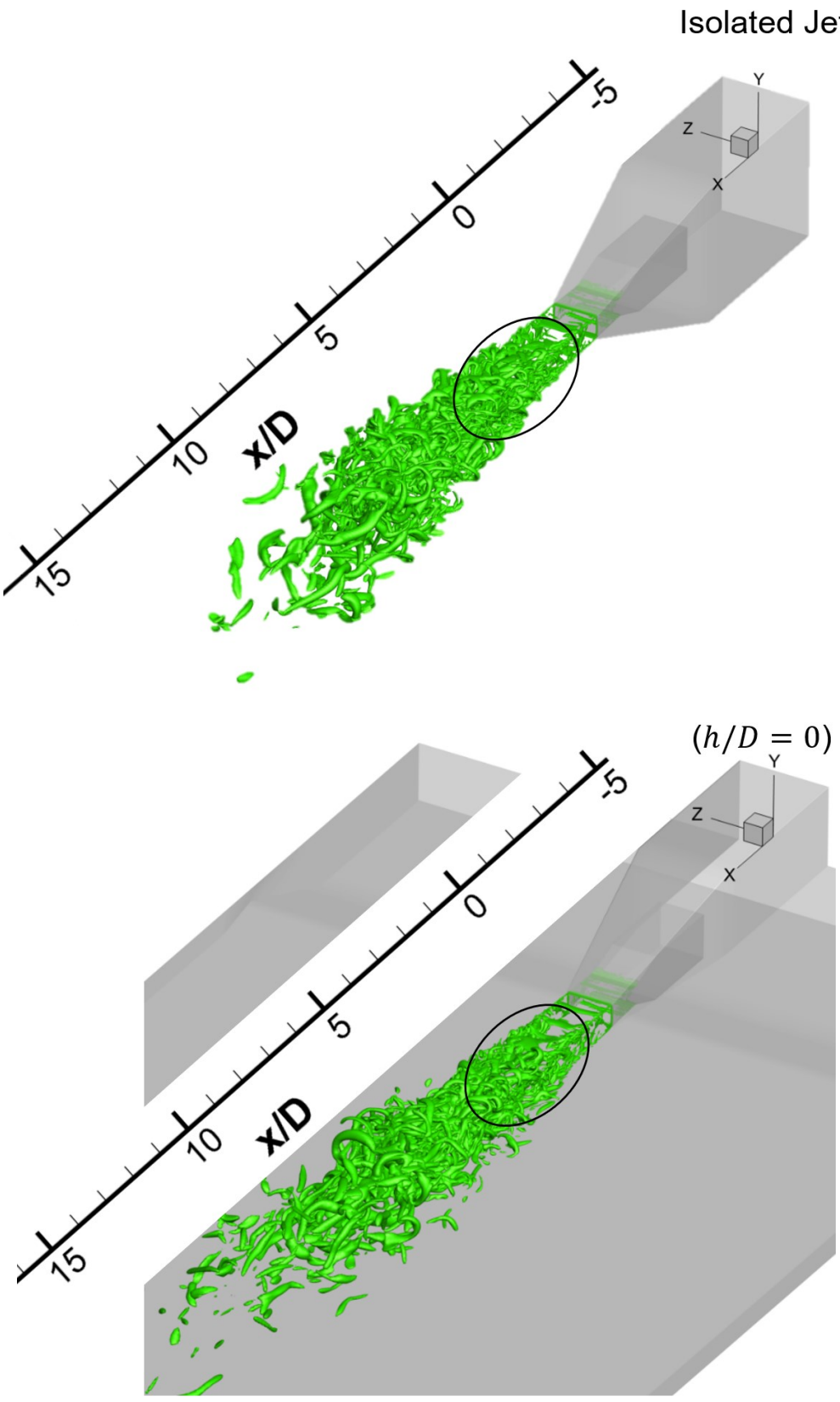

Figure 3.25 Iso-surfaces of Q-criterion $\left(1/2(U_j^2/d^2)\right)$.

Since the previous investigations illustrated effect of the flat plate on flow perturbations, and the SPL, it can be assumed that the flat plate affects the large-scale structures of the turbulence. The Q-criterion is defined as a function of rate-of-strain tensor, S_{ij}, and vorticity tensor, Ω_{ij} (Hunt et al., 1988).

In Figure 3.25, the iso-surfaces of the Q-criterion for $Q = 1/2(U_j^2/d^2)$ are shown for the isolated jet and water injection case, respectively. The value of Q is chosen to highlight the larger turbulent structures. By comparing these two figures, the effect of flat plate on the large-scale turbulent structures is illustrated. Specifically, in the turbulent region of the core of the jet ($0.5 < x/D < 4.5$), the spreading of the jet is affected by the flat plate. In this region less large concentration of eddies are observed in the wall jet flow case. This suggests that the turbulent structure is pushed forward, confirming the elongation of the turbulent structure, as previously observed by analyzing TKE. The increased turbulence in the further region ($6 < x/D < 12$), confirms the origin of increased fluctuations observed in the pressure fluctuation contours. It could be conjectured that this effect is one of the mechanisms responsible for the increase of SPL on the reflected side for the shielded ($h/D = 0$) case, along with the previously discussed trailing edge noise source.

3.4. Results for Flat Plate Reflection Case ($h/D = 3$)

To test the numerical accuracy for capturing the reflected acoustic wave in the case where the wall is at a distance from the nozzle exit, a benchmark test is carried out, and the results are reported in APPENDIX C – Verification Benchmark: Acoustic Reflection from Wall.

3.4.1. The Flow Field

Since the capability of the numerical approach capturing the reflected waves is established, the reflection case results are discussed next. The instantaneous Mach number and pressure fluctuation contours are provided here.

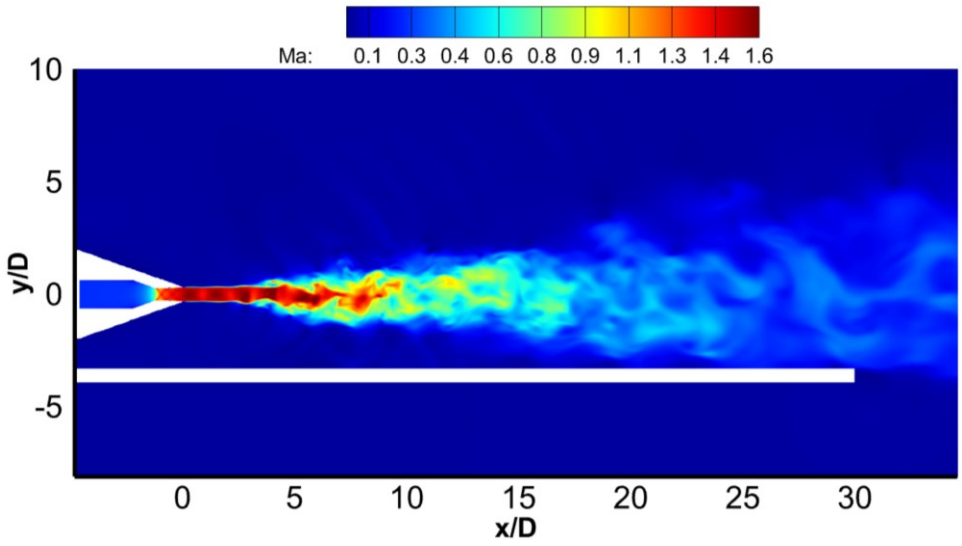

Figure 3.26 Instantaneous Mach number for the reflection case ($h/D = 3$) case.

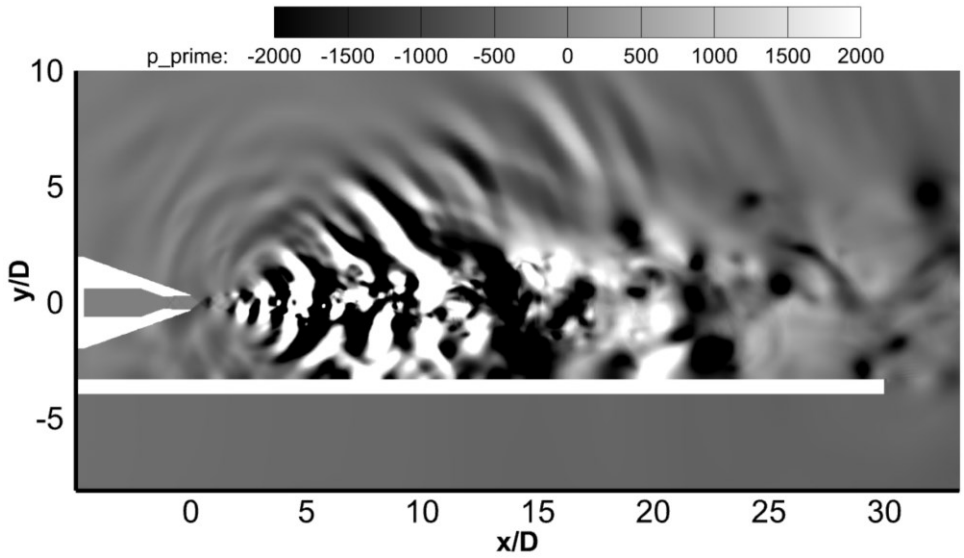

Figure 3.27 Instantaneous acoustic pressure for the reflection case ($h/D = 3$) case.

Following up on the isolated jet and wall jet cases mentioned earlier, the main objective is to investigate the effect of distance of the flat plate from the jet axis on the flow field and acoustics of the jet and compare with the baseline and wall-jet cases.

Figure 3.27 illustrates the Mach number contour for the case where plate is placed at $(h/d = 3)$. Unlike the wall jet flow case $(h/d = 0)$, the bulk of flow field is not bounded by the plate, and the jet spreads out and the jet flow barely starts sweeping on the plate after $x/D = 30$. The fluctuating component of pressure, shown in Figure 3.27 exhibits the acoustic waves reflecting from the flat plate. The dominant downstream travelling waves hit the plate at around $x/D = 5$ on the flat plate and reflect into the jet flow.

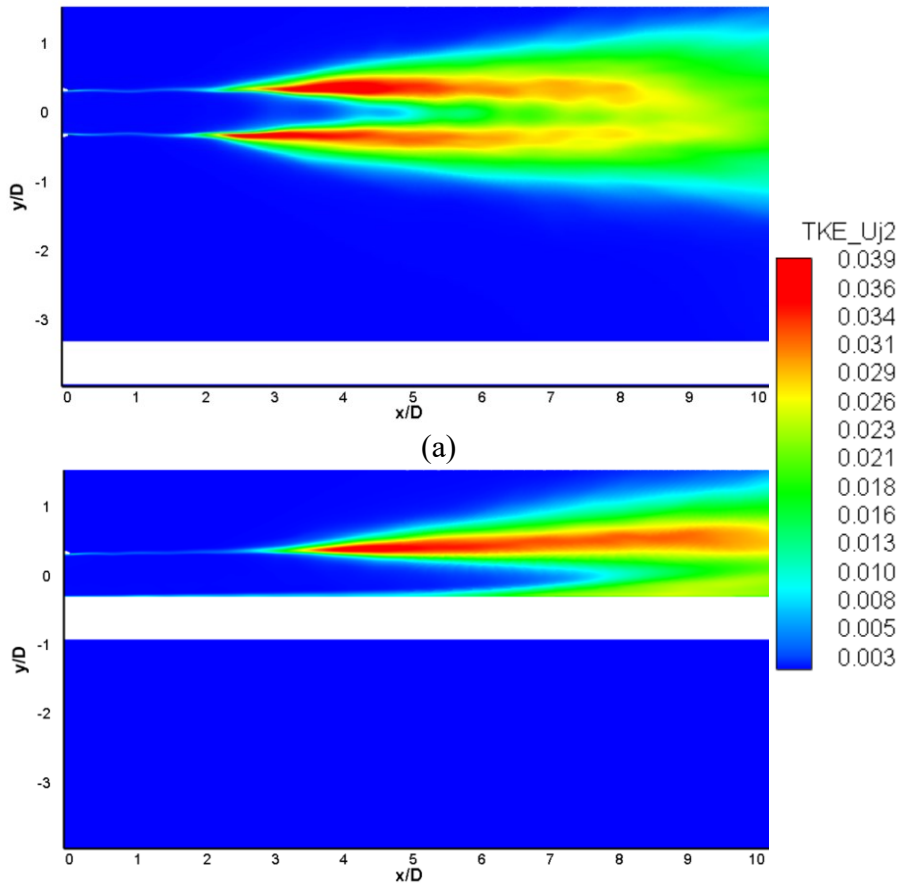

Figure 3.28 TKE normalized by jet velocity squared. (a) $(h/D = 3)$, (b) $(h/D = 0)$.

Such reflections have an impact on the turbulence structure of the jet. The effect of the location of flat plate on TKE is shown in Figure 3.28. Since the jet is not bounded by the flat plate in the ($h/D = 3$) case, the drastic shear layer extension does not occur as discussed earlier for the ($h/D = 0$) case. However, the reflections from the plate interact with the jet plume and energize the shear layer on the plate side. Hence, causing the asymmetry in the TKE structure for the ($h/D = 3$) case when compared to the isolated jet case seen in Figure 3.13.

3.4.2. Acoustic Spectra

Figure 3.29 compares SPL spectra between the reflected side and the shielded side (point A and A', $\psi = 152^o$) for the ($h/D = 3$) case, and Figure 3.30 shows the spectra for the same case for the probe locations B and B' ($\psi = 136^o$).As, seen earlier, the acoustic spectra results show favorable agreement with the corresponding experimental data, both in terms of the predicted level of acoustics, as well as the trend of spectra.

The acoustic shielding effect is visible here too. And the increase in noise levels on the reflection side, is not as drastic as the ($h/D = 0$) case. Most of the reflected noise increase is observed in just the lower frequency, when comparing Figure 3.29a and Figure 3.30a with Figure 3.18a and Figure 3.20a respectively. Whereas, the noise increase was observed for the entire range of spectral frequencies for the ($h/D = 0$). It can be concluded that, in the ($h/D = 3$) case, the noise increase in the reflected side is mainly due to interaction of the reflected waves with the jet flow and energizing the noise sources in the shear layer. On the other hand, the wall-jet case, not only has the same mechanism involved, it also introduces the trailing edge noise source as an additional source of noise that increases the reflected side noise more drastically.

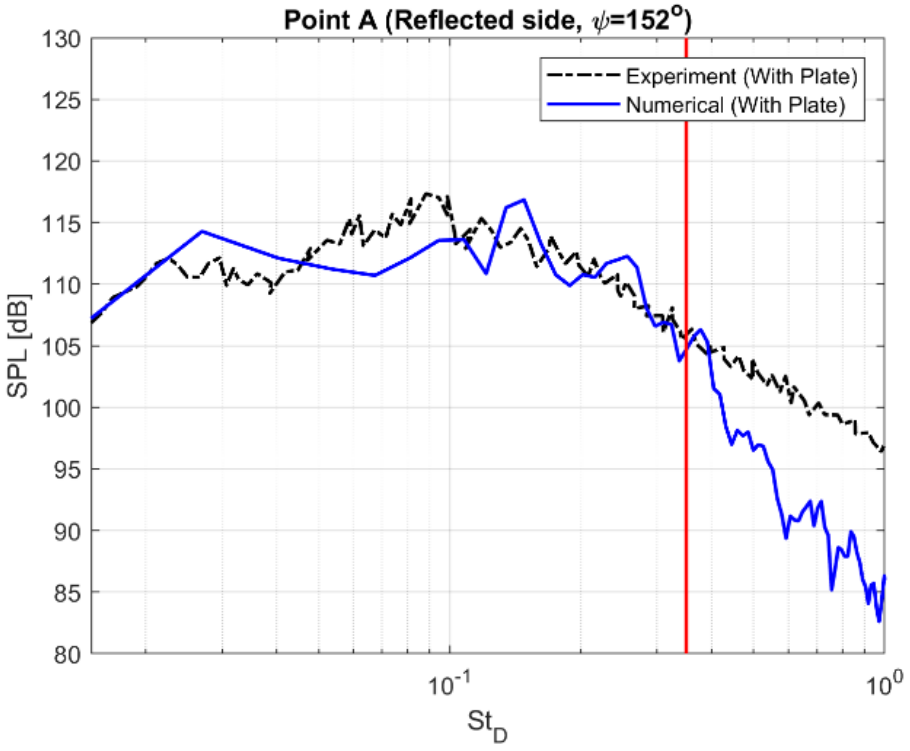

(a)

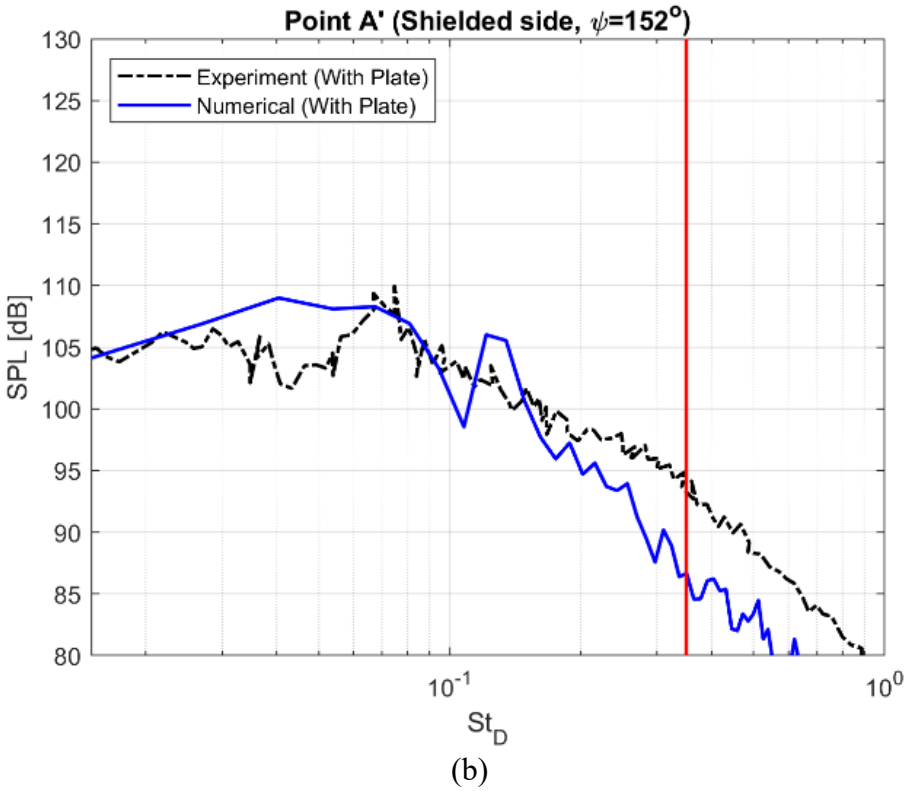

(b)

Figure 3.29 Acoustic spectra at $\psi = 152^o$ (a) reflected (A), and (b) shielded side (A'). (Jet with Flat Plate $h/D = 3$)

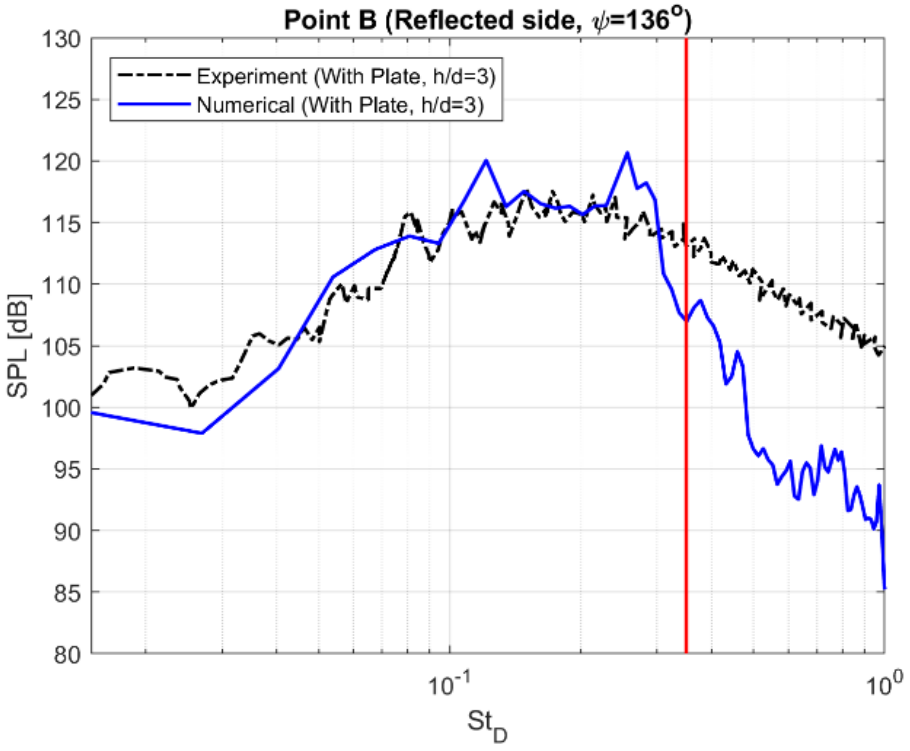

(a)

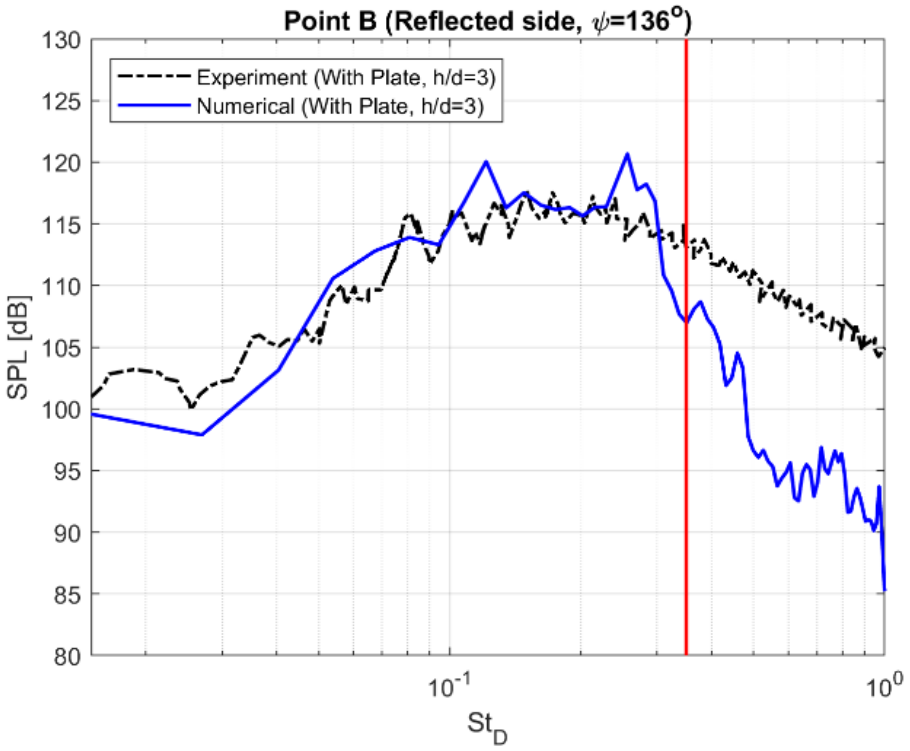

(b)

Figure 3.30 Acoustic spectra at $\psi = 136^o$ (a) reflected (B), and (b) shielded side (B'). (Jet with Flat Plate $h/D = 3$)

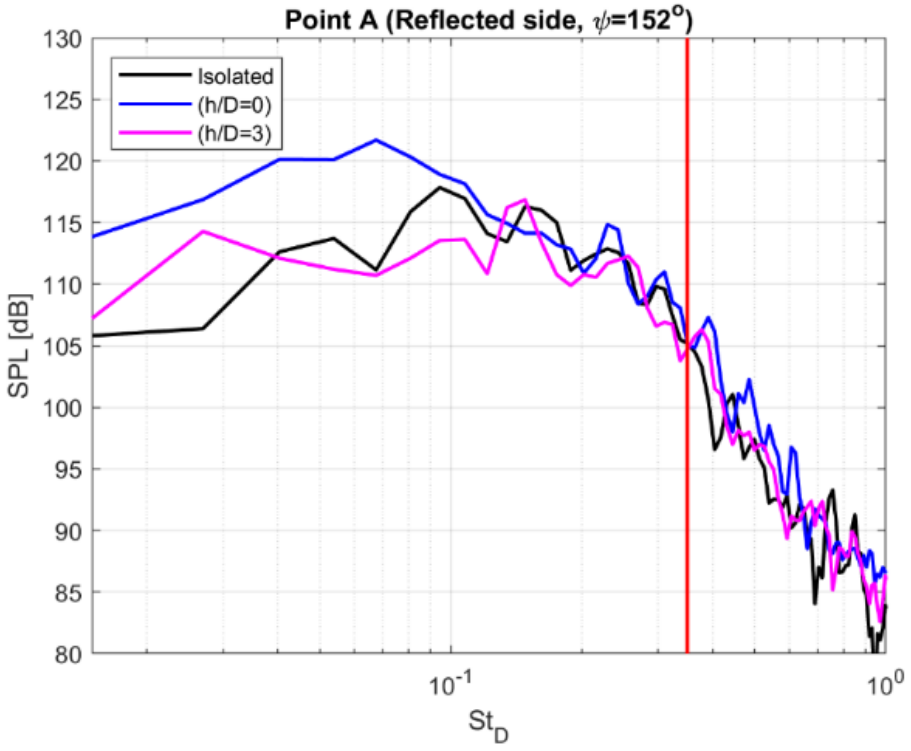

Figure 3.31 Acoustic spectra at $\psi = 152^o$ (a) reflected (A), and (b) shielded side (A'). (Isolated Jet, and Jet with Flat Plate $h/D = 0$, and 3)

The acoustic data from numerical investigations suggest that, although the flat plate design provides the reliable acoustic shielding effect in the shielded direction. However, the noise level increase in the reflected side, makes these approaches less attractive to be implemented as a fixed design for a practical engine top configuration. Hence, modifications in the shielding plate profile is suggested here to improve the noise reduction of the shielding wall in both directions. Since all the spectra agree well with the experiment, data from all cases at probe point A and A' are compared to be able to isolate and focus on the effect of (h/D). On the reflected side, the reflection-only case (h/D=3), still shows increase in noise but not as drastic as the wall-jet case (h/D=0). Although both shielded cases show effective noise reduction on the shielding side, but, both plate positions have the potential to be optimized and reduce the noise more effectively, especially for the low-to-mid frequency range ($0 < St < 0.2$). In hindsight, the reflected side noise is of importance for takeoff and fly-over phases of flight. While, the shielded side, is to be considered as the main objective for noise reduction, especially during cruise flight.

3.5. Wavy Wall Cases

The main objective is to introduce disturbances to reduce the noise. To do this, the (h/D) parameter needs to be limited to 0 or 3 for two reasons: (1) To be able to distinguish the effect of flow field vs. acoustic field. (2) To produce enough data to compare with corresponding experimental (and numerical) data for flat plate cases. Here, the theoretical background of the design of the wavy wall profile is investigated. The groundwork of estimation of several design elements are provided. Finally, numerical simulations are carried out to analysis the effectiveness of the idea of wavy wall profile.

3.5.1. Theoretical Estimation of Wall Profile Design Elements ($h/D = 3$)

The basis of the design of the wavy wall stems from the fundamental experimental and analytical investigation in literature, suggesting that introduction of disturbance in flow or acoustic field could result in ultimately attenuating the jet noise. Arbey and Ffowcs Williams (1984), conducted experiments on a circular jet that was simultaneously excited by acoustic tones. Their observations showed that, by varying the phase between two signals at harmonically related frequencies, noise control can be achieved. In addition, Mankbadi (1985b) investigated the spatial interactions between a fundamental instability wave and its harmonics and subharmonics in a turbulent round jet. The vortex pairing was identified when the subharmonic absorbs energy from the fundamental and from the mean flow. Suggesting that introduction of subharmonics can reduce the fundamental waves in the jet flow. The objective is to introduce a wavy profile on the flat plate, such that it can introduce the desired disturbances that could potentially mitigate the noise. Such wavy wall profile may have several parameters such as: amplitude, wavelength, and phase shift. These specifications are carefully described and discussed here.

To identify the dominant the frequency and wavelength of the acoustic waves, the acoustic waves along the two main radiation angles of $\psi = 136^o$, and 152^o measured from upstream of the jet axis are investigated. These radiation paths along with the horizontal line denoting the shielding plate are illustrated in Figure 3.32a on the acoustic pressure field. The acoustic pressure wave signal along the main radiation angles of $\psi = 136^o$, and 152^o, show that the waves have wavelengths of approximately around $4.5D - 5D$. This is consistent with the peak frequency observed previously in acoustic spectra (Figure 3.18 and Figure 3.20).

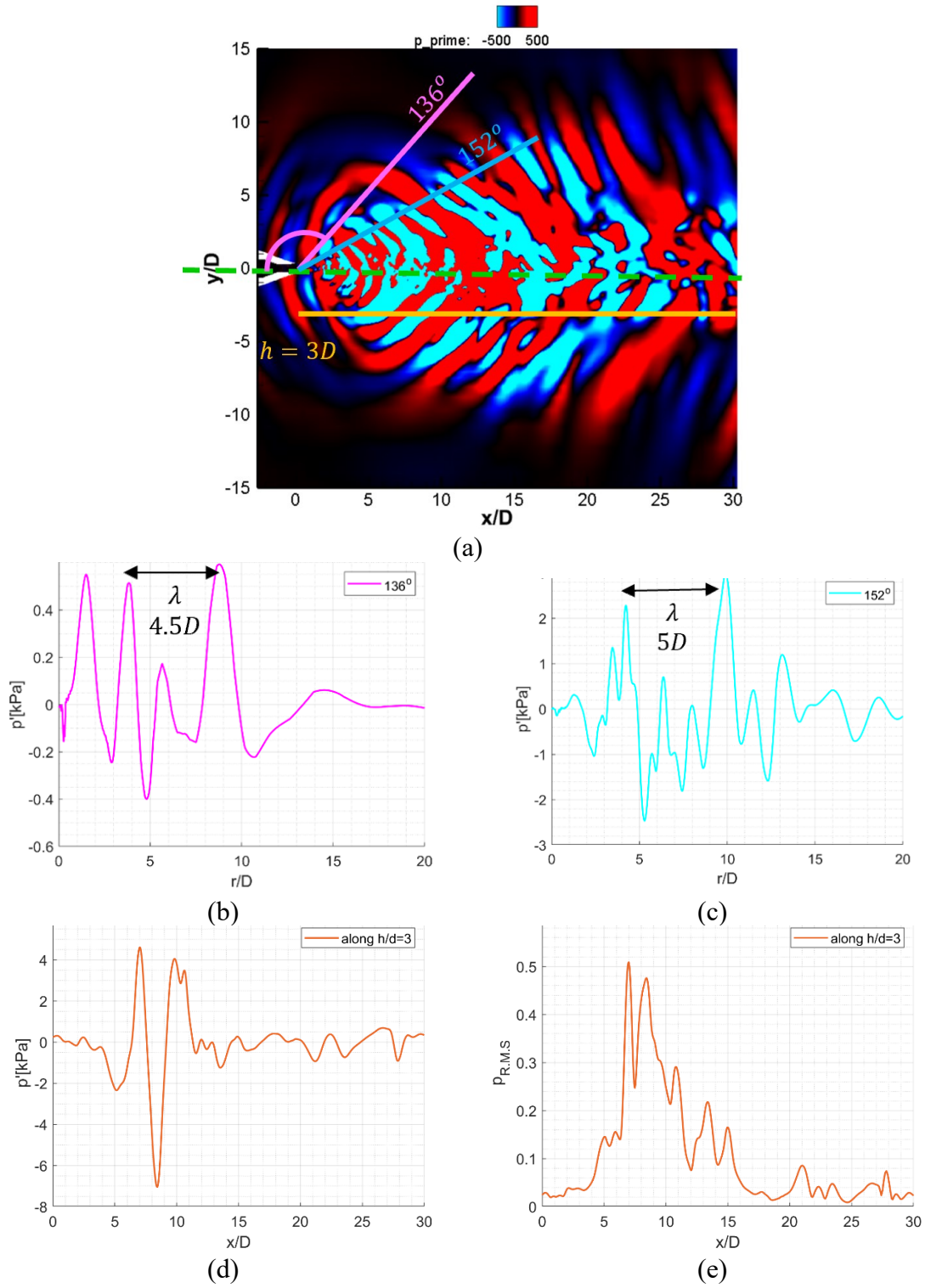

Figure 3.32 (a) Acoustic pressure field, and the measure line illustrations. The acoustic signal along (b) $\psi = 136^o$ line, (b) ψ=152^o line, (d) $x = 3D$ line. (e) RMS of pressure fluctuations along $x = 3D$ line.

The spectra shows the peak frequency occurring at $St = 0.12{\sim}0.13$, and since Strouhal number is defined as $St = fD_e/U_j$, for a wavelength defined as $\lambda = c/f$. One can easily calculate the corresponding wavelength as:

$$\lambda = \left[\frac{1}{M\ St}\right] D \tag{39}$$

Here, M is the isentropic jet exhaust Mach number. For the given peak frequencies, the wavelength would have a value of around $4.5\ D - 5\ D$. This calculation is consistent with the wavelengths observed in Figure 3.32b and Figure 3.32c. Additionally, looking at the straight line at $h = 3D$, where the shielding plate would possibly be located, similar wavelength is observed to pass this line, as illustrated in Figure 3.32d. Moreover, The RMS of pressure fluctuations shown in d suggests that the region of impact is somewhere around $x/D = 5$.

Knowing the location of impact of acoustic waves, initially a simple sinusoidal profile is suggested for the shielding wall such as:

$$y_{wall} = A_w \sin[k\left(\frac{x}{D}\right) - \phi] \tag{40}$$

where, $k = 2\ \pi/\lambda$ is the wave number, and A is the amplitude that is initially assumed to be $D/2$. This profile ensures that the waves passing the $h = 3D$ line have a π phase shift form the impact region $x/D = 5$, so that the waves would linearly cancel each other. Such wall profile is depicted in Figure 3.33.

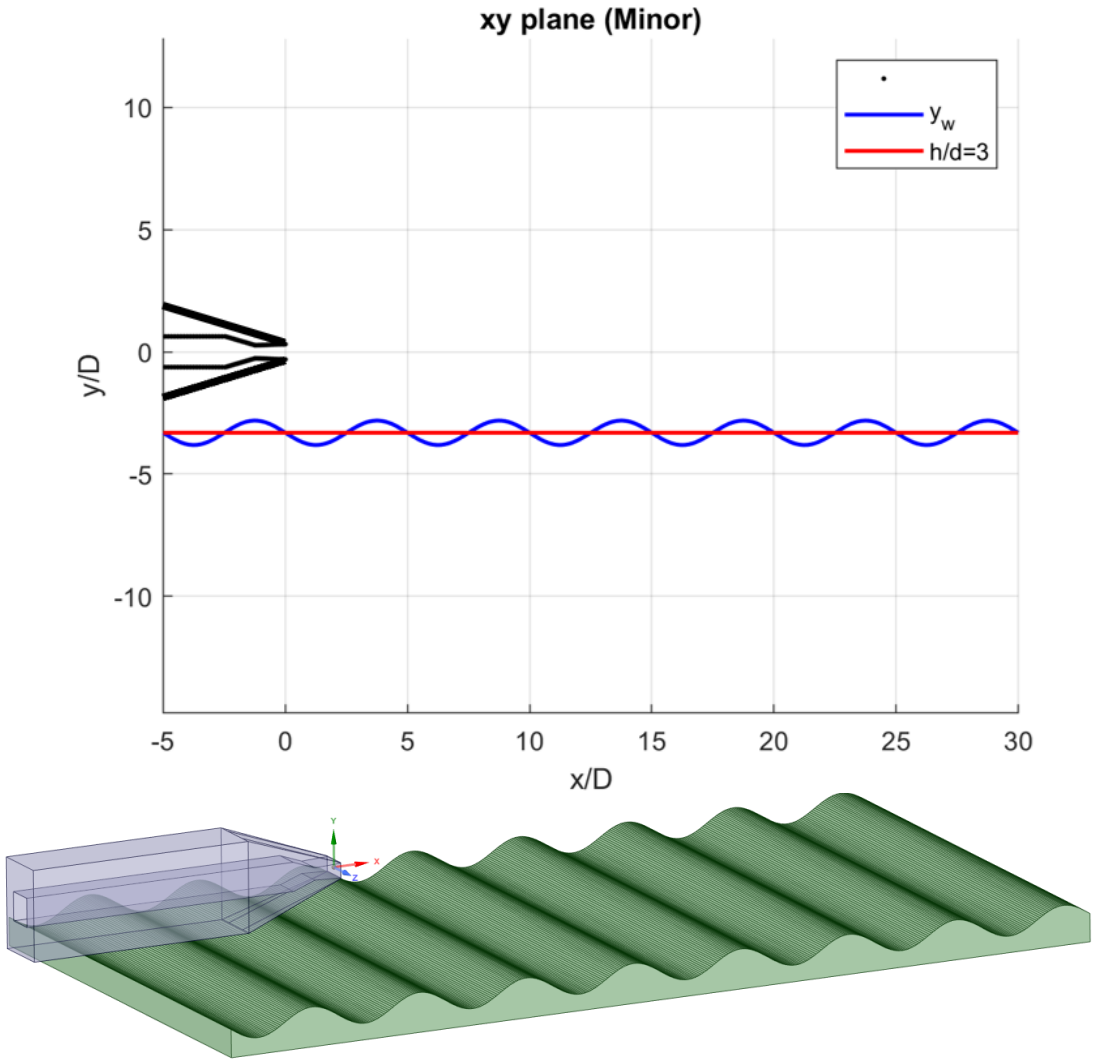

Figure 3.33 Wavy wall profile at ($h/D = 3$)

In addition to the estimation of wavelength, there needs to be an educated guess mad on the value of the amplitude. In the experimental studies carried out by Arbey and Ffowcs Williams (1984), the control signal was provided by a set of loudspeakers and providing a controllable signal. It was shown in these studies that jet noise suppression can kill the noise by adding a harmonic of the noise. These loudspeakers introduced tones as: $A_1 \sin(2\pi f_e) + A_2 \sin(2\pi\, 2f_e + \phi)$, with $\frac{A_2}{A_1} \sim 0.5$, and $A_1 \sim 2\%$ of the amplitude of

the jet exit velocity. In the combination signals, f_e is close to the dominant fundamental frequency, and the phase lag was kept as $\phi = \pi$.

Following a similar analogy, the amplitude of the wavy wall, that could provide the similar attribute by modifying the reflected waves estimated in this work.

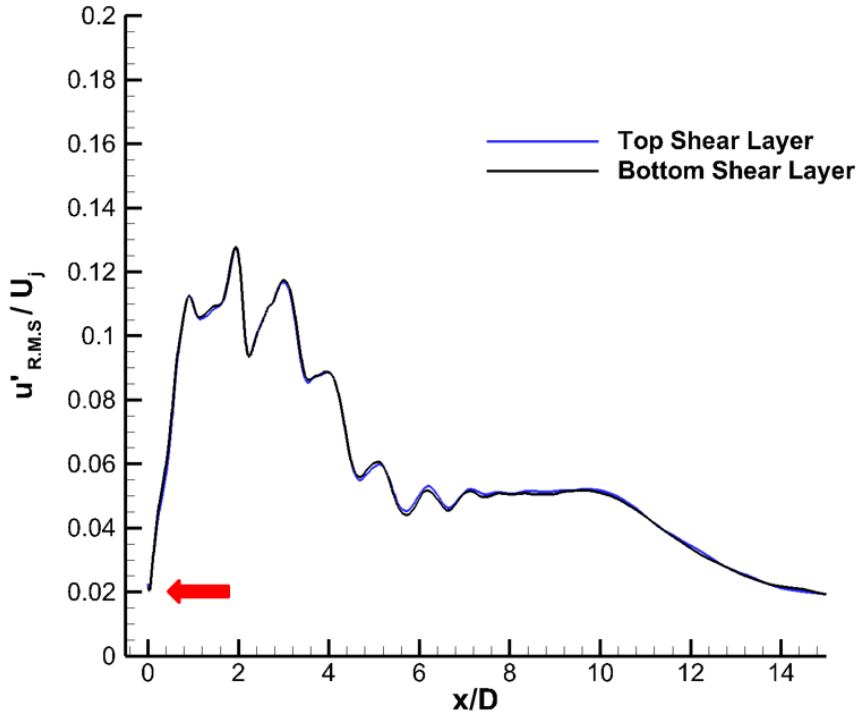

Figure 3.34 RMS of velocity fluctuation along the shear layer (Isolated Jet).

The velocity fluctuations along the shear layer of the isolated jet, normalized by the isentropic jet exit velocity, is illustrated in Figure 3.34. The velocity RMS shows the magnitude of fluctuations near the nozzle exit is ~2% of the jet exhaust velocity, shown by the red arrow in the figure. In addition, the magnitude of the fluctuations in the turbulent dissipation, or near the main location of impact as discussed earlier is ~5% of the jet exit velocity. Going back to the analogy introduced by Arbey and Ffowcs

Williams (1984), the suggested amplitude of the wave introduced must ~0.5 of the fundamental wave. Since $A_1 = 0.02\ U_j$, then A_2 from the reflection in this case, should be of the order of 1-5 %. On the Other hand, targeting $x/d = 3$ structure, the thickness of the momentum thickness is about $0.1\ D$, it can be presumed choosing amplitude of the wall to be ~$0.05D$ would be a relevant estimation for the wavy wall cases at $h/D = 3$.

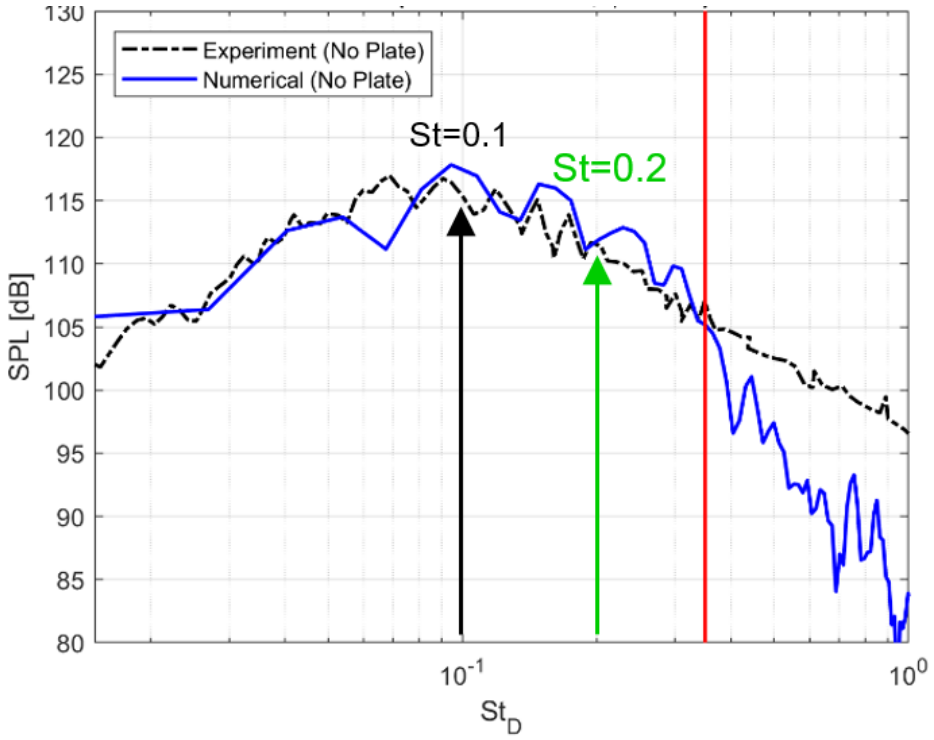

Figure 3.35 Fundamental frequency of the waves in the maximum radiation angle (Isolated Jet).

On the other hand, both Arbey and Ffowcs Williams (1984), and Mankbadi (1985b), concluded that introduction of harmonics or subharmonics can reduce the fundamental more effectively than the fundamental wave itself in certain conditions. Knowing that the fundamental wave of the isolated jet in the current study is around $St = 0.1$, a harmonic can be introduced by setting the corresponding wavy wall frequency as $St = 0.2$, which

corresponds to the wavelength of $\lambda = 2.5D$. Figure 3.35 illustrates the Fundamental frequency of the waves in the maximum radiation angle and its first harmonic for the isolated jet.

Based on the explanations described in this section, three cases of the wavy wall profile are defined. These wavy wall cases, and their corresponding parameters are listed in Table *3.2*. It should be noted that π phase shift from the impact region ($x/D = 5$), is considered in the wavy wall profile of all three cases mentioned here.

Table 3.2

Parameters of the wavy wall cases ($h/D = 3$).

	$\boldsymbol{h/D}$	$\boldsymbol{\lambda}$	$\boldsymbol{A_w}$
Case 1	3	$5D$	$0.5D$
Case 2	3	$5D$	$0.05D$
Case 3	3	$2.5D$	$0.05D$

3.5.2. Flow and Acoustic Field Results (Wavy Wall at $h/D = 3$)

The numerical simulations are carried out for the wavy wall cases, and the results are compared with the corresponding flat plate results, to provide comparison on the effect of the wavy profile on the flow and acoustic field. Here, the instantaneous acoustic pressure, SPL, and TKE contours are illustrated for the wavy wall compared with the flat plate case at $h/D = 3$.

The instantaneous fluctuating component of pressure is illustrated in Figure 3.36 for all wavy wall cases, and the flat plate ($h/D = 3$), to compare the acoustic waves, and their reflections from the different wall profiles. This figure shows that case 1, significantly amplifies the reflected waves. In fact, due to the high amplitude of the wall,

the reflections, appear to intensify the pressure fluctuations in the turbulent core of the jet as well. However, Case 2 and 3 that have smaller amplitudes, appear to somewhat control the reflections, and provide acoustic attenuation.

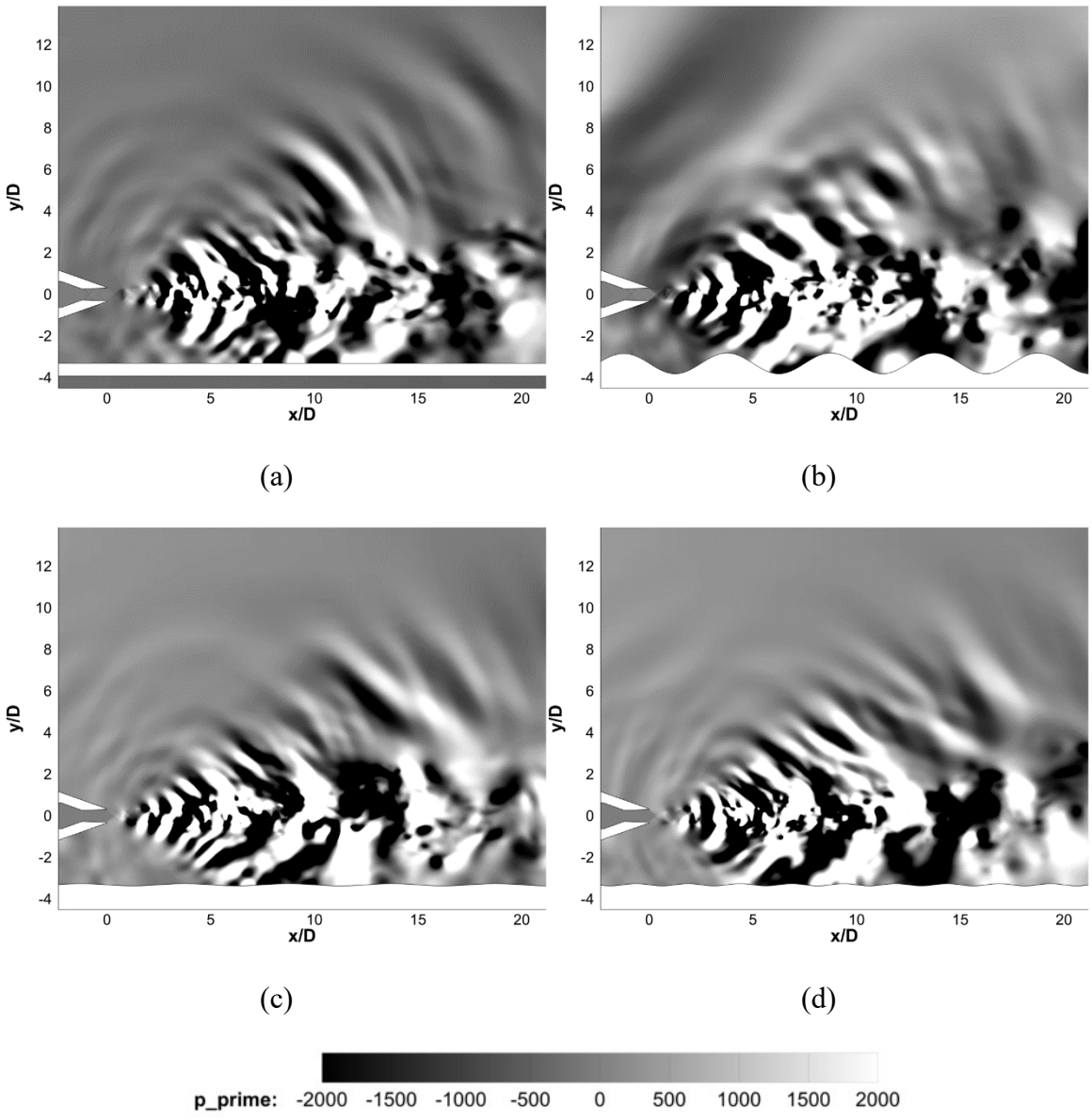

Figure 3.36 Instantaneous acoustic pressure. (a) Flat Plate ($h/D = 3$), (b) Case 1, (c) Case 2, (d) Case 3.

More specifically, the fundamental downstream travelling wave, shown in the $x/D = 15$ and $y/D = 6$ region of all contours, seem to have much smaller magnitudes in Case 2 and 3, compared with the Case 1and the flat plate case. To elaborate the effect of wavy wall on the acoustic wave, SPL is illustrated in Figure 3.37 in a similar manner for all cases.

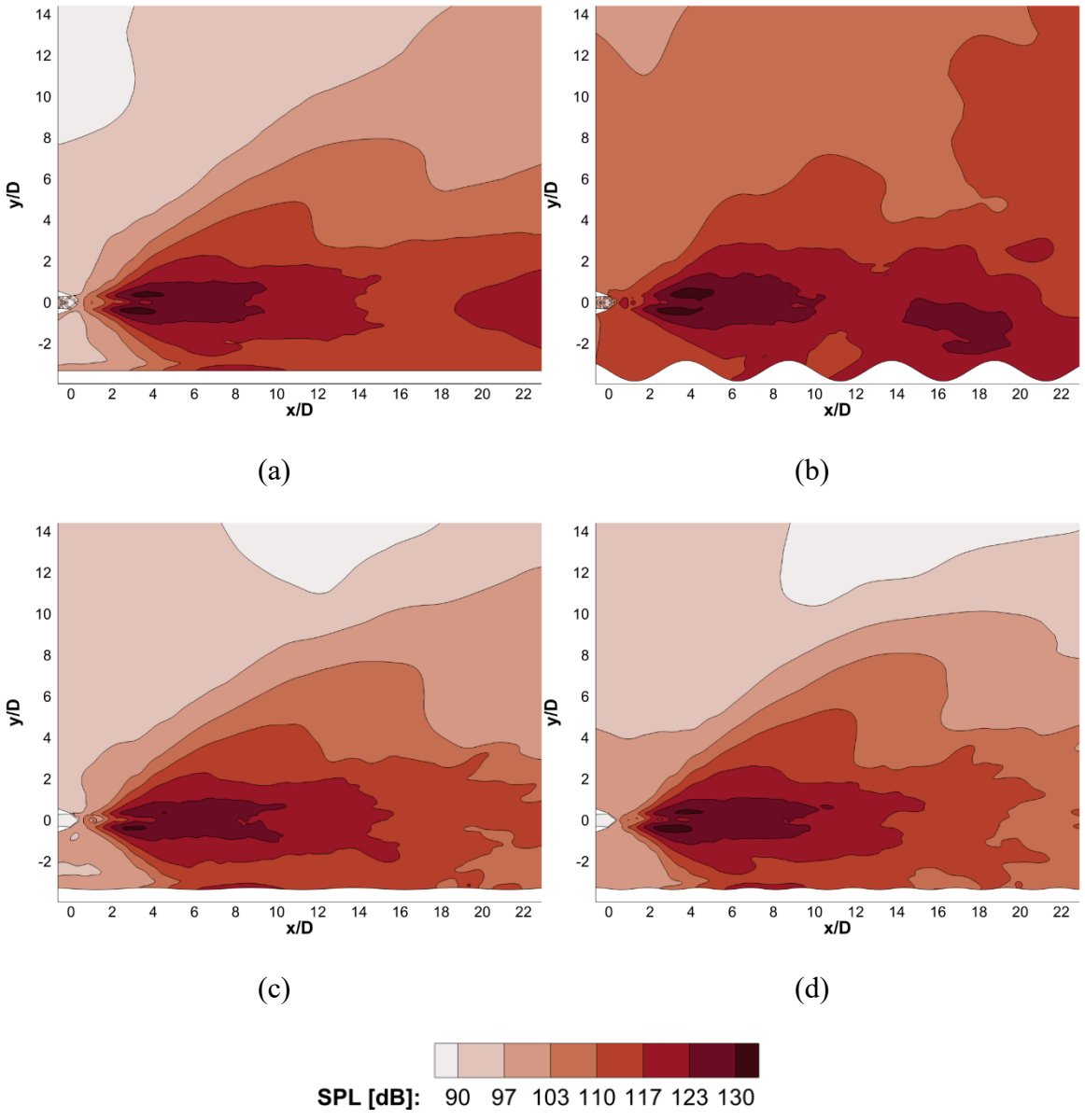

Figure 3.37 SPL. (a) Flat Plate ($h/D = 3$), (b) Case 1, (c) Case 2, (d) Case 3.

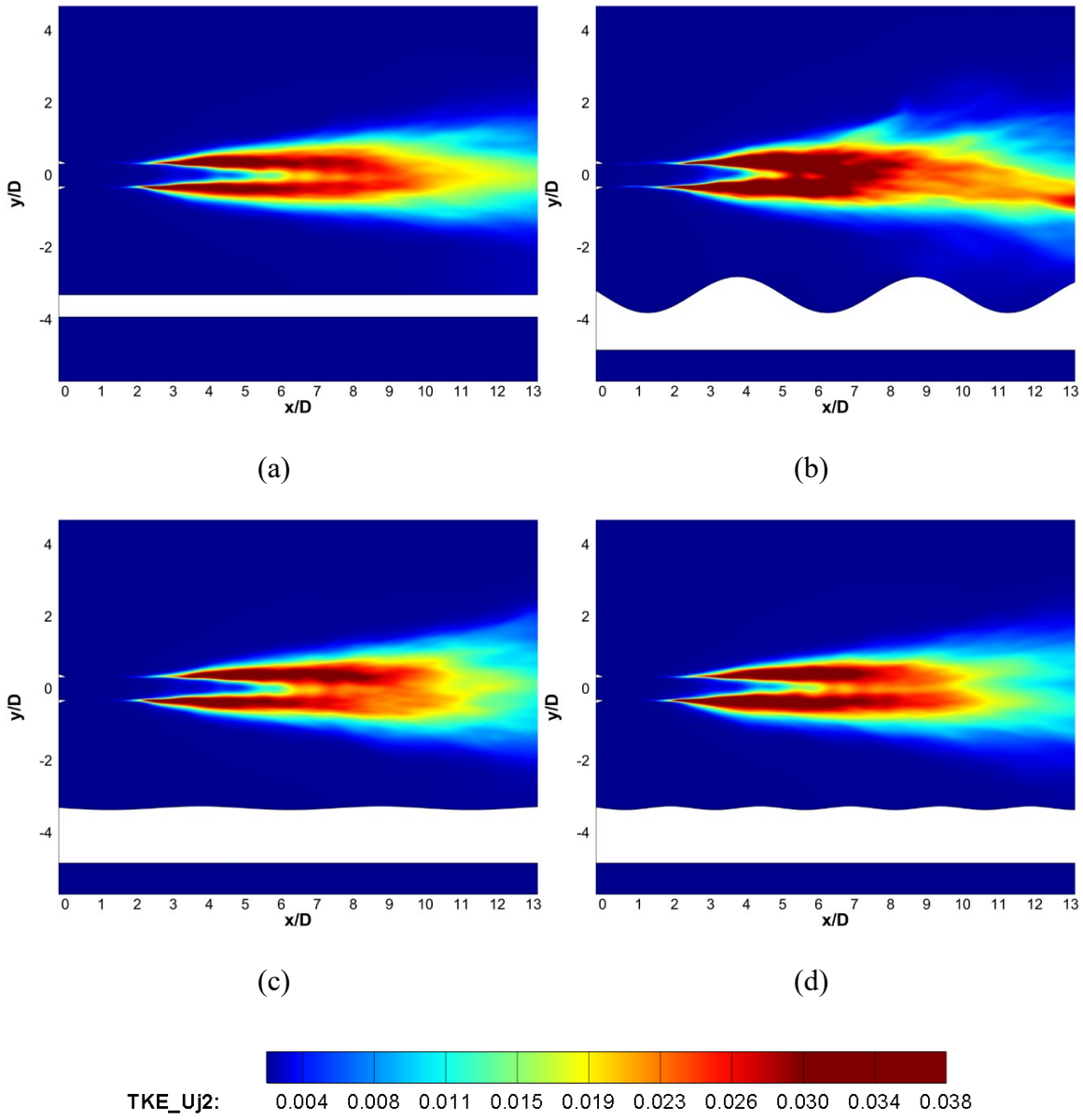

Figure 3.38 TKE normalized by jet velocity squared. (a) Flat Plate ($h/D = 3$), (b) Case 1, (c) Case 2, (d) Case 3.

Figure 3.37 clearly shows that the high amplitude wall of the Case 1 completely intensifies reflected wave in both downstream and upstream direction. On the other hand, both Case 2, and 3, clearly show that SPL is effectively reduces in the main radiation direction. It should be reminded that, Case 2 and Case 3 wall profiles have wavelengths

corresponding to the fundamental wave, and its first harmonic, respectively. But their amplitudes are much smaller than the Case 1. In fact, the profile in Case 3, appears to contain the fluctuations of the dissipation region, and consequently reduce the SPL in the main radiation angle. These provide a valuable qualitative measure illustrating that the wavy wall profiles of Case 2, and 3, effectively reduce noise. Hoverer, quantitative measure of acoustic reduction is provided in the following section.

Before focusing on the acoustic spectra SPL, it is worthwhile to investigate the effect of reflected waves and manipulated waves on the jet turbulence structure. Examining the turbulence structure of the jet can provide valuable insight on the mechanisms of acoustic reduction observed earlier in the SPL contours. Figure 3.38 compares the TKE normalized by jet velocity squared, for all wavy wall cases and the flat plate case. The kinetic energy in the shear layer is shown to be effect by the reflected waves. This figure confirms that the manipulation of the reflected waves from the walls, not only affects the acoustic field due to wave-wave interaction, but these waves reflect back and affect the instability waves in the shear layer and cause modifications to the turbulence structure of the jet. The high amplitude Case 1 excessively intensifies the shear layer. While Case 3, seems to effectively help to dissipate the fluctuations in the dissipation region of the jet. These figures show that the fluctuation in the downstream shear layer ($x/D = 11$), are effectively diminished in Case 3 when compared with the flat plate case. This may suggest that the introduction of the harmonic in Case 3, could provide more effective effect than introduction of the fundamental frequency in Case2.

3.5.3. Acoustic Spectra and Overall Noise (Wavy Wall at $h/D = 3$)

In order to deliver a quantitative assessment of the noise reduction of the wavy wall

profiles, the SPL spectra is shown in Figure 3.39 at the maximum radiation direction the reflected, and shielded side (point A and A') for the flat plate, Case 2, and 3.

Since, FAA regulations mainly enforce limitations on the perceived noise on the ground, the reflected side noise should not be viewed as a design objective. Here, the main objective is on the shielded side, which can be interpreted as the noise that reaches the ground. On the other hand, the reflected side noise could be of importance for takeoff and approach phases of flight, in terms of practical application of the design. Nevertheless, the reflected side results are provided here, as a measure of comparison with the experimental and numerical results for the flat plate cases, by providing more insight on the understanding of mechanisms by which the jet is affected due to the reflected waves.

Since the wavy wall profile in Case 1, was shown to deteriorate the SPL in the near field, only the fat field acoustic spectra from the wavy wall profiles of Case 2, and 3 are compared with the flat plate. Figure 3.39a shows that both wavy wall in Case 2, and 3 effectively reduce the noise in the reflected side by a margin of ~ 2dB almost across all ranges of frequencies. While Case 3 exhibits a more promising effect on the noise reduction as shown earlier in Figure 3.37.

Figure 3.39b, shows the SPL spectra on the shielded side. Although Case 2, exhibits some noise increase in low frequencies ($0 < St < 0.025$), but still reduces the noise throughout the higher frequency ranges ($0.03 < St < 0.3$) up to 3dB. On the other hand, Case 3, seems to provide a more effective noise reduction in the shielding side for the entire range of frequencies.

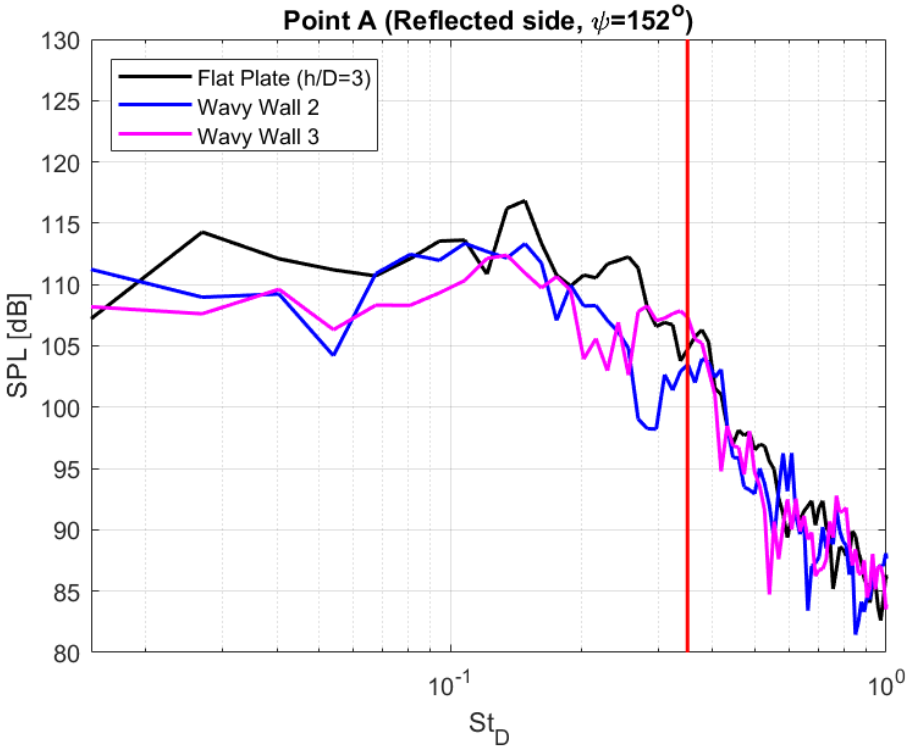

(a)

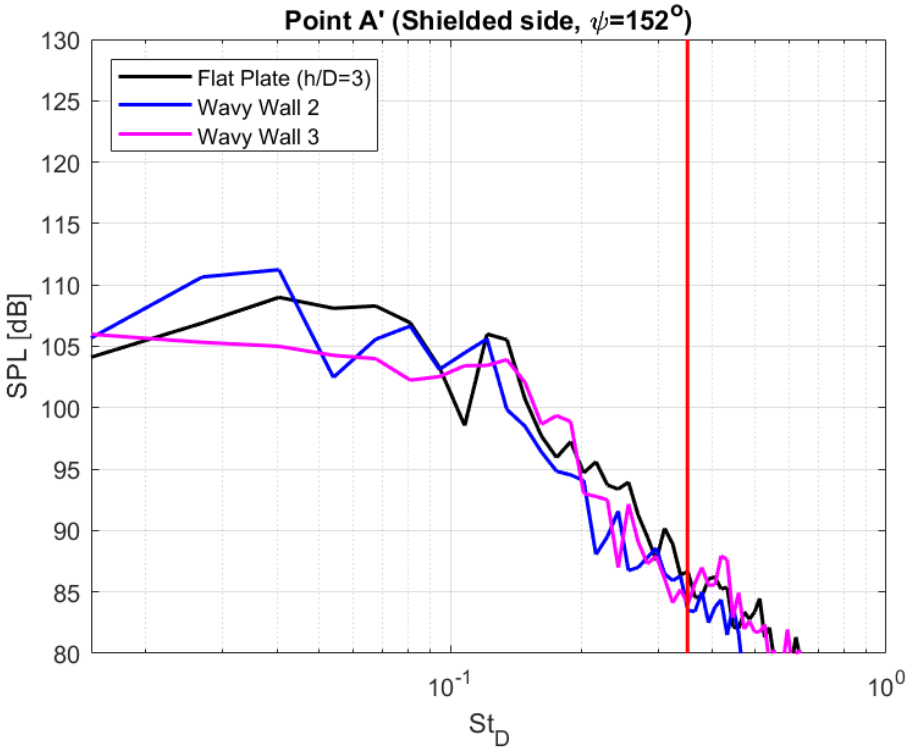

(b)

Figure 3.39 Acoustic spectra at $\psi = 152^o$ (a) reflected (A), and (b) shielded side (A'). (Flat Plate ($h/D = 3$), Case 2, and Case 3)

The acoustic spectra results, show that the wavy wall profile, can effectively reduce the noise, specifically when the wall profile imposes a harmonic of the fundamental wave, Case 3, based on the theoretical analysis envisioned earlier.

To provide a clear picture of the effectiveness of the shielding device as an acoustic reduction mechanism, the noise reduction or increase is presented in a form of $\Delta OASPL$, which is defined as:

$$\Delta\, OASPL = OASPL_{(Isolated\ Jet)} - OASPL_{(Jet-Shield\ Plate)} \tag{41}$$

Essentially, Figure 3.40a illustrates that wavy wall designs provide about 2 dB noise reduction, in the reflected side, while the flat plate merely increases the noise level by a small level. On the other hand, Figure 3.40b shows that Case 2, reduces the noise in the shielded side about 2 dB more than the flat plate shield. And Case 3, shows to provide more effective noise reduction, up to about 3dB more than the flat plate shield.

Although the OASPL results are valuable measures on showing the effectiveness of the wall profile, by comparing it with the flat plate case. But, another important aspect of the shield plate, is its effect on the peak frequency noise. This may be an even more notable factor, since the previous results have shown that the acoustic noise of the heated supersonic jet has a hump signature, where the peak corresponds to the fundamental frequency. Figure 3.41, compares the acoustic spectra at the maximum radiation direction (point A and A'), for the, isolated jet (no plate), flat plate, and the most effective wavy wall, Case 3. This figure is Focusing on peaks, and the effect of the walls on the peak noise reduction. The peak level seems to be effectively reduced by the wavy wall, when compared with the flat plat.

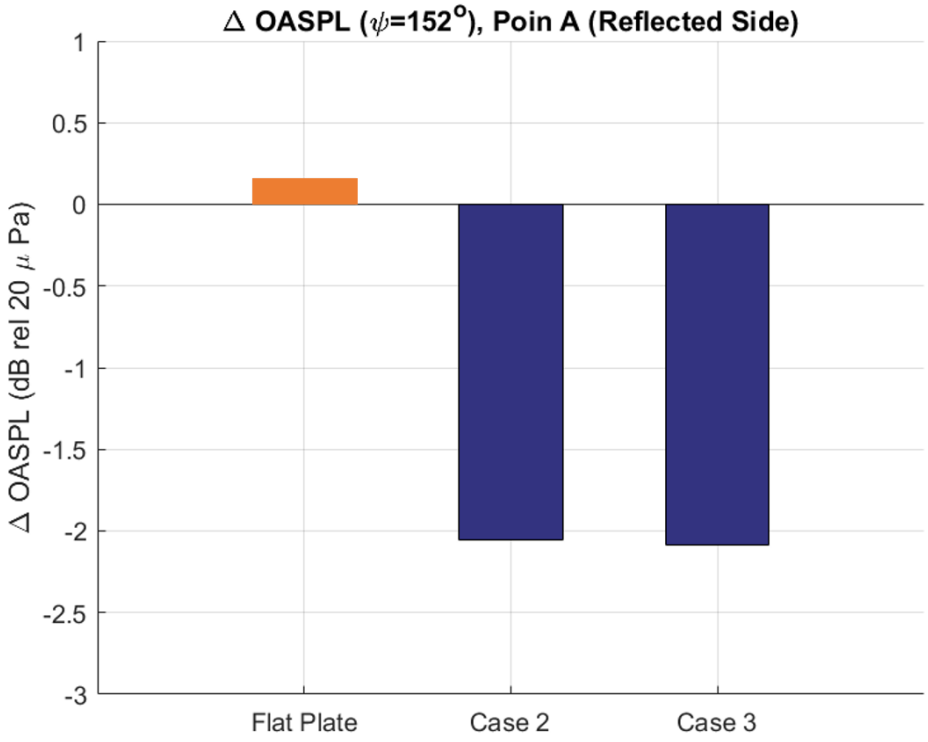

(a)

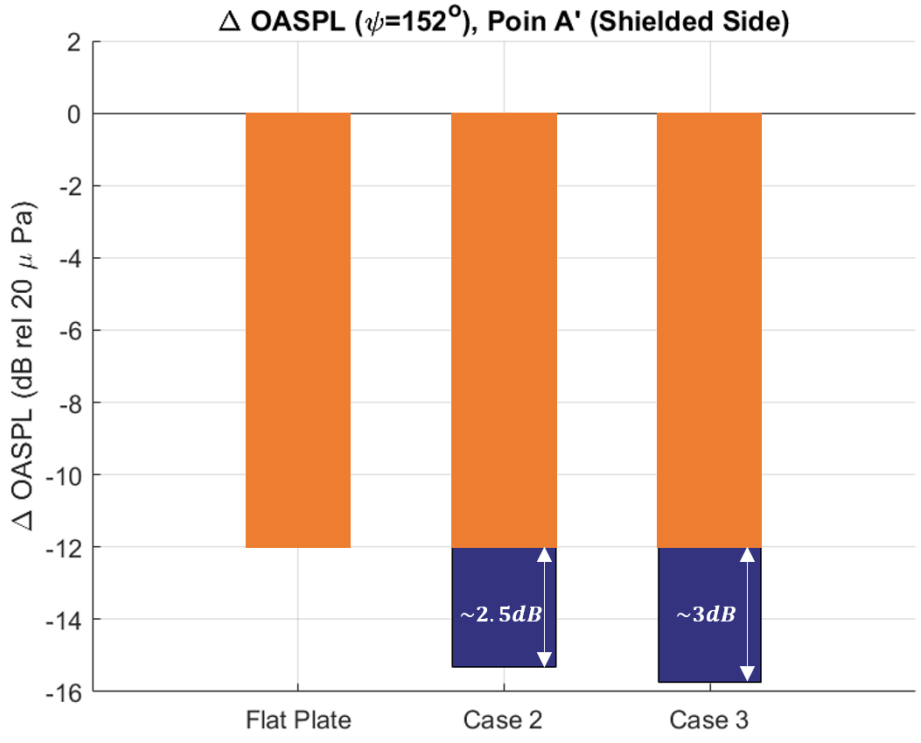

(b)

Figure 3.40 OASPL reduction effectiveness. (a) reflected side, (b) shielded side.

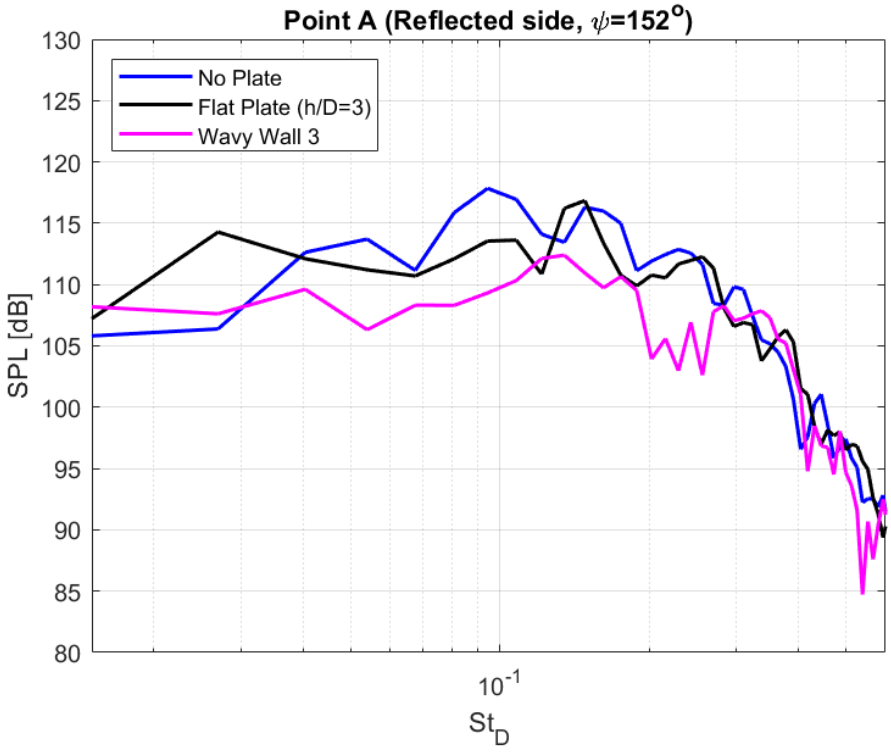

Figure 3.41 Acoustic spectra at $\psi = 152^o$ (a) reflected (A), and (b) shielded side (A'). (No Plate, Flat Plate, and Wavy Wall)

To provide a clear picture of peak noise attenuation of the two shielding device, Figure 3.42, compares the peak SPL at the far field observer probe location on the shielded sided (A'). The SPL level is averaged across the peak noise frequency range ($0.08 < St < 0.15$), for each case, a consistent comparison. Figure 3.42 shows that the wavy wall can reduce the peak noise level 3.7dB compared to the flat plate. It can be interpreted from this figure, that the wavy wall can provide up to ~42% more peak noise reduction compared with the flat plate shield.

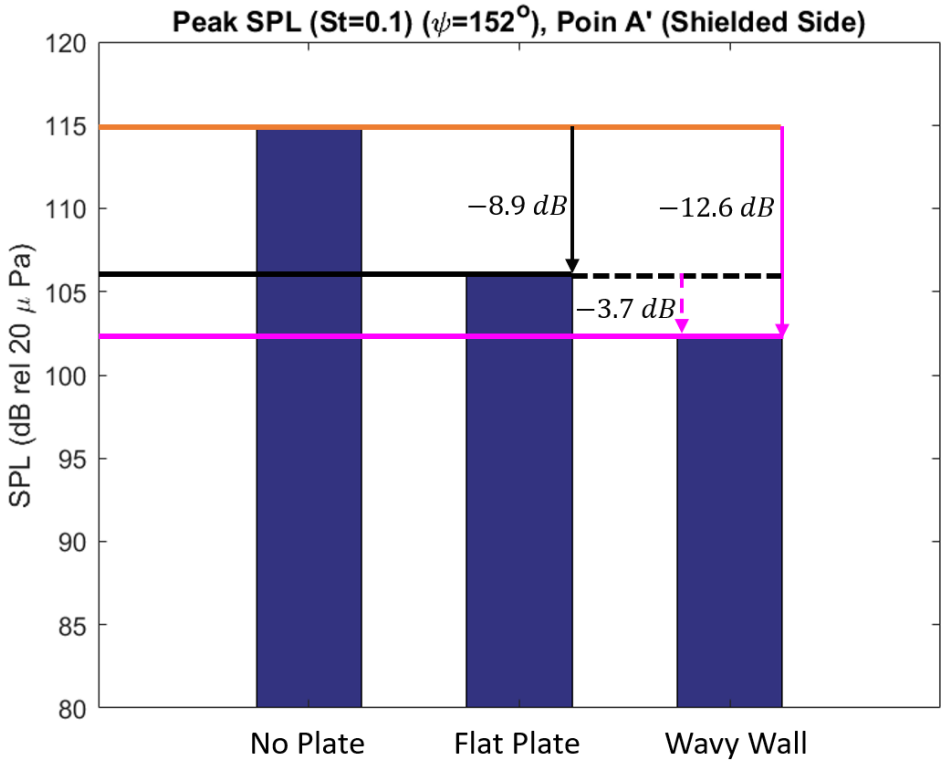

Figure 3.42 Peak noise reduction effectiveness.

To explain the mechanism responsible for the noise reductions observed by the wavy wall profile, the effect of the reflected waves on the source of the noise is investigated. Figure 3.43 shows the RMS of pressure fluctuations in the jet for the isolated jet, flat

plate, and the wavy wall case. Th contours of pressure fluctuations show that the reflection waves from the flat plate intensify the fluctuations in the lower shear layer of the jet causing an asymmetrical turbulence structure in the jet as discussed earlier. However, the manipulated reflection waves by the harmonic of the fundamental tone that are reflected wavy wall profile modify the top shear layer of the jet as well.

The RMS of pressure fluctuations along the top and bottom shear layer are compared in Figure 3.44, for the three cases. This figure clearly illustrates that fluctuations in the top shear layer is intensified by the flat plate, while the wavy wall reduces these fluctuation. This reduction is caused by the wave-wave interaction mechanism, imposed by the wavy wall's profile that introduces the waves with the harmonic of the fundamental frequency and the phase shift of $\phi = \pi$. Although both shield plates magnify the fluctuations in the bottom shear layer in Figure 3.44, but the fluctuations imposed by the wavy wall have smaller magnitude than the flat plate case. In addition, the imposed manipulated waves cause the fluctuations to be reduced in the further regions of the shear layer.

In other words, the noise reduction mechanism can be explained with the following statements: (1) The wavy wall reduces the fluctuations in the top shear layer, and (2) the intensifications of the fluctuations in the lower shear layer imposed by the wavy wall is smaller than those caused by the flat plate. These two modifications imposed by the wavy wall, suggest smaller fluctuations in noise source, and consequently lead to smaller SPL observed in the acoustic spectra.

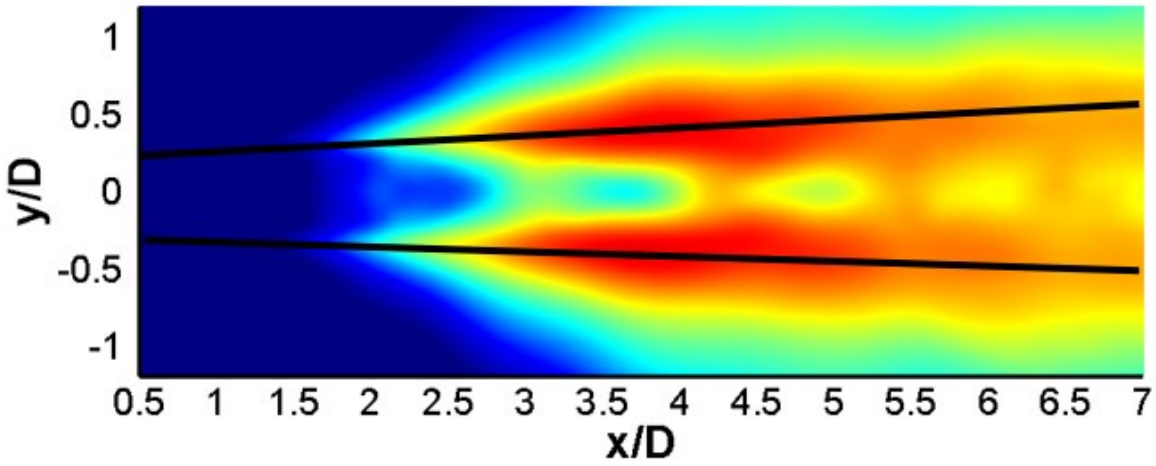

(a)

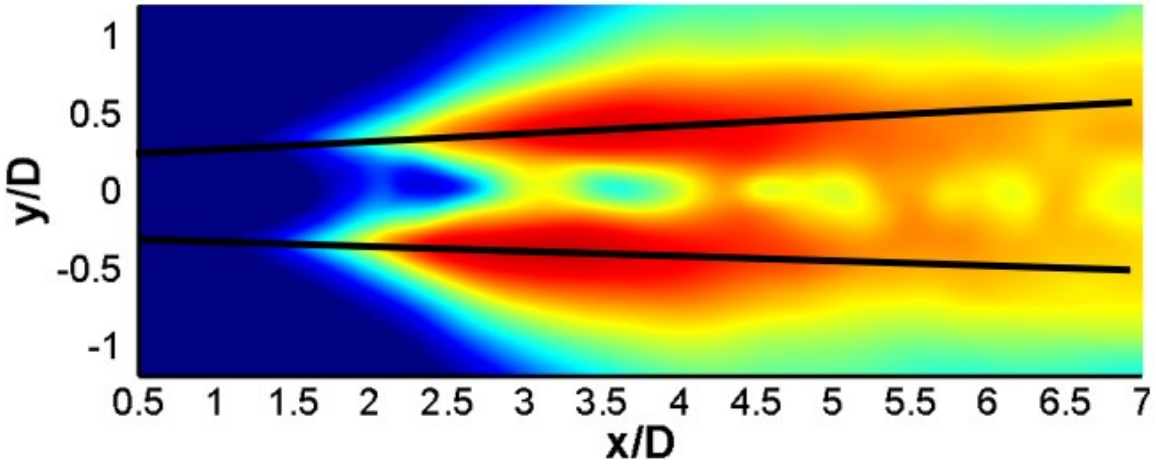

(b)

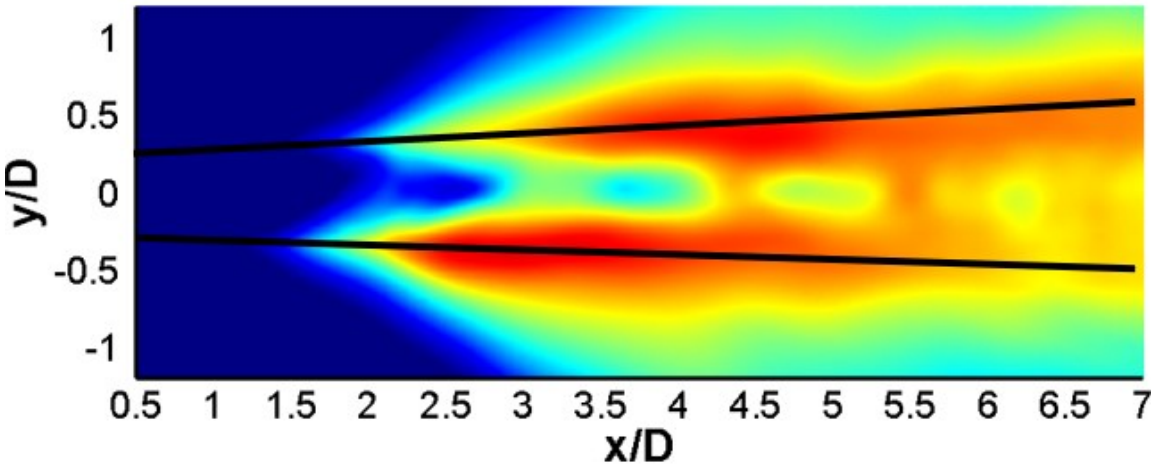

(c)

Figure 3.43 RMS of pressure fluctuations in source region. (a) No Plate, (b) Flat Plate, (c) Wavy Wall.

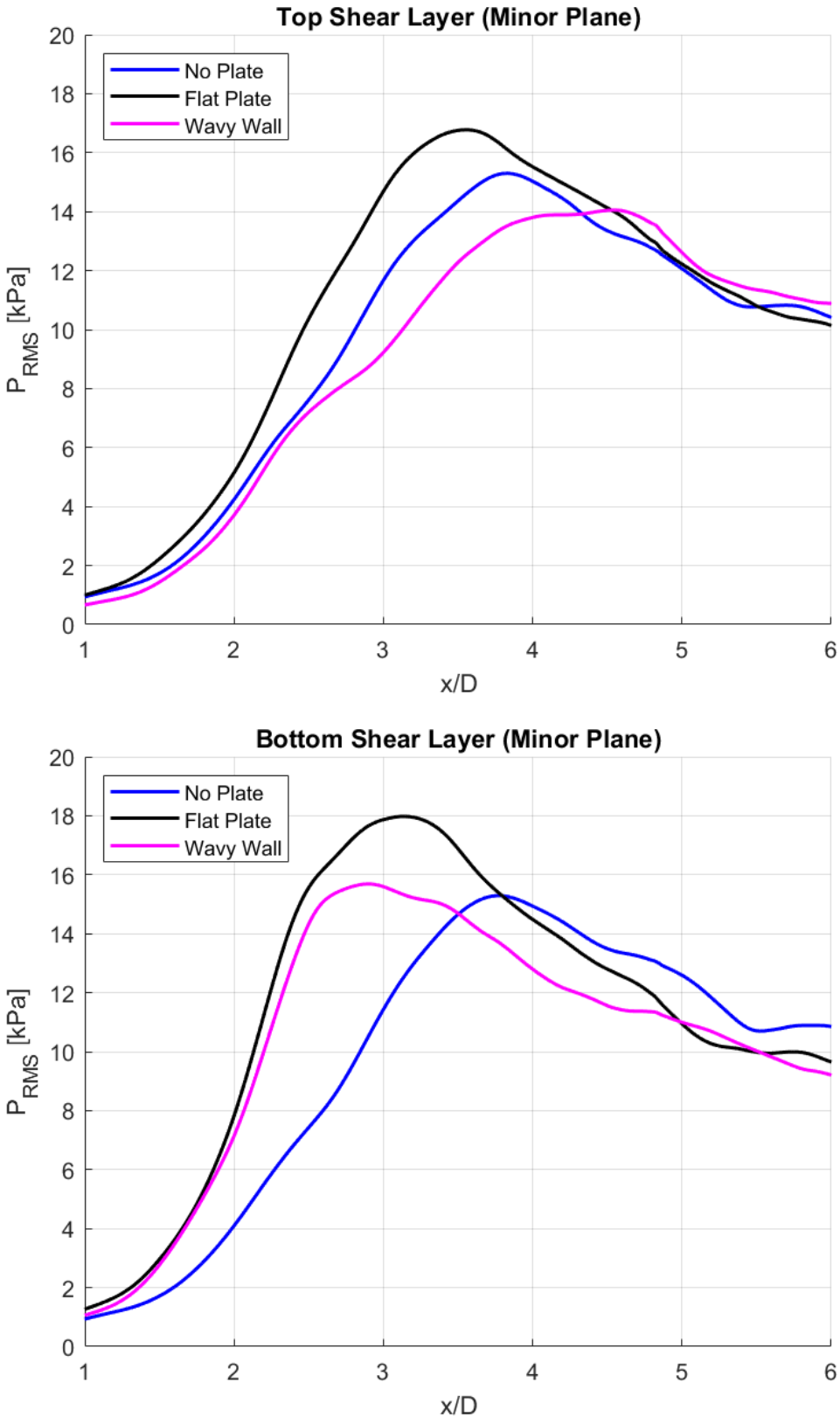

Figure 3.44 RMS of pressure fluctuations along the top and bottom shear layer.

The previous results indicate that the wavy wall reduces the noise compared to that of the flat plate shield, not only on the shielded side but also in the unshielded side. It was shown that the wavy wall designed using the wavelength of the harmonic is more effective than the one with the wavelength of the fundamental. The former is utilizing the nonlinear mode-mode interaction, while the latter is utilization linear superposition. Since the noise generation is a nonlinear process, it is not surprising that the "harmonic" wavy wall based on utilizing the nonlinear interaction is more effective. Therefore, the main objective here is to explain and verify the nonlinear mechanism associated with the harmonic-based wavy wall.

In the following figures, the magnitude of the FFT of the pressure oscillation, $|\hat{p}|$, is illustrated, representing the noise source in the initial region of the jet associated with the noise-efficient large-scale structure. The Fourier transform provides a more detailed information about the large-scale structures, by decomposing the sources and focusing on specific frequency.

First, the flat plat is compared with the isolated case in Figure 3.45. The fundamental frequency component, $St = 0.1$, is of special interest since the peak noise in the far field was observed at this frequency. The figure shows that for the isolated case, the source is equally concentrated around both the top and bottom shear layers. But when the flat plate is introduced, while it shields the bottom radiation, it has intensified the source in both the top and shear layers, due to the reflection of the acoustic waves. This increase in the sound source counterbalances the shielding effect of the plate on the bottom side, and also results in intensifying the radiated sound in the non-shielded reflected side.

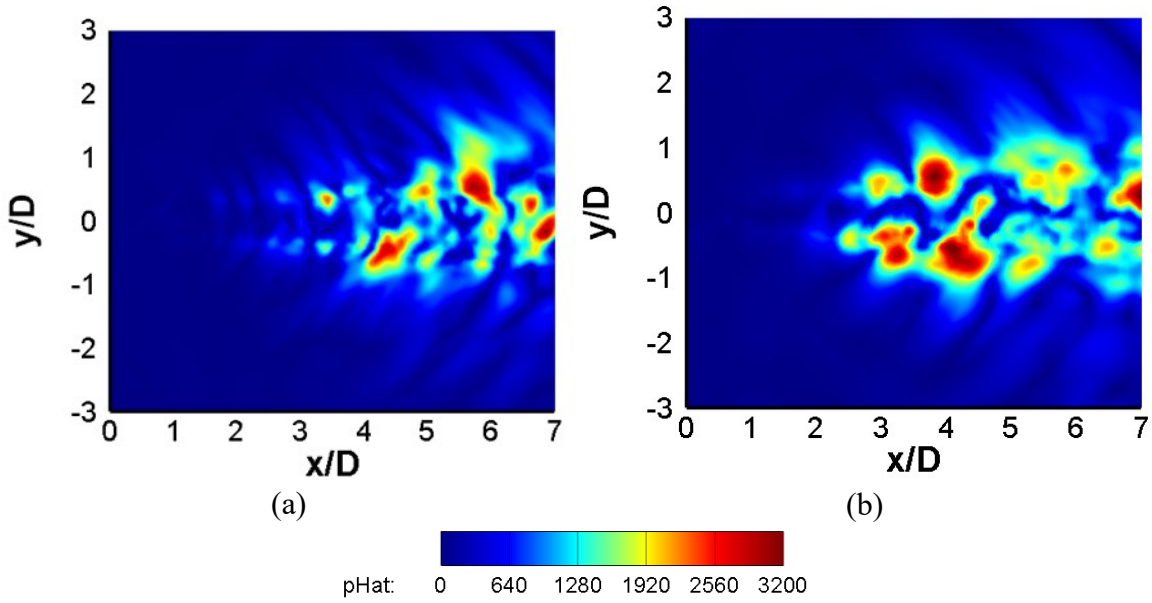

Figure 3.45 Magnitude of pressure oscillation FFT ($St = 0.1$). (a) Isolated jet, (b) Flat plate shield.

The wavy wall is designed to benefit from the shielding effect that the flat plate provides, but also reduces the sound source itself. The basic idea is to use the acoustic reflection from the plate/ wall to actually reduce the noise source, rather than intensifying it as in the flat case. The nonlinear mechanism associated with the harmonic wavy wall was based on the theoretical studies (Arbey & Ffowcs Williams, 1984; Mankbadi, 1985b).

These studies suggest that the harmonic interacts nonlinearly with the fundamental and extracts its energy. Thus, reducing the growth of the fundamental, and hence reduces the corresponding peak noise in the far field. So, the basic idea here is that instead of having a random reflection, the reflection waves can be modified to be in a particular wavelength corresponding to a given frequency. Thus, using this "wavy" reflection as an excitation mechanism, to enhance a particular frequency in the shear layer via the receptivity mechanism.

In Figure 3.46 and Figure 3.47, the harmonic wavy wall is compared with the isolated jet case. In Figure 3.46, the $St = 0.1$ (fundamental) is shown. When the harmonic wavy wall is introduced, two main mechanisms can be observed. I) The enhancement of the bottom shear layer sources is reduced when compared to that of the flat plate. II) The source in the top shear layer is substantially reduced relative to that of the isolated case or to that of the plate. This is because the harmonic nonlinearly extracts energy from this fundamental component. This is verified in Figure 3.47, which shows that the harmonic component ($St = 0.2$) is intensified by the presence of the wavy wall as it grows by extracting energy from the ($St = 0.1$) component. Since the higher frequency components are less efficient than the lower frequency ones in radiating sound, the total radiated sound, as well as the spectra peak sound, is reduced as was shown earlier in Figure 3.42.

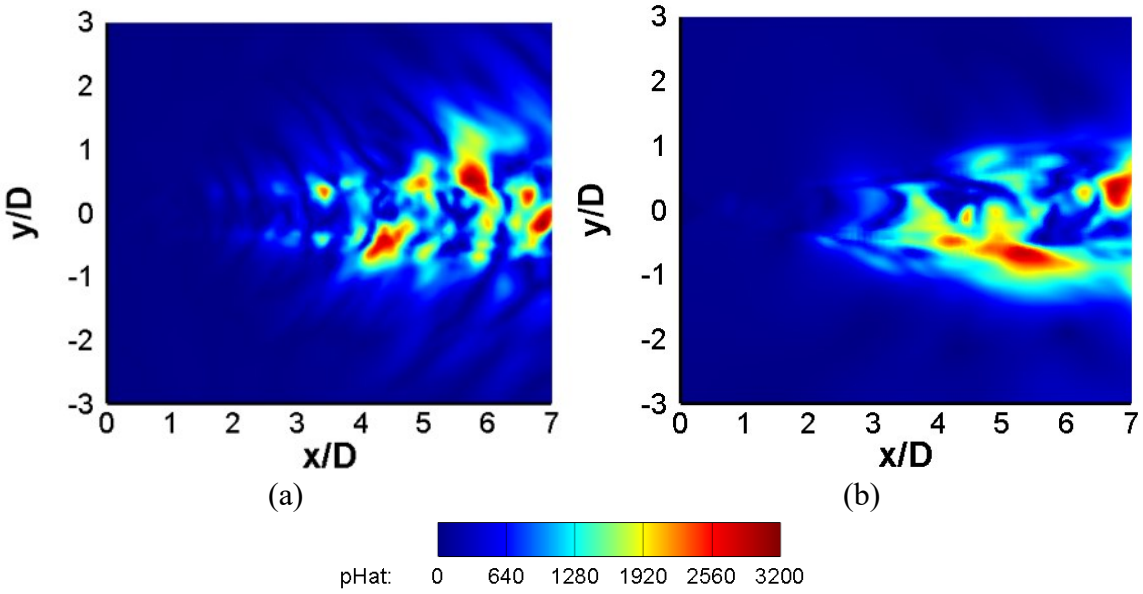

Figure 3.46 Magnitude of pressure oscillation FFT ($St = 0.1$). (a) Isolated jet, (b) Wavy Wall.

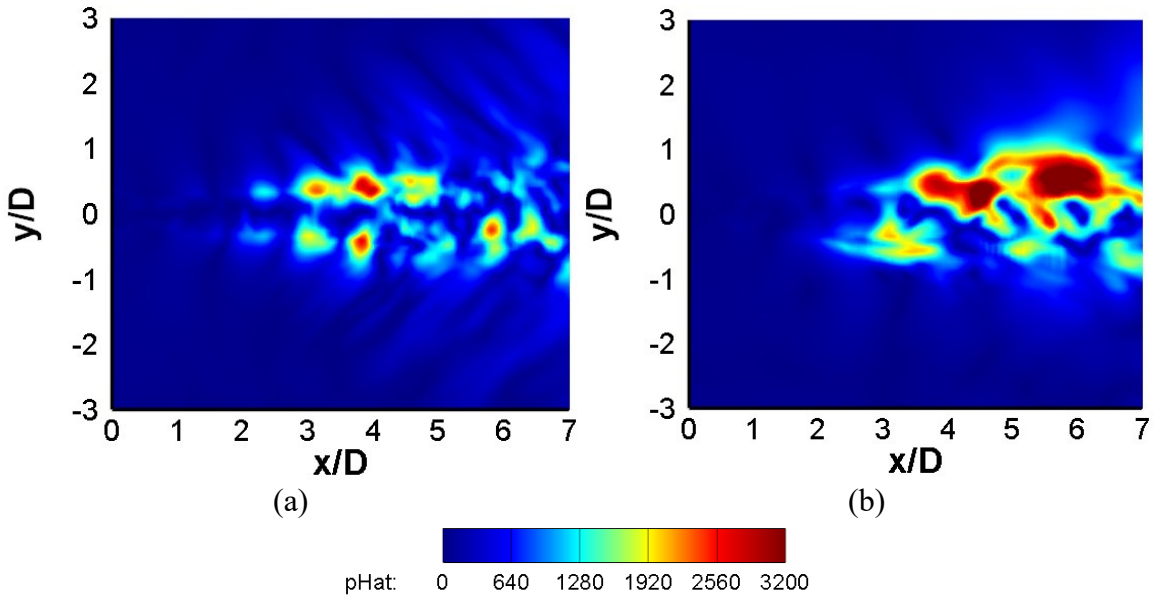

Figure 3.47 Magnitude of pressure oscillation FFT ($St = 0.2$). (a) Isolated jet, (b) Wavy Wall.

In summary, it was illustrated that the wavy wall profile can provide effective noise reduction, compared to the original flat plate shield, by manipulating the reflected waves. The manipulation of the reflected waves, based on the understanding and theoretical estimations, introduces wave-wave interaction. This wave interaction can potentially reduce the jet noise and has the potential to be used as a noise control device.

3.5.4. Theoretical Estimation of Wall Profile Design Elements ($h/D = 0$)

Following the same analogy described earlier in Section 3.5.1, the estimation of wavelength and its harmonic has to be similar for both wavy wall cases located at ($h/D = 0$) and ($h/D = 0$). However, it should be noted that two other parameters must be adjusted accordingly for the wavy wall cases $h/D = 0$. First, the amplitude of the wavy walls needs to be smaller to avoid generation of shocks in the flow. Second, the location of phase shift needs to be adjusted for these particular cases.

As it was mentioned earlier, the estimation of amplitude of wavy wall was set to 1-5

%. To avoid generation of shocks and introduction of new sources of noise, the lower end of the estimation is considered for the wavy walls when placed near the nozzle. Since the amplitude of 5% ($A = 0.05D$) estimation was selected for ($h/D = 3$) cases, the 1% estimation corresponds to the wall amplitude for ($h/D = 0$) cases.

On the other hand, to ensure the maximum effectiveness of the wavy wall on the flow perturbations, the location the phase shift start need to be reexamined. To this end, the effect of flat plate on the flow field fluctuations of the isolated jet is revisited. As it was shown earlier in the flat plate section, when the plate is located near the nozzle lip, it changes the flow field drastically. It was shown that the lower shear layer is replaced by the boundary layer which has a weaker shear, the flow is elongated in the x-direction. Figure 3.48 illustrates the effect of flat plate at $h/D = 0$ on the streamwise fluctuations along the top and bottom shear layer. The bottom shear layer is technically replaced by a boundary layer due to the presence of flat plate. Here, The RMS of velocity fluctuations are normalized by the isentropic nozzle exhaust velocity (U_j).

The boundary layer has a smaller fluctuations than the shear due to its nature up to $x/D = 2$. However, the fluctuations spike after this point due to the interactions of top shear layer. Similarly, in the top shear layer the $x/D = 2$, seems to be the onset growth of the fluctuations. This was shown earlier in Figure 3.13 and Figure 3.14. This figure suggests that the start location of manipulation of the fluctuations imposed by the wavy wall, to be positioned at $x/D = 2$. It should be noted that π phase shift from the axial distance of interest ($x/D = 2$), is considered in the wavy wall profile of the cases mentioned here.

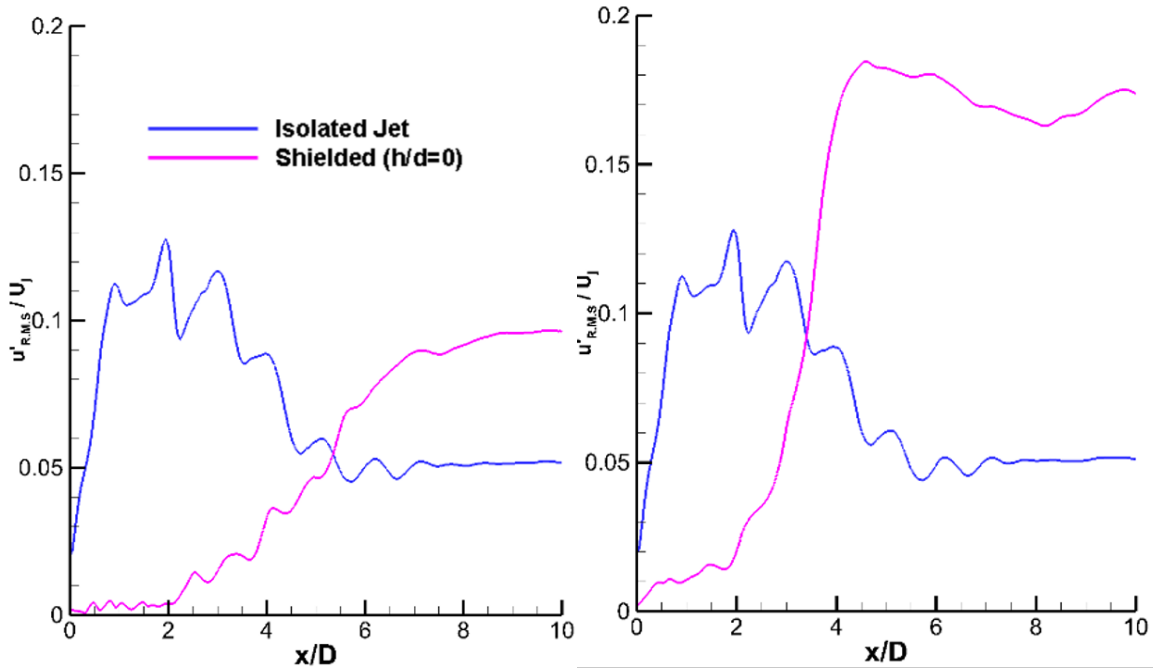

(a) (b)

Figure 3.48 RMS of velocity fluctuations along the (a) top shear layer and (b) bottom shear layer / boundary layer for isolated jet and flat plate at $h/D = 0$.

Table 3.3

Parameters of the wavy wall cases ($h/D = 0$).

	h/D	λ	A_w
Case 4	0	$5D$	$0.01D$
Case 5	0	$2.5D$	$0.01D$

3.5.5. Flow and Acoustic Field Results (Wavy Wall at $h/D = 0$)

The numerical simulations are carried out for the wavy wall cases positioned at $h/D = 0$, and the results are compared with the corresponding flat plate results, to investigate the effect of the wavy profile on the flow and acoustic field. Here, the nearfield results are illustrated for the wavy wall compared with the flat plate case at $h/D = 0$.

First, the time averaged velocity, normalized by jet exhaust velocity (U_j), is shown in Figure 3.49. The fundamental wavy wall does not seem to change the flow field.

However, the harmonic case seems to generate week shock in the jet plume such as $x/D = 3$ and 5.

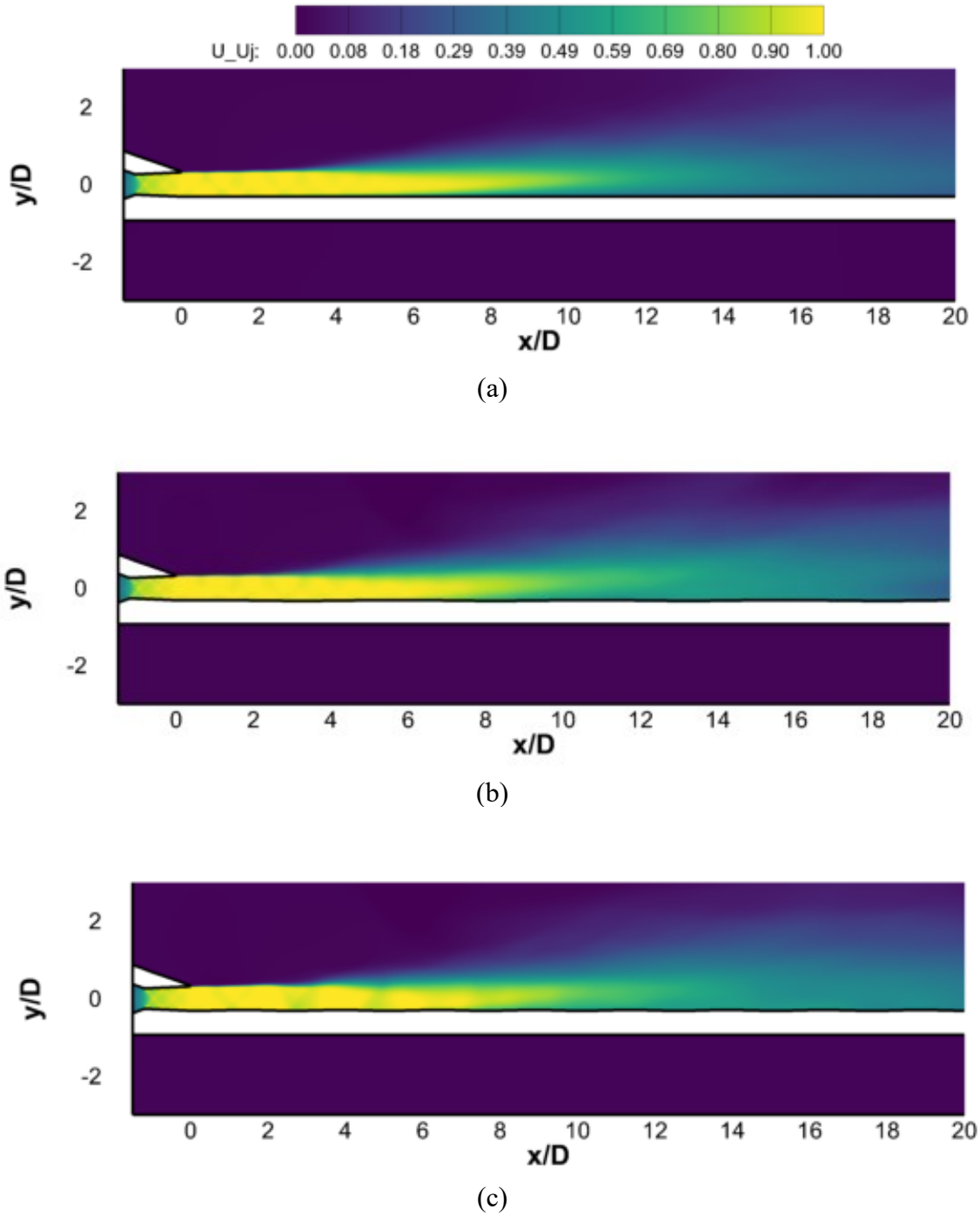

Figure 3.49 Time averaged velocity normalized by isentropic nozzle exhast velocity. (a) Flat Plate ($h/D = 0$), (b) Case 4 (fundamental), (c) Case 5 (harmonic).

To investigate this in detail, the normalized velocity along the top shear layer, centerline, and the boundary layer is shown in Figure 3.50. It can be seen that the top shear layer and the centerline is hardly affected by the wavy wall profile. But, the introduced bums on the wall, energize the boundary layer flow. The introduced weak shocks by the harmonic-wavelength case (Case 4) are clearly shown in Figure 3.50c.

In a similar fashion, cross-sectional mean velocity profile of the jet at $x/D = 2$, $x/D = 5$, and $x/D = 10$, is illusterated in Figure 3.51, to examine the effect of the wavy walls on the axial extent of the wall jet flow. Figure 3.51a shows that the harmonic wall (Case 5), slightly modifies the expansion of the jet and increases the jet exhaust velocity, in the near nozzle region ($x/D = 2$). Although the fundamental wavelength case (Case 4) does not change the spreading of the wall jet significantly, but the harmonic-wavelength case (Case 5), reduces the mean velocity of the jet by 10% further downstream ($x/D = 5$). This is shown in Figure 3.51. However, this reduction of maximum velocity in the jet plume is compensated further away ($x/D = 10$), due to the increase of velocity imposed by boundary layer growth, illustrated in Figure 3.51c.

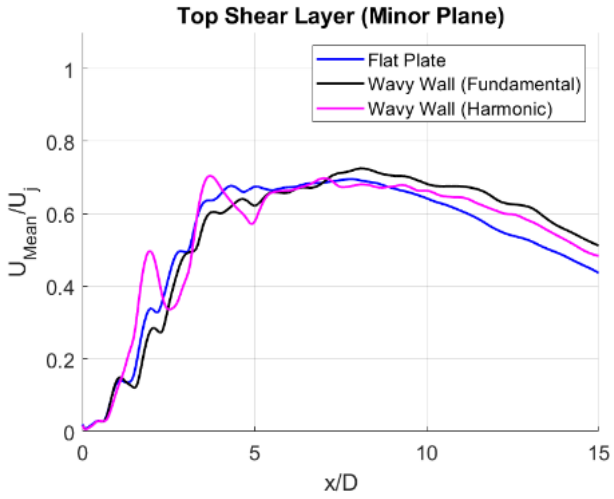

(a)

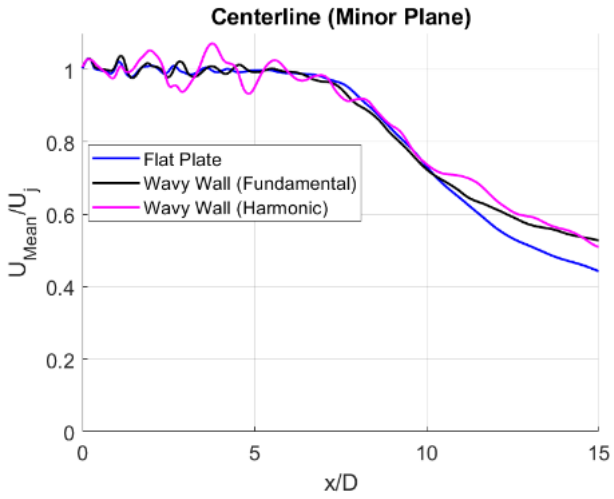

(b)

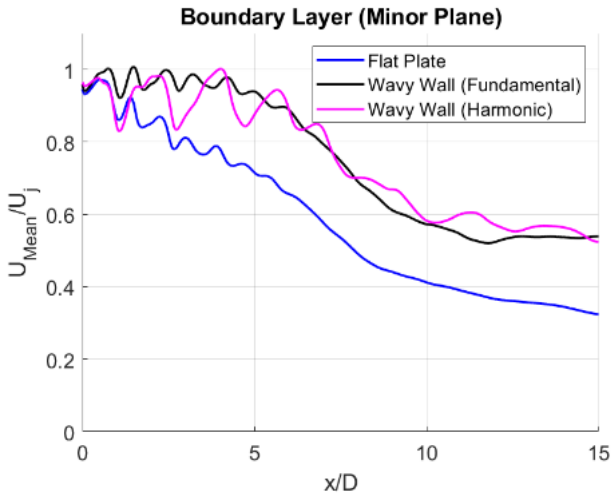

(c)

Figure 3.50 Time averaged velocity normalized by isentropic nozzle exhast velocity. (a) Top shear layer, (b) Centerline, (c) Boundary Layer.

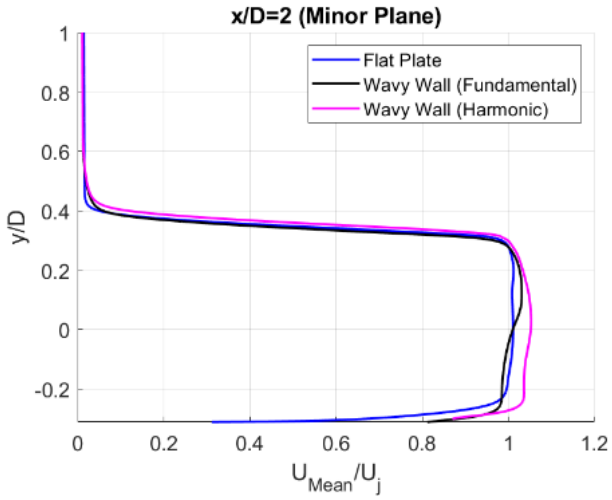

(a)

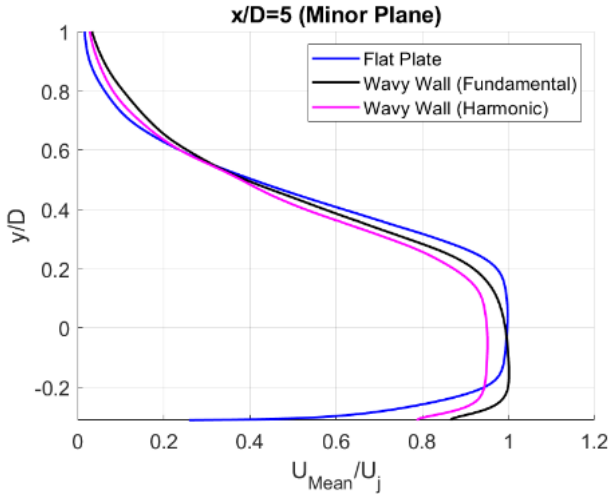

(b)

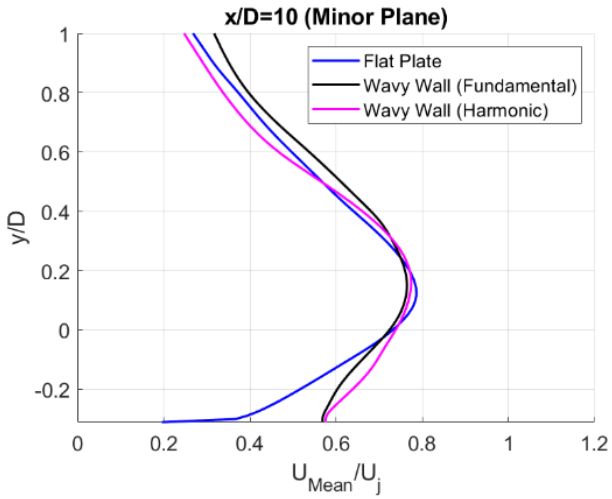

(c)

Figure 3.51 Time averaged velocity normalized by isentropic nozzle exhast velocity. (a) $x/D = 2$ (b) $x/D = 5$, (c) $x/D = 10$.

The time averaged velocity profiles explain the general characteristics of the flow. But TKE contours are shown here to provide information about the effect of the wavy walls on the turbulent structure of the flow. By comparing the TKE results for the wavy wall cases with the flat plat case in Figure 3.52. Generally, the figure shows that the introduced bumps by both harmonic and fundamental cases, increase the turbulent fluctuations in the wall boundary at somewhere around $x/D = 7$ and onwards. The bumps on the wall act as surface roughness effect in a boundary layer flow and increase the wall fluctuations. On the other hand, both wavy walls seem to reduce the top shear layer fluctuations. More specifically, the harmonic-wavelength wall effectively reduces the top shear layer fluctuation compared to the fundamental wavelength case. This effect is similar to what was observed for the $h/D = 3$ cases. The wavy wall profiles impose fluctuations corresponding to the fundamental and harmonic waves in Case 4 and 5, respectively. Such imposed fluctuations extract energy from the top shear layer fluctuations. For the $h/D = 3$ cases, the imposed fluctuations were introduced by manipulation of the reflected waves. While such frequency-specific fluctuations are imposed by the boundary layer flow.

Figure 3.53 shows these effects more clearly. The fluctuations in the boundary layer, shown in Figure 3.53c, are increased starting from $x/D = 7$, this the location of the boundary layer growth as shown earlier. The center line fluctuations of the plume are hardly affected by the wavy wall profile up to $x/D = 7$. The increased of fluctuations in the centerline, shown in Figure 3.53b, are due to the increased mixing from the boundary layer entrained to the aft of potential core. Figure 3.53a, clearly illustrates reduction of perturbations in the shear layer in the $4 < x/D < 12$ region. This figure suggests that the

harmonic-wavelength wall reduces the top shear fluctuations more effectively than the fundamental wavelength case. On the other hand, the boundary layer fluctuations are shown to be increased significantly after $x/D = 6 - 7$. Although the imposed fluctuation lead to extracting energy from the top shear layer, but the exponential growth of the fluctuation in the boundary layer itself is not desirable. Since such fluctuations act as additional source of noise.

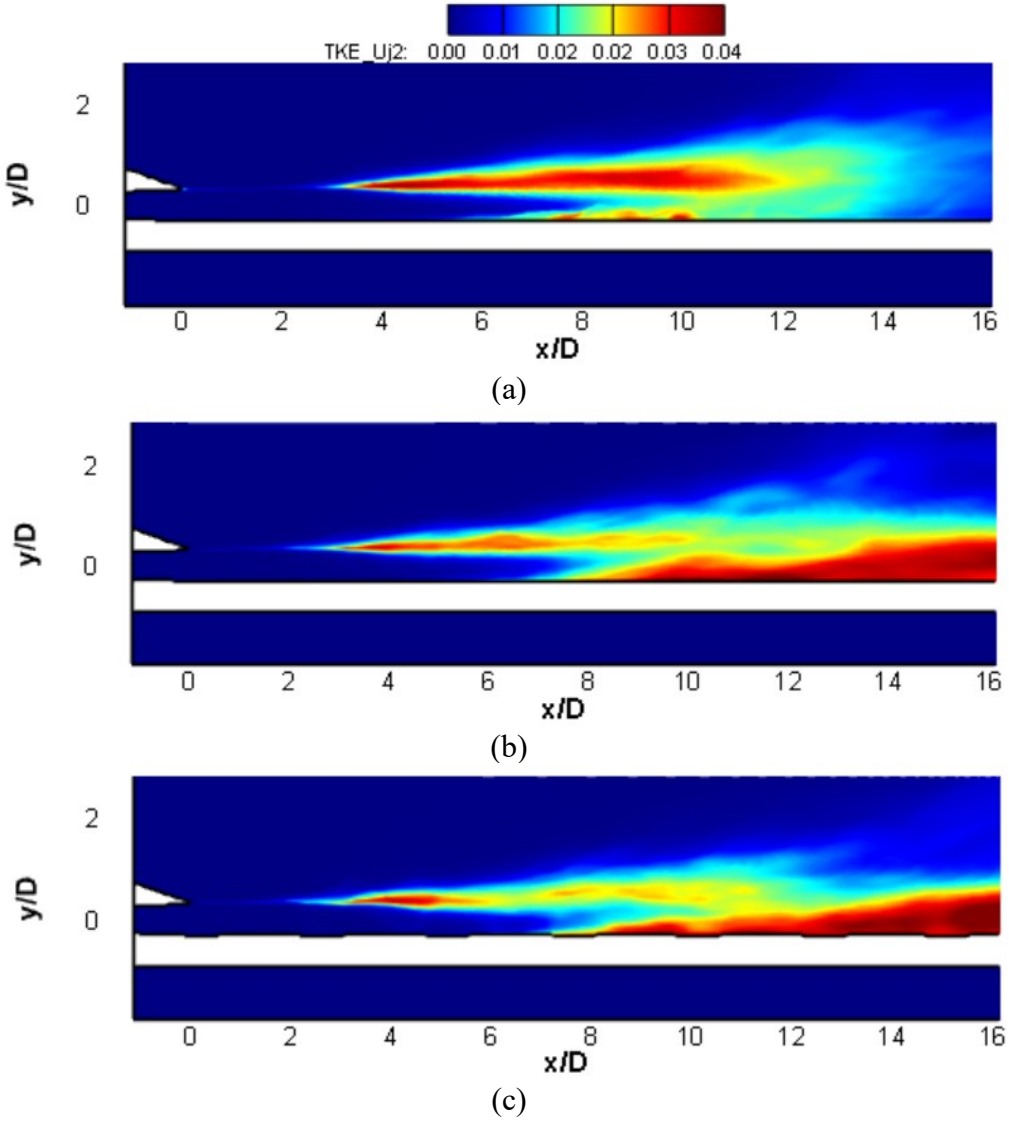

Figure 3.52 TKE. (a) Flat Plate ($h/D = 0$), (b) Case 4 (fundamental), (c) Case 5 (harmonic).

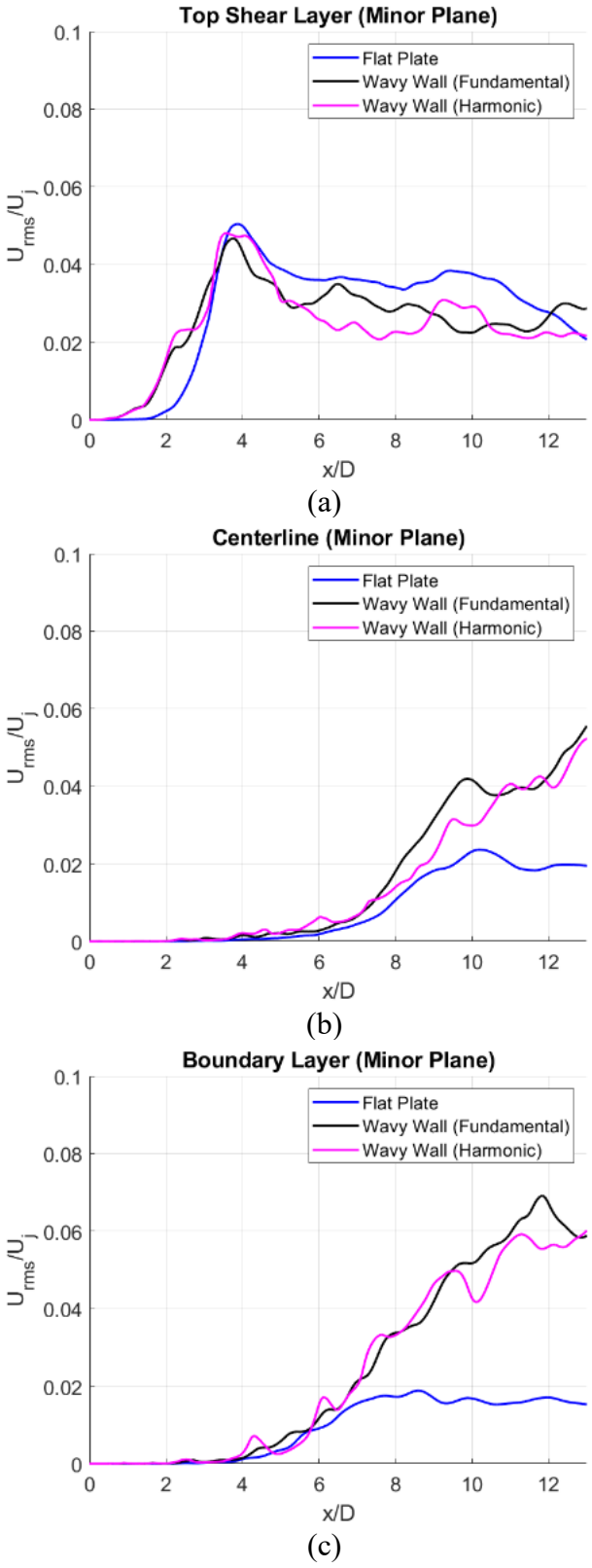

Figure 3.53 RMS of velocity fluctuations normalized by isentropic nozzle exhast velocity. (a) Top shear layer, (b) Centerline, (c) Boundary Layer.

The instantaneous fluctuating component of pressure is illustrated in Figure 3.54 for all wavy wall ($h/D = 0$) cases, and the flat plate ($h/D = 0$), to compare the acoustic waves, and their reflections from the different wall profiles. This figure suggests that the harmonic wavy wall (Case 5) appears to reduce the radiated noise very slightly on the reflected side in the main radiation directing ($x/D = 10$ and $y/D = 2 - 5$). The top shear layer pressure fluctuations appear to be reduced compared to the flat plate case. However, the fundamental wavelength case, does not seem to effectively reduce acoustic waves. Specifically, the fundamental downstream travelling wave, shown in the $x/D = 10$ and $y/D = 5$ region of all contours.

To elaborate the effect of wavy wall on the acoustic wave, SPL is illustrated in Figure 3.55 in a similar manner for all cases of $h/D = 0$. This figure shows that both cases of the wavy wall increase the noise sources in the bottom shear layer, as shown earlier. However, comparing the SPL levels in the maximum radiation angle and focusing on the $x/D = 6 - 9$ and $y/D = 1 - 5$ region, the harmonic wavy wall case seems to reduce the reflected side noise slightly.

The provided nearfield results suggest that the wavy wall located at $h/D = 0$, can have both positive and negative effects, from the noise reduction point of view. It was shown that the harmonic wavy wall reduces the top shear layer fluctuations. This reduction of fluctuations leads into some noise reduction illustrated in qualitative comparisons of the instantaneous pressure fluctuations and SPL for the wavy wall case and the flat plate case. However, no considerable noise reduction is observed in the qualitative assessment of nearfield acoustics. More specific quantitative measures are assessed by acoustic spectra in the next section

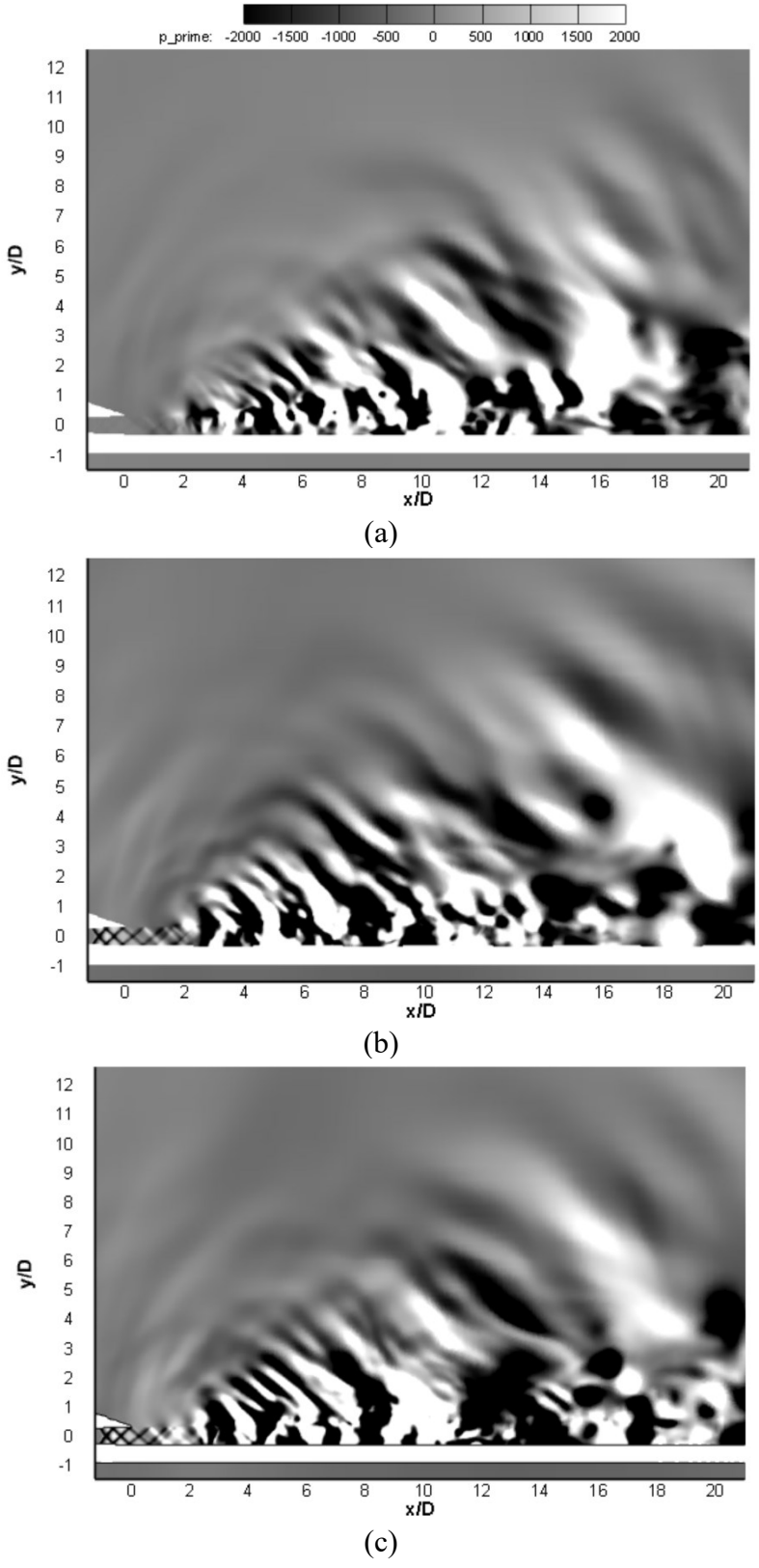

Figure 3.54 Instantaneous acoustic pressure. (a) Flat Plate ($h/D = 0$), (b) Case 4 (fundamental), (c) Case 5 (harmonic).

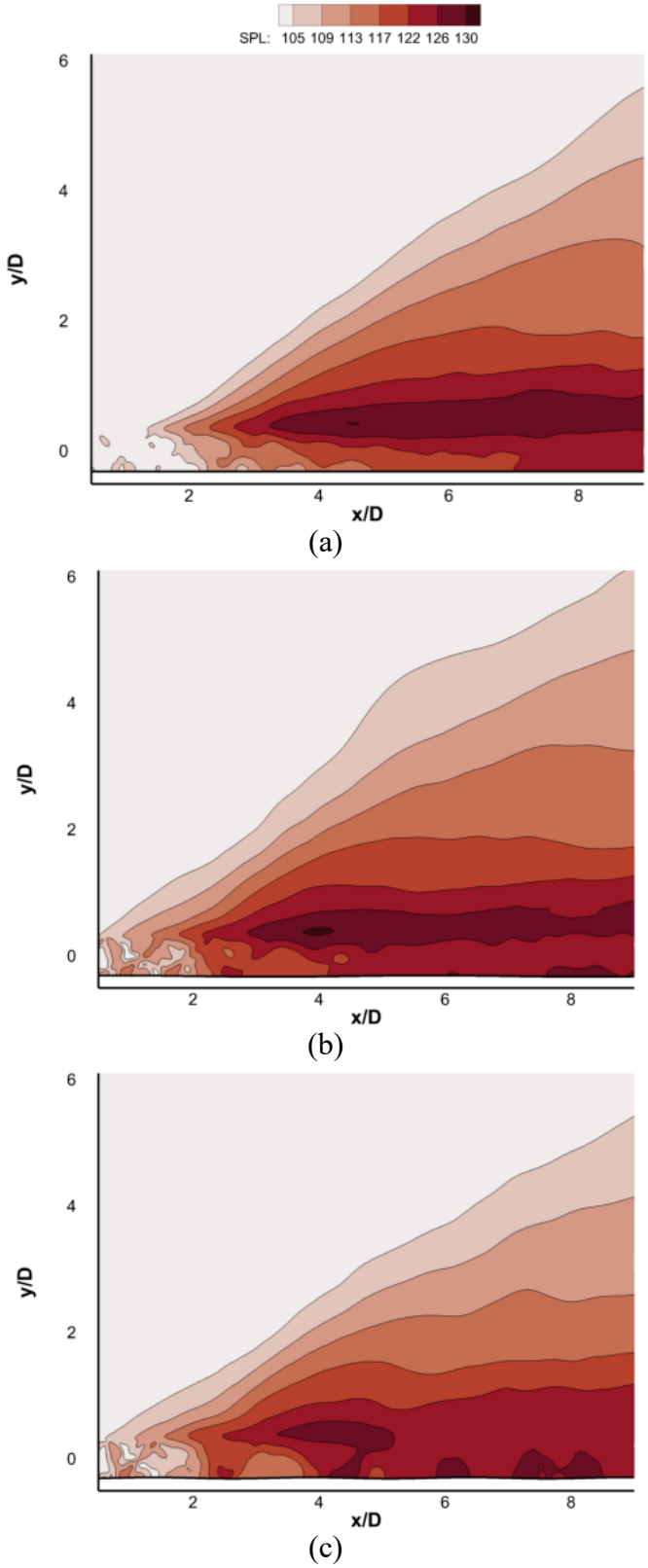

Figure 3.55 SPL. (a) Flat Plate ($h/D = 0$), (b) Case 4, (c) Case 5.

3.5.6. Acoustic Spectra (Wavy Wall at $h/D = 0$)

Quantitative assessment of the effect wavy wall at $h/D = 0$ is discussed here. The SPL spectra is shown in Figure 3.56 at the maximum radiation direction in the reflected, and shielded side (point A and A') for the flat plate, wavy wall with fundamental-wavelength (Case 4), and harmonic-wavelength (Case 5). As mentioned earlier for the acoustic analysis of the wavy wall at $h/D = 3$, the main objective is on the shielded side, which can be interpreted as the noise that reaches the ground. However, the reflected side results are provided as well, to provide more details on the effect of wavy shield on the wall jet acoustics.

Figure 3.56a shows that neither of the wavy wall cases significantly reduce the noise. The fundamental wavelength wavy wall increases the noise ~2dB on the reflected side, especially in the lower frequency range ($0 < St < 0.025$). This effect was shown previously in SPL contours in Figure 3.55. On the other hand, the harmonic-wavelength wall shows some slight reduction in the peak noise, as shown in the SPL contours.

Figure 3.56b, shows the SPL spectra on the shielded side. The figure illustrates that none of the wavy wall designs at $h/D = 0$, seems to provide effective noise reduction in the shielding side for the entire range of frequencies. Moreover, Case 4 shows some increase in noise levels, while the Case 5 does not have significant effect.

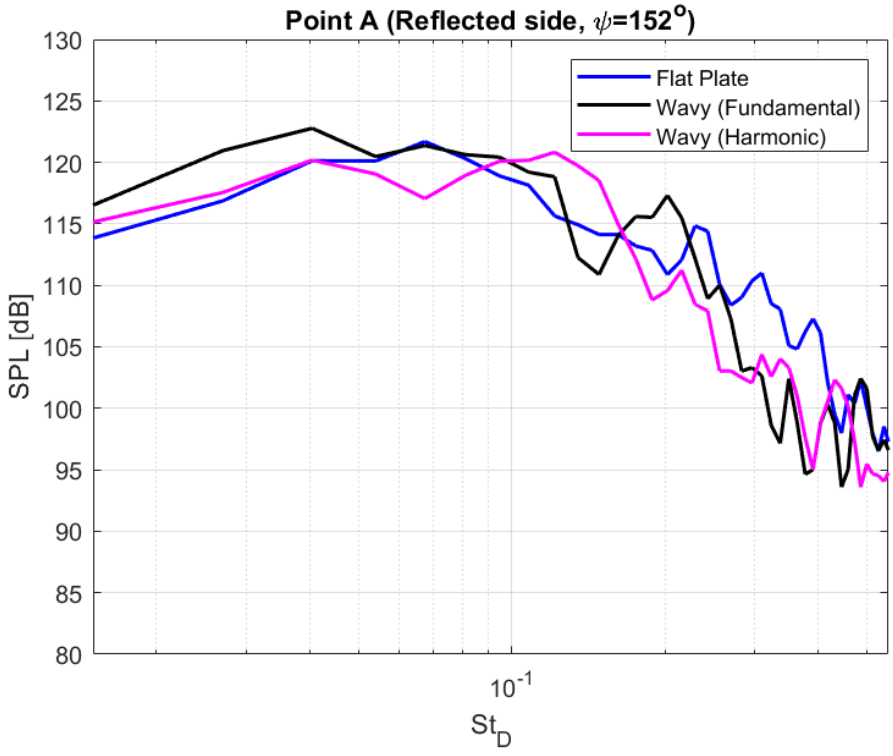

(a)

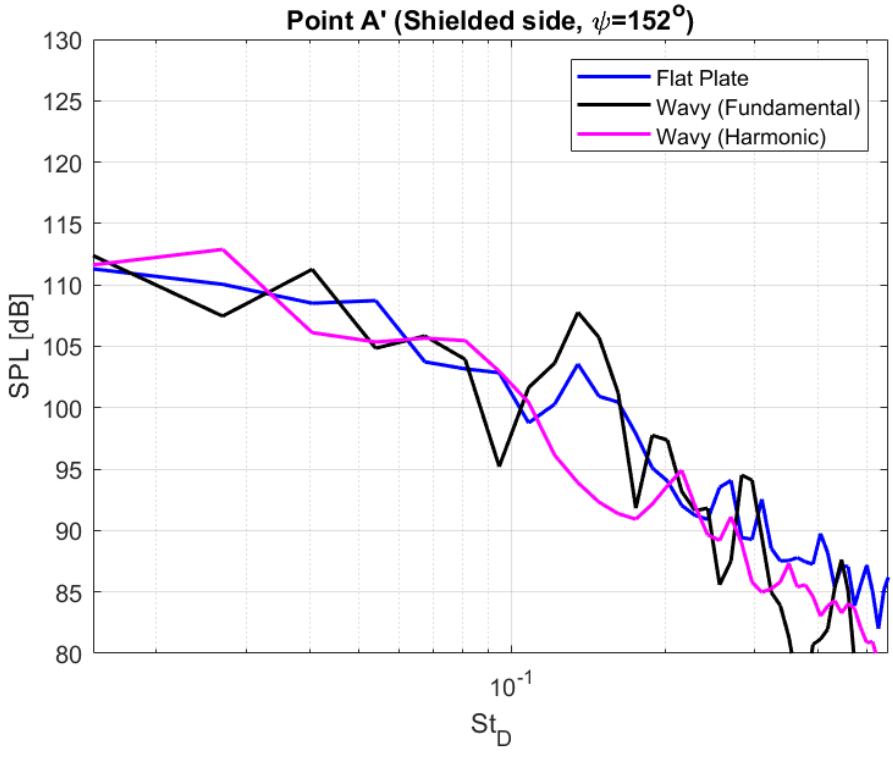

(b)

Figure 3.56 Acoustic spectra at $\psi = 152^o$ (a) reflected (A), and (b) shielded side (A'). (Flat Plate ($h/D = 0$), Case 4, and Case 5)

4. Conclusion and Future Work

In this work, two main scenarios are considered, when jet exhaust of the propulsion system interacts with solid surfaces. In Part I, Chapter 2, jet impingement on ground for a rocket lift-off is investigated. And in Part II, Chapter 3, interactions influenced by the integration of the engine with the airframe, is considered. Such complex applications require consideration of the role of acoustic-surface interactions on the noise generation of the jet and its radiation. The main concluding remarks, and objectives of each chapter is summarized here.

4.1. Concluding Remarks for Part I

The hybrid LES/URANS approach is adopted in Chapter 2 for simulation of a supersonic jet impinging on a flat plate. Water injection from the ground plate is modeled employing the VOF multiphase model to investigate the noise reduction mechanism. This is taken as a simplified model of noise suppression technique employed during rocket's launch using water injection from the launch pad. By using URANS near the walls, but LES with fine grid elsewhere, the radiated sound can be captured with feasible number of grid points. Numerical simulation of supersonic flow and its generated sound is particularly challenging when it contains water droplets. The gas-water interface is characterized by sharp density discontinuity causing numerical stiffness and instability.

Furthermore, the governing equations are strongly coupled through the introduction of the phase equation causing slow convergence. These issues were resolved by adopting a pressure-based coupled formulation of the volume-of-fluid multiphase method, and by computing corrections using an algebraic multi grid solver to accelerate convergence. The weighted QUICK-type scheme is used to improve the spatial accuracy to enable

capturing the acoustic waves. A characteristics-based, non-reflecting boundary treatment allowed the acoustic waves to propagate with no reflections at the computational boundaries. The Ffowcs Williams-Hawkings method is used to extend the directly resolved acoustics to the far field. Some of the key observations of this study for the base case (no injection) are summarized below.

The numerical approach adopted here successfully resolves the acoustic field, and it is free from reflections at the boundaries. The computed results agree favorably with the measurement of the flow fluctuations on the impingement plate, as well as with the acoustic spectra.

As for the noise sources, the shock waves were found to be weak since the jet is operating at near-ideally-expanded condition. The flow field and the acoustic pressure field indicate that the dominant noise source is the large-scale structure in the plume as it approaches the impingement plate and interacts with the unsteady vortical structure in the free shear layer at the outer edge of the wall jet.

The predicted acoustic spectra show the same level of the broadband noise as in the experiment. The frequency of the tone is also well predicted, but the level of the tone is underpredicted, which is attributed to the sampling size of the data processed to obtain the spectra.

To investigate the sensitivity of FWH surface to its radial extent on the impingement plate, a cylindrical FWH surface was considered with varying the radial extent near the impingement plate. It was concluded that the radial extent of the FWH surface has some effect, though minor, on the predicted spectra.

When water is injected from the impingement plate it affects the flow field, as well as

the radiated sound. Some of the significant observations for the effect of water on the flow and acoustic field are summarized below.

Comparing the time-averaged Mach number contours suggests that the weak shocks in the vicinity of the nozzle exit are hardly affected by the water, which is injected farther way from the impingement plate. However, the flow fluctuations along the jet sheer layer are somewhat affected by water injection. This is attributed to the momentum exchange and turbulent mixing introduced by the water injection.

The wall jet profiles show that water injection reduces the radial extent of the impinging zone. The water microjets in the present case introduce momentum that is in opposite direction to that of the wall jet and accelerates its radial decay.

Both the simulations and measurements show that water injection from the ground plane does reduce the far field sound by about 2-3 dB at low frequencies (up to 4kHz). The present computation, however, overestimates the noise reduction as compared to the experiment at higher frequencies.

By examining snapshots of the radiated field, as well as the pressure and velocity fluctuations of the jet plume and the wall jet free surface. It is concluded that there are three dominant mechanisms by which water injection reduced noise: In the first one, given the higher density of the water and the direction of injection, it reduces the physical extent of the noise-producing wall region via exchange of the momentum. Secondly, (as in the case of chevrons), the injection introduces small disturbances that interacts with the noise-efficient large-scale flow structure. This reduces the large-scale structure and hence the radiated sound. Thirdly, through scattering of the transmitted sound. As the generated sound waves propagate outward, they encounter some water droplets. This causes some

scattering of the propagating sound waves and a reduction of the amplitude of the transmitted wave.

4.2. Suggested Future Work for Part I

The numerical simulation of water injection into a supersonic medium is a challenging task, and several simplifications were considered. However, this work can be a steppingstone to consider further complicated situations.

One of the mechanisms that was not targeted in this work is the cooling effect of the cold-water injection on noise generated by a hot supersonic jet. Further investigations considering the conjugate heat transfer and phase change, could provide much deeper insight on the mechanisms involved in the noise reduction achieved by water injection. And can open several doors towards optimized designs that can provide much effective noise reduction.

Another area of research discussed in this work was to focus on the liquid-gas interaction. Further investigations on the scenarios where the water injectors are positioned near the nozzle could provide valuable insight on optimizing the noise reduction achieved via liquid injection. Since the focus of this work was interactions of the supersonic jet with solid surfaces, the near-nozzle water injection was beyond the scope of this study. Although this type of water injection may not be ideal for in-flight aircraft applications, due to the high mass flow required by the water injectors. But, the principals discussed in this work could be used to investigate water injection near the nozzle exhaust during the aircraft run-up on the runway, or to be implemented on the aircraft carrier decks for the noise rection of the aircraft fighter jets during takeoff.

4.3. Concluding Remarks for Part II

The second part of this work, the effect of shielding plate on the flow field and the acoustics of a supersonic jet is investigated. The shielding effect of a solid surface is investigated as a noise reduction approach, targeted for supersonic aircraft concepts with an integrated design of the engine and airframe. First the effect of the flat plate is investigated, and the physical mechanisms by which the aeroacoustics of the jet is affected due to position of the flat plate. Next, the possibility of introducing a wavy surface in the airframe of the shielded configuration of the top-mounted engine to reduce the source of supersonic jet noise. To assess the benefit of this idea, results are compared with the case where the surface under the engine is simply flat. A hybrid LES/URANS approach is employed to calculate both the flow and acoustic field for both the proposed wavy surface and the conventual flat surface.

To validate the computational approach, the isolated jet, and the cases where jet is exhausting parallel to a flat plate, are simulated and the results are compared with corresponding experimental measurements. For the isolated jet case the predicted flow and acoustics agree well with the data. Likewise, current numerical flow simulations and acoustic data agreed well with the corresponding experimental data of a jet issuing parallel to flat plate shield.

In addition, the latter case is examined in detail to understand why a flat shield is not quite effective. Two mechanisms were found that affect the efficiency of the flat shield. If the flat shield is close to the jet, part of the flow acts as a wall jet, and this can adversely affect the noise source. If the flat shield is away from the jet flow, the radiated acoustic field reflects from the solid surface and can amplify the jet noise source.

These two mechanisms have led us to propose a new design for the airframe surface under the top-mounted engine to utilize these two mechanisms to effectively reduce the sound source. Two technologically important cases for aircraft design namely $h/D = 3$ and 0, was considered in this work.

In the case of $h/D = 3$, the wavy wall profile is utilized such that the acoustic waves reflecting from the shield are manipulated in a way to reduce the noise source itself. This is done by estimating the Strouhal number and wavelength of the dominant noise sources in the jet flow. The wavy wall is then designated with the appropriate wavelength, phase shift and amplitude in such a way that the acoustic reflected from the wall results in reducing the sound source. Computational results of the near field have verified the successes of this concept as it clearly reduces both the strength and extent of the source when the appropriately designed wavy shield replaces the equivalent flat shield.

The computational results have verified this concept as it shows that the noise source in the initial region of the jet associated with the noise-efficient large-scale structure has been reduced when the flat surface is replaced with the wavy wall. In the shielded side the results show that this design achieves as much as 4 dB reduction of the peak noise at the maximum radiation direction, and 3 dB reduction in the total integrated spectrum noise relative to what the flat surface achieves.

On the non-shielded side, a flat surface increases the noise. On the other hand, since the wavy surface reduces the source itself, it also reduces the noise in the unshielded side by as much as 2 dB compared to the isolated jet case. Thus, the wavy wall surface can be beneficial to engines mounted on the top of the airframe or under the wing.

In the case of $h/D = 0$, the wavy wall profile is utilized such that the the boundary

layer of the jet flow is manipulated such that the introduced fluctuations can modify the flow and acoustic field. Following the same analogy described for $h/D = 3$ cases, the estimation of wavelength and its harmonic are considered in a similar fashion. However, the amplitude and the axial distance of the phase shift is adjusted according to the wall jet flow.

The nearfield results suggest that the wavy wall located at $h/D = 0$, can have both positive and negative effects on the sound source. The harmonic wavy wall reduces the top shear layer fluctuations. However, the boundary layer fluctuations at the wavy wall are shown to be increased significantly. This increased fluctuations of the boundary layer counterbalances the reduction in the top shear layer fluctuations. The computed acoustic spectra suggest that none of the wavy wall designs at $h/D = 0$, provide effective noise reduction in the shielding side, and only a slight reduction in the reflected side for the harmonic wavy wall case.

4.4. Suggested Future Work for Part II

The directional noise reduction by shielding flat plate was shown to be highly dependent on the dimensions of the plate with respect to the jet. By focusing on the flat plate effect, further investigations and sensitivity analysis on the various dimensions would provide optimal noise reduction.

The numerical simulations carried out in this work, required basis for comparison with the available experiments. Hence the exact same geometry from the experimental studies was used here. However, the more realistic concepts, discussed in Chapter1, would probably have a more sophisticated surface geometry and dimensions. The discussed mechanisms in this work can provide valuable insight to analyze the

aeroacoustics of the interaction of the jet with such solid surfaces.

Another interesting area of research could be the investigation of the shield plate during the supersonic flight. The focus of the numerical simulations in this study was to investigate the jet-surface interactions, and the simulations were carried out on the uninstalled jet, like the experiments. In addition, including the effect of incoming supersonic freestream on the jet, and interaction of the jet with the shocks generated by the shielding surface, is a much more complex problem. The groundwork of the research explained in this work can help investigations of the further complicated situations. The in-flight investigation of jet-surface interaction could lead to suggestion of much more complex designs, to target multiple aspects of the noise generation and radiation in the supersonic flight.

REFERENCES

Abgrall, R., & Karni, S. (2001). Computations of Compressible Multifluid. *Journal of Computational Physics*, 169(2), 594-623. doi: 10.1006/jcph.2000.6685

Aikens, K. M., Blaisdell, G. A., & Lyrintzis, A. S. (2015, Jan 5-9). *Analysis of Converging-Diverging Beveled Nozzle Jets Using Large Eddy Simulation with a Wall Model* [AIAA 2015-0509]. 53rd AIAA aerospace sciences meeting, Kissimmee, FL, United States. doi: 10.2514/6.2015-0509

Akamine, M., Nakanishi, Y., Okamoto, K., Teramoto, S., Okunuki, T., & Tsutsumi, S. (2015). Acoustic Phenomena from Correctly Expanded Supersonic Jet Impinging on Inclined Plate. *AIAA Journal*, 53(7), 2061-2067. doi: 10.2514/1.J053953

Alestra, S., Terrasse, I., & Troclet, B. (2003). Inverse Method for Identification of Acoustic Sources at Launch Vehicle Lift-Off. *AIAA Journal*, 41(10), 1980-1987. doi: 10.2514/2.7318

Alkislar, M. B. (2008, May 5-7). *Aeroacoustics of Mach 0.9 Jet with Chevron-Microjet Combination* [AIAA 2008-3041]. 14th AIAA/CEAS Aeroacoustics Conference (29th AIAA Aeroacoustics Conference), Vancouver, BC, Canada. doi: 10.2514/6.2008-3041

Alkislar, M. B., Krothapalli, A., & Butler, G. W. (2007). The Effect of Streamwise Vortices on the Aeroacoustics of a Mach 0.9 Jet. *Journal of Fluid Mechanic*, 578, 139-169. doi: 10.1017/S0022112007005022

Allgood, D., Saunders, G., & Langford, L. (2011, Jan 9-12). *Reduction of Altitude Diffuser Jet Noise Using Water Injection* [AIAA 2012-0680]. 50th AIAA Aerospace Sciences Meeting including the New Horizons Forum and Aerospace Exposition. doi: 10.2514/6.2012-680

Alvi, F. S., Shih, C., Elavarasan, R., Garg, G., & Krothapalli, A. (2003). Control of Supersonic Impinging Jet Flows Using Supersonic Microjets. *AIAA Journal*, 41(7), 347-1355. doi: 10.2514/2.2080

Alvi, F., Shih, C., & Krothapalli, A. (2000, Jan 8-11). *Active control of the feedback loop in high-speed jets* [AIAA 2001-0373]. 39th Aerospace Sciences Meeting and Exhibit, Reno, NV, United States. 10.2514/6.2001-373

Anderson, J. D. (1982). *Modern Compressible Flow: With Historical Perspective.* New York, NY: McGraw Hill Inc.

André, B., Castelain, T., & Bailly, C. (2013). Broadband Shock-Associated Noise in Screeching and Non-Screeching Under Expanded Supersonic Jets. *AIAA Journal*, 51(3), 665-673. doi: 10.2514/1.J052058

Annaswamy, A., Choi, J. J., Sahoo, D., Alvi, F. S., & Lou, H. (2002, Dec 10-13). Active Closed-Loop Control of Supersonic Impinging Jet Flows Using POD Models. *Proceedings of the 41st IEEE Conference on Decision and Control*, 3, 3294-3299. doi: 10.1109/CDC.2002.1184381

ANSYS® FLUENT, Release 18.2

Arbey, H., & Ffowcs Williams, J. E. (1984). Active Cancellation of Pure Tones in an Excited Jet. *Journal of Fluid Mechanics*, 149, 445-454. doi: 10.1017/S0022112084002743

Baier, F., Karnam, A., Gutmark, E. J., & Kailasanath, K. (2018, Jan 8-12). *High Temperature Supersonic Flow Measurements of a Rectangular Jet Exhausting over a Flat Surface* [AIAA 2018-0012]. 2018 AIAA Aerospace Sciences Meeting, Grapevine, Kissimmee, FL, United States. doi: 10.2514/6.2018-0012

Baier, F., Mora, P.A., Gutmark, E.J., & Kailasanath, K. (2017, Jan 9-13). *Flow Measurements from a Supersonic Rectangular Nozzle Exhausting Over a Flat Surface* [AIAA 2017-0932]. 55th AIAA Aerospace Sciences Meeting, Grapevine, TX, United States. doi: 10.2514/6.2017-0932

Barth, T. J., & Jespersen, D. C. (1989, Jan 9-12). *The Design and Application of Upwind Schemes on Unstructured Meshes*. 27th Aerospace Sciences Meeting, Reno, NV, United States. doi: 10.2514/6.1989-366

Basner, M., Clark, C., Hansell, A., Hileman, J. I., Janssen, S., Shepherd, K., & Sparrow, V. (2017). Aviation Noise Impacts: State of The Science. *Noise & Health*, 19(87), 41-50.

Bertsch, L., Snellen, M., Enghardt, L., & Hillenherms, C. (2019). Aircraft Noise Generation and Assessment: Executive Summary. *CEAS Aeronautical Journal*, 10, 3-9. doi: 10.1007/s13272-019-00384-3

Bhat, T. R. S. (1998). *Jet-Flap Installation Noise* [NASA-TN-D-6636, E-6662], NASA Lewis Research Center; Cleveland, OH, United States. https://ntrs.nasa.gov/search.jsp?R=19720011375

Bhat, T. R. S., & Blackner, A. M. (1998, Jan 12-15). *Installed jet noise prediction model for coaxial jets*. 36th AIAA Aerospace Sciences Meeting and Exhibit, Reno, NV, United States. doi: 10.2514/6.1998-79

Blackner, A. M., & Bhat, T. R. S. (1998, Jan 12-15). *Installation Effects on Coaxial Jet Noise – an Experimental Study*. 36th AIAA Aerospace Sciences Meeting and Exhibit, Reno, NV, United States. doi: 10.2514/6.1998-80

Boger, M. (2014). *Numerical Modeling of Compressible Two-Phase Flows with a Pressure-Based Method* [Doctoral Dissertation, Institute of Aerodynamics and Gas Dynamics, University of Stuttgart].

Brehm, C., Housman, J. A., & Kiris, C. C. (2016). Noise Generation Mechanisms for a Supersonic Jet Impinging on an Inclined Plate. *Journal of Fluid Mechanics*, 797, 802-850. doi: 10.1017/jfm.2016.244

Brentner, K. S, & Farassat, F. (1998). Analytical Comparison of the Acoustic Analogy and Kirchhoff Formulation for Moving Surface. *AIAA Journal*, 36(8), 1379-1386. doi: 10.2514/2.558

Bridges, J. E. (2014, Jan 13-17). *Noise from Aft Deck Exhaust Nozzles - Differences in Experimental Embodiments* [AIAA 2014-0876]. 52nd Aerospace Sciences Meeting, National Harbor, MD, United States. doi: 10.2514/6.2014-0876

Bridges, J. E., Podboy, G. G., & Brown, C. A. (2016, May 30-June 1). *Testing Installed Propulsion for Shielded Exhaust Configurations* [AIAA 2016-3042]. 22nd AIAA/CEAS Aeroacoustics Conference, Lyon, France. doi: 10.2514/6.2016-3042

Bridges, J. E., & Wernet, M. P. (2015, June 22-26). *Noise measurements of high aspect ratio distributed exhaust systems* [AIAA 2015-3119]. 21st AIAA/CEAS Aeroacoustics Conference, Dallas, TX, United States. doi: 10.2514/6.2015-3119

Brown, C. A. (2015, Jan 5-9). *An Empirical Jet-Surface Interaction Noise Model with Temperature and Nozzle Aspect Ratio Effects* [AIAA 2015-0229]. 53rd AIAA Aerospace Sciences Meeting, Kissimmee, FL, United States. doi: 10.2514/6.2015-0229

Brown, C. A. (2015, June 22-26). *Empirical Models for the Shielding and Reflection of Jet Mixing Noise by a Surface* [AIAA 2015-3128]. 21st AIAA/CEAS Aeroacoustics Conference, Dallas, TX, United States. doi: 10.2514/6.2015-3128

Brown, C. A. (2012, June 11-15). *Jet-Surface interaction test: far-field noise results.* Proceedings of the ASME. Turbo Expo: Power for Land, Sea, and Air, Volume 1: Aircraft Engine; Ceramics; Coal, Biomass and Alternative Fuels; Controls, Diagnostics and Instrumentation, Copenhagen, Denmark. doi: 10.1115/GT2012-69639

Brown, C. A., Clem, M. M., & Fagan, A. F. (2014). Investigation of Broadband Shock Noise from a Jet Near a Planar Surface. *Journal of Aircraft*, 52, 266-273. doi: 10.2514/1.C032695

Brown, G. L., & Roshko, A. (1974) On Density Effects and Large Structure in Turbulent Mixing Layers. *Journal of Fluid Mechanics*, 64(4), 775-816. doi: 10.1017/S002211207400190X

Brown, M., & Frendi, A. (2012, June 4-6). *Supersonic Jet Impingement on a Flat Plate* [AIAA 2012-2261]. 18th AIAA/CEAS Aeroacoustics Conference (33rd AIAA Aeroacoustics Conference), Colorado Springs, CO, United States. doi: 10.2514/6.2012-2261

Brown, W. H., & Ahuja, K. K. (1984, Oct 10-15). *Jet and wing/flap interaction noise*. 9th Aeroacoustics Conference, Williamsburg, VA, United States. doi: 10.2514/6.1984-2362

Castiglioni, G., & Domaradzki, J. A. (2015). A Numerical Dissipation Rate and Viscosity in Flow Simulations with Realistic Geometry Using Low-Order Compressible Navier–Stokes Solvers. *Computers & Fluids*, 119, 37-46. doi: 10.1016/j.compfluid.2015.07.004

Chan, L., Chin, C., Soria, J., & Ooi, A. (2014). Large Eddy Simulation and Reynolds-Averaged Navier-Stokes Calculations of Supersonic Impinging Jets at Varying Nozzle-to-Wall Distances and Impinging Angles. *International journal of heat and fluid flow*, 47, 31-41. doi: 10.1016/j.ijheatfluidflow.2014.02.005

Chauvet, N., Sebastien, D., & Jacquin, L. (2007). Numerical Study of Mixing Enhancement in A Supersonic Round Jet. *AIAA Journal*, 45(7), 1675-1687. doi: 10.2514/1.27497

Clem, M., Brown, C., and Fagan, A. (2013, Jan 7-10). *Background Oriented Schlieren Implementation in a Jet-Surface Interaction Test*. 51st AIAA Aerospace Sciences Meeting including the New Horizons Forum and Aerospace Exposition, Grapevine, (Dallas/Ft. Worth Region), TX, United States. doi: 10.2514/6.2013-38

Coderoni, M., Lyrintzis, A. S., & Blaisdell, G. A. (2019). Large-Eddy Simulations Analysis of Supersonic Heated Jets with Fluid Injection for Noise Reduction. *AIAA Journal*, 57(8), 3442-3455. doi: 10.2514/1.J057674

Coderoni, M., Lyrintzis, A. S., & Blaisdell, G. A. (2018). Noise Reduction Analysis of Supersonic Unheated Jets with Fluidic Injection Using Large Eddy Simulations. *International Journal of Aeroacoustics*, 17(4-5), 467-501. doi: 10.1177%2F1475472X18778285

Cole, J.N., von Gierke, H.E., Kyrazis, D.T., Eldred, K.M., & Humphrey, A.J. (1957, Dec). *Noise Radiation from Fourteen Types of Rockets in the 1,000 to 130,000 Pounds Thrust Range*. Wright Air Development Center (WADC) Technical Report, 57-354.

Crighton, D. G., & Ffowcs Williams, J. E. (1969). Sound Generation by Turbulent Two-Phase Flow. *Journal of Fluid Mechanics*, 36(3), 585-603. doi: 10.1017/S0022112069001868

Crow, S., & Champagne, F. (1971). Orderly Structure in Jet Turbulence. *Journal of Fluid Mechanics*. 48(3), 547-591. doi: 10.1017/S0022112071001745

Czech, M. J., Russell H. T, & Ronen E. (2012). Propulsion Airframe Aeroacoustic Integration Effects for a Hybrid Wing Body Aircraft Configuration. *International Journal of Aeroacoustics*, 11(3-4), 335-367. doi: 10.1260%2F1475-472X.11.3-4.335

Dahl, M. D. & Papamoschou, D. (2000). Analytical Predictions and Measurements of The Noise Radiated from Supersonic Coaxial Jets. *AIAA J*ournal, 38, 584-591. doi: 10.2514/2.1026

Datt P. (2011). Latent Heat of Vaporization/Condensation. *Encyclopedia of Snow, Ice and Glaciers*: *Encyclopedia of Earth Sciences Series*. Dordrecht, UK: Springer.

Davidson, L. (2009). Large-Eddy Simulations: How to Evaluate Resolution. *International Journal of Heat and Fluid Flow*, 30(5), 1016-1025. doi: 10.1016/j.ijheatfluidflow.2009.06.006

Davies, M. G., & Oldfield, D. E. S. (1962). Tones from a Choked Axisymmetric Jet I. Cell Structure, Eddy Velocity and Source Locations. *Acta Acustica united with Acustica*, 12(4), 257-267.

Di Francescantonio, P. (1997). A New Boundary Integral Formulation for the Prediction of Sound Radiation. *Journal of Sound and Vibration*, 202(4), 491-509. doi: 10.1006/jsvi.1996.0843

Dong, T. Z., & Mankbadi, R. R. (1999). Simulation of Unsteady Flow in Nozzle-Ejector Mixer. *Journal of Propulsion and Power*, 15(4), 539-543. doi: 10.2514/2.5476

Dong, T. Z., & Mankbadi, R. R. (1996, May 6-8). *Large-Eddy Simulations of Sound Due to Turbulence Mixing Inside an Ejector* [AIAA 1996-1731]. Aeroacoustics Conference, State College, PA, United States. doi: 10.2514/6.1996-1731

Elavarasan, R., Krothapalli, A., Venkatakrishnan, L., & Lourenco, L. (2001). Suppression of Self-Sustained Oscillations in a Supersonic Impinging Jet. *AIAA Journal*, 39(12), 2366-2373. doi: 10.2514/2.1243

Elavarasan, R., Venkatakrishnan, L., Krothapalli, A., & Lourenco, L. (2000). A PIV Study of a Supersonic Impinging Jet. *Journal of Visualization*, 2(3-4), 213-22. doi: 10.1007/BF03181438

Faranosov, G., Kopiev, V., Ostrikov, N., & Kopiev, V. A. (2016, May 30-June 1). *The Effect of Pylon on the Excess Jet-Flap Interaction Noise* [AIAA 2016-3043]. 22nd AIAA/CEAS Aeroacoustics Conference, Lyon, France. doi: 10.2514/6.2016-3043

Federal Aviation Regulation. (2005). *Noise Standards: Aircraft Type and Airworthiness Certification* (Part 36, Section 5), US Government Printing Office, Washington D.C., United States.

Ffowcs Williams, J. E., & Maidanik, G. (1965). The Mach Wave Field Radiated by Supersonic Turbulent Shear Flows. *Journal of Fluid Mechanics*, 21(4), 641-657. doi: 10.1017/S0022112065000393

Ffowcs Williams, J. E., Simpson, J., & Virchis, V. J. (1975). Crackle: An Annoying Component of Jet Noise. *Journal of Fluid Mechanics*, 71(2), 251-271. doi: 10.1017/S0022112075002558

Ffowcs Williams, J. E., & Hawkings, D. L. (1969). Sound Generation by Turbulence and Surfaces in Arbitrary Motion. *Philosophical Transactions of the Royal Society of London. Series A, Mathematical and Physical Sciences*, 264(1151), 321-342. doi: 10.1098/rsta.1969.0031

Franquet, E., Perrier, V., Gibout, S., & Bruel, P. (2015). Free Underexpanded Jets in a Quiescent Medium: A Review," *Progress in Aerospace Sciences*, 77, 25-53. doi: 10.1016/j.paerosci.2015.06.006

George, A. R., & Lyrintzis, A. S. (1986, July 9-11). *Mid-Field and Far-Field Calculations of Transonic Blade-Vortex Interactions*. AIAA 10th Aeroacoustics Conference, Seattle, WA, United States. doi: 10.2514/6.1986-1854

Giles, M. B. (1990). Nonreflecting Boundary Conditions for Euler Equations Calculations. *AIAA Journal*, 28(12), 2050-2058. doi: 10.2514/3.10521

Gliebe, P. R., (2003). *The GE90: Quiet by Design: Quieter Aircraft Engines Through Leveraging New Technologies.* Presentation for 2003 Berkeley Airport Noise Symposium, Doing the Wright Stuff: 100 years of Aviation and the Environment.

Goldstein, M. E., Leib, S. J., & Afsar, M. Z. (2019). Rapid Distortion Theory on Transversely Sheared Mean Flows of Arbitrary Cross-Section. *Journal of Fluid Mechanics*. 881, 551-584. 2019. doi: 10.1017/jfm.2019.750

Golubev, V., Lyrintzis, A., Mankbadi, R. R., Kurbatskii, K. A., & Guenthoer, B. (2014, June 16-20). *Numerical prediction of an acoustic field of a supersonic jet impinging on a plate at different inclination angles* [AIAA 2014-3308]. 20th AIAA/CEAS aeroacoustics conference, Atlanta, GA, United States. doi: 10.2514/6.2014-3308

Greenshields, C. J., Weller, H. G., Gasparini, L., & Reese, J. M. (2010). Implementation of Semi-Discrete, Non-Staggered Central Schemes in a Colocated, Polyhedral, Finite Volume Framework, For High-Speed Viscous Flows. *International Journal for Numerical Methods in Fluids*, 63(1), 1-21. doi: 10.1002/fld.2069

Greska, B., & Krothapalli, A. (2004, May 10-12). *Jet Noise Reduction Using Aqueous Microjet Injection* [AIAA 2004-2971]. 10th AIAA/CEAS Aeroacoustics Conference, Manchester, Great Britain. doi: 10.2514/6.2004-2971

Greska, B., & Krothapalli, A. (2005, May 23-25). *The Near-Field Effects of Microjet Injection* [AIAA 2005-3046]. 11th AIAA/CEAS Aeroacoustics Conference, Monterey, CA, United States. doi: 10.2514/6.2005-3046

Greska, B., Krothapalli, A., Seiner, J., Jansen, B., & Ukeiley, L. (2005, May 23-25). *The Effects of Microjet Injection on an F404 Jet Engine* [AIAA 2005-3047]. 11th AIAA/CEAS Aeroacoustics Conference, Monterey, California, United States. doi: 10.2514/6.2005-3047

Gritskevich, M. S., Garbaruk, A. V., Schütze, J., and Menter, F. R. (2012). Development of DDES and IDDES Formulations for the k-ω Shear Stress Transport Model. *Flow Turbulence and Combustion*, 88(3), 431-449. doi: 10.1007/s10494-011-9378-4

Gustavsson, J. P. R., Ragaller, P. A., Kumar, R., & Alvi, F. S. (2010, June 7-9). *Temperature Effect on Acoustics of Supersonic Impinging Jet* [AIAA 2010-3785]. 16th AIAA/CEAS Aeroacoustics conference, Stockholm, Sweden. doi: 10.2514/6.2010-3785

Hardin J. C., Ristorcelli J. R., and Tam C. K. W., (May 1995) *ICASE/LaRC Workshop on benchmark problems in computational aeroacoustics (CAA)* [NASA-CP-3300, L-17497, NAS 1.55:3300], NASA Langley Research Center, Hampton, VA, United States.

Harper-Bourne, M., & Fisher, M. J. (1973). *The Noise from Shock Waves in Supersonic Jets* [AGARD CP-131, 11-1-11-13]. AGARD Conference on Noise Mechanisms, Brussels, Belgium.

Head, R. W., & Fisher, M. J. (1976, July 20-23). *Jet/Surface Interaction Noise: -Analysis of Farfield Low Frequency Augmentation of Jet Noise due to the Presence of a Solid Shield*. 3rd Aeroacoustics Conference, Palo Alto, CA, United States. doi: 10.2514/6.1976-502

Heath, S., Brooks, T., Hutcheson, F. V., Doty, M. J., Haskin, H., Spalt, T., Bahr, C. J., Burley, C. L., Bartram, S., Humphreys, W, Lunsford, C. (2013, June 24-27). *Hybrid Wing Body Aircraft Acoustic Test Preparations and Facility Upgrades* [AIAA 2013-2623]. Ground Testing Conference, San Diego, CA, United States. doi: 10.2514/6.2013-2623

Heeb, N., Kastner, J., Gutmark, E., & Kailasanath, K. (2013). Supersonic Jet Noise Reduction by Chevrons and Fluidic Injection. *International Journal of Aeroacoustics*, 12(7-8), 679-697. doi: 10.1260%2F1475-472X.12.7-8.679

Henderson, B. & Norum, T. (2008, May 5-7). *Impact of Azimuthally Controlled Fluidic Chevrons on Jet Noise* [AIAA 2008-3062]. 14th AIAA/CEAS Aeroacoustics Conference (29th AIAA Aeroacoustics Conference), Vancouver, BC, Canada. doi: 10.2514/6.2008-3062

Henderson, B. & Norum, T. (2007, May 21-23). *Impact of Fluidic Chevrons on Supersonic Jet Noise* [AIAA 2007-3595]. 13th AIAA/CEAS Aeroacoustics Conference (28th AIAA Aeroacoustics Conference), Rome, Italy. doi: 10.2514/6.2007-3595

Henderson, B. (2010). Fifty Years of Fluidic Injection for Jet Noise Reduction. *International Journal of Aeroacoustics*, 9(1-2), 91-122. doi: 10.1260/1475-472X.9.1-2.91

Henderson, B. (2002). The Connection Between Sound Production and Jet Structure of The Supersonic Impinging Jet. *Journal of the Acoustical Society of America*, 111(2), 735-747. doi: 10.1121/1.1436069

Henderson, B., & Doty, M. (2012, Sep). *Advanced Jet Noise Exhaust Concepts in NASA's N+2 Supersonics Validation Study and the Environmentally Responsible Aviation Project's Upcoming Hybrid Wing Body Acoustics Test* [E-18503]. Virginia Tech Graduate Seminar, Blacksburg, VA, United States. https://ntrs.nasa.gov/search.jsp?R=20130000430

Henderson, B., Bridges, J., & Wernet, M. (2005). An Experimental Study of The Oscillatory Flow Structure of Tone Producing Supersonic Impinging Jets. *Journal of Fluid Mechanics*, 542, 115-137. doi: 10.1017/S0022112005006385

Hixon, D. R., Shih, S. H., Mankbadi, R. R. (1995). Evaluation of Boundary Conditions for Computational Aeroacoustics. *AIAA Journal*, 33(11), 2006-2012. doi: 10.2514/3.12940

Hixon, R. (1997, May 12-14). *On Increasing the Accuracy of Maccormack Schemes for Aeroacoustic Applications* [AIAA 1997-1586-CP]. 3rd AIAA/CEAS Aeroacoustics Conference, Atlanta, GA, United Sates. doi: 10.2514/6.1997-1586

Hixon, R., Shih, S. -H, & Mankbadi, R. R. (1997, Jan 6-9). *Effect of Coannular Flow on Linearized Euler Predictions of Jet Noise* [AIAA 1997-0284].35th Aerospace Sciences Meeting and Exhibit, Reno, Nevada, United States. doi: 10.2514/6.1997-284

Ho, C. M., & Nossier, N. S. (1981). Dynamics of An Impinging Jet – Part 1: The Feedback Phenomenon," *Journal of Fluid Mechanics*, 105, 119-142. doi: 10.1017/S0022112081003133

Honda, H., Nonomura, T., Fujii, K., & Yamamoto, M. (2011, June 27-30). *Effects of Plate Angles on Acoustic Waves from a Supersonic Jet Impinging on an Inclined Flat Plate* [AIAA 2011-3260]. 41st AIAA fluid dynamics conference and exhibit, Honolulu, Hawaii, United States. doi: 10.2514/6.2011-3260

Hunt, J. C., Wray, A. A., & Moin, P. (1988). *Eddies, Streams, and Convergence Zones in Turbulent Flows* [89N24555]. Center for Turbulence Research. Proceedings of the Summer Program, Stanford University, CA, United States.

Hutchinson, B. R., & Raithby, G. D. (1986). Multigrid Method Based on the Additive Correction Strategy. *Numerical Heat Transfer*, 9(5), 511-537. doi: 10.1080/10407788608913491

Huynh, H. T., Wang, Z. J., & Vincent, P. E. (2014). High-Order Methods for Computational Fluid Dynamics: A Brief Review of Compact Differential Formulations on Unstructured Grids. *Computers & Fluids*, 98, 209-220. doi: 10.1016/j.compfluid.2013.12.007

Ibrahim, M. K., Kunimura, R., & Naakamura, Y. (2002). Mixing Enhancement of Compressible Jets by Using Unsteady Microjets as Actuators. *AIAA Journal*, 40(4), 681-687. doi: 10.2514/2.1700

Ignatius, J. K., Sankaran, S., Kumar, R. A., Satyanarayana, T. N. V., & Chakravarthy, S. R. (2008). Suppression of Jet Noise by Staged Water Injection during Launch Vehicle Lift-Off. *International Journal of Aeroacoustics*, 7(3-4), 223-241. doi: 10.1260%2F1475-472X.7.3.223

Ignatius, J. K., Sathiyavageeswaran, S., & Chakravarthy, S. R. (2014). Hot-Flow Simulation of Aeroacoustics and Suppression by Water Injection During Rocket Liftoff. *AIAA Journal*, 53(1), 235-245. doi: 10.2514/1.J053078

Ikawa, H., & Laspesa, F. S. (1985). Ignition/Duct Overpressure Induced by Space Shuttle Solid Rocket Motor Ignition. *Journal of Spacecraft and Rockets*, 22(4), 4841-488. doi: 10.2514/3.25776

Infosources. (2018). *F-35B in hover.* Retrieved from https://www.infosources.info/article.php?aid=389

Iwamoto, J. (1990). Impingement of Under-Expanded Jets on a Flat Plate. *ASME. Journal of Fluids Engineering*, 112(2), 179-184. doi: 10.1115/1.2909385

Janos, J. J., & Hoffman, S. (1969). *Forces and Moments due to Air Jets Exhausting Parallel to Large Flat Plates in a Near Vacuum*, [NASA-TN-D-5147], NASA Langley Research Center; Hampton, VA, United States. https://ntrs.nasa.gov/search.jsp?R=19690013720

Jiang, C., Han, T., Gao, Z., & Lee, C. H. (2019). A Review of Impinging Jets During Rocket Launching. *Progress in Aerospace Sciences*, 109(100547). doi:10.1016/j.paerosci.2019.05.007

Kandula, M. (2008). Prediction of Turbulent Jet Mixing Noise Reduction by Water Injection. *AIAA Journal*, 46(11), 2714-2722. doi: 10.2514/1.33599

Karnam, A., Baier, F., Gutmark, E. J., & Kailasanath, K. (2018, Jan 8-12). *Flow Measurement and Acoustic Investigation of High Temperature Rectangular Jets* [AIAA 2018-0260]. 2018 AIAA Aerospace Sciences Meeting, Kissimmee, FL, United States. doi: 10.2514/6.2018-0260

Kibens, V., Dorris, J., Smith, D. M., & Mossman, M. F. (1999, June 28-July 1). *Active Flow Control Technology Transition: The Boeing ACE Program*. 30th Fluid Dynamics Conference, Norfolk, VA, United States. doi: 10.2514/6.1999-3507

Klein, R. (1995). Semi-Implicit Extension of a Godunov-Type Scheme Based on Low Mach Number Asymptotic I: One-Dimensional Flow. *Journal of Computational Physics*, 121(2), 213-237. doi: 10.1016/S0021-9991(95)90034-9

Krothapalli, A., Greska, B., & Arakeri, V. (2002, June 17-19). *High Speed Noise Reduction Using Microjets* [AIAA-2002-2450]. 8th AIAA/CEAS Aeroacoustics Conference & Exhibit, Breckenridge, CO, United States. doi: 10.2514/6.2002-2450

Krothapalli, A., Rajkuperan, E., Alvi, F., & Lourenco, L. (1999). Flow Filed and Noise Characteristics of a Supersonic Impinging Jet. *Journal of Fluid Mechanics*, 392, 155-181. doi: 10.1017/S0022112099005406

Krothapalli, A., Venkatakrishnan, L., Elavarasan, R., & Lourenco, L. (2000, June 12-14). *Supersonic Jet Noise Suppression by Water Injection* [AIAA-2000-2025]. 6th Aeroacoustics Conference and Exhibit, Lahaina, HI, United States. doi: 10.2514/6.2000-2025

Krothapalli, A., Venkatakrishnan, L., Lourenco, L., Greska, B., & Elavarasan, R. (2003). Turbulence and Noise Suppression of a High-Speed Jet by Water Injection. *Journal of Fluid Mechanics*. 491, 131-159. doi: 10.1017/S0022112003005226

Kurbatskii, K., & Mankbadi, R.R. (2004). Review of Computational Aeroacoustics Algorithms. *International Journal of Computational Fluid Dynamics*, 18(6), 533-546. doi: 10.1080/10618560410001673542

Kurganov, A., Noelle, S., & Petrova, G. (2000). Semi-Discrete Central-Upwind Schemes for Hyperbolic Conservation Laws and Hamilton-Jacobi Equations. *SIAM Journal on Scientific Computing*, 23, 707-740. doi: 10.1137/S1064827500373413

Kurganov, A., & Petrova, G. (2001). A Third-Order Semi-Discrete Genuinely Multidimensional Central Scheme for Hyperbolic Conservation Laws and Related Problems. *Numerische Mathematik*, 88(4), 683-729. doi: 10.1007/PL00005455

Kurganov, A., & Tadmor, E. (2000). New High-Resolution Central Schemes for Nonlinear Conservation Laws and Convection Diffusion Equations. *Journal of Computational Physics*, 160(1), 241-282. doi: 10.1006/jcph.2000.6459

Laufer, J., Schlinker, R. H., & Kaplan, R. E. (1976). Experiments on Supersonic Jet Noise. *AIAA Journal*, 14, 489-497. doi: 10.2514/3.61388

Lele, S.K. (1992). Compact Finite Difference Schemes with Spectral-like Resolution. *Journal of Computational Physics*, 103, 16-42. doi: 10.1016/0021-9991(92)90324-R

Leonard, B. P., & Mokhtari, S. (1990). *ULTRA-SHARP Non-Oscillatory Convection Schemes for High-Speed Steady Multidimensional Flow* [NASA-TM-102568], NASA Lewis Research Center; Cleveland, OH, United States. https://ntrs.nasa.gov/search.jsp?R=19900012254

Liebeck, R.H. (2002). *Design of the Blended-Wing-Body Subsonic Transport*. 40th AIAA Aerospace Sciences Meeting and Exhibit, Reno, NV, United States. doi: 10.2514/1.9084

Lighthill, M. J. (1952). On Sound Generated Aerodynamically: I. General Theory. *Proceedings of the Royal Society of London. Series A. Mathematical and Physical Sciences*, 211, 564-581. doi: 10.1098/rspa.1952.0060

Lighthill, M. J. (1954). On Sound Generated Aerodynamically: II. Turbulence as a Source of Sound. *Proceedings of the Royal Society of London. Series A. Mathematical and Physical Sciences*, 222, 1-32. doi: 10.1098/rspa.1954.0049

Liou, M.S. (1987, March 24-26). *A Generalized Procedure for Constructing an Upwind-Based TVD Scheme* [AIAA 1987-0355], 25th AIAA Aerospace Sciences Meeting, Reno, NV, United States. doi: 10.2514/6.1987-355

Liu, J., Corrigan, A. T., Kailasanath, K., Heeb, N. S., & Gutmark, E. J. (2015, May 5-9). *Numerical Study of Noise Characteristics in Overexpanded Jet Flows* [AIAA 2015-0508]. 53rd AIAA Aerospace Sciences Meeting, Kissimmee, FL, United States. doi: 10.2514/6.2015-0508

Lockheed-Martin. (2020). *Quiet Supersonic Technology (QueSST).* Retrieved from https://www.lockheedmartin.com/en-us/news/features/2020/shaping-x59-quesst.html

Lu, H.Y. (1986, July 9-11). *An Empirical Model for Prediction of Coaxial Jet Noise in Ambient Flow*. 10th Aeroacoustics Conference, Seattle, WA, United States. doi: 10.2514/6.1986-1912

Lubert, C. P. (2017). Sixty Years of Launch Vehicle Acoustics. *Proceedings of Meetings on Acoustics*, 31(1), 040004, doi: 10.1121/2.0000704

Lush, P.A. (1971). Measurements of Subsonic Jet Noise and Comparison with Theory. *Journal of Fluid Mechanics*, 46(3), 477-500. doi: 10.1017/S002211207100065X

Lyrintzis, A. S. (2003). Surface Integral Methods in Computational Aeroacoustics—From the (CFD) Near-Field to the (Acoustic) Far-Field. *International Journal of Aeroacoustics*, 2(2), 95-128. doi: 10.1260%2F147547203322775498

Lyrintzis, A. S. (1994). Review: The Use of Kirchhoff's Method in Computational Aeroacoustics, *ASME Journal of Fluids Engineering*, 116(4), 665-676. doi: 10.1115/1.2911834

Lyrintzis, A. S., & Coderoni, M. (2020). Overview of the Use of Large-Eddy Simulations in Jet Aeroacoustics. *AIAA Journal*, 58(4). doi: 10.2514/1.J058498

Lyrintzis, A., & Mankbadi, R.R. (1996). Prediction of the Far-Field Jet Noise Using Kirchhoff Method, *AIAA Journal*, 34, 413-416. doi: 10.2514/3.13079

Malbéqui, P., Davy, R., & Bresson, C. (2015). Experimental Characterization of the Acoustics of the Future Ariane 6 Launch Pad. *7th European Conference for Aeronautics and Space Sciences*, 23-38. doi: 10.13009/EUCASS2017-38

Mankbadi, R. R. (1999). Review of Computational Aeroacoustics in Propulsion Systems. *AIAA Journal of Propulsion and Power*, 15(4), 504-512. doi: 10.2514/2.5472

Mankbadi, R.R. (1994). *Transition, Turbulence, and Noise*. Kluwer Academic Press, Boston, 1994. (republished by Springer, 2013).

Mankbadi, R. R. (1992). Dynamics and Control of Coherent Structure in Turbulent Jets. *Applied Mechanics Reviews*, 45(6), 219-248. doi: 10.1115/1.3121398

Mankbadi, R.R. (1991). Multifrequency Excited Jets. *Physics of Fluids*, 3(4), 595-605. doi: 10.1063/1.858121

Mankbadi, R. R. (1985a). On the Interaction Between Fundamental and Subharmonic Instability Waves in a Turbulent Round Jet. *Journal of Fluid Mechanics*, 160, 385-419. doi: 10.1017/S0022112085003536

Mankbadi, R. R. (1985b). The Mechanisms of Mixing Enhancement and Suppression in a Circular Jet Under Excitation Conditions. *Physics of Fluids*, 28(7), 2062-2074. doi: 10.1063/1.865387

Mankbadi, R. R., & Ali, A. A. (1999). Evaluation of Subsonic Inflow Treatments for Unsteady Jet Flow. *Journal of Computational Acoustic*, 7(3), 147-160. doi: 10.1142/S0218396X99000114

Mankbadi, M. R., & Georgiadis, N. J. (2015). Examination of Parameters Affecting Large-Eddy Simulations of Flow Past a Square Cylinder. *AIAA Journal*, 53(6), 1706-1712. doi: 10.2514/1.J053684

Mankbadi, R. R., Hayder, M. E., & Povinelli, L. A. (1994). The Structure of Supersonic Jet Flow and Its Radiated Sound. *AIAA Journal*, 31(5), 897-906. doi: 10.2514/3.12072

Mankbadi, R. R., Hixon, D. R, Shih, S. -H., & Povinelli, L. A. (1998). Use of Linearized Euler Equations for Supersonic Jet Noise Prediction. *AIAA Journal*, 36(2), 140-147. doi: 10.2514/2.7495

Mankbadi, R. R., Hixon, R., & Povinelli, L.A. (2000, June 12-14). *Very Large Eddy Simulations of Jet Noise* [AIAA 2000-2008]. 6th AIAA/CEAS Aeroacoustics Conference, Lahaina, HI, United States. doi: 10.2514/6.2000-2008

Mankbadi, R. R., & Liu, J. T. C. (1984). Sound Generated Aerodynamically Revisited: Large-Scale Coherent Structure in a Turbulent Jet as a Source of Sound. *Philosophical Transactions of the Royal Society of London. Series A, Mathematical and Physical Sciences*, 311, 183-217. doi: 10.1098/rsta.1984.0024

Mankbadi, R.R., & Liu, J.T.C. (1981). A Study of the Interactions between Large-Scale Coherent Structures and Fine-Grained Turbulence in a Round Jet. *Philosophical Transactions of the Royal Society of London. Series A, Mathematical and Physical Sciences,* 298, 54l-602. doi: 10.1098/rsta.1981.0001

Mankbadi, R., Lo, S. C., Lyrintzis, A., Golubev, V., Dewan, Y., & Kurbatskii, K. (2016). Hybrid LES-RANS Simulations of a Jet Impinging on a Flat Plate. *International Journal of Aeroacoustics*, 15(4-5), 535-553. doi: 10.1177/1475472X16642355

Mankbadi, R. R., Raman, G., & Rice, E. (1989, Jan 8-11). *Phase Development and Its Role on Subharmonic Control*. 28th Aerospace Sciences Meeting, Reno, NV, United States. doi: 10.2514/6.1990-503

Mankbadi, R. R., Shih, S-H, Hixon, D. R., & Povinelli, L. A. (2000). Direct Computation of Jet Noise Produced by Large-Scale Axisymmetric Structures. *Journal of Propulsion and Power*, 16(2), 207-215. doi: 10.2514/2.5585

Marcantoni, L. F. G., Tamagno, J. P., & Elaskar, S. A. (2012). High Speed Flow Simulation Using Openfoam. *Mecánica Computacional*, 31(16), 2939-2959.

Marchesse, Y., Gervais, Y., & Foulon, H. (2002). Water Injection Effects on Hot Supersonic Jet Noise. *Comptes Rendus Mécanique*, 330(1), 1-8. doi: 10.1016/S1631-0721(02)01418-3

Margason, R. (1993). Fifty Years of Jet in Cross Flow Research. *AGARD Meeting on Computational and Experimental Assessment of Jets in Cross Flow,* AGARD-CP-534 (Advisory Group for Aerospace Research and Development), 1, 1-141.

Martens, S., & Haber, L. (2008, June 9-13). *Jet Noise Reduction for High Speed Exhaust Systems* [GT2008-50455]. *ASME Turbo Expo 2008: Power for Land, Sea, and Air. Volume 6: Turbomachinery, Parts A, B, and C.*, 805-814, Berlin, Germany. doi: 10.1115/GT2008-50455

Martlew, D. L. (1969). Noise Associated with Shock Waves in Supersonic Jets. *AGARD CP* 42, 7-1-7-10.

McInerny, S. (1990, Oct 22-24). *Rocket Noise-A Review* [AIAA 1990-3981-CP]. 13th Aeroacoustics Conference, Tallahassee, FL, United States. doi: 10.2514/6.1990-3981

McLaughlin, D., Kno, C.W., & Papamoschou, D. (2008, Jan 7-10). *Experiments on the Effect of Ground Reflections on Supersonic Jet Noise* [AIAA 2008-22]. 46th AIAA Aerospace Sciences Meeting and Exhibit, Reno, NV, United States. doi: 10.2514/6.2008-22

Mead, C.J., & Strange, P.J.R. (1998, June 2-4). *Under-wing Installation Effects on Jet Noise at Sideline* [AIAA 1998-2207]. 4th AIAA/CEAS Aeroacoustics Conference, Toulouse, France. doi: 10.2514/6.1998-2207

Mengle, V.G., Elkoby, R., Brusniak, L., & Thomas, R.H. (2006, May 8-10). *Reducing Propulsion Airframe Aeroacoustic Interactions with Uniquely Tailored Chevrons: 3. Jet-Flap Interaction* [AIAA 2006-2435]. 12th AIAA/CEAS Aeroacoustics Conference (27th AIAA Aeroacoustics Conference), Cambridge, MA, United States. doi: 10.2514/6.2006-2435

Menter F.R., & Kuntz M. (2004). *Adaptation of Eddy-Viscosity Turbulence Models to Unsteady Separated Flow Behind Vehicles. The Aerodynamics of Heavy Vehicles: Trucks, Buses, and Trains*. Lecture Notes in Applied and Computational Mechanics, Springer, Berlin, Heidelberg, 19, 339-352. doi: 10.1007/978-3-540-44419-0_30

Menter F.R., Kuntz M., & Langtry, R. (2003). Ten Years of Industrial Experience with the SST Turbulence Model. *Turbulence, Heat and Mass Transfer*, 4(1), 625-632.

Mora, P., Baier, F., Kailasanath, K., & Gutmark, E.J. (2014). Acoustics from a Rectangular Supersonic Nozzle Exhausting Over a Flat Surface. *Journal of the Acoustical Society of America*, 140, 4130-4141. doi: 10.1121/1.4967158

Nagata, Y., Nonomura, T., Fujii, K., & Yamamoto, M. (2013). Analysis of Acoustic-Fields generated by Supersonic Jet Impinging on an Inclined Flat Plate and a Curved Plate. *International Journal of Aerospace and Lightweight Structures*, 3(3), doi: 10.3850/S2010428613000068

Nakai, Y., Fujimatsu, N., & Fujii, K. (2006). Experimental Study of Underexpanded Supersonic Jet Impingement on an Inclined Flat Plate. *AIAA Journal*, 44(11), 2691-2699. doi: 10.2514/1.17514

NASA. (2017). *Flying Wing Aircraft*. Retrieved from https://www.nasa.gov/content/flying-wing-a-regular-sight

NASA. (2017). *NASA-Boeing X-48C Hybrid Wing Body aircraft*. Retrieved from https://www.nasa.gov/topics/aeronautics/features/X-48_research_ends.html

Nonomura, T., Goto, Y., & Fujii, K. (2011). Aeroacoustic Waves Generated from a Supersonic Jet Impinging on an Inclined Flat Plate. *International Journal of Aeroacoustics*, 10(4), 401-425. doi: 10.1260/1475-472X.10.4.401

Nonomura, T., Honda, H., Nagata, Y., Yamamoto, M., Morizawa, S., Obayashi, S., & Fujii, K. (2015). Plate-Angle Effects on Acoustic Waves from Supersonic Jets Impinging on Inclined Plates. *AIAA Journal*, 54(3), 816-827. doi: 10.2514/1.J054152

Norum, T. (2004, May 10-12). *Reductions in Multi-Component Jet Noise by Water Injection* [AIAA 2004-2976]. 10th AIAA/CEAS Aeroacoustics Conference, Manchester, Great Britain. doi: 10.2514/6.2004-2976

Norum, T. D., & Seiner, J. M. (1982). Broadband Shock Noise from Supersonic Jets. *AIAA Journal*, 20(1), 68-73. doi: 10.2514/3.51048

Nossier, N. S., & Ho, C. (1982). Dynamics of an Impinging Jet – Part 2: The Noise Generation. *Journal of Fluid Mechanics*, 116, 379-391. doi: 10.1017/S0022112082000512

Osipov, V., Khasin, M., Hafiychuk, H., Muratov, C., Watson, M., & Smelyanskiy, V. (2015). Mitigation of Solid Booster Ignition Over Pressure by Water Aerosol Sprays. *Journal of Spacecraft and Rockets*, 52(3), 928-943. doi: 10.2514/1.A33110

Panda, J., & Mosher, R. (2013). Microphone Phased Array to Identify Liftoff Noise Sources in Model-Scale Tests. *Journal of Spacecraft and Rockets*, 50(5), 1002-1012. doi: 10.2514/1.A32433

Panda, J., & Mosher, R. (2011, Jan 4-7). *Use of a Microphone Phased Array to Determine Noise Sources in a Rocket Plume* [AIAA 2011-0974]. 49th Aerospace Sciences Meeting, Orlando, FL, United States. doi: 10.2514/6.2011-974

Panda, J., Mosher, R. N., & Porter, B. J. (2014). Noise Source Identification During Rocket Engine Test Firings and a Rocket Launch. *Journal of Spacecraft and Rockets*, 51(6), 1761-1772. doi: 10.2514/1.A32863

Papamoschou, D., & Mayoral, S. (2011, Jan 4-7). *Jet Noise Shielding for Advanced Hybrid Wing-Body Configuration*. 49th AIAA Aerospace Sciences Meeting including the New Horizons Forum and Aerospace Exposition, Orlando, FL, United States. doi: 10.2514/6.2011-912

Pierce, A. D. (1989). *Acoustics: An Introduction to Its Physical Principles and Applications*. New York, NY: Springer.

Podboy, G.G. (2012, June 11-15). *Jet-Surface Interaction est: Phased Array Noise Source Localization Results*. Proceedings of the ASME. Turbo Expo: Power for Land, Sea, and Air: Aircraft Engine; Ceramics; Coal, Biomass and Alternative Fuels; Controls, Diagnostics and Instrumentation, pp. 381-414, Copenhagen, Denmark. doi: 10.1115/GT2012-69801

Poinsot, T. J., & Lele. S. K. (1992). Boundary Conditions for Direct Simulation of Compressible Viscous Flows. *Journal of Computational Physics*, 101, 104-129. doi: 10.1016/0021-9991(92)90046-2

Powell, A. (1953). On the Mechanism of Choked Jet Noise. *Proceedings of the Physical Society of London, Section B*, 66(12), 1039-1056.

Powell, A., Umeda, Y., & Ishii, R. (1992). Observations of the Oscillation Modes of Choked Circular Jets. *Journal of the Acoustical Society of America*, 92(5), 2823-2836. doi: 10.1121/1.404398

Powers R.W., McLaughlin, D.K., & Morris, P. J. (2018). Noise Reduction with Fluidic Inserts in Supersonic Jets Exhausting Over a Simulated Aircraft Carrier Deck. *Journal of Aircraft*, 55 (1), 310-324. doi: 10.2514/6.2015-2374

Prasad, C., & Morris, P. (2019). Effect of Fluid Injection on Turbulence and Noise Reduction of a Supersonic Jet. *Philosophical Transactions of the Royal Society A*, 377(2159). doi: 10.1098/rsta.2019.0082

Ragaller, P. A., Annaswamy, A. M., Gustavsson, J. P. R., & Alvi, F. S. (2011). *Impinging Jet Noise Suppression Using Water Microjets*. 49th AIAA Aerospace Sciences Meeting including the New Horizons Forum and Aerospace Exposition, Orlando, FL, United States. doi: 10.2514/6.2011-913

Raman, G. (1999). Supersonic Jet Screech: Half-Century from Powell to the Present. *Journal of Sound and Vibration*, 225(3), 43-571. doi: 10.1006/jsvi.1999.2181

Raman, G., Rice, E.J., & Mankbadi R.R. (1988). Saturation and the Limit of Jet Mixing Enhancement by Single Frequency Plane Wave Excitation: Experiment and Theory [AIAA 1988-3613-CP], 1st National Fluid Dynamics Conference, Cincinnati, OH, United States. doi: 10.2514/6.1988-3613

Raman, G., & Rice, E. J. (1991). Axisymmetric Jet Forced by Fundamental and Subharmonic Tones. *AIAA Journal*, 29(7), 1114-1122. doi: 10.2514/3.10711

Salehian, S., Kurbatskii, K., Golubev, V. V., & Mankbadi, R. R. (2018, Jan 8-12). *Numerical Aspects of Rocket Lift-off Noise with Launch-Pad Aqueous Injection* [AIAA 2018-519]. 2018 AIAA Aerospace Sciences Meeting, Kissimmee, FL, United States. doi: 10.2514/6.2018-0519

Salehian, S., & Mankbadi, R. R. (2020a, Jan 6-10). *A Review of Aeroacoustics of Supersonic Jets Interacting with Solid Surfaces* [AIAA 2020-0006]. AIAA Scitech 2020 Forum, Orlando, FL, United States. doi: 10.2514/6.2020-0006

Salehian, S., & Mankbadi, R. R. (2020b). Jet Noise in Airframe Integration and Shielding. *Applied Sciences, 10(2), 511*. doi: 10.3390/app10020511

Salehian, S., & Mankbadi, R. R. (2020c). Simulations of Rocket Launch Noise Suppression with Water Injection from Impingement Pad. *International Journal of Aeroacoustics*, 19(3-5), 207-239. doi: 10.1177%2F1475472X20930653

Salehian, S., & Mankbadi, R. R. (2019). *Numerical Simulation of Acoustic Shielding Effect on Supersonic Jets* [AIAA 2019-3822]. AIAA Propulsion and Energy 2019 Forum, Indianapolis, IN, United States. doi: 10.2514/6.2019-3822

Schlinker, R. H. (1975). *Supersonic Jet Noise Experiments*. [Doctoral Dissertation, University of Southern California].

Sheplak, M., & Spina, E. F. (1994). Control of High-Speed Impinging-Jet Resonance. *AIAA Journal*, 32(8), 1583-1588. doi: 10.2514/3.12147

Shih, S. H., Hixon, D. R., & Mankbadi, R. R. (1997). Zonal Approach for Computational Aeroacoustics. *AIAA Journal of Propulsion and Power*, 13(6), 745-758. doi: 10.2514/2.5247

Shivashankara, B.N., & Blackner, A.M. (1997, May 12-14). *Installed Jet Noise* [AIAA 1997-1601-CP]. 3rd AIAA/CEAS Aeroacoustics Conference, Atlanta, GA, United States. doi: 10.2514/6.1997-1601

Sinha, A., Towne, A., Colonius, T., Schlinker, R. H., Reba, R., Simonich, J. C., & Shannon, D. W. (2018). Active Control of Noise from Hot Supersonic Jets. *AIAA Journal*, 56(3), 933-948. doi: 10.2514/1.J056159

Smagorinsky, J. (1963). General Circulation Experiments with the Primitive Equations. I. The Basic Experiment. *Monthly Weather Review*, 91(3), 99-164. doi: 10.1175/1520-0493(1963)091<0099:GCEWTP>2.3.CO;2

Southern I.S. (1980, June 4-6). *Exhaust noise in flight: The Role of Acoustic Installation Effects*. 6th Aeroacoustics Conference, Hartford, CT, United States. doi: 10.2514/6.1980-1045

Straka, M., Fiebach, A., Eichler, T., & Koglin, C. (2018). Hybrid Simulation of a Segmental Orifice Plate. *Flow Measurement and Instrumentation*, 60, 124-133. doi: 10.1016/j.flowmeasinst.2018.02.006

Strelets, M. (2001, Jan 8-11). *Detached Eddy Simulation of Massively Separated Flows*. 39th Aerospace Sciences Meeting and Exhibit, Reno, NV, United States. doi: 10.2514/6.2001-879

Tam, C. K. W. (2009). Mach Wave Radiation from High-Speed Jets. *AIAA Journal*, 47(10), 2440-2448. doi: 10.2514/1.42644

Tam, C. K. W. (1995). Supersonic jet noise. *Annual Review of Fluid Mechanics*, 27, 17-43. doi: 10.1146/annurev.fl.27.010195.000313

Tam, C. K. W., & Chen, P. (1994). Turbulent mixing noise from supersonic jets. *AIAA Journal*, 32, 1774-1780. doi: 10.2514/3.12173

Tam, C. K. W., & Dong, Z. (1994). Wall Boundary Conditions for High-Order Finite-Difference Schemes in Computational Aeroacoustics. *Theoretical and Computational Fluid Dynamics*, 6, 303-322. doi: 10.1007/BF00311843

Tam, C. K. W., Viswanathan, K., Ahuja, K. K., & Panda, J. (2008). The Sources of Jet Noise: Experimental Evidence. *Journal of Fluid Mechanics*, 615, 253-292. doi: 10.1017/S0022112008003704

Tam, C. K. W., & Webb, J. C. (1993). Dispersion-Relation-Preserving Finite Difference Schemes for Computational Acoustics. *Journal of Computational Physics*,107, 262-281. doi: 10.1006/jcph.1993.1142

Tam, C. K. W., & Zaman, K. B. M. Q. (2000). Subsonic Jet Noise from Non-Axisymmetric and Tabbed Nozzles. *AIAA Journal*, 38(4), 592-599. doi: 10.2514/2.1029

The Aviation Geek Club. (2020). *Military Aviation.* Retrieved from https://theaviationgeekclub.com/tag/f-22-raptor/

Thomas, R. H. (2003). *Aeroacoustics of Propulsion Airframe Integration: Overview of NASA's Research* [NOISE-CON Paper 105]. NASA Langley Research Center; Hampton, VA. United States. https://ntrs.nasa.gov/search.jsp?R=20030065859

Thompson, K. W. (1987). Time Dependent Boundary Conditions for Hyperbolic Systems. *Journal of Computational Physics*, 68(1), 1-24. doi: 10.1016/0021-9991(87)90041-6

Thompson K.W. (1990). Time-Dependent Boundary Conditions for Hyperbolic Systems, II. *Journal of Computational Physics*, 89(2), 439-461. doi: 10.1016/0021-9991(90)90152-Q

Thurow, B., Samimy, M., & Lempert, W. (2004). Compressibility Effects on Turbulence Structures of Axisymmetric Mixing Layers. *Physics of Fluids*, 15(6), 1755-1765. doi: 10.1063/1.1570829

Troclet, B., Alestra, S., Terrasse, I., Jeanjean, S., & Srithammavanh, V. (2007). Identification of Overpressure Sources at Launch Vehicle Liftoff Using an Inverse Method. *Journal of Spacecraft and Rockets*, 44(3), 597-606. doi: 10.2514/1.21577

Troclet, B., Chemoul, B., Roux, P., Gely, D., & Elias, G. (1999, Dec). *Synthesis of Vibroacoustic Studies Performed During ARIANE 5 Program* [ONERA-TP--01-038]. Office National d'Etudes et de Recherches Aerospatiales (ONERA), 92 – Chatillon, France. http://hdl.handle.net/10068/605

Trout, T. R., & McLaughlin, D. K. (1982). Experiments on the Flow and Acoustic Properties of a Moderate-Reynolds-Number Supersonic Jet. *Journal of Fluid Mechanics*, 116, 123-156. doi: 10.1017/S0022112082000408

Tsutsumi, S., Fukuda, K., Takaki, R., Shima, E., Fujii, K., & Ui, K. (2008, July 21-23). *Numerical Study on Acoustic Radiation for Designing Launch-Pad of Advanced Solid Rocket* [AIAA 2008-5148]. 44th AIAA/ASME/SAE/ASEE Joint Propulsion Conference & Exhibit, Hartford, CT, United States. doi: 10.2514/6.2008-5148

Tsutsumi, S., Kato, S., Fukuda, K., Takaki, R., & Ui, K. (2009, Jan 5-8). *Effect of Deflector Shape on Acoustic Field of Launch Vehicle at Lift-Off* [AIAA 2009-328]. 47th AIAA Aerospace Sciences Meeting including The New Horizons Forum and Aerospace Exposition, Orlando, FL, United States. doi: 10.2514/6.2009-328

Ubbink, O. (1997). *Numerical Prediction of Two Fluid Systems with Sharp Interfaces*. [Doctoral Dissertation, Imperial College of Science] London, England.

U.S Department of Defense. (2018). *F-14 Tomcat launching from the aircraft carrier USS Kitty Hawk.* Retrieved from https://www.defense.gov/observe/photo-gallery/igphoto/2001239179/

U.S Department of Defense. (2017). *U.S. Navy F/A-18E Super Hornet of Strike Fighter Squadron 115 launches from the flight deck of the aircraft carrier USS Ronald Reagan.* Retrieved from https://www.defense.gov/observe/photo-gallery/igphoto/2001841985/

Van Albada, G. D., Van Leer, B., & Roberts, W. (1997). A Comparative Study of Computational Methods in Cosmic Gas Dynamics. *Upwind and High-Resolution Schemes*. Springer, Berlin, Heidelberg, 95-103. doi: 10.1007/978-3-642-60543-7_6

Venkatakrishnan, V. (1993, Jan 11-14). *On the Accuracy of Limiters and Convergence to Steady State Solutions* [AIAA 1993-0880].1st Aerospace Sciences Meeting, Reno, NV, United States. doi: 10.2514/6.1993-880

Versteeg, H. K., & Weeratunge M. (2007). *An Introduction to Computational Fluid Dynamics: The Finite Volume Method*. Pearson Education, New York.

Viswanathan, K. (2004). Aeroacoustics of Hot Jets. *Journal of Fluid Mechanics*, 516, 39-82. doi: 10.1017/S0022112004000151

Viswanathan, K. (2002). Analysis of the Two Similarity Components of Turbulent Mixing Noise. *AIAA Journal*, 40, 1735-1744. doi: 10.2514/2.1878

Viswanath, K., Johnson, R., Corrigan, A., Kailasanath, K., Mora, P., Baier, F., & Gutmark, E. (2017). Flow Statistics and Noise of Ideally Expanded Supersonic Rectangular and Circular Jets. *AIAA Journal*, 3425-3439. doi: 10.2514/1.J055717

Vu, B. T., Moss, N. R., & Sampson, Z. (2014, June 16-20). *Multi-Phase Modeling of Rainbird Water Injection*. 44th AIAA Fluid Dynamics Conference, Atlanta, GA, United States. doi: 10.2514/6.2014-3076

Washington, D., & Krothapalli, A. (1998, June). *The Role of Water Injection on the Mixing Noise Supersonic Jet* [AIAA-1998-2205]. 4th AIAA/CEAS Aeroacoustics Conference, Toulouse, France. doi: 10.2514/6.1998-2205

Wilcox, D. C. (1998). *Turbulence Modeling for CFD*. La Canada, CA: DCW Industries, Inc.

Wiley, A., Choutapalli, I., Kumar, R., & Alvi, F. (2007, Jan 4-7). *Noise and Flowfield Characteristics of a Supersonic Jet Impinging on a Porous Surface* [AIAA 2010-273]. 48th AIAA Aerospace Sciences Meeting Including the New Horizons Forum and Aerospace Exposition, Orlando, FL, United States. doi: 10.2514/6.2010-273

Worden, T., Gustavsson, J., Shih, C., & Alvi, F. S. (2013, May 27-29). *Acoustic Measurements of High-Temperature Supersonic Impinging Jets in Multiple Configurations* [AIAA 2013-2187]. 19th AIAA/CEAS Aeroacoustics Conference, Berlin, Germany. doi: 10.2514/6.2013-2187

Yeoh, G. H., & Tu, J. (2009). *Computational Techniques for Multiphase Flows* (1st ed.). Amsterdam, Netherlands: Elsevier.

Zaman, K. B. M. Q., & Hussain, A. K. M. F. (1980). Vortex Pairing in a Circular Jet Under Controlled Excitation. Part 1: General Jet Response. *Journal of Fluid Mechanics*. 101(3), 449-491. doi: 10.1017/S0022112080001760

Zaman, K.Q., Fagan, A.F., Bridges, J.E., & Brown, C.A. (2015, June 22-26). *Investigating the Feedback Path in a Jet-Surface Resonant Interaction* [AIAA 2015-2999]. 21st AIAA/CEAS Aeroacoustics Conference, Dallas, TX, United States. doi: 10.2514/6.2015-2999

Zoppellari, E., & Juve, D. (1998, June 2-4). *Reduction of Hot Supersonic Jet Noise by Water Injection* [AIAA 1998-2204]. 4th AIAA/CEAS Aeroacoustics Conference, Aeroacoustics Conferences, Toulouse, France. doi: 10.2514/6.1998-2204

List of Publications

Salehian, S., Kurbatskii, K., Golubev, V. V., & Mankbadi, R. R. (2018, Jan 8-12). *Numerical Aspects of Rocket Lift-off Noise with Launch-Pad Aqueous Injection* [AIAA 2018-519]. 2018 AIAA Aerospace Sciences Meeting, Kissimmee, FL, United States. doi: 10.2514/6.2018-0519

Salehian, S., & Mankbadi, R. R. (2020, Jan 6-10). *A Review of Aeroacoustics of Supersonic Jets Interacting with Solid Surfaces* [AIAA 2020-0006]. AIAA Scitech 2020 Forum, Orlando, FL, United States. doi: 10.2514/6.2020-0006

Salehian, S., & Mankbadi, R. R. (2020). Jet Noise in Airframe Integration and Shielding. *Applied Sciences, 10(2), 511*. doi: 10.3390/app10020511

Salehian, S., & Mankbadi, R. R. (2020). Simulations of Rocket Launch Noise Suppression with Water Injection from Impingement Pad. *International Journal of Aeroacoustics*, 19(3-5), 207-239. doi: 10.1177%2F1475472X20930653

Salehian, S., & Mankbadi, R. R. (2019). *Numerical Simulation of Acoustic Shielding Effect on Supersonic Jets* [AIAA 2019-3822]. AIAA Propulsion and Energy 2019 Forum, Indianapolis, IN, United States. doi: 10.2514/6.2019-3822

APPENDIX A – Verification Benchmark: Pulsating Sphere

To validate the FWH formulation implemented in OpenFOAM, the pulsating sphere verification is tested, and presented here.

The pulsating sphere is modeled on the source boundary using the formulation documented by Pierce and Beyer (1989). In this test case, the parameters of the pulsating sphere, and specifications of the acoustic radiation medium are:

- Radius of the pulsating sphere: $R = 0.1\ m$
- Velocity oscillations:$\hat{v}_s = iU_0 \sin(2\pi f t)$
- Velocity amplitude: $U_0 = 0.01\ m/s$
- Frequency:$f = 100\ Hz$
- Speed of sound: $c = 100\ m/s$
- Density of gas: $\rho = 14.18 \frac{kg}{m^3}$

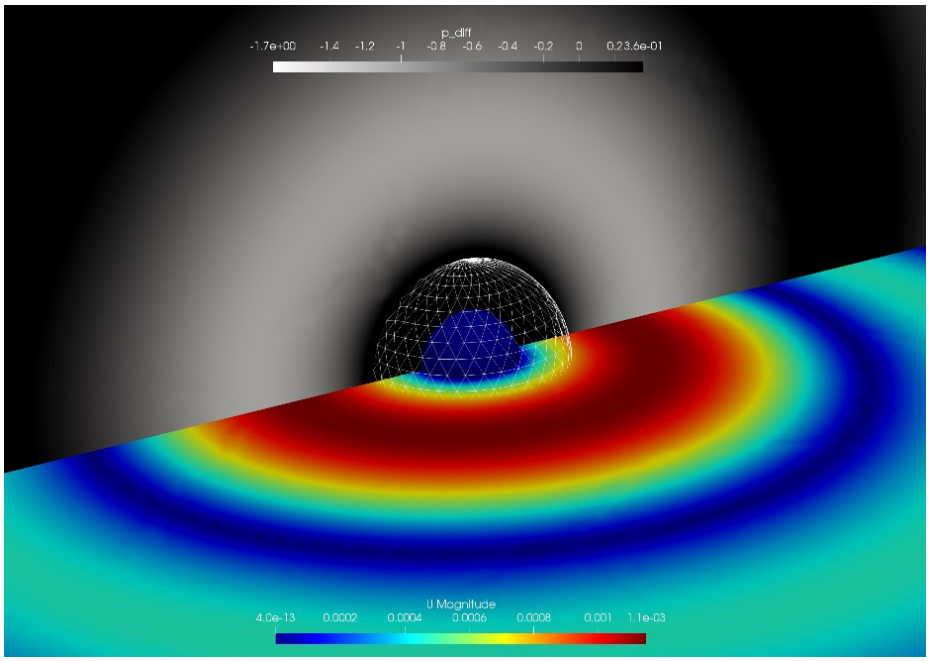

Figure A.1 Pulsating sphere and the FWH surface in the computational domain

Figure A.1 illustrates the pulsating sphere in the computational domain. Two FWH surfaces are used for this study. First one is right on the surface of the sphere, and the second one is at $2R$, shown as the white grid in the figure. The collected data from the two FWH surfaces are collected and compared with the analytical solution at the far field location of $r = 10R$. The analytical solution for the pulsating sphere is:

$$\hat{p} = Re\left(\frac{\rho c U_0 k R^2}{r(1+ikR)} U_0 \sin(2\pi f t)\, e^{-ik(r-R)}\right) \tag{A-1}$$

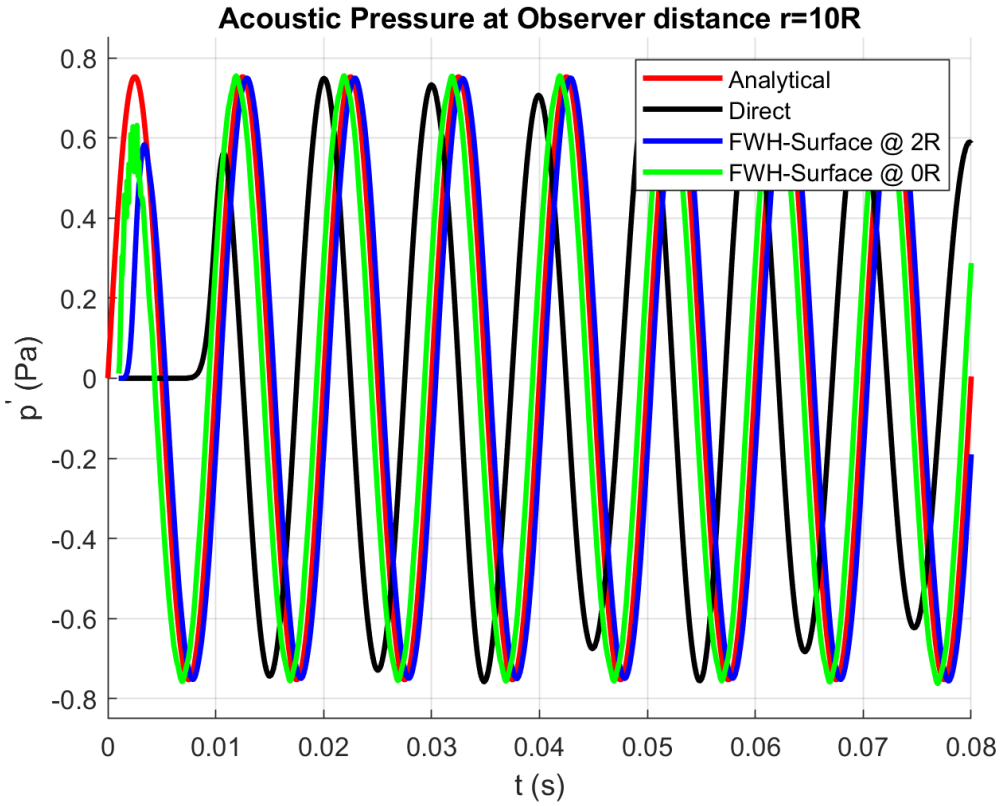

Figure A.2 Acoustic pressure time history at the observer location.

Figure A.2 illustrates the acoustic pressure time history at the observer location. The far field acoustics obtained from FWH formulations using both FWH surface input data

are compared with the analytical solution and the direct data from the coarse region of the grid. The FWH surfaces maintain the grid spacing of 15 cell points per wavelength, while the coarse region of the stretched-out observer location ion the computational grid has the grid spacing of equivalent to one cell point wavelength. Obviously, the direct data cannot predict the far field acoustics due to the low level of accuracy of the grid in this region.

The calculated acoustic time history from the FWH surface at 2R is in excellent agreement with the analytical data (less than 0.1% relative error).

APPENDIX B – Verification Benchmark: Shock Capturing

The Converging-Diverging Verification (CDV) Nozzle is a verification case involving the flow of inviscid, non-heat-conducting air through a converging-diverging nozzle. This is a classic one-dimensional, steady, compressible flow problem discussed in most compressible flow textbooks, such as Anderson (1984). The numerical results from OpenFoam "*rhoCentralFoam*" solver are compared with the data provided by NASA Glenn Research Center benchmark problem (Liou, 1987).

This case involves steady, inviscid, non-heat-conducting flow through a converging-diverging nozzle. The plenum total pressure and total temperature are assumed constant. The values used in this case are presented in below. The nature of the flow is determined by the exit static pressure, p_{exit}, to total pressure, p_o. Three values of exit static pressure are examined which result in three types of flows:

i. subsonic, isentropic flow ($p_{exit}/p_o = 0.89$)

ii. supersonic flow with a normal shock in the diffusing section ($p_{exit}/p_o = 0.75$)

iii. supersonic, isentropic flow ($p_{exit}/p_o = 0.16$)

To demonstrate the shock capturing capability of the solver, the coarse axisymmetric grid with the grid spacing of 24×200 is used from the benchmark database.

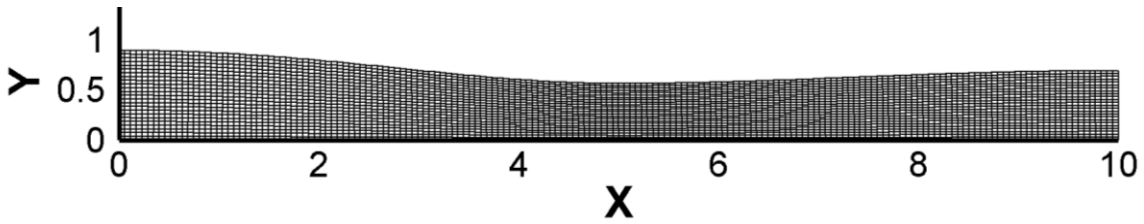

Figure B.1 Computational grid of the nozzle provided by NASA-GRC benchmark.

The comparison data consists of static pressures and Mach number distributions along the centerline of the nozzle as computed from one-dimensional, steady, inviscid, compressible flow theory.

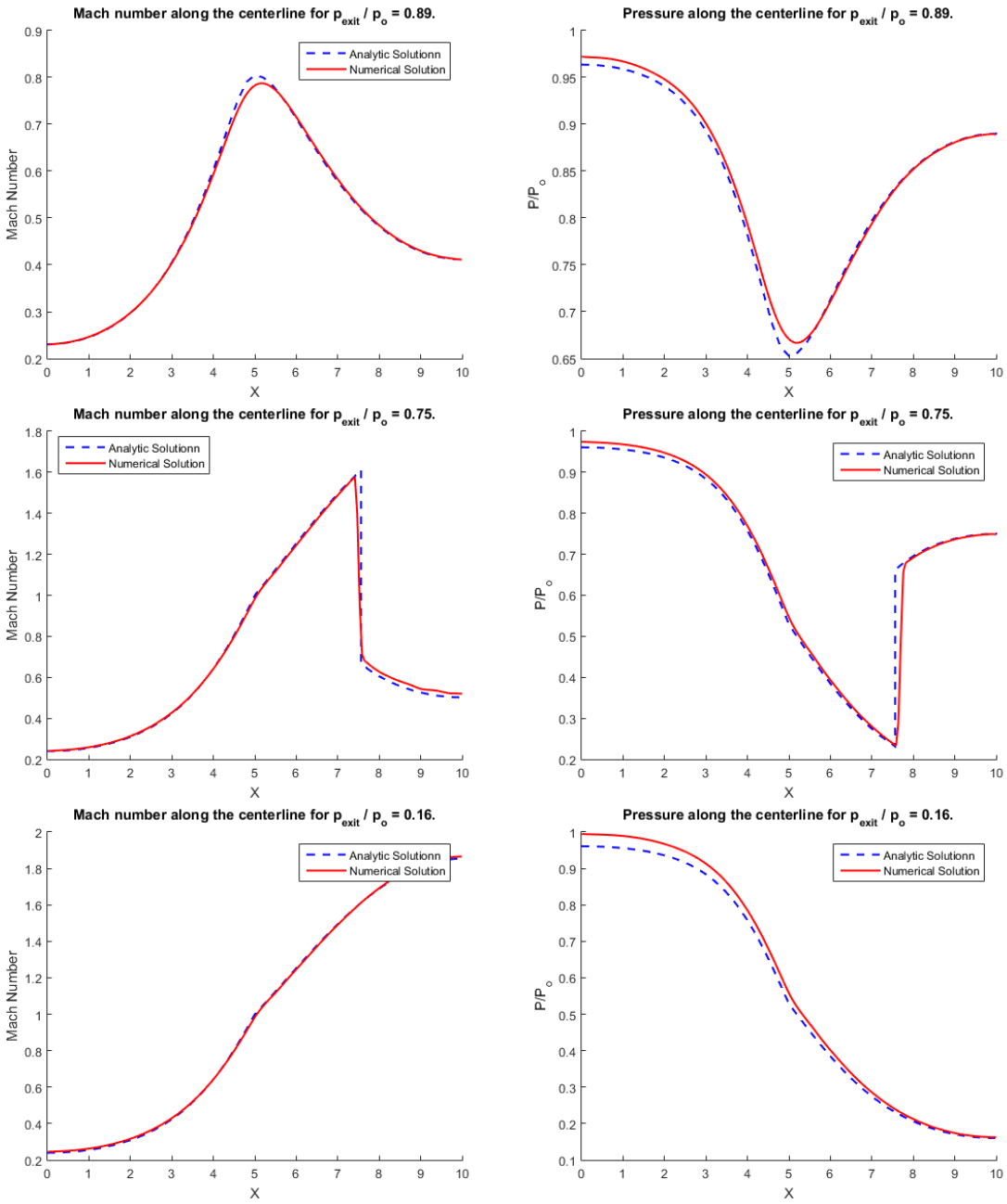

Figure B.2 Mach number (left) and static pressure (right) along the centerline for all 3 cases. Top *($p_{exit}/p_o = 0.89$),* Middle *($p_{exit}/p_o = 0.75$),),* Bottom *($p_{exit}/p_o = 0.16$).*

APPENDIX C – Verification Benchmark: Acoustic Reflection from Wall

To test the numerical accuracy for capturing the reflected acoustic wave in the case where the wall is at a distance from the nozzle exit, a simple benchmark problem is considered.

Consider the reflection of a two-dimensional acoustic pulse by a plane wall as investigated by Tam and Dong (1994) for finite difference numerical simulations. The fluid is inviscid and is at rest at time $t = 0$. An acoustic pulse is generated by an initial pressure disturbance with a Gaussian spatial distribution centered at $(0, 20)$. The wall is located at $y = 0$. The initial conditions are:

$$p = \epsilon\, exp(-\alpha[\, x^2 + (y - 20)^2]) \tag{C-1}$$

In addition, $\rho = p$, and $u = v = 0$. where, the pulse parameters are: $\epsilon = 0.01$, and $\alpha = \ln(2)\ /9$. This model problem is used to study the convection effect and to assess the quality of the imposed boundary conditions. The numerical simulation is non dimensional such that it can be compared with analytical solution. In the numerical simulation the time step Δt is set equal to 0.07677. This value of Δt satisfies the numerical stability requirement. On solid surfaces acoustic scattering takes place. Hence, the no-penetration rule is enforced by imposing $\partial p/\partial n = 0$ for pressure, and zero normal velocity $\boldsymbol{u}.\hat{n} = 0$. As mentioned earlier, since the acoustic equations are inviscid, only a condition for the normal component of the velocity is needed while the tangential component may slip at the wall.

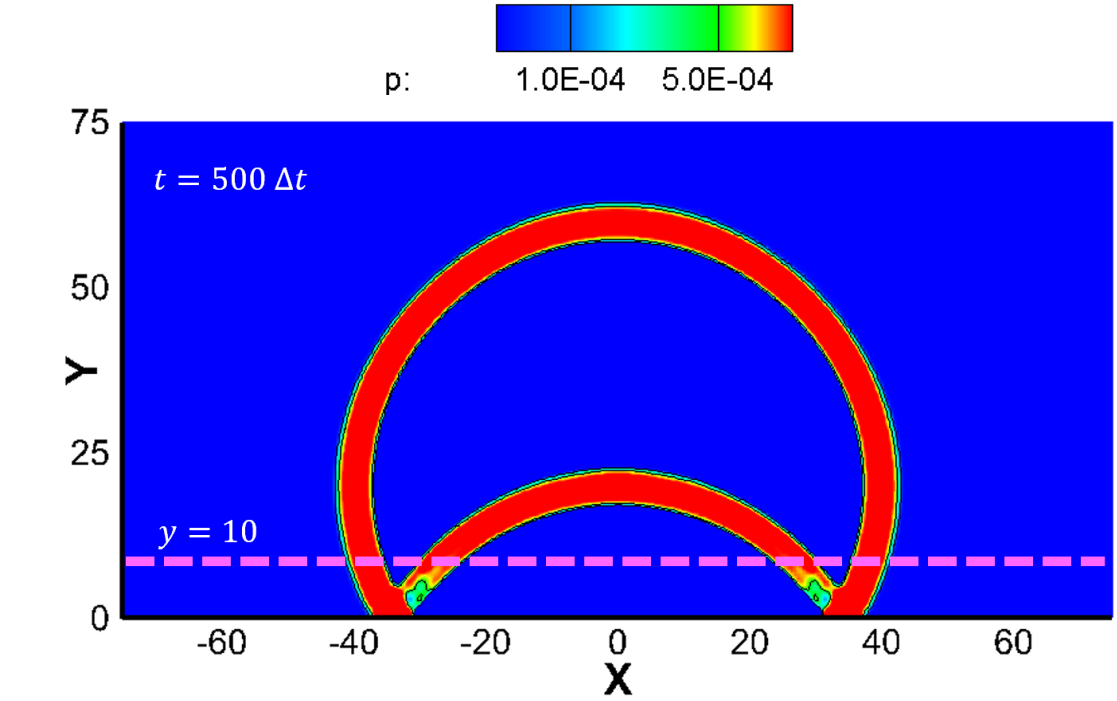

(a)

(---, $p = 5\ x\ 10^{-4}$ - - -, $p = 10^{-4}$ . . ., exact solution.)

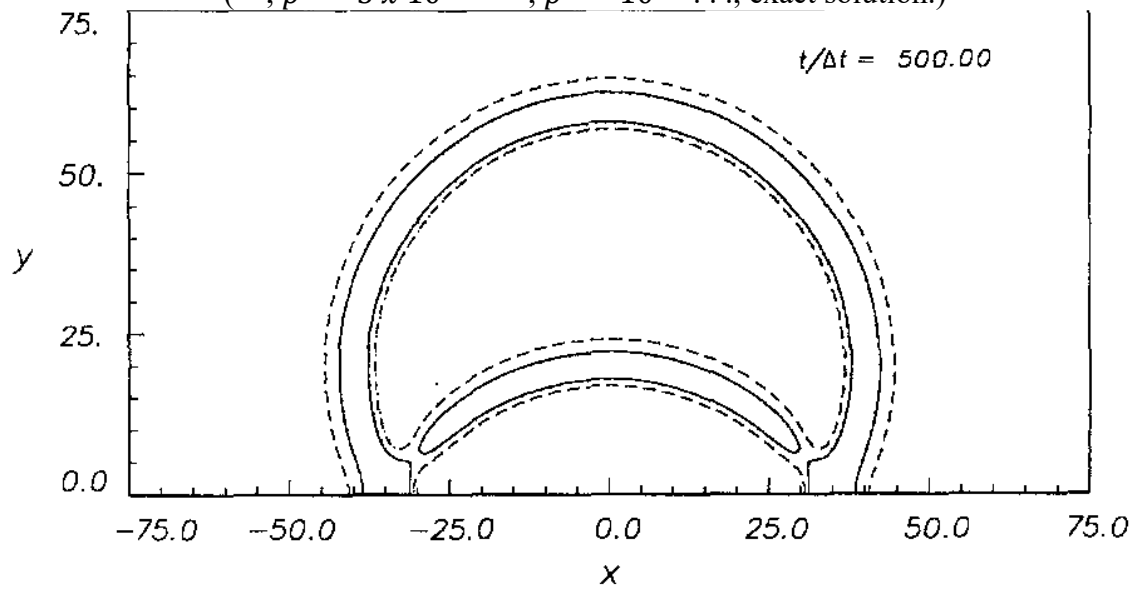

(b)

Figure C.1 Pressure contour patterns associated with the reflection of an acoustic pulse by a solid wall at y = 0. (a) Current numerical results, (b) Exact solution (Tam & Dong, 1997).

Figure C.1 shows the calculated pressure contour patterns associated with the acoustic pulse at 500-time steps, compared with results reported by Tam and Dong (1997). The corresponding contours of the exact solution are also plotted in this figure. At 500-time steps, the entire pulse has effectively been reflected off the wall creating a double pulse pattern; one from the original source and the other from the image source below the wall. The analytical solution is of this benchmark problem (Hardin et al., 1995) is:

$$p'(\boldsymbol{x},t) = \frac{\epsilon}{2\alpha}\int_0^\infty \left\{ e^{-\frac{\zeta^2}{4\alpha}} \cos(\zeta t)\,[J_0(\zeta\eta) + J_0(\zeta\xi)]\zeta \right\} d\zeta \qquad \text{(C-2)}$$

where $\eta = \sqrt{x^2 + (y-20)}$ and $\xi = \sqrt{x^2 + (y+20)}$. Here, J_0 is a Bessel function of the first kind and zero order.

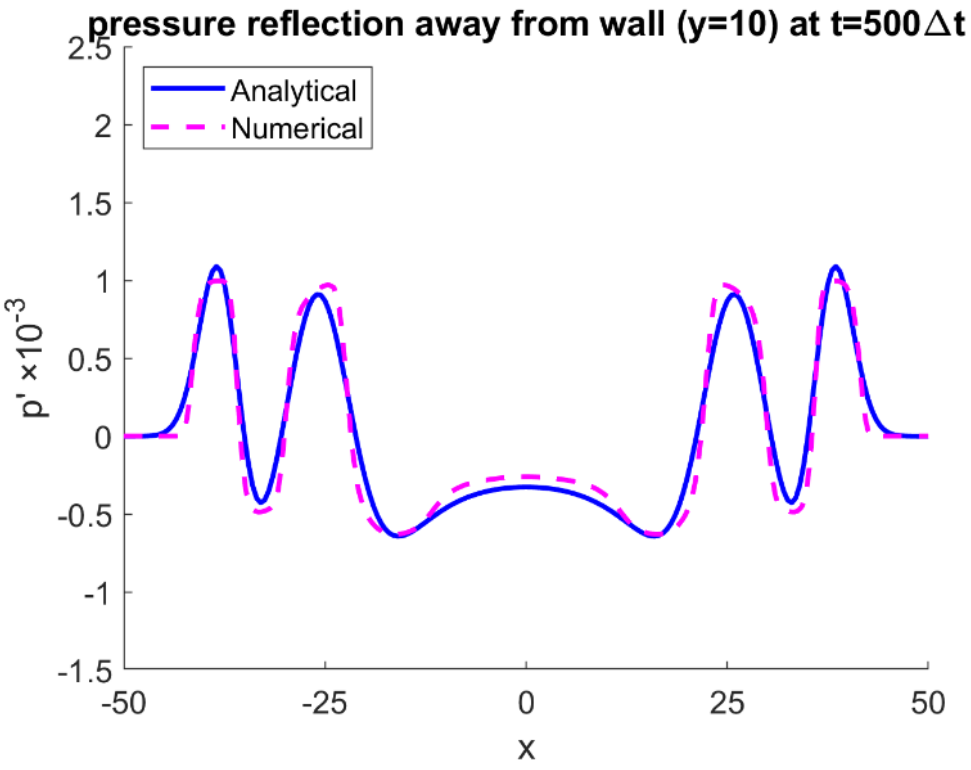

Figure C.2 Comparison of the reflected pressure patterns at 500-time steps along the y=10 line with the analytical solution.

Figure C.1 and C.2 prove that by using the boundary condition and numerical procedure mentioned in Chapter 3, the predicted reflected waves from the solid surface are calculated accurately, and the results perfectly agree with the analytical solution.